Dynamics and Nonlinearities of the Electro-Mechanical Coupling in Inertial MEMS

Luis Alexandre Rocha

Dynamics and Nonlinearities of the Electro-Mechanical Coupling in Inertial MEMS

Proefschrift

ter verkrijging van de graad van doctor
aan de Technische Universiteit Delft,
op gezag van de Rector Magnificus prof. dr. ir. J.T. Fokkema,
voorzitter van het College voor Promoties,
in het openbaar te verdedigen op 24 januari 2005 om 10:30 uur

door

Luis Alexandre MACHADO DA ROCHA

Licenciado em Engenharia Electrónica Industrial, Universidade do Minho, Portugal

geboren te Guimarães, Portugal

Dit proefschrift is goedgekeurd door de promotor:
Prof.dr.ir. G.C.M. Meijer

Toegevoegd promotor:
Dr.ir. R.F. Wolffenbuttel

Samenstelling promotiecommissie:

Rector Magnificus,	Technische Universiteit Delft, voorzitter
Prof.dr.ir. G.C.M. Meijer	Technische Universiteit Delft, promotor
Dr.ir. R.F. Wolffenbuttel	Technische Universiteit Delft, toegevoegd promotor
Prof.dr. P.J.French	Technische Universiteit Delft
Prof.dr. J.H. Correia	Universidade do Minho, Portugal
Prof.dr.rer.nat. G. Wachutka	Technische Universität München, Germany
Prof.dr. P. Enoksson	Chalmers University of Technology, Sweden
Dr. E. Cretu	Melexis, Belgium

ISBN: 90-8559-025-6

To my parents,

Para os meus pais,

TABLE OF CONTENTS

1

Introduction

1.1 Microengineering

Mankind is now in the beginning of the 21st century and in the middle of what is commonly referred to information society [1.1]. Information is everywhere and knowledge is just a click away. This is the era where man can spend years and years learning and still assimilates only a small amount of the global available knowledge. These are the times where for each problem solved, two or more new problems arise with increasing complexity, where human curiosity is never satisfied and keeps on searching, finding and discovering sometimes beyond what is humanely possible.

Naturally this global knowledge about the surrounding world has enabled a countless number of new devices and applications and a better understanding of the physics behind them [1.2]. The curiosity and desire to go beyond lead mankind to explore the outer space in the second half of the 20th century [1.3] and about the same time guided men to the exploration of the bottom, envisioned by Feynman [1.4]: "*What are the possibilities of small but movable machines? They may or may not be useful, but they surely would be fun to make*". It turned out that the miniaturization of mechanical parts - machines - is not

only fun to make but it is also useful and an increasing number of applications in a variety of industrial and medical fields are being pursued. The small miniaturized world opened the doors for a new engineering paradigm: ***Microengineering***.

Microengineering is the engineering field where multiple physical domains (electrical, mechanical, thermal, optical, chemical, magnetic) meet each other in the microscale range. Although small in size, it is an engineering field that evolved to a collection of technological capabilities that impact many disciplines. A subject field within the microengineering is the MEMS field. Microelectromechanical systems (MEMS) refer to mechanical devices that have a characteristic length of less than 1 mm but more than 1 μm, combining electrical and mechanical components and fabricated using integrated-circuit batch-processing technologies. Even if the definition is widely accepted, the name of the field varies from MEMS in USA to Microsystems in Europe and Micromechatronics in Japan. Feynman's vision has become a reality and this multidisciplinary field has witnessed explosive growth during the last decade.

Unlike Integrated Circuits (IC) where the explosive growth rate in the 1970´s culminated into a dominant technology (MOS circuitry) [1.5], the MEMS field shows a higher diversity and a slower learning curve [1.6]. Two complementary arguments can explain this trend: the state-of-the-art is best described by the fact that on one hand the technology is progressing at a very high rate, whereas on the other hand there is a huge technological diversity within the MEMS field. Most of the times (if not always) the rate of progress far exceeds that of our understanding of the physics involved. MEMS have a huge and recognized potential for innovation. However, the actual implementation is hampered by the multidisciplinary complexity. The result is an approach that is best described by leap forward rather than first trying to understand the problem and the physics involved. Rather than having reached maturity, the MEMS field has not yet evolved from the initial trial and error approach, and the lack of a solid foundation of the underlying fundamentals contribute to the failure of some proposed applications [1.6]. There are nevertheless, many successful applications and the MEMS market is estimated to reach $68 billion by 2005 according to NEXUS (The Network of Excellence in Multifunctional MicroSystems).

The objective of the work presented in this thesis is to provide a better understanding of some of the fundamental MEMS underlying mechanisms. The focus is on the electromechanical coupling and the emphasis on the dynamics and nonlinearities involved.

1.2 Electro-Mechanical Nonlinearities

A characteristic of MEMS devices is the strong coupling between the various domains involved. When the characteristic dimensions of the elements decrease from the macroscale level to the micrometer size, the effects related to the device volume, such as gravity become negligible as compared to surface effects such as adhesive and friction effects [1.7]. This implies that the reasoning based on the macroscopic level experience is no longer valid. The coupling between domains can therefore be much stronger than at the macroscale level and can be the incentive to some innovative applications [1.8].

The focus of this thesis is on the coupling between the electrical and mechanical domains for the particular case of electrostatically actuated parallel-plate devices. A lot of microdevices are included in this description: actuators, accelerometers and tunable capacitors are examples. All these devices have in common a mechanical structure that is actuated by electrostatic forces.

The coupling between electrical and mechanical domains is not exclusive of the MEMS field, and yet there are characteristics that are unique in MEMS. Electrical and mechanical coupling can be observed in electrical motors, air compressors and true RMS-to-DC converters. The last one is a very good example of the coupling between the electrical and mechanical domains at the macro level (Fig. 1.1).

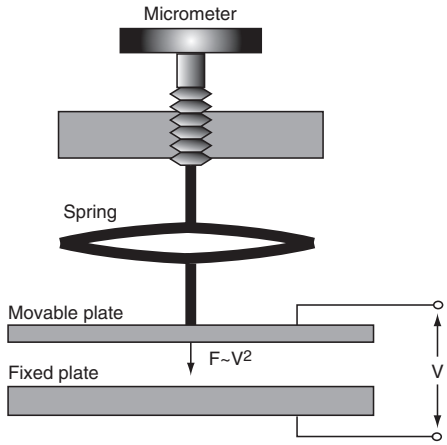

Figure 1.1 Electrostatic RMS voltmeter

The electrostatic voltmeter uses the attracting forces in a direction perpendicular to the capacitor plates [1.9]. The movable electrode is connected to a counteracting

mechanical spring and damping is provided by the air between the plates. If a voltage is applied to the capacitor electrodes an electrostatic force, proportional to the square of the voltage, is generated. The resulting displacement can be measured by using a micrometer. In this example the coupling between the mechanical and electrical domains enables the measurement of a electrical parameter (RMS value) through the measurement of a mechanical variable (displacement). Due to the construction and material properties the macro device is limited to very small displacements. Moreover, at high voltage levels, voltage breakdown occurs across the capacitor.

The uniqueness of the μ-domain results from the fact that device operation is not limited by electrostatic breakdown, but rather by *pull-in* of the microstructure. This property is due to Paschen's law, which indicates that breakdown in the narrow-gap regime is governed by the number of ionisable molecules available. Typical values are 10^8 V/m at a 5 μm wide gap [1.10]. Considering this value for breakdown voltage and the dimensions of a typical microstructure, breakdown is unlikely to take place at the μ-domain. Since the interaction between the electrical and mechanical domains becomes tighter with device miniaturization, interesting nonlinear phenomena are observed. The nonlinearities are mainly in the electrical domain (the electrostatic forces are inversely proportional to the square of the capacitor gap) and in the fluidic domain (the damping forces at the microscale level are highly nonlinear). A unique nonlinear feature of the electro-mechanical coupling is the "***pull-in phenomenon***". It was first reported in 1967 [1.11] when a resonant gate transistor (RGT) exploring the electro-mechanical coupling had to deal with this nonlinearity. If the same configuration of Fig. 1.1 is assumed for a microdevice and a voltage V is applied, an electrostatic force between the two electrodes is generated. Since the electrostatic force in a vertical field is inversely proportional to the square of the deflection and the restoring elastic force is, in a first approximation, linear with deflection, an unstable system results in case of a deflection, v, beyond a critical value, v_{crit}. The *pull-in voltage*, V_{pi}, is defined as the voltage that is required to reach the critical deflection. This unique MEMS characteristic has been subject of several studies [1.12]-[1.17] but there is still a lack of understanding of some static and dynamic aspects that might contribute for the improvement of a large number of applications. A promising new application is to exploit a particular meta-stable equilibrium during a nonlinear dynamic transition to achieve high sensitivity to perturbation forces.

Since pull-in depends mainly on dimensions, residual stress level and design, it has been used to characterize structural materials in surface micromachining processes [1.12], [1.13]. Unlike the case of the comb drive, which is based on area-varying capacitors, the design of vertical electrostatic actuators relies on gap-width varying capacitors and the pull-in phenomenon has to be considered [1.14]. Pull-in causes the displacement range due to electrostatic force to be limited to one-third of the gap between the electrodes, in case of a motion perpendicular to the capacitor plate orientation. This effect

also limits the dynamic range of capacitive accelerometers operating in the feedback mode. Charge drive (voltage drive with a series capacitance), rather than direct voltage drive can be used to circumvent pull-in, however, at the expense of attainable maximum force for given device dimensions [1.15]. Pull-in has also been proposed for use as voltage reference [1.16], [1.17].

1.3 Motivation

The unexplored potential of the dynamics of MEMS and their nonlinearities are the motivation for this work. A better understanding of the mechanisms behind the nonlinear electro-mechanical coupling leads to a more efficient device design and to the improvement of a variety of existing applications. The static and dynamic study of the pull-in phenomenon started as the main goal of the work, but the full nonlinear dynamic analysis performed goes beyond the scope of the pull-in phenomenon and at a certain point becomes a general analysis and modelling platform for the class of electrostatically actuated MEMS devices.

One of the objectives of this thesis was to build a general analytical modelling platform for electrostatically actuated MEMS devices. The modelling must provide sufficient detail about the physics involved along with a simple interface for a proper nonlinear dynamic analysis. The use of fabricated MEMS structures (Fig. 1.2) designed to exploit the electro-mechanical coupling brings the necessary experimental verification to the modelling platform and enables the actual exploitation of the nonlinear dynamics of electrostatically actuated MEMS.

The pursuit of a better understanding of the underlying mechanisms of the electro-mechanical coupling has been with the application in the sensor field in mind. I am convinced that the exploitation of the tight electro-mechanical interaction in MEMS will become essential in the global MEMS market and for serving key applications in the sensor field. The thesis presents this trend and some new applications are proposed. The fabricated structures play here a major role as they enable the experimental verification of the new proposed applications. The use of a mature fabrication technology directed the focus of the research towards the design, modelling and application issues rather than on technological issues.

It is the author's conviction that a smart integration of the MEMS structures into fully integrated microsystems, merging sensors, actuators and microelectronics based on

a good understanding of the physics involved will open the door to new applications and to the improvement of a variety of existing ones.

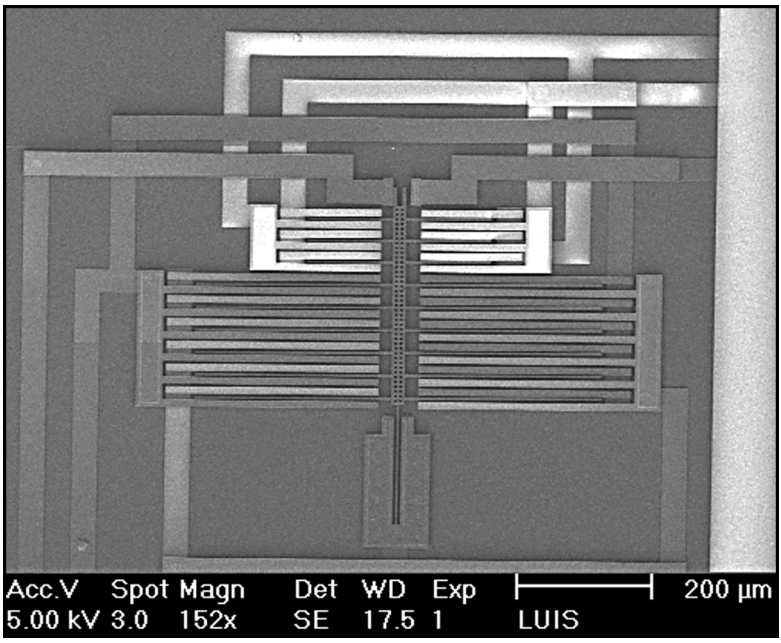

Figure 1.2 Fabricated microdevice

1.4 Organization of the Thesis

The work presented here started as a pull-in study and evolved towards the more global context of nonlinear dynamics in MEMS devices. This is also reflected in the thesis organization. Starting from the basic static pull-in analysis, the general understanding and modelling of the nonlinear dynamics of MEMS devices is achieved (chapters 3,4 and 5). The enhanced knowledge level of understanding obtained is subsequently used in several applications (chapters 6,7 and 8). Naturally any theory or analysis should be tested by experimental validation. The structures used during the work for experimental verification and the technology used to fabricate them are introduced in the beginning of the thesis.

Chapter 2 describes the surface micromachining technology used for fabrication of the devices designed and used during the work. The Bosch foundry has been used dur-

ing this work in the framework of the Europractice program. A short illustration of the fabrication process, together with an introduction to the fabricated devices, makes the content of this chapter.

The pull-in phenomenon is analysed and modelled from a static perspective in chapter 3. The analysis is performed for both one and two-degrees-of-freedom devices and the consistency of the modelling is proven by comparing the analytical models with finite element simulations and experimental results. Two different methodologies are used and the energy-based approach turns out to be the most appropriate method for the more complex configurations. Pull-in models are obtained for different electrostatic actuation modes (symmetric and asymmetric configurations) and for the bi-stable pull-in behaviour.

Chapter 4 makes the transition between the static and dynamic analysis and full large-signal dynamic models verified through experimentation are derived for the 1D and 2D case. Dynamic modelling is without doubt the most complex and challenging task in the MEMS field and a good understanding of the damping mechanism in MEMS devices is essential for a correct dynamic MEMS analysis. The damping analysis and modelling performed in this chapter is based on a strong and solid physical background and the enhanced knowledge acquired greatly benefits the nonlinear dynamic analysis performed in chapter 5.

The dynamic behaviour of electrostatically actuated parallel-plate devices is analysed both qualitatively and quantitatively in chapter 5. The diversity and complexity of dynamic behaviour as opposed to the more monotonous static behaviour is enhanced here. A general description of the nonlinear dynamics is pursued and the special case of a dynamic pull-in transition is analysed and modelled. Dynamic simulations and measurements prove the consistency of the dynamic analysis and open the window for some new applications.

As an application of the nonlinear dynamic analysis, a new voltage drive method for extended stable displacement range is introduced in chapter 6. The voltage drive pull-in limitation is amongst the most undesired nonlinear effects and the new proposed method enhances both the benefits of a solid foundation of the underlying mechanisms and the effectiveness of dynamic voltage drive.

In chapter 7, the nonlinear pull-in dynamic behaviour is the base for a high sensitivity accelerometer based on pull-in time. The innovative aspect of this concept is the use of a highly sensitive meta-stable force equilibrium to measure external disturbing forces. A full-system for dynamic pull-in operation is proposed and the system is analysed with respect to the device operation and the mechanical-thermal noise.

Chapter 8 introduces a new application based on the static pull-in behaviour. A voltage reference based on the pull-in voltage is analysed with respect to long-term stability. The theoretical temperature dependence is in agreement with measurements. This analysis has led to an electro-mechanical compensation technique capable to reduce this effect to a negligible level. The long-term stability analysis closes the pull-in study and highlights the long-term problems faced by pull-in based applications.

Finally, the last chapter summarizes the thesis and a new application is proposed by the author. It is the author's conviction that the dynamic applications proposed here are just a small glimpse of the full possibilities of exploring the MEMS dynamic behaviour. Exploring the potential of integrating digital signal processing and MEMS devices can lead to very interesting applications and opens the door to a new concept: ***Adaptive Mechanics***.

1.5 References

[1.1] European Commission, *IST 2000: Realising an Information Society for All*, Brussels, Belgium, 2000.

[1.2] S. Middelhoek and S.A. Audet, *Silicon Sensors*, Delft: TUDelft Press, 1994

[1.3] Nasa, *Apollo Program Summary Report*, Lyndon B. Johnson Space Center, Houston, USA, 1975.

[1.4] R.P. Feynman, "There's Plenty of Room at the Bottom" *in Miniaturization*, pp. 282-296, Reinhold Publishing, New York, 1961.

[1.5] R.F. Wolffenbuttel, *Silicon Sensors and Circuits: On-Chip Compability*, London: Chapman and Hall, 1996.

[1.6] S.D. Senturia, "Perspectives on MEMS, Past and Future: The Tortuous Pathway from Bright Ideas to Real Products" *in Proc. Transducers'03*, Boston, USA, June 8-12 2003, pp. 10-15.

[1.7] M. Wautelet, “Scaling laws in the macro-, micro- and nanoworlds”, *Eur. J. Phys.*, 22 (2001) 601-611.

[1.8] E. Cretu, *Inertial MEMS Devices, Modeling, Design and Applications*, PhD thesis, TUDelft, Delft, 2003.

[1.9] E.W. Golding, *Electrical Measurements and Measuring Instruments, 4th Edition*, Sir Isaac Pitman & Sons, Ltd, London, 1955

[1.10] T. Ono, D.Y. Sim and M. Esashi, “Micro Discharge and Electric Breakdown in a Micro Gap”, *J. Micromech. Microeng.*, 10 (2000) 445-451.

[1.11] H.C. Nathanson, W.E. Newell, R.A. Wickstrom and J.R. Davis, “The Resonant Gate Transistor”, *IEEE Trans. Electron Devices,* 14 (1967) 117-133.

[1.12] S.T. Cho, K. Najafi and K.D. Wise, “Internal Stress Compensation and Scaling in Ultrasensitive Silicon Pressure Sensors”, *IEEE Trans. Electron Devices,* 39 (1992) 836-842.

[1.13] P.M. Osterberg and S.D. Senturia, “M-Test: A test Chip for MEMS Material Property Measurement Using Electrostatically Actuated Test Structures”, *J. Microelectromech. Syst.,* 6 (1997) 107-118.

[1.14] H.A.C. Tilmans, and R. Legtenberg, "Electrostatically driven vacuum-encapsulated polysilicon resonators, Part 2, Theory and performance", *Sensors and Actuators*, A 45 (1994) 67-84.

[1.15] R. Nadal-Guardia, A. Dehé, R. Aigner and L.M.Castañer, "Current drive models to extend the range of travel of electrostatic microactuators beyond the voltage pull-in point”, *J. Microelectromech. Syst.*, 11 (2002) 255-263.

[1.16] A.S. Oja, J. Kyynäräinen, H. Seppä and T. Lampola, "A micromechanical DC-voltage reference", *in CPEM'00 Conf. Dig.*, Sydney, Australia, 14-19 May 2000, pp. 701-702.

[1.17] L.A. Rocha, E. Cretu and R.F. Wolffenbuttel, "Analysis and Analytical Modeling of Static Pull-In with Application to MEMS-Based Voltage Reference and Process Monitoring", *J. Microelectromech. Syst.,* 13 (2004) 342-354.

2

Technology Used for Fabrication of Devices

2.1 Introduction

To prove the new ideas and concepts introduced in this thesis, several sets of microelectromechanical devices were designed and fabricated. All these devices have been fabricated using Bosch surface/epi micromachining process [2.1], [2.2]. Bosch foundry services have been made available within the framework of Europractice multi-project wafer (MPW) runs. The use of a mature, well characterized and stable fabrication technology with a clear set of design rules helps decoupling the design process from the fabrication in the silicon foundry. This allows the research to focus more on the design and simulation, rather than on technology development. This chapter focuses exclusively on the technological aspects of the surface micromachining process used. First a brief description of the technology is presented. Next, the fabricated devices, with their main characteristics are shown.

The use of a surface/epi micromachining process with an active layer in excess of 10 μm, rather than the use of conventional surface or bulk micromachining processes had to do with the goal of the research. The process used is ideal for the fabrication of electrostatically actuated microstructures. The flexibility of the process enabled the design

of different structures suitable for nonlinear dynamic analysis and pull-in study. The relatively high thickness of the active layer provides sufficient sidewall area for electrostatic actuation and a sufficiently large capacitive change for capacitive readout measurement. Moreover the damping effect in this kind of devices is sufficiently high for a meaningful study of the physics involved. The same is difficult to accomplish if a surface micromachining (with active layer thickness of about 2 μm) is used. Conventional Bulk micromachining processes (without DRIE) are not so suitable for coupled electro-mechanical dynamical analysis, and do not present the same design freedom offered by surface/epi micromachining processes.

2.2 Bosch Surface Micromachining Process

The main characteristic of the Bosch surface micromachining process, usually referred to as the "Bosch-process", is the relatively thick polycrystalline silicon layer (10.6 μm), where the free-standing structures are to be defined. A patented RIE (Reactive Ion Etching) is used after the deposition of the polysilicon layer for structuring.

The fabrication process flow is presented in Fig. 2.1.

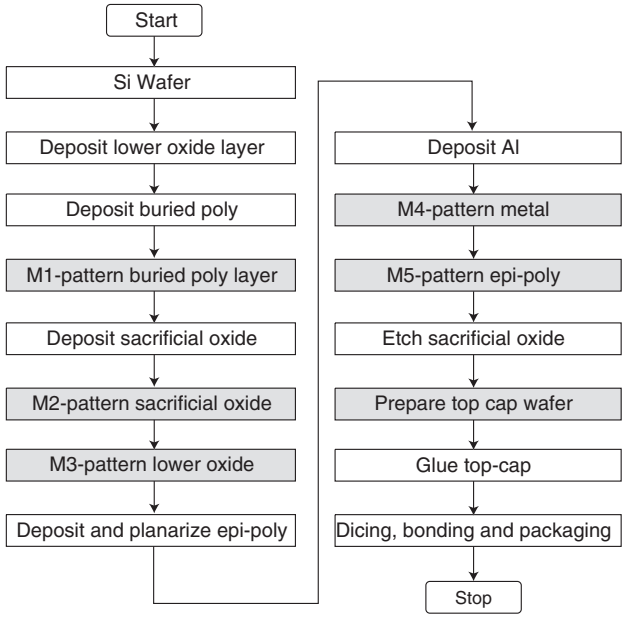

Figure 2.1 Bosch-process flow diagram

The process steps represented by a grey box in Fig. 2.1 are the structuring/etching phases using masks. The chip dimensions ($4.6 \times 4.9\ mm^2$) and bond pad positioning are standard for all the Multiple-Project-Wafer (MPW) designs, and so, the mask needed for top cap structuring is the same for all chips. From a design perspective, only 5 masks are to be submitted to the foundry service.

A brief description of each of the process steps is presented next:

1. The starting point is a 6" silicon wafer. It is the support of the chip. A thin layer of SiO_2 is then deposited to electrically separate the silicon substrate from the rest.
2. A thin polysilicon layer is subsequently deposited. It is often used as a buried interconnect layer for electrically shielding the active structure or for sensing when capacitive detection of the vertical movement of the active structure is required.
3. The buried polysilicon is patterned by using the first mask (M1). Fig. 2.2 provides an illustration of this step.

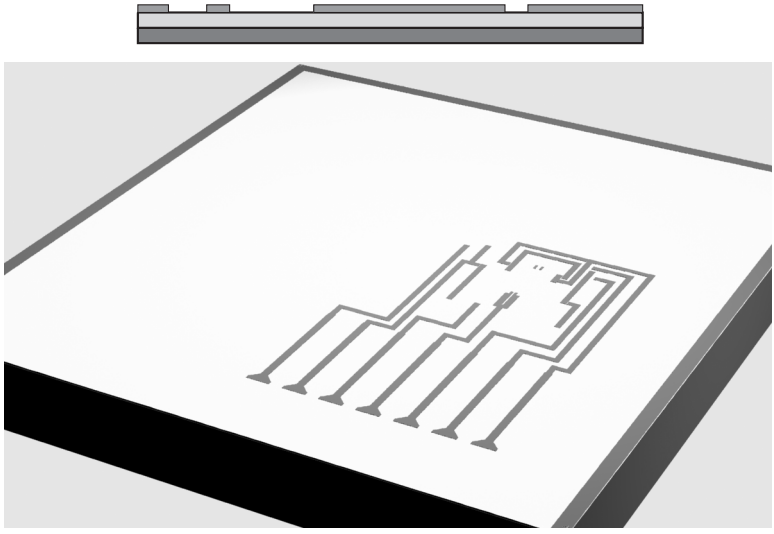

Figure 2.2 Patterning of the buried polysilicon layer

4. After structuring of the buried polysilicon, the sacrificial layer which in this process is SiO_2 is deposited. Plasma enhanced chemical vapour deposition (PECVD) is used for depositing the thin SiO_2 film in a single wafer process. In Chemical-Vapour Deposition (CVD) processes precursor gases (often diluted in

carrier gases) are delivered into the reaction chamber at room temperature. As they come into contact with a heated substrate they decompose and form a solid phase which is deposited. The other reaction products are extracted from the chamber.

5. The second mask (M2) is used for the etching of the upper oxide layer. The open etched holes are used to provide electrical connection between buried and active polysilicon layers and also mechanically anchor the active structure to the buried polysilicon. A 2D vertical section and a 3D image of this step are represented in Fig. 2.3.

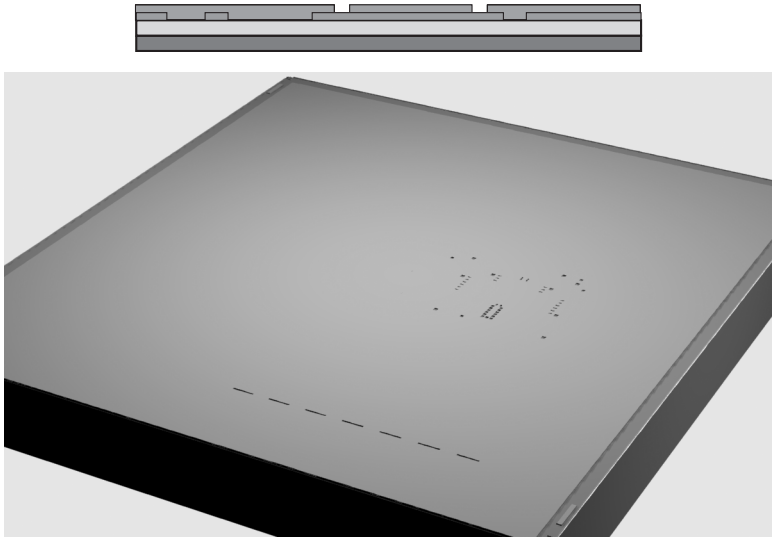

Figure 2.3 Deposition and etching of SiO_2 sacrificial layer

6. Next a third mask (M3) is used to realise a contact to the substrate by removing both oxide layers before growth of epitaxial silicon. This helps interconnecting the silicon wafer substrate to electrodes placed on the surface.

7. A thick epitaxial polysilicon layer is then deposited. This is the active layer where the movable structures are to be defined. Epitaxial growth at about 700 nm/min is used to yield a 10.6 μm thick polysilicon layer on top of the sacrificial oxide [2.3]. The main advantage for using an epitaxial reactor is the achievable growth rate. Because of the much higher temperatures growth rates 200 times bigger than in a conventional LPCVD reactor can be achieved.

8. After the deposition of the active polysilicon, a planarization step is performed in order to get a smooth surface.

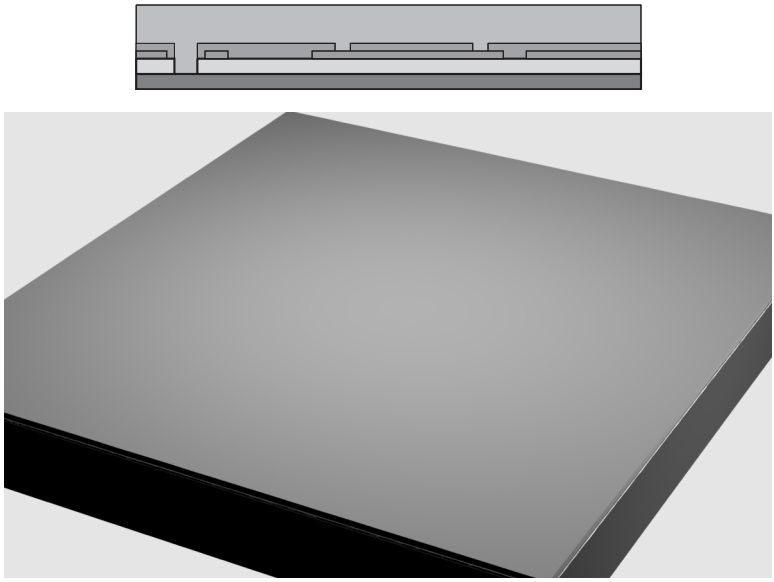

Figure 2.4 Epi-polysilicon deposition and planarization

9. An aluminium layer is deposited on the surface.
10. The metal layer is patterned using the fourth mask (M4). It is primarily used to define bond pads. Fig. 2.5 illustrates this process step.
11. The fifth mask (M5) is used for structuring the epi-polysilicon layer. This is the essential mask for the micromachined structures, as it defines the dimensions of the active polysilicon layer. A Bosch-patented Reactive Ion Process (RIE) is used [2.4]. This process is a deep reactive ion etching in an inductively coupled plasma (DRIE-ICP) [2.1] and is a fast and selective process with aspect ratios up to 20:1 (etch depth versus opening width). The anisotropy of the vertical etching step is set by time-multiplexing etching and passivation pulses. SF_6 plasma is used for the etch steps, while the side walls are covered with C_4F_8 during the passivation steps. The etching process stops when it reaches the silicon oxide of

the sacrificial layer. A very thin passivation layer is then deposited on the vertical walls. A 2D vertical section and a 3D image of this step are illustrated in Fig. 2.6.

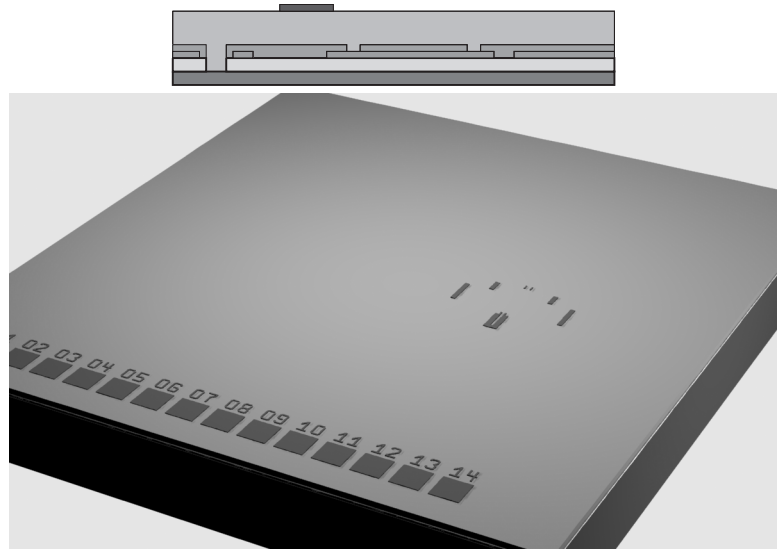

Figure 2.5 Metal deposition and patterning

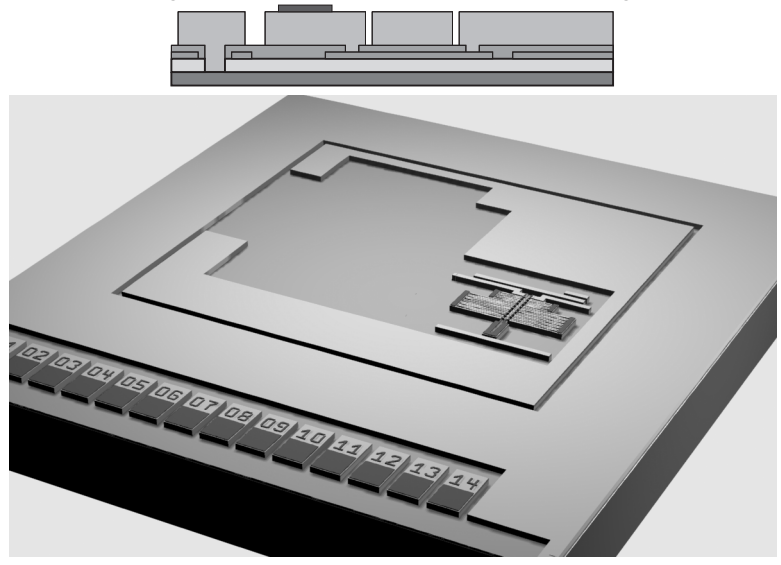

Figure 2.6 Patterning of the active polysilicon layer

12. Release of the structures by an isotropic etching step. The isotropic RIE etches the SiO_2 (through the holes created in the preceding step) under the structured active layer, while the vertical walls are protected by the deposited passivation layer. In the end, the structures are released, and the full free-standing geometry is defined.
13. A second silicon wafer is prepared and patterned for use as a top cap.
14. The movable MEMS structure is hermetically sealed by gluing the two wafers. The bondpads provide the connections to the structures under the top cap, using the buried polysilicon layer. 2D vertical sections in Fig. 2.7 illustrate the structure after oxide isotropic etching and top cap glueing.

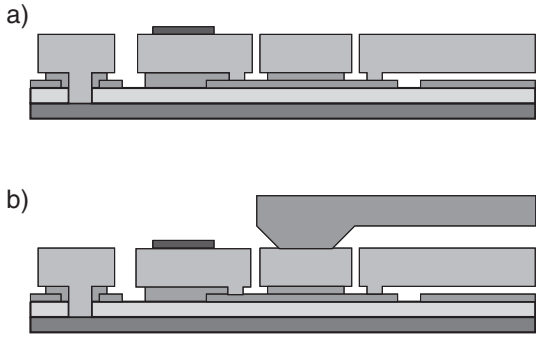

Figure 2.7 Vertical sections after a) RIE oxide etching and b) top cap glueing

15. The wafer is sawn and the individual dies are bonded and packaged into ceramic packages.

2.3 Fabricated Chips

Two chips with three different structures have been used during this work. They have been designed and fabricated using Bosch foundry services and were intended for the analysis and study of the nonlinear dynamics in parallel-plate electrostatic MEMS devices.

The first chip fabricated is shown in Fig. 2.8. It has two distinct MEMS structures. The one on top of Fig. 2.8 is an inverted balance structure (Fig. 2.9). It has a very peculiar 2 degrees-of-freedom (2-DOF) movement and has both the sensing and actuation capacitor pairs built as horizontal arms on the left and right side of the inertial central

bar mass component. The one below has a “classic” geometry, with folded beams as suspensions and separate gap-varying capacitors for sensing and electrostatic driving (Fig. 2.10). The suspension defines the dominant degree-of-freedom as the displacement perpendicular to the plane of the capacitors. As a consequence, the behaviour of the structure is described by a simple 1-DOF model, which makes it an excellent test structure for both static and dynamical analysis as compared to the more elaborated inverted balance structure. Both structures are independent and are accessible through the chip bondpads.

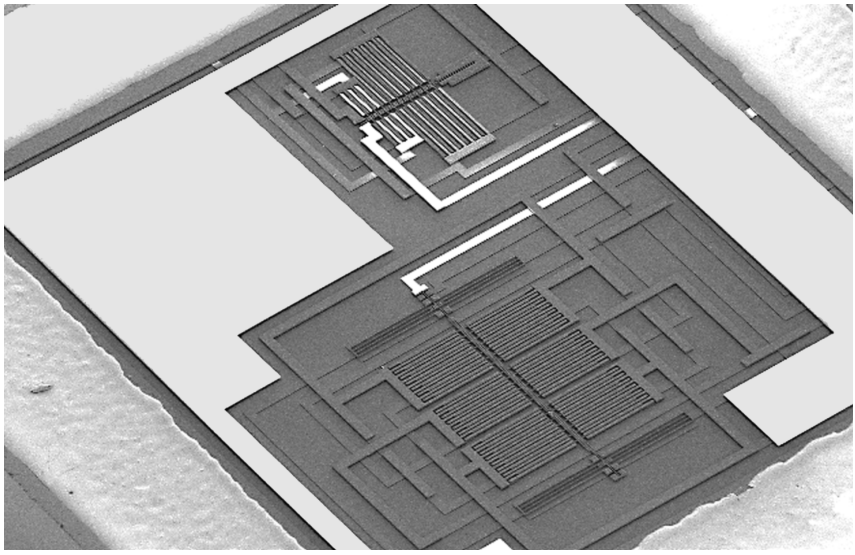

Figure 2.8 SEM photograph of a Bosch fabricated die

The Bosch process is very suitable for the fabrication of structures that incorporate both actuation and sensing capacitors with independent access from the exterior. The buried polysilicon layer is ideal for the interconnection of the various sets of capacitors and allows the design of very interesting capacitor combinations. The main limitation of the process is the maximum size of the free-standing structures. The maximum size is about 1 mm, which is small for applications that require many actuation/sensing electrodes. Another constraint is the relatively small mass of the structures. Even if the design is optimised for high mass values, the etch holes needed for the release of the free-standing structure limit the maximum achievable mass. Nevertheless, the combination of a mature technology with a good design flexibility made the Bosch process the obvious choice for the design of the devices needed for the nonlinear dynamic analysis pursued in this research.

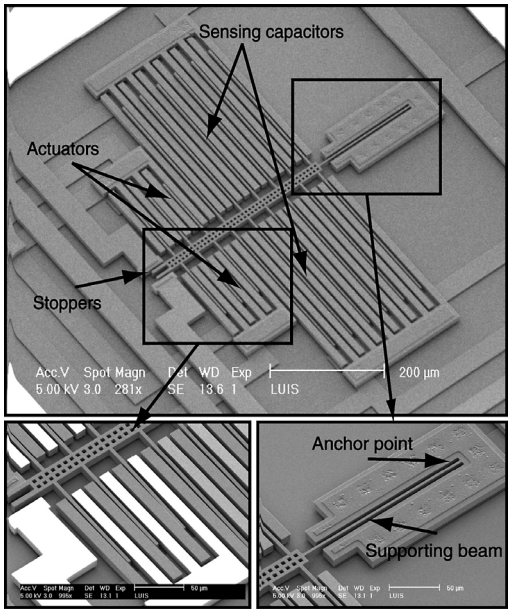

Figure 2.9 Fabricated inverted balance structure

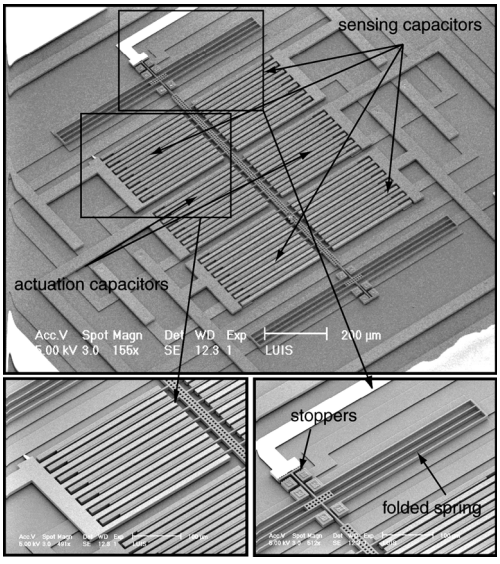

Figure 2.10 Fabricated structure with folded-beam suspension

The second chip fabricated is shown in Fig. 2.11, and contains two twin structures. The twin structures (Fig. 2.12) are an upgrade of the first fabricated 1-DOF device. They have a similar 1-DOF behaviour, but they are more robust (due to the geometry), more reliable, and due to the increased number of arms they have higher capacitance changes.

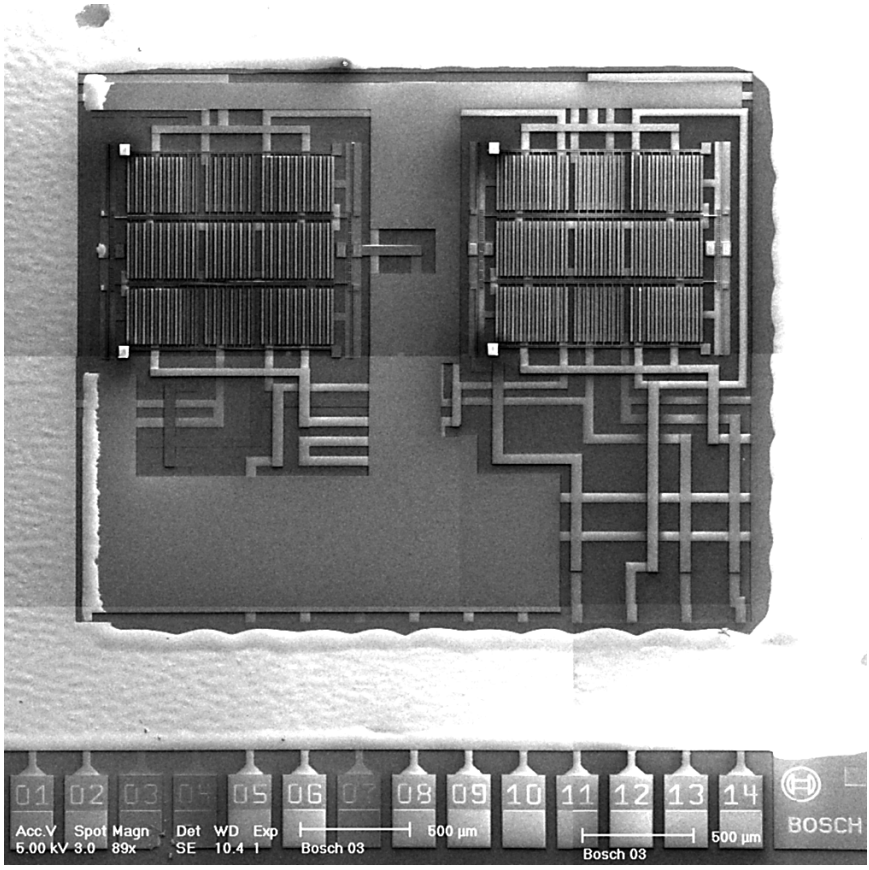

Figure 2.11 Photograph of one fabricated chip with two twin structures

Both chips are available either capped (hermetically sealed) with neon at $0.6 \times 10^5 Pa$ as the gas medium or uncapped (the structures are in contact with the air). This conveniently allows the study of the structure behaviour under different gas and pressure conditions.

All three structures are analysed in more detail in the next chapters. The use of a mature technology, as is the case of the “Bosch-process” allowed us to prove ambitious ideas without spending time on technology development and to verify various static and dynamic models.

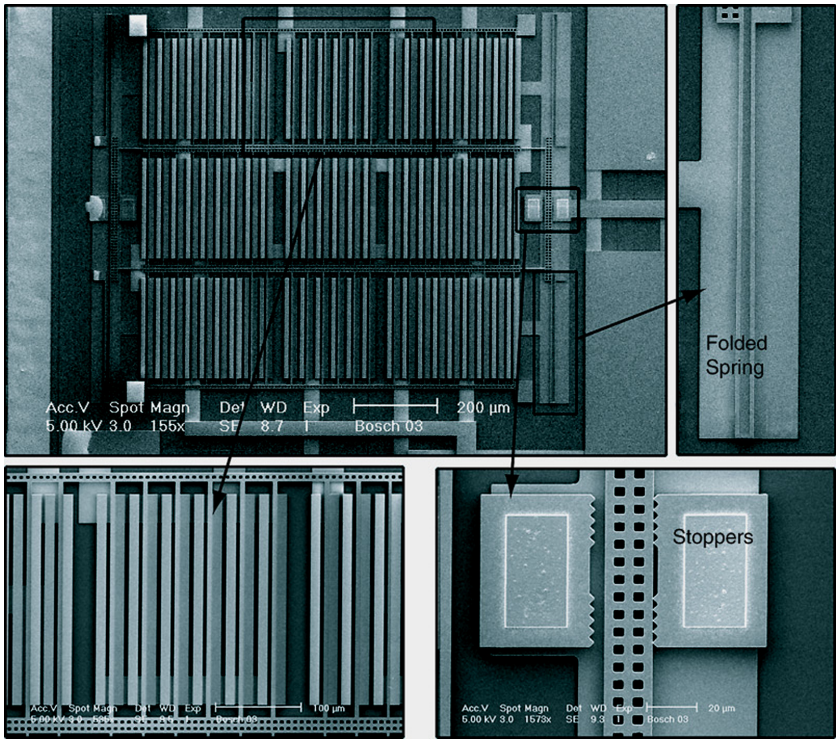

Figure 2.12 Photograph of a fabricated microdevice

2.4 References

[2.1] C. Gahn, S. Finkbeiner and M. Furtsch, “The Bosch Silicon Micromachining Foundry Service”, *in Proc. Eurosensors XVI*, Prague, Czech Republic, 15-18 September 2002, pp. 441-442.

[2.2] Bosch, *Silicon Surface Micromachining Foundry Design Rules*, version 3.0, 14 June 2002.

[2.3] M. Offenberg, F. Laermer, B. Elsner, H. Munzel and W. Riethmuller, “A Novel Process for a Monolithic Integrated Accelerometer”, *in Proc. Transducers’95*, Stocholm, Sweden, 25-29 June 1995, pp. 589-592.

[2.4] F. Laermer and A. Schilp, German Patent DE 4241045 (US-Pat. #5501893).

3

Nonlinear Static Analysis: The Pull-In Phenomenon

3.1 Introduction

In this chapter, a methodology that allows a mathematical description of the pull-in phenomenon is developed. The emphasis is on an enhanced understanding rather than the accuracy of the behavioural prediction. Pull-in is the loss of stability at a given state of the system and the stability study allows, for a given structure and dimensions, the computation of the evolution of the equilibrium points towards instability and the voltage at which stability is lost.

Two different levels of analysis of pull-in have to be considered at this point: *static* and *dynamic* pull-in analysis. When considering pull-in due solely to the electrostatic action, a static pull-in analysis is assumed. The inertia and damping terms are neglected in this simplified approach and the variation of the voltage is considered slow enough so that the equilibrium is at anytime obtained by the static components. The more universal approach is based on dynamic analysis, which takes into account the inertial and damping effects and the additional effect of an external acceleration. These may significantly change the pull-in voltage threshold. This chapter deals with static pull-in analysis only. Pull-in is analysed dynamically in chapter 5.

Pull-in has been modelled and experimentally verified in the scientific literature on the subject [3.1]-[3.9]. Since pull-in is governed by strongly nonlinear equations, the modelling approach has to deal with these nonlinearities: for most of the cases, a linearized model can not predict accurately the device behaviour and numerical iterative methods have to be employed instead of analytical methods.

This chapter starts by introducing the methodology for the pull-in study which is subsequently applied to the simplest one-degree-of-freedom (1-DOF) case. After the comparison of the models with experimental data, the method is extended to include the two-degrees-of-freedom (2-DOF) case. Similarly to the 1-DOF model, the simulation results are compared with experiments. The use of the simplest 1-DOF model gives the insight needed to understand the mechanisms involved in the pull-in effect. The more complex 2-DOF analysis and results provide the basis to extend the modelling to n-degrees of freedom devices. Starting with the simpler 1-DOF case enables the development of a path that almost naturally leads towards 2-DOF devices. Moreover this approach facilitates the detailed overview of the modelling framework.

3.2 Analysis Methodology

The basic phenomenon is the loss of stability of the equilibrium position. The device under analysis will move until a dynamic equilibrium of forces is obtained:

$$F_{inertia} + F_{damping} + F_{elastic} + F_{electrostatic} = 0 \quad \textbf{(3.1)}$$

The actuation voltage is included as a parameter, u, and the generalized displacement of the device as x. As inertia and damping forces are neglected on the static analysis, Eqn. (3.1) can be reduced to:

$$F_{elastic} + F_{electrostatic} = 0 \quad \textbf{(3.2)}$$

Both the electrostatic force ($F_{electrostatic} = F(x, u)$) and the elastic force ($F_{elastic} = -kx$) depend on the displacement x. The *equilibrium position,* x^*, for a given applied voltage u, is obtained by solving Eqn. (3.2). The stability study of the equilibrium position provides the necessary information to understand the system evolution, for changes in the parameter u.

Two methods are usually used for the analysis and modelling of the bifurcation of equilibrium positions:

1. *The dynamic system approach,* where the system is described by a set of differential equations. Basically after obtaining the governing equations with the behaviour of the electromechanical device the equilibrium points are obtained and an analysis of its stability is performed. This usually involves computing the equilibrium position, followed by a linearized stability analysis. For this purpose, the governing equations are expanded in a power series with respect to the considered state. The method is rather cumbersome for a symbolic computational approach or if variables that depend on time and position must be used (involving partial differential equations). However, this is the preferred method for implementation when using a simulator to solve the full nonlinear differential equation system.

2. *The variational approach - energy method.* The dynamical system is replaced by simpler mathematical models, namely by functions or functionals. With the gradient or variational derivative of these functions or functionals the corresponding equations to calculate the equilibrium positions which govern the long term behaviour of the system, are obtained. In practice, after obtaining the energy functional *U(x,u)*, the set of equilibrium points correspond to the solution of the equation:

$$\frac{\partial U}{\partial x}(x, u) = 0 \tag{3.3}$$

   The stability of the equilibrium points is given by the sign of the second variation of the functional *U(x,u)*, which for the one dimensional case is given by:

$$U_2 = \frac{\partial^2 U}{\partial x^2}(x, u) \tag{3.4}$$

   If $U_2 > 0$, then the equilibrium is stable. The changing in the sign of U_2 indicates the threshold of stability for the given equilibrium point.

   The energy method approach is possible if the following assumptions are satisfied: (1) it is assumed that the parameters are varied quasi-statically, (2) the forces acting on the system can be derived from a potential and (3) the points of interest are the equilibrium points and not the motion describing the transition between equilibrium states. This is the case when a static analysis on the pull-in is conducted.

Both approaches have strong and weak points. The dynamic approach grants a better understanding of the full system at the cost of the use of more complex differential equations. The energy method is more suitable for a pure analytical treatment. For more

complex cases this will be the preferred method for achieving analytical solutions or approximations.

3.3 1-DOF Pull-in Model

The device to be analysed is the lumped electromechanical structure depicted in Fig. 3.1. This is the general case of parallel plate electrostatic actuators and it is used as the vehicle to test the methodologies proposed.

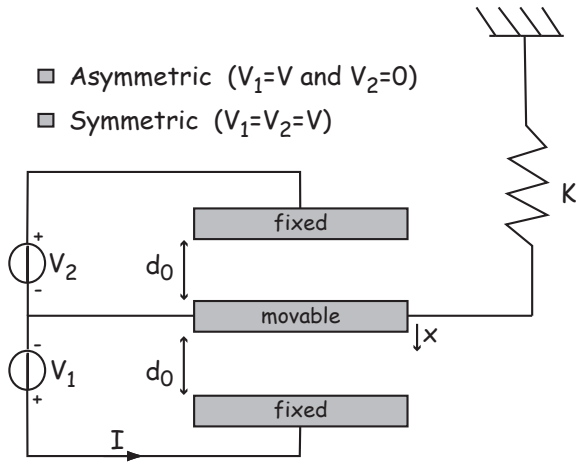

Figure 3.1 General lumped electromechanical device for pull-in analysis

The device allows two distinct modes of operation. The first mode, *asymmetric*, where $V_1=V$ and $V_2=0$. This is the simplest possible case and it is most frequently encountered in scientific literature on electrostatic actuation. The second mode, *symmetric*, with $V_1=V_2=V$ corresponds to the case where two fixed plates are on either side of a movable plate. The structure is operated symmetrically which implies that in the zero-voltage position the spacing between the two fixed electrodes and the movable is equal and both are actuated with the same voltage. Both modes of operation are analysed here in terms of pull-in voltage and release voltage.

3.3.1 Asymmetric Mode of Operation

The asymmetric mode is the classic situation of the parallel-plate case. Two parallel plates separated by an initial gap, d_0, and a linear elastic restoring force. The movable

plate has 1-DOF which varies the interplate distance. Both methodologies, dynamic approach and energy method are applied for the pull-in analysis.

3.3.1.1 Dynamic System Approach

Since just a static analysis is of interest, Eqn. (3.2) is used. The equilibrium position is obtained when the elastic force, $F_{elastic} = -kx$, balances the electrostatic one:

$$F_{electrostatic} = \frac{1}{2}C(x)V^2\frac{1}{(d_0 - x)} = \frac{1}{2}C_0V^2\frac{d_0}{(d_0 - x)^2} \quad \textbf{(3.5)}$$

Solving Eqn. (3.2) results in a polynomial equation of the 3rd order in x. For small values of the voltage V, the dependence of the forces on the displacement is shown in Fig. 3.2. Three equilibrium points can be seen (corresponding to the zeros of the 3rd order polynomial) in the graph. Two of them are in the interplate gap $x \in [0, d_0]$. The third, although mathematically correct, is impossible to reach from a physical point of view, since it is situated beyond the achievable mechanical displacement.

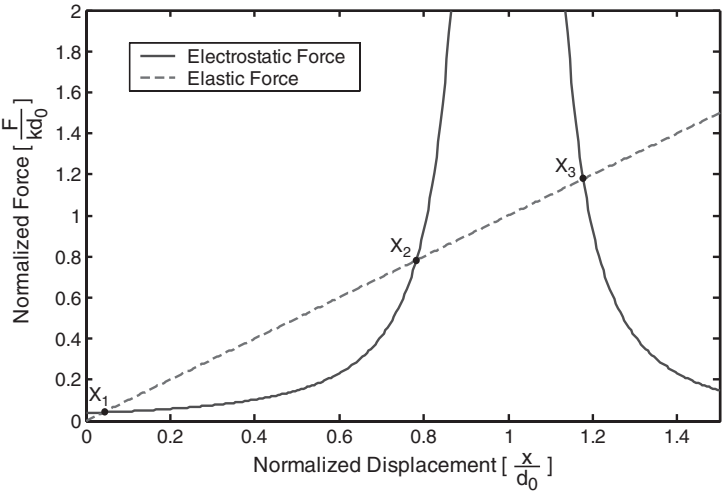

Figure 3.2 Variation of the system forces with x

Since solution X_3 is not important from the physical point of view, the focus of the analysis will be the interval [0, d_0]. In this interval there are two equilibrium solutions, X_1 and X_2, with the first stable and the second unstable. This can be seen by assuming small perturbations on the displacement x around the equilibrium positions. Around position X_1, a small increment of x, causes a larger restoring force ($F_{elastic}$) as compared

to the push-away one ($F_{electrostatic}$), restoring the equilibrium position. The same is true if x decreases. In this case the electrostatic force becomes larger than the elastic one moving the plate to its equilibrium point. For the unstable solution, X_2, any small perturbation on the equilibrium position, makes the pull-away force larger than the restoring force, pushing the displacement even further away from the initial equilibrium.

For small values of V, an equilibrium point exists and the system is stable. The question that needs to be answered is: at what voltage level does the system becomes unstable? To answer that an expression for the net force is written:

$$F_{net} = F_{eletrostatic} + F_{elastic} = \frac{C_0 d_0 V^2}{2(d_0 - x)^2} - kx, \tag{3.6}$$

and differentiated with respect to x:

$$\frac{\partial F_{net}}{\partial x} = \frac{C_0 d_0 V^2}{(d_0 - x)^3} - k \tag{3.7}$$

Stability requires:

$$\frac{\partial F_{net}}{\partial x} < 0 \Rightarrow k > \frac{C_0 d_0 V^2}{(d_0 - x)^3} \tag{3.8}$$

At the threshold of stability $F_{net} = 0$ and the critical point, x_{crit} is defined by:

$$k = \frac{C_0 d_0 V^2}{(d_0 - x)^3} \Rightarrow x = \frac{C_0 d_0 V^2}{2k(d_0 - x)^2} = \frac{d_0 - x}{2} \Rightarrow x_{crit} = \frac{d_0 - x_{crit}}{2} \Rightarrow x_{crit} = \frac{1}{3} d_0 \tag{3.9}$$

The pull-in (or snap-down) voltage, V_{pi}, is the necessary voltage to reach the critical deflection, x_{crit}, and can be obtained by inserting the critical displacement in Eqn. (3.2):

$$V_{pi} = \sqrt{\frac{8}{27} \frac{d_0^2 k}{C_0}} \tag{3.10}$$

For voltage levels higher than the pull-in voltage, the elastic force can no longer compensate for the electrostatic force and the movable plate will collapse towards the fixed one. In a practical device, electrical short-circuit should be avoided and the movable plate hits a mechanical stopper before it reaches the surface of the other plate.

3.3.1.2 The Variational Approach - Energy Method

The energy method is also used for the asymmetric mode of operation. The objective is to illustrate the application of the method rather than giving a new insight into the stability problem. The general configuration is the *asymmetric mode* of operation. The use of the energy method involves the sequential application of a procedure. Here it is used in the static pull-in analysis of the 1-DOF case:

1. An expression for the total potential energy as a function of the generalized coordinates in the mechanical (generalized displacement vector $\vec{x}$) and electrical domain (voltage parameter V) must be defined. In order to apply the principle of minimum potential energy, a closed system is necessary (the energy of the electric supply must be included).

   For the electromechanical system in analysis, the total energy can be written as:

   $$U(x, V) = U_{elastic}(x) + U_{electric}(x, V) \tag{3.11}$$

   Elastic Energy: the energy stored in the mechanical spring. Assuming a linear elastic regime the energy is:

   $$U_{elastic}(x) = \frac{1}{2}kx^2 \tag{3.12}$$

   Electrical Energy: the energy stored in the capacitor plus the energy of the electric supply. The energy stored in the capacitor for a constant voltage actuation is given by:

   $$U_{cap}(x, V) = \frac{1}{2}C(x)V^2 = \frac{1}{2}C_0V^2\frac{d_0}{(d_0 - x)} \tag{3.13}$$

   The energy stored in the voltage source considering the positive sense for the current I as drawn in Fig. 3.1 can be calculated by:

   $$\begin{aligned} U_{supply}(x, V) &= -\int VIdt = -\int VdQ = -C(x)V^2 \\ &= -C_0V^2\frac{d_0}{(d_0 - x)} \end{aligned} \tag{3.14}$$

   The total potential energy is the sum of the three partial energies:

$$U(x, V) = U_{elastic}(x) + U_{cap}(x, V) + U_{supply}(x, V) = \frac{1}{2}kx^2 - \frac{1}{2}C_0V^2\frac{d_0}{(d_0 - x)} \quad (3.15)$$

2. Determine the set of equilibrium positions, x^*, for a given voltage V, by minimizing the total potential energy. For the general case:

$$\frac{\partial U}{\partial x_i}(\vec{x}, V) = 0, \qquad i \in 1 \ldots n \Rightarrow x^* \quad (3.16)$$

3. The stability of the equilibrium positions is determined. The second variation is considered $\left(\frac{\partial^2 U}{\partial x_i \partial x_j}(x^*, V)\right)$ and the stability is given by the sign of the determinant of the equilibrium points. An equilibrium point is stable when:

$$\left|\frac{\partial^2 U}{\partial x_i \partial x_j}(x^*, V)\right| \geq 0 \quad (3.17)$$

4. The stability of the equilibrium points depends on the applied voltage. The pull-in voltage is determined from the condition of loss of stability of the equilibrium point.

Starting from the potential $U(x,V)$ defined in Eqn. (3.15), the first and second variations are computed and a study of the stability of the equilibrium positions, for changes on the control parameter V, is performed. A more generic representation of the parallel-plate case is achieved if a normalization of the energy and the variables of interest (x, V) is effectuated. This is useful, because the system can be fully characterized irrespective of the numerical values of the involved coefficients. The displacement, x, is normalized to the maximum achievable displacement:

$$x_n \equiv \frac{x}{d_0}, \quad (3.18)$$

so that it will vary between 0 and 1. The energy is normalized in respect to the maximum elastic energy:

$$U_n \equiv \frac{U}{\frac{1}{2}kd_0^2} \quad (3.19)$$

The normalization of the energy suggests the normalization for the voltage:

$$V_n \equiv \frac{V}{d_0 \sqrt{\frac{k}{C_0}}} \tag{3.20}$$

With the normalized variables the normalized total potential energy can be expressed as:

$$U_n(x_n, V_n) = x_n^2 - \frac{V_n^2}{1 - x_n} \tag{3.21}$$

For a given applied normalized voltage, V_n, the equilibrium position is determined from the critical point condition (minimization of the potential energy): $\frac{dU_n}{dx}(x_{n,eq}) = 0$, and the stability is checked by the sign of the second variation, $U_{n2} = \frac{d^2 U_n}{dx_n^2}(x_{n,eq})$. If $U_{n2} > 0$, the equilibrium position, $x_{n,eq}$ is stable. For $U_{n2} < 0$, the equilibrium position is unstable. If $U_{n2} = 0$ then higher derivatives have to be considered to check whether the equilibrium position, $x_{n,eq}$, is a local minimum or not. In traditional nonlinear theory this is called the *critical case in the sense of Ljapunov* [3.10]. In this case nonlinear behaviour dominates the stability of the solution and usually marks the transition from a stable to unstable behaviour. Therefore the critical case is used for determining the pull-in voltage.

The easiest way to determine the pull-in voltage and the position where the loss of stability occurs is to solve the system of equations:

$$\begin{cases} \frac{dU}{dx}(x, V) = 0 \\ \frac{d^2 U}{dx^2}(x, V) = 0 \end{cases} \tag{3.22}$$

for the variables (x_{crit},V_{pi}). The result is the same as for the dynamic approach and given by Eqn. (3.9) and Eqn. (3.10). The use of normalized variables makes the computation easier and the analysis is valid for any value of the spring constant, initial gap distance and zero-voltage capacitance.

An interesting analysis is to check the evolution of the equilibrium positions with increasing voltage. The equation of equilibrium points gives a set of three solutions that

can be plotted against the normalized applied voltage. The result is a *bifurcation diagram* for the generic parallel-plate case and it is shown in Fig. 3.3.

The stable equilibrium point, for $V_n \le V_{n,pi}$, is represented by the continuous line while the other two solutions are drawn with dotted lines. The equilibrium solution corresponding to $x_n > 1$, although stable, is physically impossible to achieve (does not satisfy the physical constraint $x_n \le 1$). The branch corresponding to the stable solution meets the unstable one at $V_n = V_{n,pi}$, and both roots become complex (conjugate) for $V_n > V_{n,pi}$. In the diagram, the branch continuing after $V_n > V_{n,pi}$ corresponds to the modulus of the two complex conjugate roots.

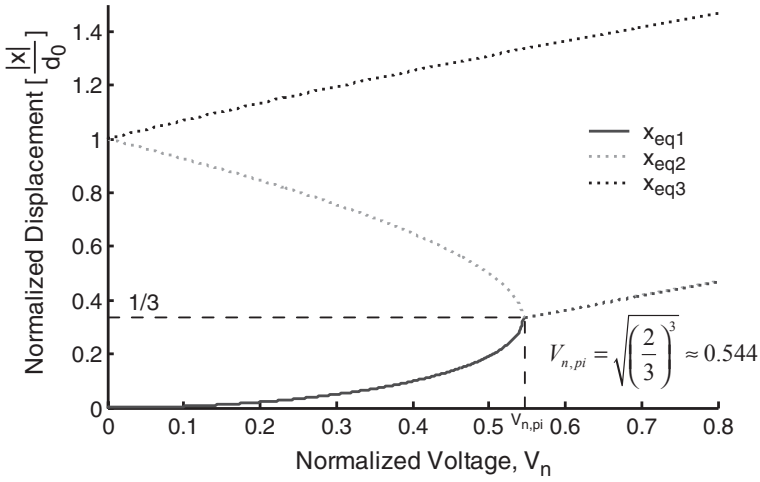

Figure 3.3 Bifurcation diagram for the asymmetric mode of operation

In conclusion the pull-in voltage for the 1-DOF asymmetric mode of operation is given by:

$$V_{pi,asym} = \sqrt{\frac{8}{27}} d_0 \sqrt{\frac{k}{C_0}} \tag{3.23}$$

The pull-in voltage depends just on device dimensions (capacitor and mechanical spring) and on the material properties. In what follows a pull-in analysis to the symmetric mode of operation is performed.

3.3.2 Symmetric Mode of Operation

This is the case where two fixed plates on either side of a movable plate, equally distanced in the zero-voltage position are actuated with the same voltage (see Fig. 3.1 with $V_1=V_2=V$). An intuitive analysis suggests that the symmetric drive would yield a larger pull-in voltage as compared to the asymmetric mode of operation. In the asymmetrically operated device, the electrostatic force is counteracted by the elastic beam force until the movable plate collapses at the pull-in threshold. In the symmetric case, however, the electrostatic fields are in a first approximation balanced. Since the *difference between the electrostatic forces is balanced by the elastic force* in the symmetric case, the pull-in is expected to be more abrupt and to take place at a larger value of the applied voltage as compared to asymmetric drive.

Once again both the dynamic system approach (equilibrium of forces) and the energy method are applied. If one uses the dynamic system approach the equilibrium position is obtained when the elastic force balances the two electrostatic forces:

$$\begin{aligned} F_{elect1} &= \frac{1}{2} C_0 V^2 \frac{d_0}{(d_0 - x)^2} \\ F_{elect2} &= -\frac{1}{2} C_0 V^2 \frac{d_0}{(d_0 + x)^2} \end{aligned} \tag{3.24}$$

The determination of the static equilibrium positions results in a polynomial equation of the 5th order in x. The five equilibrium points (resulting from the 5th order polynomial) can be seen in Fig. 3.4 for small values of the applied voltage, V. Two of them are outside the interplate gap $x \in [-d_0, d_0]$ (X_1 and X_5) while the remaining three are within the interval of interest.

A stability analysis to the three points inside the interplate gap, $\{X_2, X_3$ and $X_4\}$, reveals the existence of one stable point, X_3, and two unstable ones, X_2 and X_4. To find the voltage at which stability is lost a net force can be defined as:

$$F_{net} = \frac{1}{2} C_0 V^2 \frac{d_0}{(d_0 - x)^2} - \frac{1}{2} C_0 V^2 \frac{d_0}{(d_0 + x)^2} - kx\,, \tag{3.25}$$

and the derivative with respect to the displacement x is expressed as:

$$\frac{\partial F_{net}}{\partial x} = \frac{C_0 d_0 V^2}{(d_0 - x)^3} + \frac{C_0 d_0 V^2}{(d_0 + x)^3} - k \tag{3.26}$$

The equilibrium point X_3, which in the symmetric mode is constant (x=0), is stable for $\frac{\partial F_{net}}{\partial x} < 0$. This results in:

$$\frac{\partial F_{net}}{\partial x}(0, V) < 0 \Rightarrow \frac{2C_0V^2}{d_0^2} - k < 0 \Rightarrow V < \sqrt{\frac{kd_0^2}{2C_0}} \tag{3.27}$$

The two other equilibrium points inside the physical constraint, X_2 and X_4, are unstable for $V < \sqrt{\frac{kd_0^2}{2C_0}}$ and stable afterwards (but then they are not real and correspond to touch-down points).

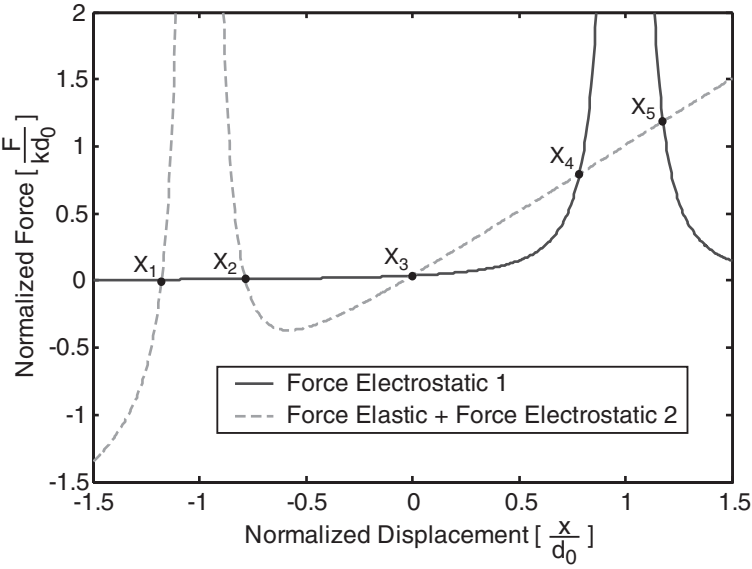

Figure 3.4 Variation of the symmetric system forces with x

The use of the variational approach implies the computation of the total potential energy of the system. In this case the total potential energy just needs an extra term, as compared to the asymmetric case, due to the electrostatic energy stored in the second capacitor. Analogous to the asymmetric case, and considering the energy from the voltage sources, the total potential energy is given by:

$$U(x, V) = \frac{1}{2}kx^2 - \frac{1}{2}C_0V^2\frac{1}{\left(1-\frac{x}{d_0}\right)} - \frac{1}{2}C_0V^2\frac{1}{\left(1+\frac{x}{d_0}\right)} = \frac{1}{2}kx^2 - C_0V^2\frac{1}{1-\left(\frac{x}{d_0}\right)^2} \tag{3.28}$$

Both the first and second variations of the potential are needed. The first variation results from taking the derivative of the potential with respect to x:

$$\frac{\partial U}{\partial x} = x\left(k - \frac{2C_0d_0^2V^2}{(d_0^2-x^2)^2}\right), \tag{3.29}$$

and the second variation results when the derivative of the first variation with respect to x is performed:

$$\frac{\partial^2 U}{\partial x^2} = k + C_0d_0V^2\left(\frac{1}{(x-d_0)^3} - \frac{1}{(x+d_0)^3}\right) \tag{3.30}$$

If the system of equations of (3.22) is solved using Eqns. (3.29) and (3.30) the pull-in voltage is found:

$$V_{pi} = \sqrt{\frac{1}{2}d_0^2\frac{k}{C_0}} \tag{3.31}$$

A more generic analysis is obtained by normalizing the variables considering Eqns. (3.18)-(3.20). The bifurcation diagram for the symmetric mode of operation using normalized variables is shown in Fig. 3.5. The five equilibrium positions are shown for increasing control parameter (applied voltage). The upper and lower curves, though stable, correspond to the equilibrium positions outside the physical domain. The continuous line correspond to the stable position ($x_n=0$), for $V_n<V_{n,pi}$ and the doted lines represent the remaining unstable positions for $V_n<V_{n,pi}$. The branch continuing after $V_n>V_{n,pi}$ correspond to the real part of the complex roots.

In conclusion, the pull-in voltage for the 1-DOF symmetric mode of operation is given by:

$$V_{pi,\,sym} = \sqrt{\frac{1}{2}}d_0\sqrt{\frac{k}{C_0}} \tag{3.32}$$

A comparison between the two discussed modes of operation leads to the following qualitative differences:

1. Unlike the asymmetric case, the equilibrium position *x=0* does not vary with applied voltage for symmetric operation.
2. A symmetrically driven device requires a larger value of the applied voltage (about 30%), as compared to asymmetric drive. This occurs because the elastic force equilibrates the difference between the two opposite electrostatic forces.
3. The pure symmetric case is an idealized situation. In practice small technology-related imperfections generate asymmetries that contribute to the lowering of the pull-in voltage. Experimental measurements show that the role of these technological imperfections is much stronger in the symmetric mode as compared to asymmetrically operated devices.

A short analysis to the two methods reveals that the energy method approach is more suitable for obtaining simplified analytic design formulas. It will be the preferred method for a global analysis of the more complex cases. The dynamic system approach provides a better understanding of the physics behind the pull-in phenomenon. It is more intuitive than the energy method but it can be rather complex for higher-order systems.

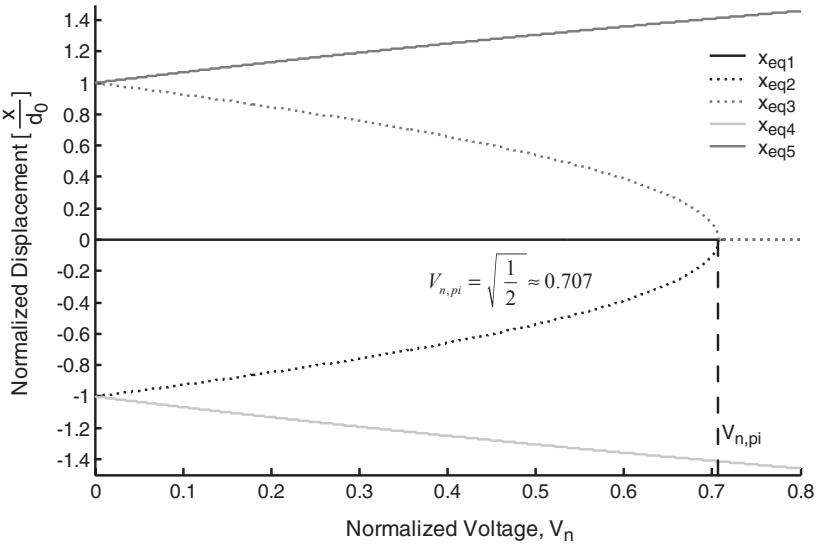

Figure 3.5 Bifurcation diagram for the symmetric mode of operation

3.3.3 Hysteresis of Pull-In

One important aspect associated with the pull-in phenomenon is its bi-stable regime that originates an electromechanical hysteresis [3.11],[3.12]. When pull-in occurs, there is an imbalance between the electrostatic and elastic forces and the resulting net force drives the movable part towards the fixed-electrode. In practice a mechanical stopper usually prevents the movable plate from reaching the counter-electrode, and thus avoiding short circuiting the capacitor electrodes. When the stopper is reached a reaction force develops, and the static equilibrium is re-established.

In this section the mechanisms behind the hysteresis will be analysed and modelled. It should be emphasized that the hysteresis in an electrostatic actuator is not due to a parasitic or practical device limitation such as sticking. Rather it is a fundamental feature. The stopper position is not the cause of hysteresis but it determines its magnitude.

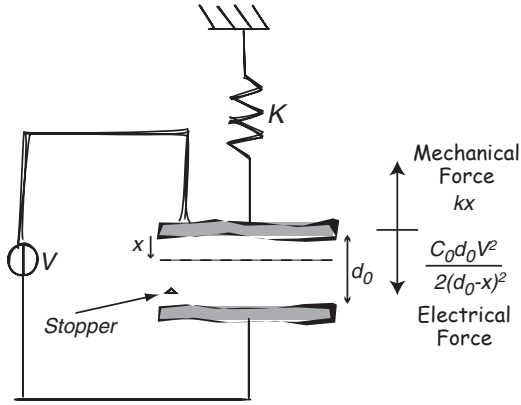

Figure 3.6 Simple parallel-plate configuration

The bi-stable regime associated with the pull-in phenomenon is analysed using the parallel-plate structure (asymmetric mode) of Fig. 3.6. The stopper is positioned somewhere between the values of the critical displacement ($x_{crit} = (1/3)d_0$) at pull-in and the full gap distance ($x = d_0$), to prevent the beam from hitting the counter-electrode and thus compromising reliability and short-circuiting the capacitor.

The normalization of the variables involved, using Eqns. (3.18) and (3.20), together with the normalization of the forces to the maximum elastic force:

$$F_n \equiv \frac{F}{kd_0} \ , \tag{3.33}$$

allows performing an analysis valid for any C_0, k and d_0. The normalized elastic and electrostatic forces are described by:

$$F_{n,elastic}(x_n) = x_n \tag{3.34}$$

$$F_{n,elect}(x_n, V_n) = \frac{V_n^2}{2(1-x_n)^2} \tag{3.35}$$

Fig. 3.7 illustrates the variation of the normalized electrostatic and elastic forces with the normalized displacement. Pull-In occurs when the elastic force can no longer balance the electrostatic one ($V_{pi}=V_4$). After pull-in the structure will stop at the designed stopper position (in this example at $x_n=0.6$), where the electrostatic force equals the sum of the elastic force with the reaction force of the stopper ($F_{reaction}$).

In this new equilibrium position the imbalance between electrostatic and elastic forces ($F_{n,elect}(0.6,V_4)$ in Fig. 3.7) is higher than at the pull-in onset ($x_n = 1/3$). A lower voltage ($V_r=V_3$) is required to reach a balance between the electrostatic and elastic forces ($F_{n,elect}(0.6,V_3)$ in Fig. 3.7). There are two distinct displacement solutions for this equilibrium of forces (the reaction force of the stopper becomes zero, $F_{reaction}=0$). As already seen in the previous sections the larger displacement solution is unstable, leading to the release of the movable part back to the lower equilibrium position when the voltage decreases below a critical release voltage (V_r). The hysteresis amplitude is reduced when moving the displacement constraint, as imposed by the mechanical stopper position, closer to the critical displacement at pull-in.

The goal of the hysteresis model is to find the release voltage, V_r, at which the elastic force equals the electrostatic one at the stopper position. For the 1-DOF case that can be done by solving the equation:

$$\frac{dU}{dx}(x, V) = 0, \tag{3.36}$$

in V, and considering the known stopper position as the displacement x. If the stopper is placed at the normalized position ($y_n \equiv y/d_0$) the following expression for the release voltage is found (asymmetric mode of actuation):

$$V_{r,asym} = (1-y_n)\sqrt{2y_n}d_0\sqrt{\frac{k}{C_0}} \tag{3.37}$$

Similarly, for the symmetric case the release voltage can be expressed as:

$$V_{r,sym} = \frac{(1-y_n^2)}{\sqrt{2}} d_0 \sqrt{\frac{k}{C_0}} \tag{3.38}$$

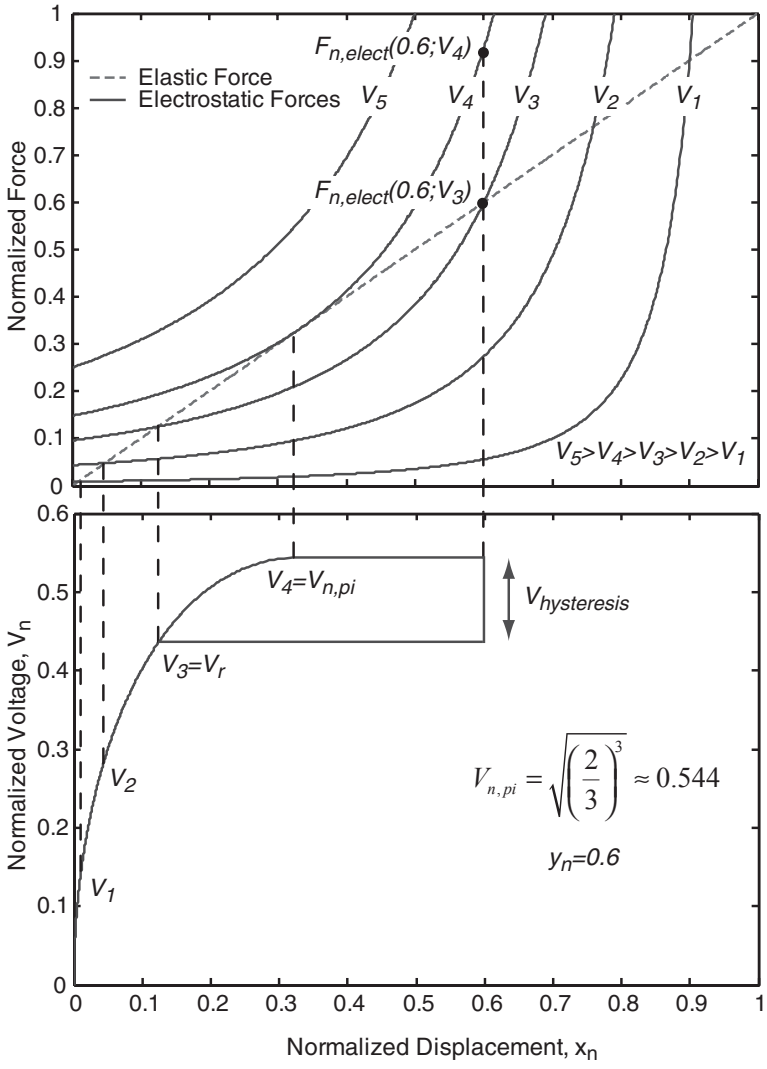

Figure 3.7 Explaining hysteresis

3.4 Experimental Results for the 1-DOF Pull-In Model

One of the designed devices presented in chapter 2 is used as a test structure for experimental validation of the pull-in models (Fig. 3.8). It is basically a laterally (1-DOF only) movable beam with folded beam suspension at both ends and electrodes extending perpendicular to the axial direction. Three sets of electrodes in the same plane are used. One set for electrostatic actuation in the direction normal to the electrode area and the other two for capacitive displacement measurement.

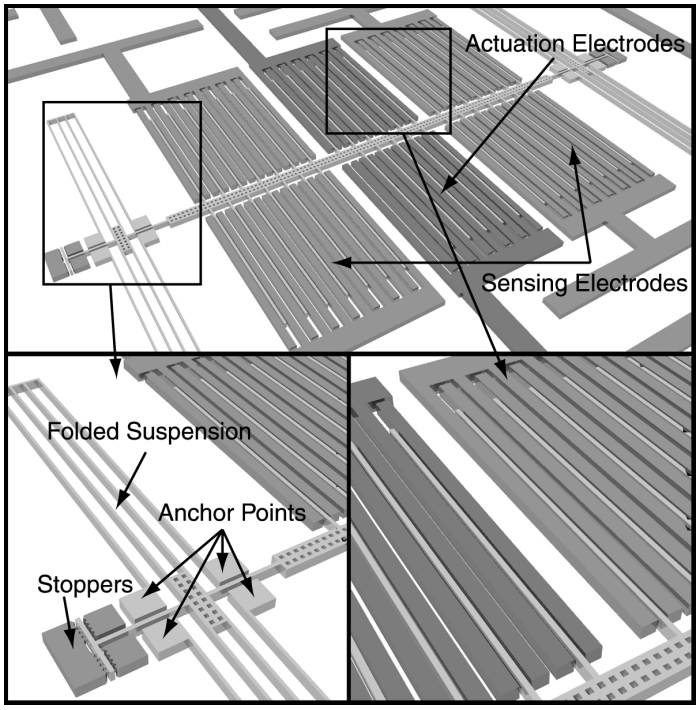

Figure 3.8 Drawing of the microdevice used for testing

For the application of the derived 1-DOF models to the test structure the lumped elements, elastic spring and zero-displacement capacitance, need to be computed.

3.4.1 Elastic Spring

The spring constant of the device can be found by applying elementary elasticity equations to the folded beams as is done in the next section.

3.4.1.1 Deflection of Beams

When a beam is subjected to a transverse load, as shown in Fig. 3.9, it will deform into a deflection curve, *v(x)* [3.13]. From the figure the following equations can be found:

$$ds^2 = dx^2 + dv^2 \tag{3.39}$$

$$\frac{dv}{dx} = \tan\theta \tag{3.40}$$

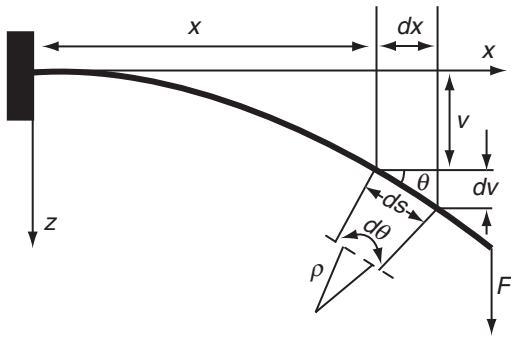

Figure 3.9 Deflection curve of a beam

Using these equations and writing $v' = dv/dx$, the curvature κ can be expressed as:

$$\kappa = \frac{1}{\rho} = \frac{d\theta}{dx} = \frac{d(\operatorname{atan}(v'))}{dx}\frac{dx}{ds} = \frac{v''}{1+(v')^2}\frac{dx}{ds} = \frac{v''}{[1+(v')^2]^{3/2}} \tag{3.41}$$

From theory it is found that if the slope v' is small and $(v')^2 \ll 1$ [3.13], Eqn. (3.41) can be simplified to:

$$\kappa = \frac{d^2v}{dx^2}, \tag{3.42}$$

which is valid for deflections that are small when compared to the beam length. According to Hooke's law, the curvature at any point in the beam is related to the bending moment *M* at that point according to:

$$\kappa = -\frac{M}{EI_y}, \tag{3.43}$$

where *E* is the Young's modulus and I_y is the second area momentum, which is determined by the shape of the beam cross-section:

$$I_y = \int_x \int_z z^2 dz dx \tag{3.44}$$

For a beam of width w_b and height h_b (rectangular shape), the second area momentum is given by:

$$I_y = \int_{-\frac{w_b}{2}}^{\frac{w_b}{2}} \int_{-\frac{h_b}{2}}^{\frac{h_b}{2}} z^2 dz dx = \frac{1}{12} w_b h_b^3 \tag{3.45}$$

The sign convention of the bending moment is such that a positive bending moment results in a negative curvature and vice-versa. For small beam deflections the equation describing the deflection curve of a beam is:

$$\kappa = \frac{d^2 v}{dx^2} = -\frac{M}{EI_y} \tag{3.46}$$

This equation can be used to determine the deflection curve of a beam, provided that the boundary conditions are known.

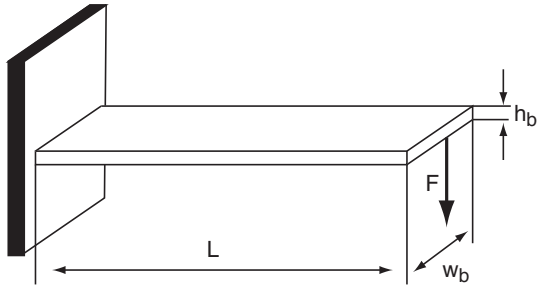

Figure 3.10 Cantilever beam with applied force

For the simple case of a cantilever beam with rectangular shape (cross section of height h_b and width w_b), clamped at one end, an applied shear force F causes the bending of the beam (Fig. 3.10). From the equilibrium conditions of a beam element dx, the shear force V and the intensity of a distributed load q are related to the moment M by $V = dM/dx$ and $q = -dV/dx$ respectively [3.13]. Therefore the basic differential equation, describing the deflection curve $v(x)$ of the cantilever beam resulting from a force F, is given by:

$$EI_y \frac{d^2}{dx^2} v(x) = F(L - x) \tag{3.47}$$

which is valid for small slopes and linear elastic materials. The boundary conditions for the cantilever beam are: *v(0)=0* and $dv/dx|_{x=0} = 0$. With these boundary conditions the solution for the deflection curve is:

$$v(x) = \frac{x^2}{6EI_y}F(3L-x) \tag{3.48}$$

The equation shows that the beam displacement is linearly proportional to the applied force and thus the beam acts like a spring. The maximum value is obtained at the free end:

$$v_{max} = \frac{L^3}{3EI_y}F \tag{3.49}$$

3.4.1.2 Equivalent Folded Spring

The microdevice under test has folded beam suspension (Fig. 3.11). If the trusses joining the folded-beam segments are rigid (achievable by proper design), the displacement for an applied force F reduces to the simple case of the cantilever beam used as an example in the previous section [3.14]:

$$x = \frac{1}{4}\frac{L^3}{3EI_y}F \tag{3.50}$$

For beams of length L, width w_b and height h_b, and taking into account that the device has 4 folded springs as the one showed in Fig. 3.11 the equivalent elastic spring of the device is:

$$k = 16\frac{3EI_y}{L^3} = 4Ew_b\left(\frac{h_b}{L}\right)^3 \tag{3.51}$$

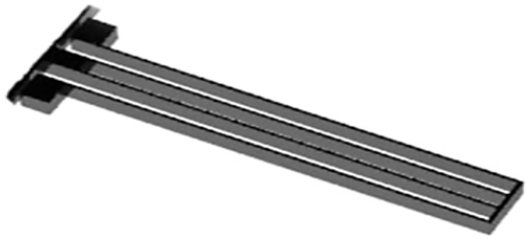

Figure 3.11 Folded spring

3.4.2 Experimental Measurements

A microphotograph of the fabricated device used in the experiments is presented in Fig. 3.12. The device is composed of four folded beams $375\mu m$ long, $2.8\mu m$ wide and $10.6\mu m$ thick connected to a central rigid bar. This results in a equivalent mechanical spring of 2.877 N/m. Mechanical stoppers are placed on either side of the central movable structure limiting the displacement range to the interval $[-1.75\mu m, 1.75\mu m]$, and thus avoiding electrical contact between the movable and fixed plates of the gap-varying capacitors.

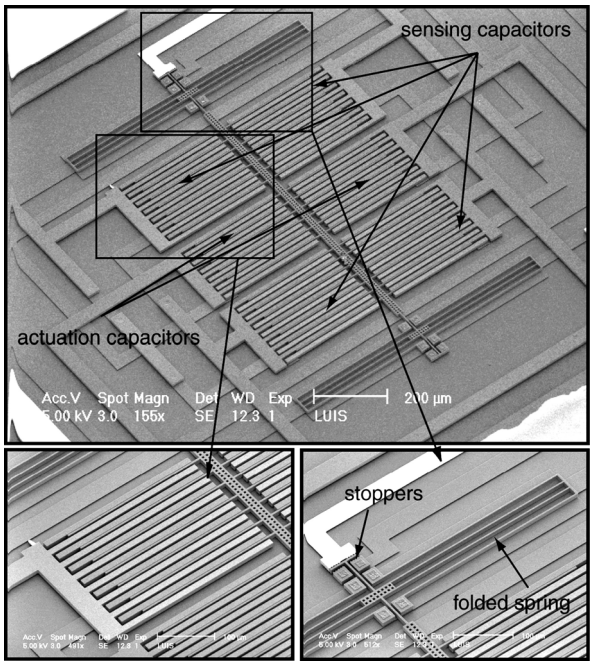

Figure 3.12 Microdevice used for the 1-DOF pull-in measurements

Three differential capacitors sets are defined, two for displacement sensing, and the other one for actuation. The actuation set of capacitors is composed of 12 parallel-plate capacitors, connected in parallel, with a zero-displacement gap $d_0 = 2\mu m$. The parallel-plates have a length, $l_c = 280\mu m$ and a width, $w_c = 10.6\mu m$. Neglecting the fringe fields, the total zero-displacement capacitance is:

$$C_0 = 12\varepsilon_0\varepsilon_r\frac{l_c w_c}{d_0} = 157\times10^{-15}F, \tag{3.52}$$

where $\varepsilon_0 = 8.854\times10^{-12}N^{-1}m^{-2}C^2$ is the vacuum permittivity and ε_r the relative permittivity of the medium between the parallel-plate electrodes ($\varepsilon_r = 1$ for atmospheric air at room temperature). From here on, the notation $\varepsilon = \varepsilon_0\varepsilon_r$ is used.

The theoretical computation for the static pull-in and release voltages using Eqns. (3.23), (3.32), (3.37) and (3.38) results in the graphs presented in Fig. 3.13.

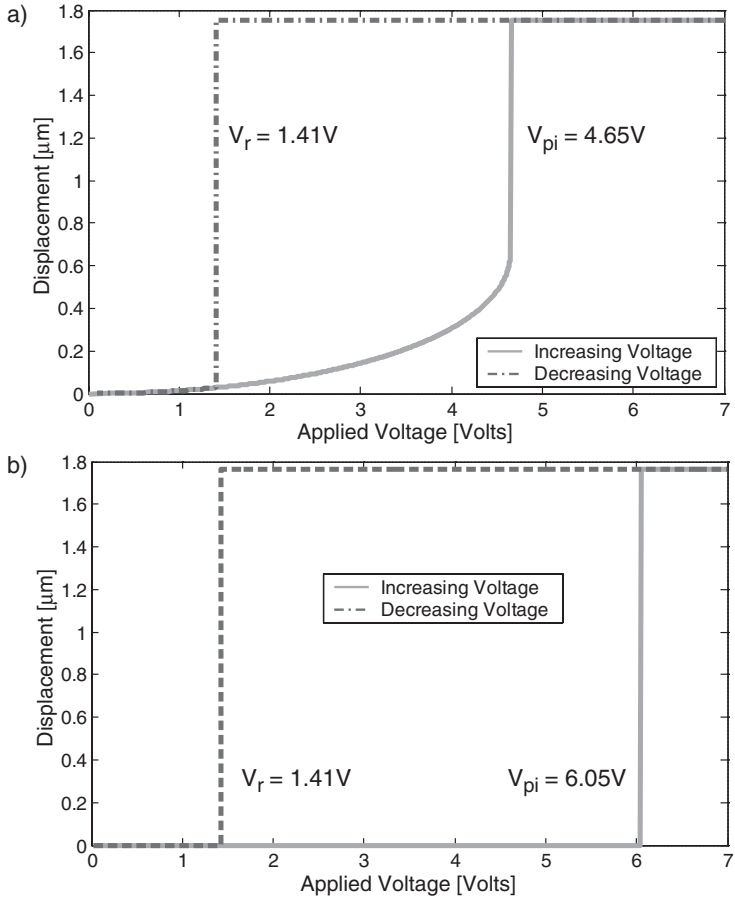

Figure 3.13 Theoretical pull-in and release voltages for 1-DOF a) asymmetrically and b) symmetrically driven microdevices

The experimentally measurements are presented in Fig. 3.14. As expected, the asymmetric drive presents a parabolic change on the capacitance until the pull-in is reached, and the symmetric case presents a much sharper transition at pull-in. The technological process uncertainties and statistical variations could account for the differences between the theoretical model and experimental measurements. The symmetric mode is more sensitive to process tolerances as predicted, resulting in a bigger difference between measured and predicted pull-in and release voltages.

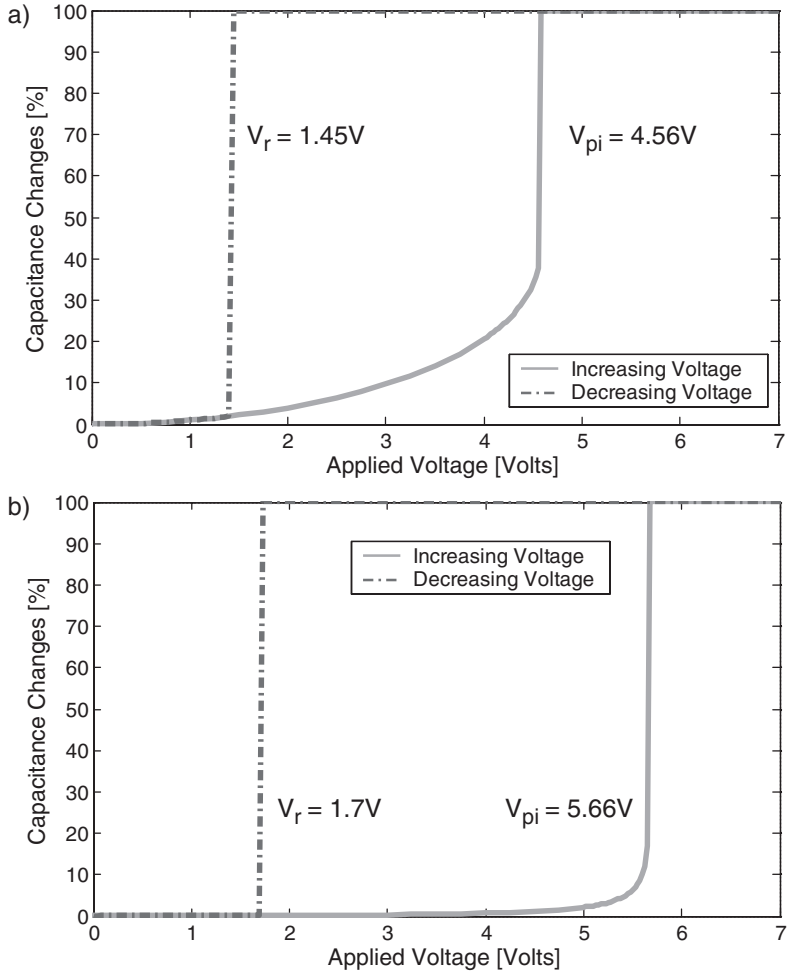

Figure 3.14 Measured pull-in and release voltages for 1-DOF structure for a) asymmetric and b) symmetric drive.

3.5 2-DOF Pull-in Model

In the previous section, a pull-in analysis for a force-actuated structure with 1-DOF was performed. The folded spring on both ends of the movable bar ensured the 1-DOF. The next step is to make the transition to a moment actuated device [3.15]. This device offers unique opportunities for stable pull-in, but has essentially a 2-DOF displacement behaviour. A drawing of the device is shown in Fig. 3.15.

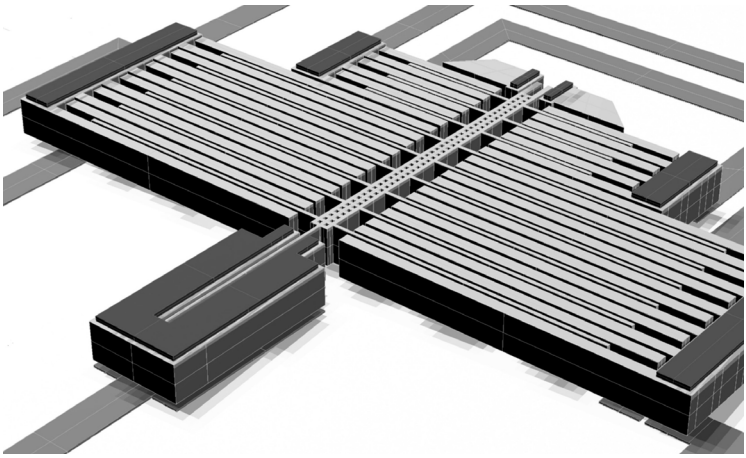

Figure 3.15 Drawing of the inverted-pendulum device

The movable device is divided into the single-side clamped elastic beam, which stores the elastic energy, and a rigid top structure, which acts as a rigid extension of the beam and serves as a support for the capacitors.

A sketch of the structure with the main geometrical parameters is presented in Fig. 3.16. The simplified model reduces the comb finger array structure to a single equivalent plate, placed at an equivalent distance t_x from the top of the beam. Four separate capacitors are defined (C_{rb}, C_{rt}, C_{lb}, C_{lt}), sharing a common movable plate. The movement of the device is fully characterized by two generalized parameters in the mechanical domain (see Fig. 3.17):

1. w_1, the linear bending displacement at the tip of the elastic beam caused by the resultant shear force.
2. φ_1, the bending angle at the free end of the beam associated with a bending moment.

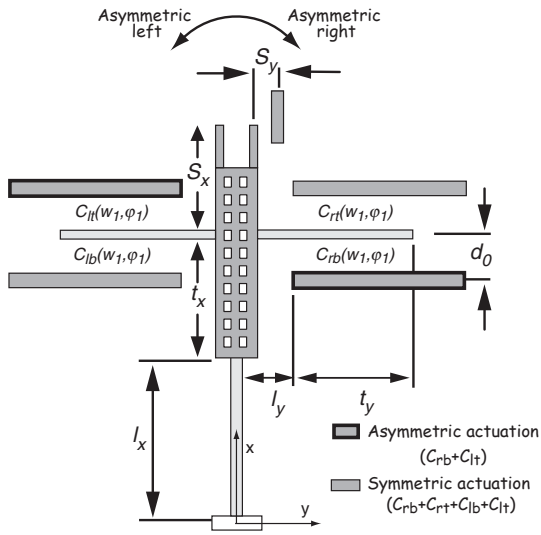

Figure 3.16 Geometrical parameters for the single-side clamped structure

As for the 1-DOF case, two modes of operation are defined: asymmetric and symmetric. In the case of asymmetric actuation the voltage is applied between two sets of electrodes only: the upper set on one side of the moving bar and the lower set on the other side, yielding an unbalanced electrostatic force counteracted by the restoring elastic force. In case of a symmetric drive the voltage is applied across all four sets of electrodes (see Fig. 3.16).

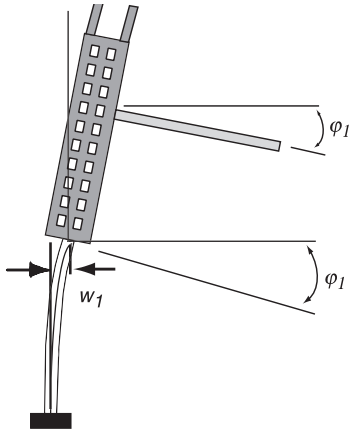

Figure 3.17 Identification of the state variables used in the 2-DOF model

The total potential energy of the system, U, is composed by the elastic energy stored in the beam, U_{els}, and the electrostatic energy stored in the capacitors, U_{elect}. If a common-mode voltage is considered, the total potential energy is fully determined by three independent state variables, two mechanical and one electric:

$$U(w_1, \varphi_1, V) = U_{els}(w_1, \varphi_1) - \frac{1}{2} C_{tot}(w_1, \varphi_1) V^2 \tag{3.53}$$

Here $C_{tot}(w_1, \varphi_1)$ is the total capacitance contributing to the electrostatic energy. The pull-in voltage can be found by solving the equation (stability condition):

$$\begin{vmatrix} \dfrac{\partial^2 U}{\partial w_1^2} & \dfrac{\partial^2 U}{\partial w_1 \partial \varphi_1} \\ \dfrac{\partial^2 U}{\partial \varphi_1 \partial w_1} & \dfrac{\partial^2 U}{\partial \varphi_1^2} \end{vmatrix} (w_{1,pi}, \varphi_{1,pi}, V_{pi}) = 0, \tag{3.54}$$

in variable V_{pi}. The critical equilibrium position $(w_{1,pi}, \varphi_{1,pi})$ corresponds to the equilibrium position determined from:

$$\begin{bmatrix} \dfrac{\partial U}{\partial w_1} \\ \dfrac{\partial U}{\partial \varphi_1} \end{bmatrix} (w_{1,pi}, \varphi_{1,pi}, V_{pi}) = \begin{bmatrix} \dfrac{\partial U_{els}}{\partial w_1} - \dfrac{1}{2} \dfrac{\partial C_{tot}}{\partial w_1} V_{pi}^2 \\ \dfrac{\partial U_{els}}{\partial \varphi_1} - \dfrac{1}{2} \dfrac{\partial C_{tot}}{\partial \varphi_1} V_{pi}^2 \end{bmatrix} (w_{1,pi}, \varphi_{1,pi}) = \begin{bmatrix} 0 \\ 0 \end{bmatrix} \tag{3.55}$$

The last three equations, Eqns. (3.54) and (3.55), can be reduced into two algebric equations by isolating and eliminating V_{pi} from the equations:

$$\frac{\partial U_{els}}{\partial \varphi_1} \frac{\partial C_{tot}}{\partial w_1} - \frac{\partial U_{els}}{\partial w_1} \frac{\partial C_{tot}}{\partial \varphi_1} = 0 \tag{3.56a}$$

$$\begin{aligned} &\left(\frac{\partial^2 U_{els}}{\partial w_1^2} \frac{\partial C_{tot}}{\partial w_1} - \frac{\partial U_{els}}{\partial w_1} \frac{\partial^2 C_{tot}}{\partial w_1^2} \right) \left(\frac{\partial^2 U_{els}}{\partial \varphi_1^2} \frac{\partial C_{tot}}{\partial w_1} - \frac{\partial U_{els}}{\partial w_1} \frac{\partial^2 C_{tot}}{\partial \varphi_1^2} \right) \\ &\quad - \left(\frac{\partial^2 U_{els}}{\partial w_1 \partial \varphi_1} \frac{\partial C_{tot}}{\partial w_1} - \frac{\partial U_{els}}{\partial w_1} \frac{\partial^2 C_{tot}}{\partial w_1 \partial \varphi_1} \right)^2 = 0 \end{aligned} \tag{3.56b}$$

Eqns. (3.56a) and (3.56b) assume $\frac{\partial^2 U}{\partial w_1 \partial \varphi_1} = \frac{\partial^2 U}{\partial \varphi_1 \partial w_1}$. The solution of these equations directly yields the pull-in critical positions $(w_{1,pi}, \varphi_{1,pi})$. The pull-in voltage can then be calculated by using:

$$\frac{\partial U_{els}}{\partial w_1} - \frac{1}{2}\frac{\partial C_{tot}}{\partial w_1} V_{pi}^{\ 2} = 0 \qquad or \qquad \frac{\partial U_{els}}{\partial \varphi_1} - \frac{1}{2}\frac{\partial C_{tot}}{\partial \varphi_1} V_{pi}^{\ 2} = 0$$
$$V_{pi} = \sqrt{\frac{2\partial U_{els}/\partial w_1}{\partial C_{tot}/\partial w_1}}\Bigg|_{w_{1,pi},\, \varphi_{1,pi}} = \sqrt{\frac{2\partial U_{els}/\partial \varphi_1}{\partial C_{tot}/\partial \varphi_1}}\Bigg|_{w_{1,pi},\, \varphi_{1,pi}} \tag{3.57}$$

3.5.1 Asymmetric Mode

In the asymmetric mode of operation the electrostatic energy resumes to the energy stored in the capacitors $C_{rb}(w_1, \varphi_1)$ and $C_{lt}(w_1, \varphi_1)$. Analytical expressions for the elastic and electrostatic energies are derived in the next sections.

3.5.1.1 Elastic Energy

The general deformation curve for one-side clamped beam with shear force and bending moment acting at the free end can be find by solving:

$$EI_y \frac{d^2}{dx^2} v(x) = M + F(L - x)\,, \tag{3.58}$$

with the boundary conditions *v(0)=0* and $dv/dx|_{x=0} = 0$. The general deformation curve and angle are:

$$v(x) = \frac{x^2}{6EI_y}[3M + F(3L - x)] \tag{3.59a}$$

$$\varphi(x) = \frac{dv}{dx}(x) = \frac{x}{2EI_y}[2M + F(2L - x)] \tag{3.59b}$$

To completely characterize the mechanical state of the beam, the bending curve should be determined by the coordinates $w_1 = v(L)$ and $\varphi_1 = v'(L)$. It is possible to express the bending solution as given by Eqns. (3.59a) and (3.59b), in function of (w_1, φ_1) as:

$$v(x) = \frac{x^2}{L}\left[3\frac{w_1}{L} - \varphi_1 + \frac{x}{L}\left(\varphi_1 - 2\frac{w_1}{L}\right)\right] \quad \textbf{(3.60a)}$$

$$\varphi(x) = \frac{x}{L}\left[6\frac{w_1}{L} - 2\varphi_1 + 3\frac{x}{L}\left(\varphi_1 - 2\frac{w_1}{L}\right)\right] \quad \textbf{(3.60b)}$$

The total elastic energy stored in the beam is therefore [3.13]:

$$U_{els}(w_1, \varphi_1) = \frac{1}{2}EI_y\int_0^L\left(\frac{\partial\varphi}{\partial x}\right)^2 dx = \frac{2EI_y}{L}\left[\varphi_1^2 - \frac{3}{L}\varphi_1 w_1 + 3\left(\frac{w_1}{L}\right)^2\right] \quad \textbf{(3.61)}$$

There are three types of terms involved in Eqn. (3.61):

1. Terms involving the contribution of the shear force only: $\frac{6EI_y}{L^3}w_1^2 \equiv \frac{1}{2}k_{xx}w_1^2$.

2. Terms involving the bending angle at the beam end: $\frac{2EI_y}{L}\varphi_1^2 \equiv \frac{1}{2}k_{\varphi\varphi}\varphi_1^2$.

3. The cross-coupling term: $-\frac{6EI_y}{L^2}w_1\varphi_1 \equiv \frac{1}{2}k_{x\varphi}w_1\varphi_1$, due to the fact that the two chosen coordinates are independent, but not orthogonal.

3.5.1.2 Electrostatic Energy

The electrostatic energy depends on the variation of the equivalent capacitors, formed by the movable top arm and the fixed plates. Since the variation is not linear, the exact dependence of the capacitor with respect to the generalized coordinates used, $C(x, y, \varphi)$, is required. The force associated with the displacement is given by the derivative of the capacitance with respect to the coordinates used.

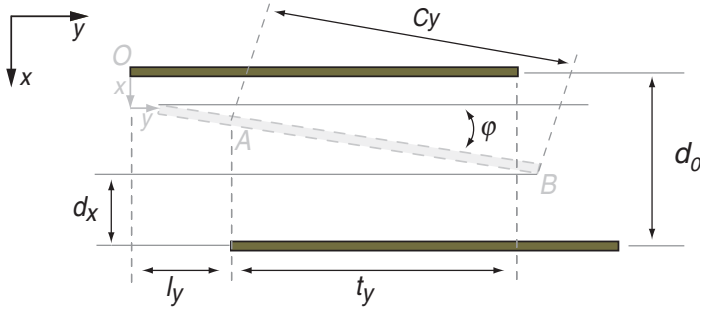

Figure 3.18 General configuration for fixed *x, y* and φ values

In order to compute the general dependence law for a general capacitor movement the configuration presented in Fig. 3.18 is considered. For an arbitrary set (x, y, φ) the configuration of Fig. 3.18 reduces to the geometry of Fig. 3.19.

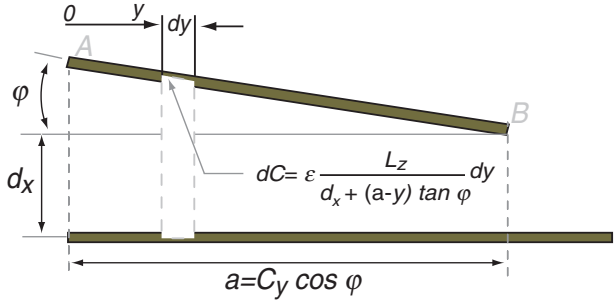

Figure 3.19 Geometry used for capacitance computation

By writing down the relations for the parameters C_y and d_x:

$$C_y = t_y + l_y + \frac{y - ly}{\cos(\varphi)} \tag{3.62}$$

$$d_x = d_0 - (ty + l_y)\sin(\varphi) - x \ , \tag{3.63}$$

and neglecting the fringe fields, the total capacity can be found:

$$C(x, y, \varphi) = \int_0^{C_y \cos(\varphi)} \varepsilon \frac{h_z}{\mathrm{d}_x + (C_y \cos(\varphi) - y)\tan(\varphi)} dy \tag{3.64}$$

$$= \varepsilon \frac{h_z}{\tan(\varphi)} \ln\left[1 + \tan(\varphi)\frac{y - l_y + (l_y + t_y)\cos(\varphi)}{d_0 - x - (l_y + t_y)\sin(\varphi)}\right]$$

With the general dependence law for the capacitor, the next step is the coupling of the generalized coordinates (x, y, φ) to the mechanical coordinates (w_1, φ_1) that describe the 2-DOF device. From Figs. 3.16, 3.17 and 3.18 the following relations are found:

$$x_0 = t_x(1 - \cos(\varphi_1)) \tag{3.65a}$$

$$y_0 = w_1 + t_x \sin(\varphi_1) \tag{3.65b}$$

$$\varphi_0 = \varphi_1 \tag{3.65c}$$

Using Eqn. (3.64) and Eqns. (3.65a)-(3.65c) the four capacitors, as defined in Fig. 3.16, are given by:

$$C_{rb}(w_1, \varphi_1) = C(x_0, y_0, \varphi_0)$$
$$= \varepsilon \frac{h_z}{\tan(\varphi_1)} \ln\left[1 + \tan(\varphi_1) \frac{(l_y + t_y)\cos(\varphi_1) + w_1 + t_x \sin(\varphi_1) - l_y}{d_0 - t_x + t_x \cos(\varphi_1) - (l_y + t_y)\sin(\varphi_1)}\right] \quad \textbf{(3.66a)}$$

$$C_{lt}(w_1, \varphi_1) = C(-x_0, -y_0, \varphi_0)$$
$$= \varepsilon \frac{h_z}{\tan(\varphi_1)} \ln\left[1 + \tan(\varphi_1) \frac{(l_y + t_y)\cos(\varphi_1) - w_1 - t_x \sin(\varphi_1) - l_y}{d_0 + t_x - t_x \cos(\varphi_1) - (l_y + t_y)\sin(\varphi_1)}\right] \quad \textbf{(3.66b)}$$

$$C_{rt}(w_1, \varphi_1) = C(-x_0, y_0, -\varphi_0) = C_{lt}(-w_1, -\varphi_1) \quad \textbf{(3.66c)}$$

$$C_{lb}(w_1, \varphi_1) = C(x_0, -y_0, -\varphi_0) = C_{rb}(-w_1, -\varphi_1) \quad \textbf{(3.66d)}$$

The electrostatic energy for the asymmetric case is given (considering $(w_1, \varphi_1) = (0, 0)$ as zero-level energy) by:

$$U_{elect} = -\frac{1}{2} V^2 [C_{rb}(w_1, \varphi_1) + C_{lt}(w_1, \varphi_1) - 2C_0] \ , \quad \textbf{(3.67)}$$

where $C_0 = \varepsilon \frac{h_z t_y}{d_0}$ is the zero-displacement capacitance.

3.5.1.3 Numerical Algorithms Used

The elastic energy depends polynomially on (w_1, φ_1), so its symbolic derivatives do not present a severe computational challenge. The main difficulty arises from the dependency of the electrostatic energy on the mechanical variables, which makes a purely analytical solution not practical. For the asymmetric mode of operation, Eqns. (3.56a) and (3.56b) can not be solved analytically and numerical solutions must be used. Two different algorithms capable of tracking the changes in the equilibrium position while the voltage is increased from zero until the system becomes unstable (pull-in voltage is reached) were implemented:

1. The first, based on the energy method, uses the ramping of the voltage from the initial value V_0, towards the increase of positive values. For each voltage value the stability points are computed, by approximating the general potential in Taylor series around the previously computed equilibrium point, $\{w_{1,eq}[k\text{-}1], \varphi_{1,eq}[k\text{-}$

1]}. This makes it possible to track the evolution of the equilibrium point as a function of *V*. For the computed values of ($w_{1,eq}$, $\varphi_{1,eq}$), the determinant of the associated Hessian at that point is computed. If it is zero, the critical equilibrium point is reached and the pull-in voltage is found.

2. The second algorithm is based on the equilibrium of forces and also uses the ramping of the voltage from an initial value V_0, towards the increase of positive values. For each voltage value an iterative method is performed. Initially using the first partial derivatives of the electrostatic energy, the electrostatic force $F_{elect} = \frac{\partial U}{\partial w_1}$ and moment $M_{elect} = \frac{\partial U}{\partial \varphi_1}$ are computed using the previously computed equilibrium point, {$w_{1,eq}$[*k-1*], $\varphi_{1,eq}$[*k-1*]}. Then, using Eqns. (3.59a) and (3.59b) a new equilibrium point {$w_{1,eq}$[*k*], $\varphi_{1,eq}$[*k*]} is computed. If $F(w_{1,eq}[k], \varphi_{1,eq}[k]) - F(w_{1,eq}[k-1], \varphi_{1,eq}[k-1]) > \delta$ the process is reinitiated and a new equilibrium point is found based on the previously computed one. When $F(w_{1,eq}[k], \varphi_{1,eq}[k]) - F(w_{1,eq}[k-1], \varphi_{1,eq}[k-1]) \le \delta$, the iteration process ends, corresponding to the balance between the elastic and electrostatic forces and moments at the equilibrium position {$w_{1,eq}$[*k*], $\varphi_{1,eq}$[*k*]}.

   An illustration of the iterative method is shown in Fig. 3.20 for the simple 1-DOF case. The pull-in voltage is found when the iterative method does not converge which means that the elastic force and moment can no longer compensate for the electrostatic counterpart.

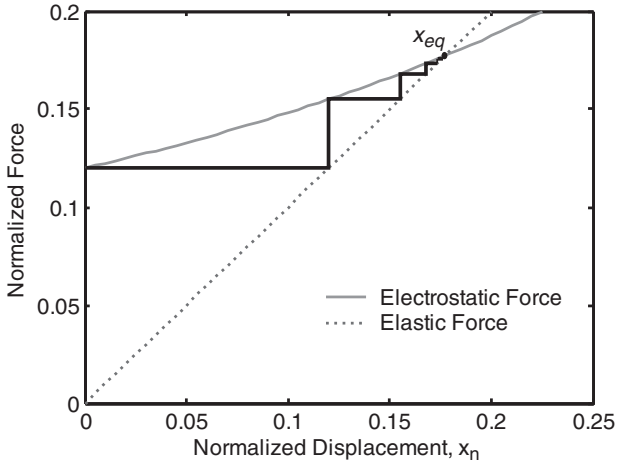

Figure 3.20 Illustration of the iterative method for the simplest 1-DOF case

3.5.2 Symmetric Mode

In this case the energy stored in the four equivalent capacitors has to be considered. The elastic energy is the same as for the asymmetric case and given by Eqn. (3.61). The electrostatic energy is given by:

$$U_{elect} = -\frac{1}{2}V^2[C_{rb}(w_1, \varphi_1) + C_{rt}(w_1, \varphi_1) + C_{lb}(w_1, \varphi_1) + C_{lt}(w_1, \varphi_1) - 4C_0] \quad \textbf{(3.68)}$$

Unlike the case of the asymmetric drive where a numerical method is required to find the pull-in voltage, an approximate analytical expression for the pull-in can be derived for the symmetric mode of operation.

The expression for the electrostatic energy is rather complex, but in the symmetric drive the structure retains its zero-displacement equilibrium position $(w_1, \varphi_1) = (0, 0)$ until the pull-in is reached. This suggests an approximation of the potential by a Taylor series around the known equilibrium position. Since the use of the variational approach needs the first and second variations, the first two terms of the Taylor series are sufficient for an approximation. Using the known equilibrium position, $(w_1, \varphi_1) = (0, 0)$, in Eqn. (3.54), an analytical expression for the pull-in voltage of the symmetric drive is found:

$$V_{pi,sym} = \sqrt{\frac{3}{2}}d_0\sqrt{\frac{t_y}{(-3d_0^2(l_y + t_y) + 2t_y(3l_y^2 + 3l_y t_y + t_y^2))}\frac{1}{C_0}\frac{EI_y}{l_x}} \quad \textbf{(3.69)}$$

3.5.3 2-DOF Hysteresis Model

The mechanisms behind the bi-stable regime for the 2-DOF case are basically the same as for the 1-DOF case and were already discussed in section 3.3.3. In what concerns the modelling of the hysteresis, the 2-DOF case presents an extra unknown: the bending angle and the displacement at the stopper position. However, device geometry (see Figs. 3.16 and 3.17) allows writting an expression relating stopper position and the unknown state coordinates at the sttopers:

$$S_y = w_{1,stopper} + (t_x + S_x)\sin(\varphi_{1,stopper}) \quad \textbf{(3.70)}$$

If the system of equations composed by Eqns. (3.55) and (3.70) is solved in variables $(w_{1,stopper}, \varphi_{1,stopper}, V_r)$ the release voltage, the stopper bending angle and the displacement can be found. Since the dependence of the total capacitance on (w_1, φ_1) is rather complex and an approximation around the zero-displacement position would not predict the correct behaviour, an analytical solution is not possible. Nevertheless, the

system can be solved numerically for both types of actuation: asymmetric and symmetric drive.

3.6 Experimental Results for the 2-DOF Pull-In Model

The structure used for experimental validation of the 2-DOF pull-in models is presented in Fig. 3.21 and corresponds to the model presented so far. The device is basically a free-standing lateral beam ($200\mu m$ long, $3\mu m$ wide and $10.6\mu m$ thick) anchored at one end (the base) only. The beam can be deflected by electrostatic actuation in the plane of the wafer using a voltage applied across the parallel-plate capacitors ($2\mu m$ gap). These are composed of two sets of electrodes located alongside the free-standing tip (on the top), with counter electrodes mechanically anchored to the substrate. The deflection can be measured using a set of differential sense capacitors also located alongside the free-standing tip (on the bottom). Stoppers are placed for limiting the lateral motion.

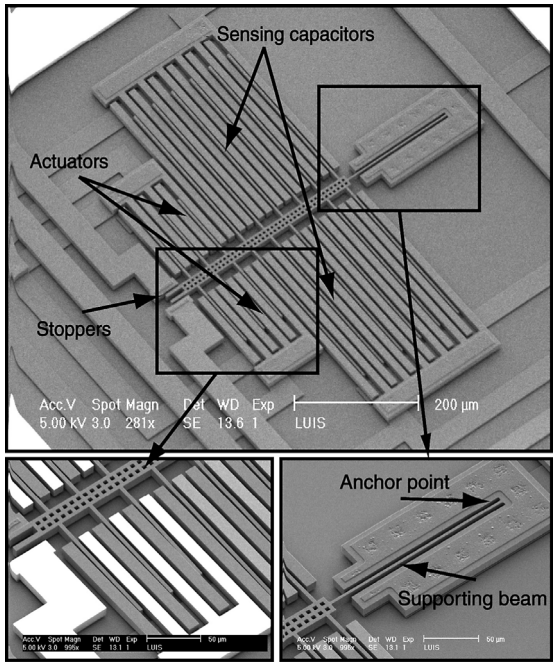

Figure 3.21 Microphotograph of the single-side clamped device

First, the 2-DOF pull-in model was applied to the device. The main dimensions (see Fig. 3.16) and material properties needed for numerical computation of the pull-in and release voltages are: $l_x = 200\mu m$, $w_b = 10.6\mu m$, $h_b = 3\mu m$, $d_0 = 2\mu m$, $t_y = 110\mu m$, $l_y = 30\mu m$, $t_x = 274\mu m$, $S_x = 88\mu m$, $S_y = 3.25\mu m$ and $E = 163\times10^9 Pa$.

Finite element modelling (FEM) was also performed, and the results are compared to the analytical model results and to the experimental results. The predicted pull-in voltage from the analytical model is $V_{pi} = 9.24V$ for the asymmetric drive. The trajectory of the equilibrium point as a function of the applied voltage is shown in Fig. 3.22, from both the analytical and FEM models.

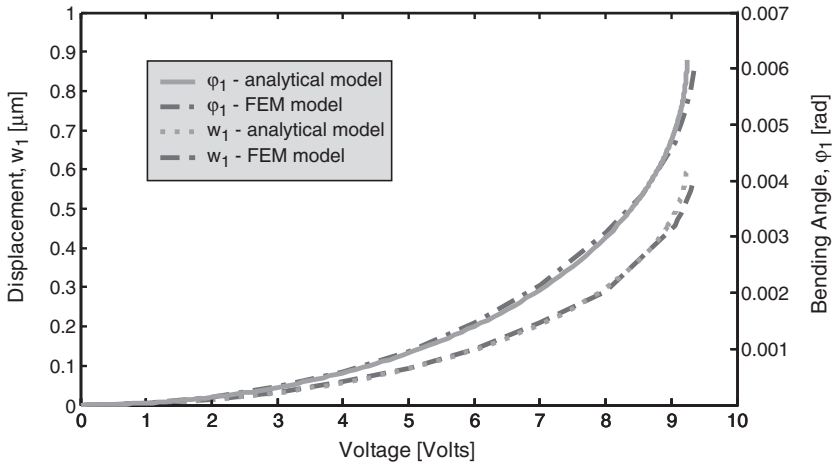

Figure 3.22 Variation of the equilibrium point with applied voltage

The results for the 2-D FEM model are presented in Fig. 3.23. Using contact elements in Ansys, the pull-in and release voltages of the structure have been computed. The simulations predicted a pull-in voltage of $V_{pi,FEM} = 9.3V$ and a release voltage of $V_{r,FEM} = 9.15V$. The clear agreement with the outcome of the analytical model demonstrates that such physical analytical modelling approaches may be used as well for higher dimensional structures (2 or more degrees of freedom).

Using the 2-DOF hysteresis model the release voltage was computed for both actuation modes. The predicted capacitance variation with the electrostatic actuation, for both the asymmetric and symmetric case, is shown in Fig. 3.24.

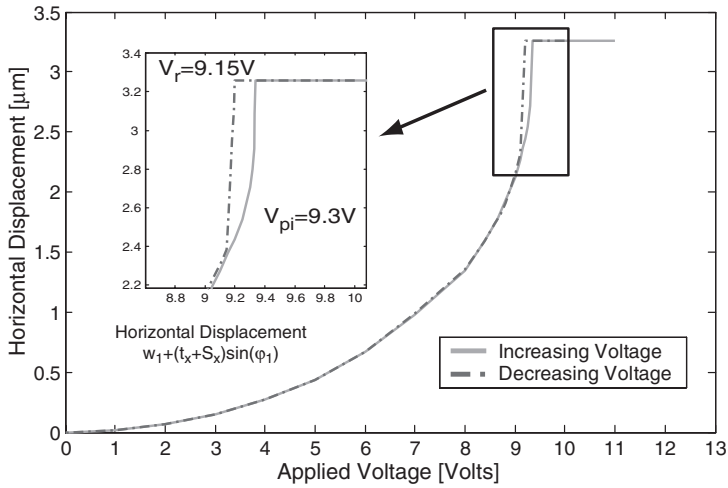

Figure 3.23 Results of FEA simulation on an asymmetrically operated device

For comparison the experimental results are shown in Fig. 3.25. There are two distinct cases for the asymmetric drive case (see Fig. 3.16), corresponding to a driving voltage applied on the right-bottom and left-top electrodes (*asymmetric right*), or on the right-top and left-bottom electrodes (*asymmetric left*). In the ideal case, the symmetry of the structure predicts an identical behaviour in this situation, with changes in the signs of the state variables w_1, φ_1. In reality, the different measured values for the asymmetric right and left cases indicate a deviation of the structure from the assumed model. The easiest explanation is that the structure zero-voltage position is not at $(w_1, \varphi_1) = (0, 0)$ as expected, but rather the beam is already bent $(w_1, \varphi_1)\big|_{V=0} = (w_0, \varphi_0)$. Residual stress and (vertical and lateral) gradients are usually present in a structural layer fabricated in a surface micromachining process, like the one used. As the entire structure has only one anchor point, the residual stress will not cause this initial bending. However, a stress gradient would displace the structure from the initial zero position.

Among the mechanical properties specified for the epi-poly structural layer is a vertical stress gradient of 1.3 ± 2 MPa/μm [3.16] (i.e., in the direction normal to the plane of the wafer). This stress gradient cannot be the cause of the different left-right pull-in voltages measured, because such a gradient would originate a bending of the beam away from the substrate plane causing no change on the initial zero position. A possible cause can be an in-plane (lateral) stress gradient (i.e., parallel to the plane of the wafer). Infor-

mation on a lateral gradient stress is not available, but reinterpretation of the measurements performed (in several 2-DOF devices) suggests a value of about ±0.2 MPa/μm.

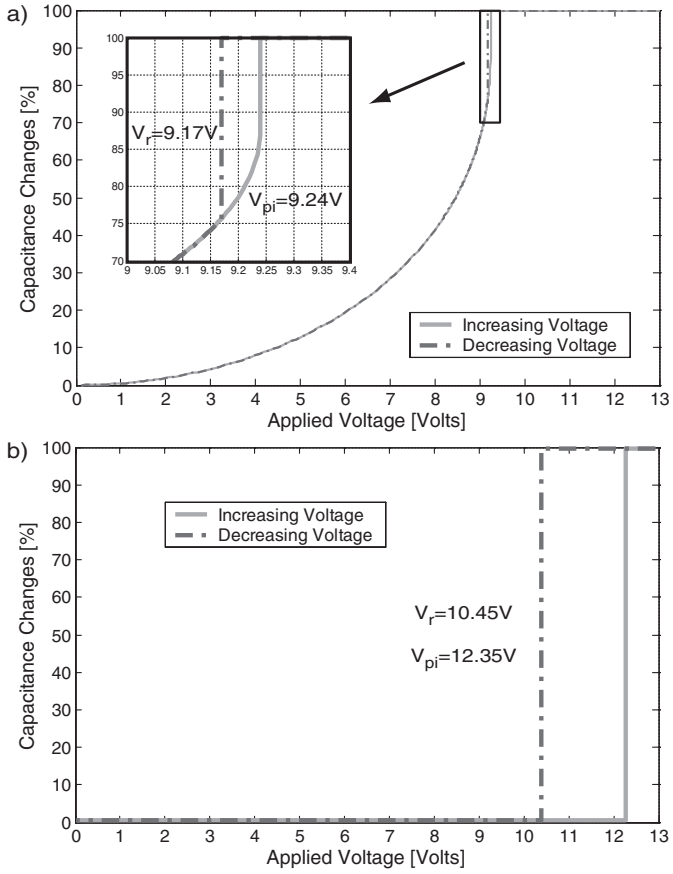

Figure 3.24 Results of the 2-DOF model for a device a) asymmetrically and b) symmetrically driven

If beam stress theory is used [3.17], the displacement and angle caused by the stress gradient can be calculated. Values of $(w_0, \varphi_0) = (2.45\times10^{-2}\mu m, 2.45\times10^{-4} rad)$ have been computed for a 0.2 MPa/μm stress gradient. The effect of the stress gradient is added to the model by adding an additional energy term:

$$U_{stress}(w_0, \varphi_0) = \frac{2EI_y}{l_x}\left(\varphi_0^2 - 3\varphi_0\frac{w_0}{l_x} + 3\left(\frac{w_0}{l_x}\right)^2\right) \quad \textbf{(3.71)}$$

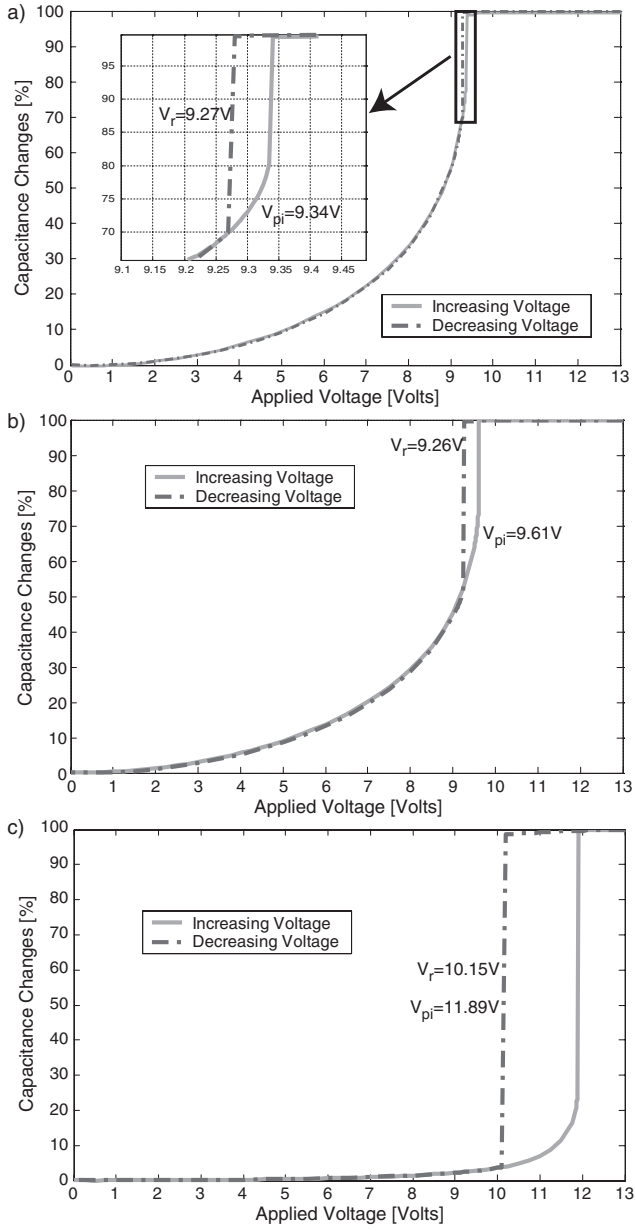

Figure 3.25 Experimental results for a device a) asymmetrically right, b) asymmetrically left and c) symmetrically driven

With this refinement to the model, a comparison between the analytical model and the experimental measurements is presented in Table 3.1. There is a good agreement between the predicted and experimental results. The small deviations (less than 5%) are due to process tolerances and uncertainties regarding the value of the Young's Modulus.

TABLE 3.1 Experimental data and numerical computed values for the pull-in and release voltages, in the presence of lateral stress gradients

	Asymmetric right		Asymmetric left		Symmetric	
	V_{pi} (V)	V_r (V)	V_{pi} (V)	V_r (V)	V_{pi} (V)	V_r (V)
Analytical model results	9.06	9.01	9.41	9.3	11.54	10.28
Experimental results	9.34	9.27	9.61	9.26	11.89	10.15

The refinement of the model by inclusion of the bending caused by a stress gradient leads to a better agreement with the observed experimental results. This is especially true for the symmetric drive, where the incorrect assumption of a stable $(w_1, \varphi_1) = (0, 0)$ position has the strongest impact. The initial zero-voltage bending induces an asymmetry in the configuration which lowers the pull-in voltage value, as compared to the ideal case.

3.7 Conclusions

The pull-in of electrostatically actuated microstructures has been studied as a nonlinear static effect. the static pull-in aspects are amongst the most focused nonlinearities in MEMS devices and have been thoroughly studied in literature. The static analysis performed here opens the door to the study of the nonlinear dynamic MEMS aspects, where the pull-in phenomenon has to be reinterpreted from a dynamic point of view.

A large signal model and an analysis methodology for 1-DOF and 2-DOF MEMS devices have been presented. The good agreement between the analytical model and the experimental results on all relevant aspects leads to the conclusion that analytical models can be used to characterize the electromechanical static behaviour of microdevices with acceptable accuracy. The energy method approach is suitable for obtaining simplified analytical design formulas, as the pull-in voltage for symmetric actuation of the inverted balance structure. It is the preferred method for a global analysis of the more complex cases. Non-ideal terms (as residual stress gradients for instance) can easily be incorporated to refine the model. The dynamic system approach provides a better understanding of the physics behind the pull-in phenomenon. It is more intuitive than the

energy method but it lacks the capability to easily describe the more complex higher-order systems.

The analytical modelling has provided the insight leading to a number of significant conclusions on basic device performance not previously drawn from FEM. Besides that, significant gains in design cycle time are achieved as compared to FEM on the same computer.

The asymmetric drive can be used as a versatile tool for measuring in-plane stress gradients in the structural layer in a surface micromachining process, by alternating between applying the voltage to the upper left-lower right and lower left-upper right electrodes. The simplicity of the pull-in measurements makes the asymmetric drive an efficient and easy tool on material characterization.

To finalize, hysteresis is intrinsic to device operation, but is predictable for a given drive mode and stopper position.

3.8 References

[3.1] H.A.C. Tilmans and R. Legtenberg, "Electrostatic Driven Vacuum-Encapsulated Polysilicon Resonators, part II, Theory and Performance", *Sensors and Actuators*, A 45 (1994) 67-84.

[3.2] S. Pamidighantam, R. Puers, K. Baert and H.A.C. Tilmans, "Pull-In Voltage Analysis of Electrostatically Actuated Beam Structures with Fixed-Fixed and Fixed-Free End Conditions", *J. Micromech. Microeng*., 12 (2002) 458-464.

[3.3] Y. Nemirovsky and O.B. Degani, "A Methodology and Model for the Pull-In Parameters of Electrostatic Actuators", *J. Microelectromech. Syst.,* 10 (2001) 601-615.

[3.4] O.B. Degani, Y. Yaniv, E. Socher and Y. Nemirovsky, "Modeling the Pull-In Parameters of Electrostatic Actuators with a Novel Lumped Two Degrees of Freedom Pull-In Model", *in Proc. Transducers'01*, Munich, Germany, 10-14 June 2001, pp.288-291.

[3.5] E.R. Konig and G. Wachutka, “Analysis of Unstable Behavior Ocurring in Electro-Mechanical Microdevices”, *in Proc. MSM’99*, San Juan, Puerto Rico, 19-21 April 1999, pp. 330-333.

[3.6] L. Castañer, A. Rodríguez, J. Pons and S.D. Senturia, “Pull-In Time-Energy product of Electrostatic Actuators: Comparison of Experiments with Simulation”, *Sensors and Actuators*, A 83 (2000) 263-269.

[3.7] L.A. Rocha, E. Cretu and R.F. Wolffenbuttel, “The Pull-In of Symmetrically and Asymmetrically Driven Microstructures and the Use in DC Voltage References”, *in Proc. IMTC’02*, Anchorage, USA, 21-23 May 2002, pp. 759-764.

[3.8] L.A. Rocha, E. Cretu and R.F. Wolffenbuttel, “Analysis and Analytical Modeling of Static Pull-In with Application to MEMS-Based Voltage Reference and Process Monitoring”, *J. Microelectromech. Syst.,* 13 (2004) 342-354.

[3.9] E. Cretu, *Inertial MEMS Devices, Modeling, Design and Applications*, PhD thesis, TUDelft, Delft, 2003.

[3.10] Hans Troger and Alois Steindl, *Nonlinear Stability and Bifurcation Theory*, New York, Springer-Verlag, 1991.

[3.11] J.R. Gilbert, G.K. Ananthasuresh and S.D. Senturia, “3D Modeling of Contact Problems and Hysteresis in Coupled Eletro-Mechanics”, *in Proc. MEMS’96*, San Diego, USA, 11-15 February 1996, pp. 127-132.

[3.12] L.A. Rocha, E. Cretu and R.F. Wolffenbuttel, “Hysteresis in the Pull-In of Microstructures”, *in Proc. MME’02*, Sinaia, Romania, 6-8 October 2002, pp. 335-338.

[3.13] J.M. Gere and P. Timoshenko, *Mechanics of Materials; Third SI Edition*, London, U.K.: Chapman and Hall, 1991.

[3.14] W. C. Tang, T.-C. H. Nguyen, and R. T. Howe, “Laterally driven polysilicon-microstructures”, *Sensors and Actuators*, A 20 (1989) 25-32.

[3.15] L.A. Rocha, E. Cretu and R.F. Wolffenbuttel, “Full Characterisation of Pull-In in Single-Sided Clamped Beams”, *Sensors and Actuators*, A 110 (2004) 301-309.

[3.16] Bosch, *Micromachining Foundry Design Rules*, version 2.01.2000.

[3.17] D.L. Daryl and L. Logan, *Mechanics of Materials*, New York, USA: Harper-Collins, 1991, pp. 241-256.

4

Modelling of MEMS Dynamics

4.1 Introduction

The modelling of MEMS dynamics is not a trivial task and represents one of the biggest challenges in the MEMS field. The high number of physical phenomena acting together at the microscale level, not only contributes to the complexity of the problem, but also makes the use of a general modelling platform incorporating all the physical phenomena difficult to build.

In this chapter, a generic approach for the modelling of MEMS dynamics is pursued. The starting point is the simple electromechanical system with parallel-plate actuation. This is often the case of the vast majority of MEMS structures and the modelling challenges for such a simple device are already considerable. In the modelling of MEMS devices, four energy domains are usually considered: thermal, mechanical, fluidic and electrical. For simplification the dynamics due to temperature changes are usually neglected and the use of a static temperature is sufficient. The mechanical and electrical domains are relatively easy to model. The fluidic domain represents the biggest modelling challenge.

The gaseous medium surrounding the MEMS device at the microscale level results in major forces acting on the device during its motion. These forces are highly nonlinear and depend on the surrounding medium, geometry and device movement. The gas film forces obey to nonlinear partial differential equations that can be analytically solved for the simplest movements: movement in the direction perpendicular to the capacitor area, and tilt motion. The simple 1-DOF movement of a parallel-plate type of structure is the starting point for the gas film forces analysis [4.1]. The analysis allows us to build a generic modelling platform for this type of devices. For the more complex movements and geometries, numerical methods have to be employed. Finite Element Modelling (FEM) [4.2] or Finite Differences (FD) [4.3], [4.4] are the normally used numerical methods. A new approach based on FD is pursued in this thesis to solve the more complex cases. The models are verified using measurements obtained from fabricated devices.

4.2 The Micromechanical Structure Governing Equations

The simplified prototype of a parallel-plate microelectromechanical actuator is presented in Fig. 4.1. Four lumped elements are used for a physical modelling of the device: a movable parallel-plate capacitor actuated by a voltage supply, the mass of the movable structure, an elastic spring (suspension system) and a damper. If an external acceleration is present, a_{ext}, the equilibrium of forces is expressed as:

$$F_{inertia} + F_{damping} + F_{elastic} + F_{elect} = ma_{ext}, \tag{4.1}$$

where $F_{inertia} = m\ddot{x}$ is the inertia force, $F_{damping} = b\dot{x}$ is the damping force, $F_{elastic} = kx$ is the elastic restoring force and $F_{elect} = \dfrac{C_0 d_0 V^2}{2(d_0 - x)^2}$ is the electrostatic force caused by a voltage V applied to a capacitor with initial value C_0 and initial gap distance d_0.

From a dynamic point of view the structure is mechanically represented by a second order system if a linear damping coefficient (this is not true, but is a valid assumption for a qualitative analysis) is considered. If the voltage applied is zero, the system is linear, and the equation of motion becomes:

$$m\frac{\mathrm{d}^2 x}{\mathrm{d}t^2} + b\frac{\mathrm{d}x}{\mathrm{d}t} + kx = ma_{ext} \tag{4.2}$$

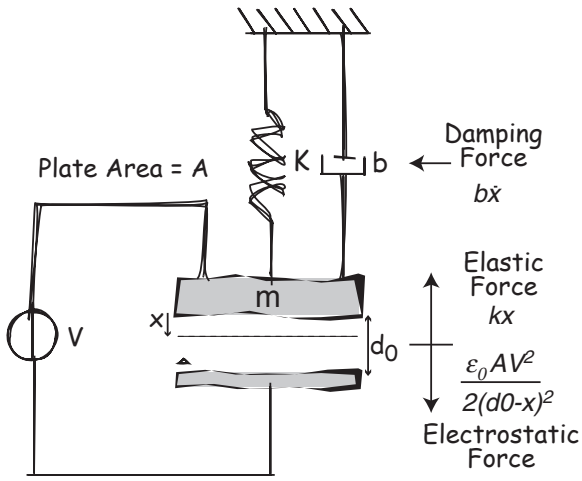

Figure 4.1 Actuator schematic

Eqn. (4.2) can be reformulated into a more convenient form, to emphasize the main parameters characterizing the dynamics of the system:

$$\frac{\mathrm{d}^2 x}{\mathrm{d}t^2} + \frac{\omega_0}{Q}\frac{\mathrm{d}x}{\mathrm{d}t} + \omega_0^2 x = a_{ext}(t), \tag{4.3}$$

where $\omega_0 = \sqrt{\frac{k}{m}}$ is the *natural resonant frequency* of the system, and $Q = \frac{\sqrt{km}}{b}$ is the *quality factor* (a measure of the losses in the system). Sometimes instead of the quality factor an equivalent parameter, the *damping factor*, defined as $\zeta = \frac{1}{2Q}$ is used.

The two parameters, Q (or equivalently ζ) and ω_0, dictate the dynamic behaviour. From a designer's perspective the choice of this parameters depends upon the application but usually both time-response and frequency-response specifications must be met.

The second order system of Eqn. (4.3) is usually defined in terms of the quality factor Q. For Q=0.5, the system is defined as *critically damped*. This is the case when the system reaches its equilibrium without oscillations and in the shortest possible time. It is the border between the *overdamped* case, Q<0.5, where the equilibrium position is reached without oscillations, and the *underdamped* case, Q>0.5, where the static equi-

librium is reached after an oscillatory transitory regime. Another important value is $Q = 1/(\sqrt{2})$, which corresponds to a maximum flat response in the frequency domain.

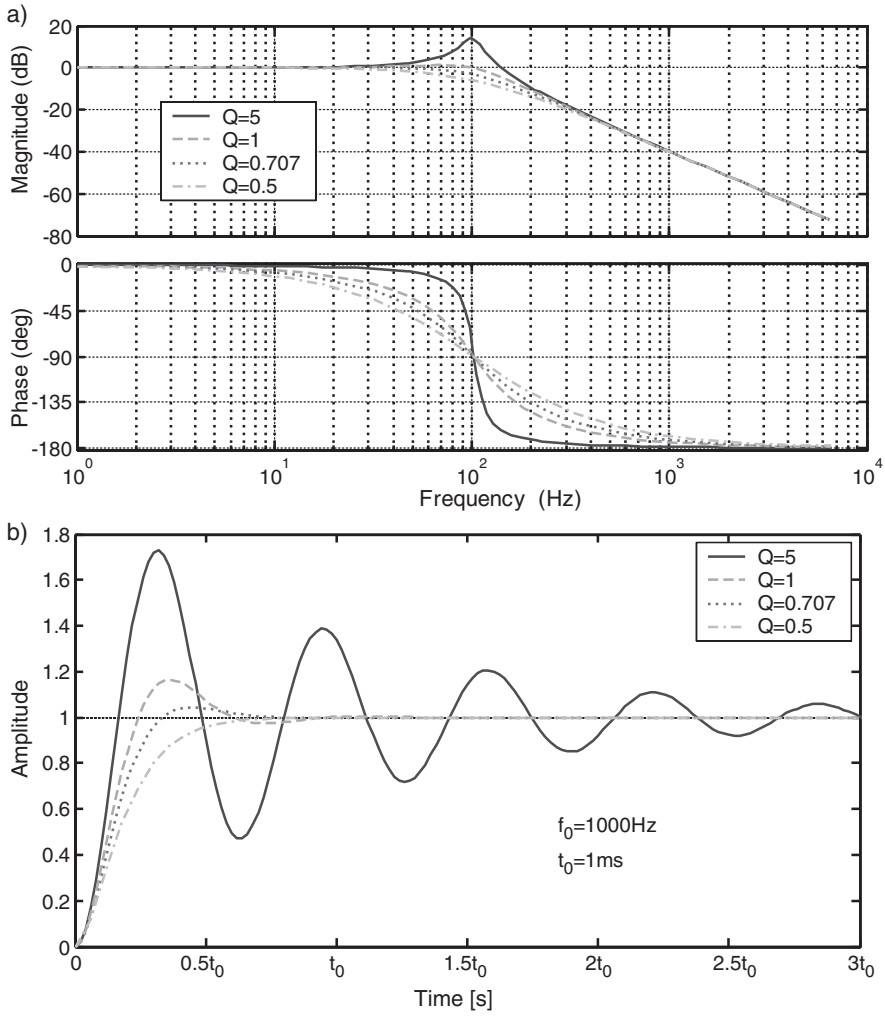

Figure 4.2 Response of a 2nd order system in the a) frequency and b) time domain

In Fig. 4.2 the system response in both frequency and time domain is shown for different values of the quality factor. Harmonic excitation was assumed for the frequency response, and for the time response a step-input external acceleration is applied. In both cases no voltage is applied across the capacitor plates.

When the voltage applied is not zero, Eqn. (4.1) can be rewritten as (considering a position and velocity dependent damping coefficient):

$$m\frac{\mathrm{d}^2 x}{\mathrm{d}t^2} + b\left(x, \frac{\mathrm{d}x}{\mathrm{d}t}\right)\frac{\mathrm{d}x}{\mathrm{d}t} + kx = ma_{ext} + F_{elect}, \tag{4.4}$$

If the notation form $\dot{x} = f(x, V)$ is adopted, Eqn. (4.4) becomes:

$$\begin{aligned} \dot{x} &= y \\ \dot{y} &= a_{ext} + \frac{1}{m}\left(\frac{C_0 d_0 V^2}{2(d_0 - x)^2} - kx - b(x, y)y\right) \end{aligned} \tag{4.5}$$

The notation of Eqn. (4.5) is very useful for understanding the number of state variables of the differential equation and its' relations. It is also very useful when one wants to solve differential equations using simulation tools. A block diagram of a Simulink^{TM} model for Eqn. (4.5) is presented in Fig. 4.3 ($C_0 d_0 = \varepsilon_0 A$ and constant damping coefficient b). The use of simple integrator blocks, common to the majority of simulation languages, is the key for the simulation of differential equations. Simulink is the platform used for the modelling of MEMS dynamics in this chapter. Since it is a high level modelling language it allows a huge flexibility and most of the MEMS components can be included in the model.

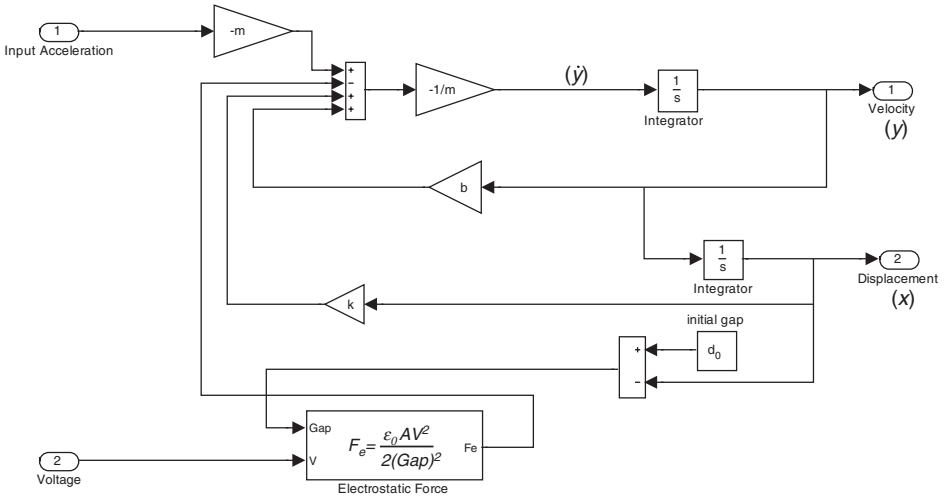

Figure 4.3 Simulink block diagram

Except for the nonlinear damping coefficient, all the other parameters can be easily obtained based on the dimensions and geometry of the structure. The mass for instance, provided that it can be assumed rigid can be modelled with a lumped model such that it is concentrated in a single point as an effective mass. The lumped spring constant can be evaluated by applying elementary elasticity equations and the electrostatic force obeys to the electrostatic laws. The damping coefficient is a more complicated subject. Consequently the focus of the next section is on the fluidic domain.

4.3 Squeeze-Film Damping

The movement of a parallel-plate type of device, where the gap size between the plates changes in an oscillatory manner, squeezing the trapped fluid out and sucking it in, gives origin to squeeze-film damping (Fig. 4.4). Fluid (usually air) is trapped between the movable electrode and the fixed one, resulting in squeeze-film forces that can not be neglected.

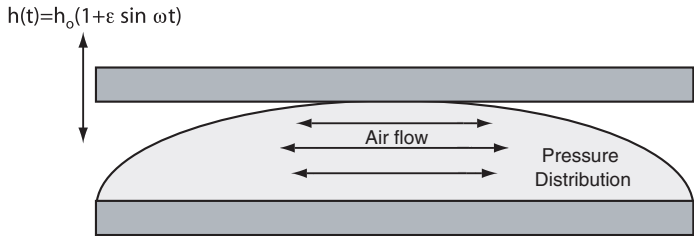

Figure 4.4 Schematic of squeeze-film damping

The relation between velocity, pressure, density and viscosity for an isotropic Newtonion fluid with a laminar gas flow between two moving plates can be calculated by using the Navier-Stokes equations and the continuity equation. A number of simplifying assumptions can be made for the squeeze-film problem:

1. *Curvature*: The surface of the capacitor plates are parallel and most of the motion is perpendicular to the surfaces. The critical dimension is the film thickness, which is considered uniform. This greatly simplifies the governing equations.
2. *Isothermal*: Since volumes are small and surface areas are large, the thermal contact between the solid and fluid is very good in MEMS devices. Besides that the most common MEMS materials have a relatively large heat capacity. For both these reasons, the gas film can be assumed isothermal and therefore the density is proportional to the absolute pressure.

3. *Inertia*: Since inertial forces are small when compared to viscous forces for typical MEMS dimensions, the gas inertia can be neglected. The contribution of the gas inertia can be considered small when the Reynolds number with respect to squeeze motion is small and the condition for this is that $\rho\omega h^2/\eta \ll 1$ [4.5]. Here ω is the frequency of the movement of the electrode, ρ the density, η the viscosity of the gas and h is the film thickness (with air at atmospheric pressure, $\eta=1.8.10^{-5}$ Pa.s, $\rho=1.29$ kg/m^3 and for a film thickness $h=2\mu$m, this assumption is valid up to frequencies $\omega<3.48$ Mrad/s).

With these assumptions the Navier-Stokes equations and the continuity equation can be simplified into the compressible-gas-film Reynolds equation [4.5],[4.6], written here for the two-dimensional case:

$$\frac{\partial}{\partial x}\left(\frac{h^3\rho}{\eta}\frac{\partial p}{\partial x}\right)+\frac{\partial}{\partial y}\left(\frac{h^3\rho}{\eta}\frac{\partial p}{\partial y}\right) = 12\frac{\partial}{\partial t}(\rho h), \tag{4.6}$$

where p is the pressure, ρ the density, η the viscosity of the gas and h is the film thickness. Since ρp^{-n} is a constant and for an isothermal process $n=1$, the density ρ can be replaced with pressure p.

4.3.1 Rarefaction Effects

A common concern in squeeze-film theory is the correct use of the continuum hypothesis considering that the device scale continues to be reduced. At a certain limit the typical intermolecular distances are comparable to the device dimensions and the use of continuum fluid equations can not describe any more the appropriate flow behaviour. For gases, the Knudsen number (K_n) relates the gas specific mean free path (λ) and the film thickness:

$$K_n = \frac{\lambda}{h} \tag{4.7}$$

For small Knudsen numbers ($K_n<0.01$) the flow is continuous and the continuum fluid equations apply. In practical MEMS devices the gas flow is in the transitional ($0.01 \le K_n \le 3$) or in the molecular ($K_n>3$) region. In the molecular region the continuity assumption breaks down and the Boltzmann transport equation has to be used to describe the flow. For an accurate damping analysis, the damping model must be valid for any K_n (rarefaction effects must be included).

For small Knudsen numbers the Navier-Stokes equations can be used with a single modification - the boundary condition at the fluid-solid interface is changed from the

standard non-slip condition to that of a slip-flow condition, where the velocity at the surface wall is related to the Knudsen number and the gradient of the gas velocity in the normal direction of the wall [4.7]:

$$u_w = \frac{2-\alpha}{\alpha}\lambda\frac{\partial u}{\partial n}, \tag{4.8}$$

α is the tangential momentum accommodation coefficient (TMAC) and is defined as the fraction of molecules which are diffusively reflected. The TMAC which depends on the gas, on the surface material and roughness, has to be determined experimentally and typically lies between 0.2 and 0.8. Experimental measurements [4.8] show that smooth silicon has a TMAC of about 0.7 in contact with several common used gases.

Even if the slip-flow theory is only valid for low Knudsen numbers it is commonly used at much higher K_n. Since other approaches (solving the Boltzmann equation or using direct simulation Monte Carlo computations) are more cumbersome the adoption of the slip-flow theory beyond its range of applicability becomes interesting. For simple geometries the usage of the slip-flow theory for high K_n values provides adequate results.

In gas film theory the slip-flow condition is usually included in the viscosity coefficient. This way the resulting coefficient is an *effective viscosity* η_{eff}: that takes into account the rarefaction effects. It is given by:

$$\eta_{eff} = \frac{\eta}{Q_{pr}(K_n)}, \tag{4.9}$$

where $Q_{pr}(K_n)$ is the relative flow rate coefficient and is the ratio between the flow rate coefficient and the continuum flow rate. Since it is function of the Knudsen number, it depends on the film thickness and on the static pressure value, P_a, because the mean free path is inversely proportional to pressure:

$$\lambda = \frac{P_0}{P_a}\lambda_0 \tag{4.10}$$

Here λ_0 is the mean free path at pressure P_0. References [4.7] and [4.9] present various functions for $Q_{pr}(K_n)$. A simple experimental approximation for $Q_{pr}(K_n)$ presented in [4.9], that results from fitting the relative flow rate coefficient to the values reported in [4.10] is used in this thesis:

$$Q_{pr}(K_n) = 1 + 9.638(K_n)^{1.159} \tag{4.11}$$

Due to the gas rarefaction, Eqn. (4.6) can be modified giving origin to the modified Reynolds equation as shown in [4.10], [4.11]. For two very close surfaces in the *xy*-plane moving in the *z*-axis direction and with non-uniform distance *h*, the modified Reynolds equation describing the pressure changes *p* relative to the wall velocity is:

$$\frac{\partial}{\partial x}\left(h^3 \rho Q_{pr} \frac{\partial p}{\partial x}\right) + \frac{\partial}{\partial y}\left(h^3 \rho Q_{pr} \frac{\partial p}{\partial y}\right) = 12\eta \frac{\partial}{\partial t}(\rho h) \tag{4.12}$$

4.3.2 Analytical Solution for Parallel Surfaces

When the two surfaces move perpendicularly, the gap separation (film thickness) *h* is not a function of either *x* or *y* positions. Pressure *p*, is generally function of both place and time and Q_{pr} is a function of *p* and *h*. The partial derivative of Eqn. (4.12) is therefore:

$$\frac{h^3}{12\eta}\left[pQ_{pr}\left(\frac{\partial^2 p}{\partial x^2} + \frac{\partial^2 p}{\partial y^2}\right) + \left(Q_{pr} + p\frac{\partial Q_{pr}}{\partial p}\right)\left(\left(\frac{\partial p}{\partial x}\right)^2 + \left(\frac{\partial p}{\partial y}\right)^2\right)\right] = \frac{\partial}{\partial t}(ph) \tag{4.13}$$

This nonlinear partial differential equation can be linearized if small displacements h_z relative to the initial gap separation h_0 are considered. If $h = h_0 + h_z$, with $h_z \ll h_0$, the dynamic pressure change Δp will be small relative to the ambient pressure P_a ($p = P_a + \Delta p$, with $\Delta p \ll P_a$) and Eqn. (4.13) is linearized to:

$$\frac{h_0^3 Q_{pr}}{12\eta}\left(\frac{\partial^2 \Delta p}{\partial x^2} + \frac{\partial^2 \Delta p}{\partial y^2}\right) - \frac{h_0}{P_a}\frac{\partial \Delta p}{\partial t} = \frac{\partial h_z}{\partial t} \tag{4.14}$$

The solution of the linearized Reynolds equation, Eqn. (4.14), depends on the boundary conditions, basically the surface and gap geometry. For rectangular rigid plates moving in the direction normal to the surface plane, the pressure distribution for a sinusoidal excitation can be found analytically [4.5]. The solution has two components: one in-phase with the surface movement and another out-of-phase due to the compressibility properties of the gas film. The in-phase component acts as a spring force and the out-of-phase component provides the squeeze-film damping force. The damping and spring forces, acting on the surfaces can be expressed as an infinite series and are given by:

$$\frac{F_d}{h_z} = \frac{64\sigma P_a A}{\pi^6 h_0} \sum_{m,n=odd} \frac{m^2 + (n/\beta)^2}{(mn)^2\left[(m^2 + (n/\beta)^2)^2 + \frac{\sigma^2}{\pi^4}\right]}$$

$$\frac{F_s}{h_z} = \frac{64\sigma^2 P_a A}{\pi^8 h_0} \sum_{m,n=odd} \frac{1}{(mn)^2\left[(m^2 + (n/\beta)^2)^2 + \frac{\sigma^2}{\pi^4}\right]} \quad \textbf{(4.15)}$$

where $A = wl$ is the surface area for a rectangle with length l and width w, β is the ratio between length and width ($\beta = l/w$), m and n are odd integers and σ is the squeeze number. For an angular frequency ω the squeeze number is given by:

$$\sigma = \frac{12\eta_{eff} w^2}{P_a h_0^2}\omega \quad \textbf{(4.16)}$$

The solution to the linearized Reynolds equation depends on the frequency and besides being difficult to implement it is not suitable for a transient analysis. For low frequencies the damping force depends linearly on the velocity of the plate and the film behaves as a pure damper. At higher frequencies the relation becomes nonlinear and the spring force increases. At these frequencies the film is acting like a spring. The frequency where the damping force is equal to the spring force is referred to as the cut-off frequency and can be approximated by using the first term of Eqn. (4.15) and Eqn. (4.16) as:

$$\omega_c = \frac{\pi^2 P_a h_0^2}{12\eta_{eff}}\left(\frac{1}{l^2} + \frac{1}{w^2}\right) \quad \textbf{(4.17)}$$

A very suitable approach to model the solution of the linearized Reynolds equation is presented in [4.9] where the damping force can be represented by a network of frequency independent spring-damper elements, as shown in Fig. 4.5, which have the same

transfer function of the initial solution. The sections in Fig. 4.5 represent the terms of the series expansion and the same odd indices as used in Eqn. (4.15) apply.

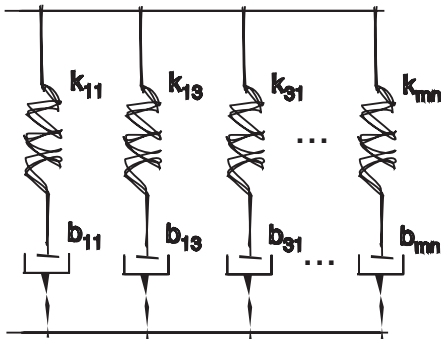

Figure 4.5 Gas-film damping model for parallel surfaces

The relation between the velocity $\frac{\mathrm{d}x}{\mathrm{d}t}$ (x is the displacement) and the force $F_{m,n}$ in one of the sections of the spring-damper network can be described by the differential equation:

$$\frac{\mathrm{d}x}{\mathrm{d}t} = \frac{1}{k_{m,n}}\frac{dF_{m,n}}{dt} + \frac{1}{b_{m,n}}F_{m,n} \tag{4.18}$$

If all signals are sinusoidal with a single angular frequency ω, the velocity and force can be transferred to the complex domain and Eqn. (4.18) becomes:

$$j\omega\bar{x} = \frac{1}{k_{m,n}}j\omega\bar{F}_{m,n} + \frac{1}{b_{m,n}}\bar{F}_{m,n}, \tag{4.19}$$

where $\bar{x}$ and $\bar{F}_{m,n}$ are complex coefficients. The total damping force, is the sum of all the forces in the parallel sections:

$$\bar{F}_t = \sum_{m,n=odd} \bar{F}_{m,n} = \bar{x} \sum_{m,n=odd} \frac{j\omega k_{m,n} b_{m,n}}{k_{m,n} + j\omega b_{m,n}} \tag{4.20}$$

The imaginary and real parts of the ratio $\frac{\bar{F}_{m,n}}{\bar{x}}$, which represent the out-of-phase and in-phase parts respectively, are:

$$
\begin{aligned}
Im\left(\frac{\bar{F}_{m,n}}{\bar{x}}\right) &= \frac{k_{m,n}^2 b_{m,n}\omega}{k_{m,n}^2 + \omega^2 b_{m,n}} \\
Re\left(\frac{\bar{F}_{m,n}}{\bar{x}}\right) &= \frac{b_{m,n}^2 k_{m,n}\omega^2}{k_{m,n}^2 + \omega^2 b_{m,n}}
\end{aligned}
\tag{4.21}
$$

The frequency dependency in Eqn. (4.15) is satisfied by the derived Eqn. (4.21). By making that $Im(\bar{F}_{m,n}/\bar{x}) = F_d/h_z$ and $Re(\bar{F}_{m,n}/\bar{x}) = F_s/h_z$, the component values of $b_{m,n}$ and $k_{m,n}$ for the spring-damper system are found:

$$
\begin{aligned}
b_{m,n} &= \frac{768 A \eta_{eff}}{\pi^6 h_0^3 (mn)^2 \left(\frac{m^2}{w^2} + \frac{n^2}{l^2}\right)} \\
k_{m,n} &= \frac{64 A P_a}{\pi^4 h_0 (mn)^2}
\end{aligned}
\tag{4.22}
$$

The advantage of representing the infinite series solution of the linearized Reynolds with a network of spring-damper elements is at the level of the implementation of the new solution. Each of the spring-damper sections is a first order system with a certain gain and time constant represented by Eqn. (4.18), which is very easy to implement (it uses a single integrator block) in any simulation program. A Simulink block diagram for the first section of the network is shown in Fig. 4.6.

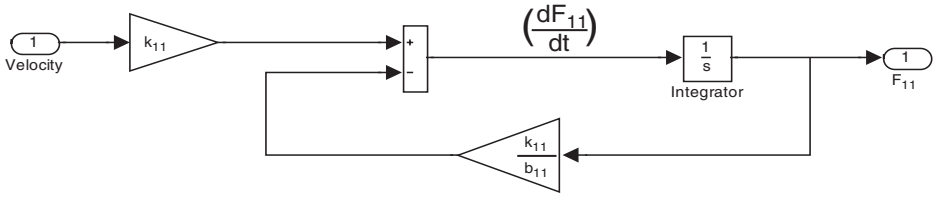

Figure 4.6 Simulink diagram block for a spring-damper section

4.3.3 Large-Displacement Analytical Model

The solution derived in the last section is only valid for small displacements around the initial film thickness h_0. For the majority of the MEMS applications the assumption of small displacements is not true and an analytic solution for the modified Reynolds equation can not be derived. This is especially true for pull-in studies and some other applications that use the full gap of the electrostatic actuator.

For large-displacement conditions FEM or finite-difference methods are usually used, however for the simple case of parallel-surfaces with uniform gap distance an approximate large-displacement model can be derived [4.1], [4.12]. If an uniform film thickness is considered (this is the case for the simple parallel-plate electrostatic actuator) and the pressure changes Δp, are small compared to the static pressure P_a ($p = P_a + \Delta p$, with $\Delta p \ll P_a$), the modified Reynolds equation, Eqn. (4.12), reduces to:

$$\frac{h^3 Q_{pr}(h, P_a)}{12\eta}\left(\frac{\partial^2 \Delta p}{\partial x^2} + \frac{\partial^2 \Delta p}{\partial y^2}\right) - \frac{h}{P_a}\frac{\partial \Delta p}{\partial t} = \frac{\partial h}{\partial t} \tag{4.23}$$

Since small displacements relative to the initial film thickness are not considered, Eqn. (4.23) models accurately the squeeze-film forces for any large-displacement condition as long as the pressure variations are negligible, when compared to the ambient pressure. The similarities between Eqn. (4.14) and Eqn. (4.23) are evident and differ only in two aspects: initial film thickness h_0 and η_{eff} in Eqn. (4.14) are replaced by h and $\eta / Q_{pr}(h, P_a)$ in Eqn. (4.23), respectively. This suggests that the nonlinear solution of Eqn. (4.23) can be approximated by replacing h_0 and η_{eff} in the component values that resulted from solving the linearized Reynolds equation. The new modified components become:

$$\begin{aligned} b_{m,n}(h) &= \frac{768 A \eta}{\pi^6 h^3 Q_{pr}(h, P_a)(mn)^2\left(\frac{m^2}{w^2} + \frac{n^2}{l^2}\right)} \\ k_{m,n}(h) &= \frac{64 A P_a}{\pi^4 h (mn)^2} \end{aligned} \tag{4.24}$$

The difference between the components of Eqn. (4.24) and Eqn. (4.22) resides on the fact that the modified components of Eqn. (4.24) depend on variable parameters which change with the current displacement value of the device. Since the gap distance and the effective viscosity depend on the displacement, each of the spring-damper sections is now defined by a first order system with variable gain and time constant. The total damping force is the sum of several damping forces of the type:

$$F_{m,n} = b_{m,n}(h)\frac{dx}{dt} - \frac{b_{m,n}(h)}{k_{m,n}(h)}\frac{d\dot{F}_{m,n}}{dt} \tag{4.25}$$

The full differential equation, Eqn. (4.4), describing the movement of a 1-DOF parallel-plate electrostatically actuated MEMS device where x is the displacement and $h=h_0-x$ is the large-displacement gap distance can be rewritten as:

$$m\frac{\mathrm{d}^2 x}{\mathrm{d}t^2} + (F_{1,1} + F_{1,3} + F_{3,1} + \ldots + F_{m,n}) + kx = ma_{ext} + F_{elect} \tag{4.26}$$

Adopting the notation $\dot{X} = f(X)$ yields for the overall nonlinear system:

$$\begin{aligned}
\dot{x} &= y \\
\dot{y} &= -\frac{1}{m}[(F_{1,1} + F_{3,1} + \ldots + F_{m,n}) + kx - a_{ext} - F_{elect}] \\
\dot{F}_{1,1} &= k_{1,1}(h)y - \frac{k_{1,1}(h)F_{1,1}}{b_{1,1}(h)} \\
\dot{F}_{3,1} &= k_{3,1}(h)y - \frac{k_{3,1}(h)F_{3,1}}{b_{3,1}(h)} \\
\dot{F}_{m,n} &= k_{m,n}(h)y - \frac{k_{m,n}(h)F_{m,n}}{b_{m,n}(h)}
\end{aligned} \tag{4.27}$$

The differential Eqn. (4.27) describes analytically the movement of a 1-DOF device where squeeze-film forces are included accounting for compressibility effects and large-displacements. Although the equation is highly nonlinear it can be implemented using simple integrators blocks and displacement controlled parameters in any simulation program. This analytical approach is very suitable for the simulation of full-system parallel-plate based MEMS devices.

4.3.4 Border Effects

The squeeze-film model for parallel surfaces presented in the previous sections was derived from the assumption of trivial boundary condition, i.e, the gas at the surface borders is at ambient pressure [4.5], [4.9]. This condition is true if the surface dimensions are large compared to the film thickness. However, in practical devices the flow escaping from the damper borders might have a significant effect on the damping coefficient. This is especially true in surface-micromachined MEMS devices where the structure thickness is just a few times larger then the film thickness, i.e., the length and width of the damper are comparable to the film thickness (gap size). Measurements and 3D flow simulations performed in [4.13] show that the fringe effects considerably increase the damping force (35%), for ratios between surface width and gap size as high as 20.

In order to include the border effects on the analytically derived squeeze-film model, a modified surface length $l_0 = l + \Delta l$ and surface width $w_0 = w + \Delta w$ are used. The value of the new surface extension is such that the damping coefficient for the elongated surface with trivial conditions, has the same value as the damping coefficient of the real device size with border effects has shown in Fig. 4.7. Two different methods have been proposed in literature to compute the effective surface dimensions l_0 and w_0: analytical approach using acoustic boundary conditions [4.14], [4.15] or 3D FEM simulations [4.2], [4.13].

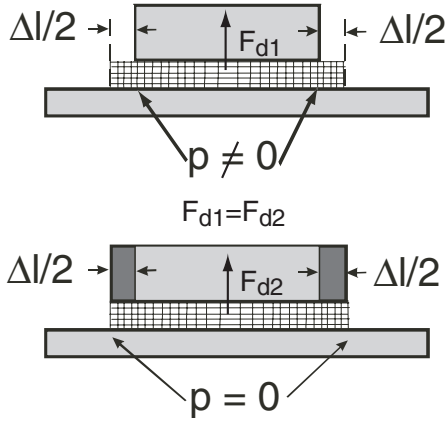

Figure 4.7 Surface elongation for modelling the border effects

4.3.4.1 Acoustic Boundary Conditions

If it is considered that the flow channel continues outside the parallel-plate surface border, the border flow can be modelled in a simple way. Assuming that the pressure drops linearly in the imaginary channel elongation of length $\Delta l/2$:

$$\left.\frac{\partial p}{\partial n}\right|_{border} = \pm\frac{p}{\Delta l/2}, \tag{4.28}$$

where n is a coordinate normal to the border, a first order approximation for the modified length l_0 and surface width w_0 due to the end effects can be derived [4.14]:

$$l_0 = l + \Delta l = l\frac{\sqrt{1+3A_l}(1+4A_w)^{3/8}}{\sqrt{1+3A_w}(1+4A_l)^{1/8}}$$
$$w_0 = w + \Delta w = w\frac{\sqrt{1+3A_w}(1+4A_l)^{3/8}}{\sqrt{1+3A_l}(1+4A_w)^{1/8}} \quad (4.29)$$

The values for coefficients A_l and A_w depend on a relative elongation $\Delta L(D, L)$, and can be expressed by [4.15]:

$$A_l = \frac{\Delta L(D, L_l)}{L_l}$$
$$A_w = \frac{\Delta L(D, L_w)}{L_w}, \quad (4.30)$$

where $L_l = l/h$ and $L_w = w/h$. An approximation for the relative elongation $\Delta L(D, L)$, based on flow rate values calculated from the Boltzmann equation [4.16], is presented in [4.15]:

$$\Delta L = \frac{8}{3\pi}\frac{1+2.471D^{-0.659}}{1+0.5D^{-0.5}L^{-0.238}}, \quad (4.31)$$

Here D is the inverse Knudsen number and for a rectangular channel is given by:

$$D = \frac{\sqrt{\pi}}{2K_n} \quad (4.32)$$

4.3.4.2 Extraction of Elongations Through FEM Simulations

Another method used to predict the border effects on parallel surfaces of different aspect ratios relative to the gap size was proposed in [4.2]. A set of 3D FEM simulations were performed and based on the results approximations for the elongations were proposed. The Navier-Stokes equations were solved assuming isothermal and no-slip boundary conditions (continuum flow regime).

A 3D model similar to the one used during the FEM simulations is shown in Fig. 4.8. The effective elongation for each of the sides was first extracted from 2D FEM simulations. Subsequently, the elongations derived on the 2D simulations were used (while ignoring the corner flow) together with the results of the 3D simulations and an

approximation for the drag forces acting on the side walls of the moving plate was proposed.

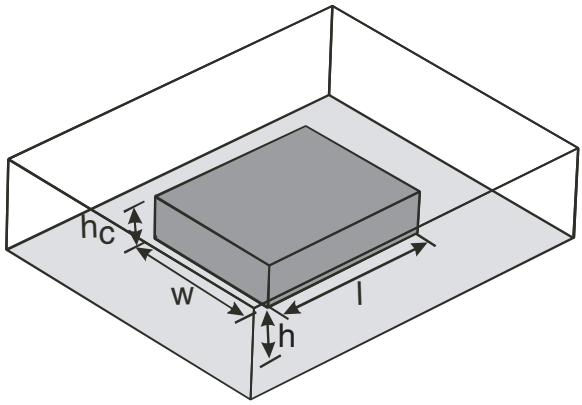

Figure 4.8 3D FEM model

For a parallel-plate configuration with linear movement the effective elongation reported in [4.2] is:

$$\begin{aligned} l_0 &= l + 1.3h \\ w_0 &= w + 1.3h \end{aligned} \tag{4.33}$$

The mechanical damper that models the drag forces on the side walls of the moving plate is approximated to:

$$b_{drag} = \frac{1}{2.2\eta_{eff} l \sqrt{\frac{l + 7.1h_c}{h}} + 2.2\eta_{eff} w \sqrt{\frac{w + 7.1h_c}{h}}} \tag{4.34}$$

In order to include the border effects in the squeeze-film large-displacement model, revised values of the components for the spring-damper network are used:

$$\begin{aligned} b_{m,n}(h) &= \frac{768 l_0 w_0 \eta}{\pi^6 h^3 Q_{pr}(h, P_a)(mn)^2 \left(\frac{m^2}{{w_0}^2} + \frac{n^2}{{l_0}^2} \right)} \\ k_{m,n}(h) &= \frac{64 l w P_a}{\pi^4 h (mn)^2} \end{aligned} \tag{4.35}$$

It should be noted that the value of $k_{m,n}$, used to model the compressibility of the gas is not affected by the border effects and thus the effective elongation does not apply. The total damping force is now the force given by all the forces in the spring-damper network plus the drag force:

$$F_t = \sum_{m,n=odd} b_{m,n}(h)\frac{dx}{dt} - \frac{b_{m,n}(h)}{k_{m,n}(h)}\frac{d\dot{F}_{m,n}}{dt} + b_{drag}\frac{dx}{dt} \tag{4.36}$$

The model based on the 3D FEM simulations is simpler and gives better results than the model based on the acoustic boundary conditions [4.2]. It is used as the preferred method to model the border effects in this thesis.

4.3.5 Finite Difference Model

For devices with more complex geometries or devices with displacements not uniform along the surface, the Reynolds equation can not be solved analytically and the model derived for rectangular surfaces is not sufficient. To model these cases Finite Element Modelling (FEM) or Finite Differences (FD) are usually used.

The use of FEM or FD is a very effective way of modelling the squeeze-film damping. However, the use of FEM or FD is not to suitable to the modelling of the full device dynamics (Eqn. (4.4)). In [4.3] and [4.17] a model based on FD was implemented with an electrical equivalent circuit. This approach is not very flexible and the use of controlled electrical elements makes it a complicated approach. A more flexible and simple approach was proposed in [4.4] where the full dynamic behaviour of a MEMS device is simulated in Simulink. Both the squeeze-film FD model and the displacement governing equation are implemented inside Simulink, which makes the method very flexible. A detailed overview of this approach is presented here.

If two surfaces in the direction of the *xy*-plane with non-uniform gap distance *h* are moving in the *z*-axis direction, the modified Reynolds equation, Eqn. (4.12) applies. Since *p* and *h* are functions of both place and time in this configuration and Q_{pr} is a function of *p* and *h*, the partial derivation of Eqn. (4.12) yields:

$$\begin{aligned} &ph^3 Q_{pr}\left(\frac{\partial^2 p}{\partial x^2} + \frac{\partial^2 p}{\partial y^2}\right) + \left(3ph^2 Q_{pr} + ph^3\frac{\partial Q_{pr}}{\partial h}\right)\left(\frac{\partial h}{\partial x}\frac{\partial p}{\partial x} + \frac{\partial h}{\partial y}\frac{\partial p}{\partial y}\right) + \\ &\left(h^3 Q_{pr} + ph^3\frac{\partial Q_{pr}}{\partial p}\right)\left[\left(\frac{\partial p}{\partial x}\right)^2 + \left(\frac{\partial p}{\partial y}\right)^2\right] = 12\eta\frac{\partial(ph)}{\partial t} \end{aligned} \tag{4.37}$$

For large-displacement conditions the velocities tend to be quite high and the limitations of the Reynolds equation must be taken into consideration. One of the assumptions when the Reynolds equation was derived from the Navier-Stokes equation was the fluid inertia. If $\rho\omega h^2/\eta \ll 1$ the gas inertia can be neglected but gas rarefaction is not accounted for. A new condition that accounts for the rarefaction effects was suggested in [4.17], which states that if:

$$\frac{\omega\rho_0 h^2 Q_{pr} P_a}{\eta P_0} \ll 1 \ , \tag{4.38}$$

where ρ_0 is the gas density at pressure P_0 and Q_{pr} is calculated for P_a and h, the gas inertia can be neglected.

For the finite difference model the surface is first divided into a rectangular grid of $M \times N$ elements. It should be noted that the method is suitable for all kind of different shapes, but our focus will be on a rectangular shape. On a *xy*-plane, the elements have coordinates $x = m \cdot \Delta x$ and $y = n \cdot \Delta y$ with $m = 0 \ldots M-1$ and $n = 0 \ldots N-1$. The pressure $p(x, y)$ at the discrete points is expressed as $p_{m,n}$ and the spatial derivatives of p in Eqn. (4.37) are replaced with finite difference approximations [4.18]:

$$\frac{\partial^2 p}{\partial x^2} = \frac{p_{m+1,n} - 2p_{m,n} + p_{m-1,n}}{(\Delta x)^2} \tag{4.39a}$$

$$\frac{\partial^2 p}{\partial y^2} = \frac{p_{m,n+1} - 2p_{m,n} + p_{m,n-1}}{(\Delta y)^2} \tag{4.39b}$$

$$\frac{\partial p}{\partial x} = \frac{p_{m+1,n} - p_{m-1,n}}{2\Delta x} \tag{4.39c}$$

$$\frac{\partial p}{\partial y} = \frac{p_{m,n+1} - p_{m,n-1}}{2\Delta y} \tag{4.39d}$$

In terms of modelling the surface displacement h acts as the input for the squeeze-film model, and the output is the force acting on the surface due to pressure changes. If a rigid structure with movements along the *z*-axis is considered, as is usually the case with MEMS devices, the rigid surface can have three modes of motion: 1 linear movement and 2 tilting movements. These fundamental surface movements can be expressed as functions of *x* and *y*. As a result the spatial derivatives of h in Eqn. (4.37) can be easily evaluated. Likewise, the partial derivatives of Q_{pr} with respect to p and h are also easily evaluated.

If the finite differences are implemented at each mesh point and assuming a rigid surface, Eqn. (4.37) reduces to a time differential equation:

$$FD_{m,n} = 12\eta\left(p_{m,n}\frac{\partial h}{\partial t} + h\frac{\partial p_{m,n}}{\partial t}\right), \tag{4.40}$$

where $FD_{m,n}$ is just the left-hand side of Eqn. (4.37). This results in a set of $M \times N$ time differential equations. Eqn. (4.40) suggests that the initial problem reduces to solve a simple differential equation. As the surface displacement h acts as the input, and we are interested in the pressure at each mesh point, Eqn. (4.40) can be rewritten as:

$$\frac{\partial p_{m,n}}{\partial t} = \frac{FD_{m,n}}{12\eta h} - \frac{p_{m,n}}{h}\frac{\partial h}{\partial t} \tag{4.41}$$

The total damping force acting on the surface is obtained by adding the force at each mesh point:

$$F_{FD} = A_{eff}\sum_{m=0}^{M-1}\sum_{n=0}^{N-1} p_{m,n} \tag{4.42}$$

Here A_{eff} is the effective area where the pressure acts. For a linear movement perpendicular to the surface plane $A_{eff} = \Delta x \Delta y$.

When Eqn. (4.41) is implemented at each mesh point and the spatial derivatives are evaluated using the finite difference approximations, the remaining problem is the computation of the time derivatives. If the implementation is done in Simulink, the finite differences are used to solve the squeeze-film forces and the Simulink ODE solvers are used to solve the governing equation of the MEMS device. The method is suitable to model the dynamics of MEMS regardless of the geometry and movement of the device, while accounting for large-displacement and rarefaction effects.

In order to have an acceptable accuracy using finite differences a large number of mesh points is necessary. A high number of mesh points implies a more complex implementation and a longer computational time. The use of a low level language (C language) inside of Simulink [4.4], [4.19] allows the implementation of a simple and efficient finite difference algorithm with parameterized components, which greatly contributes to model flexibility. Mesh size, gas properties or surface size can be changed efficiently when this approach is used.

Eqn. (4.37) can not be solved without the definition of the boundary conditions. If trivial boundary conditions are used the pressure at the open borders is settled as being at ambient pressure. A more realistic model is obtained if the border effects on the sur-

face borders are considered. Theses effects can be modelled by elongation, which can easily be implemented by adding an extra element outside the surface where the pressure is considered at ambient pressure. Fig. 4.9 shows a rectangular grid of 6×3 elements. It is a representation of the finite difference proposed method where the border effects are considered.

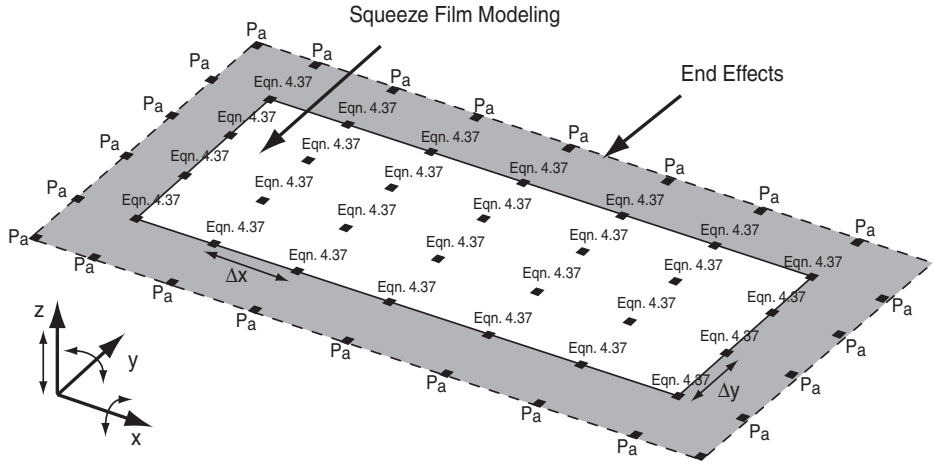

Figure 4.9 Finite difference rectangular grid of 6x3 elements with border effects included

4.4 1-DOF Modelling

In the last section, a generic modelling platform for simulation of MEMS dynamics was presented. In this section the method is applied to a real 1-DOF surface-micromachined MEMS structure. Both the large-displacement model and the finite differences model are used and compared to measured data for validation of the proposed models.

The 1-DOF structure used here is the same MEMS device used for verification of the 1-DOF static pull-in model and is depicted in Fig. 4.10. The values for the actuation

capacitance and for the spring constant were already computed in chapter 3. The main device parameters are presented in Table 4.1.

TABLE 4.1 Main parameters of the 1-DOF microdevice used

Fixed Parameter	Value
Mechanical spring (k)	*2.877 N/m*
Mass (m)	*2.3 μg*
Resonance frequency (f_0)	*5.7 kHz*
Initial gap distance(d_0)	*2μm*
C_{d0} (zero-displacement actuation capacitor)	*157 fF*
C_{s0} (zero-displacement sensing capacitor)	*368 fF*
Total nº of arms	*40*

As it can be seen from Fig. 4.10, the differential actuation and sensing capacitors are the cause of the squeeze-film damping. Both the actuation and the sensing capacitors have the same size which allows building the damping model for one arm only. The total damping force is found by multiplying the output of the single arm model by the total number of arms. A closer view to one of the arms, Fig. 4.11, gives a better perspective of the components that cause the squeeze-film damping.

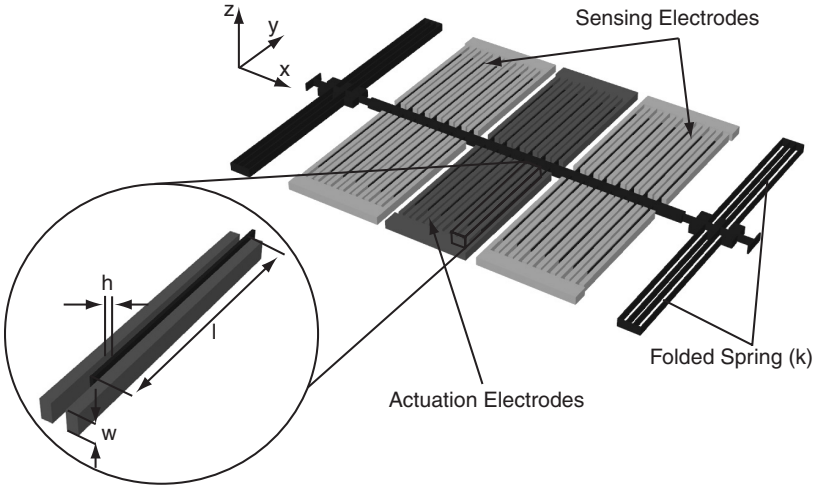

Figure 4.10 Drawing of the 1-DOF microdevice

The large-signal displacement model derived in the previous section was for a single parallel-plate configuration. This device has the movable arm connected between two fixed electrodes and therefore two gas films are present. Since the gap distances are different each film must be modelled separately. Besides the two films the substrate underneath the movable arm, just 2 μm away, must also be considered (Fig. 4.11). The model derived for a single parallel-plate configuration does not take into account the presence of a substrate but as the spaces between the substrate and movable arm and between the fixed and movable arms are within the same order of magnitude the possible changes on the damping forces due to the substrate must be evaluated.

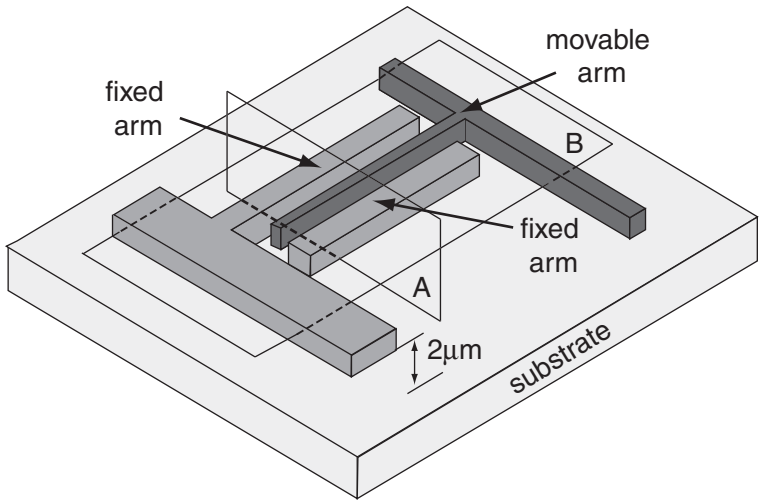

Figure 4.11 Single arm configuration

4.4.1 Substrate Effect Evaluation Using FEM

Although the spacing between substrate and movable arm does not change with arm motion, it could change the damping force in two ways:

1. Slip-flow damping.
2. Changes in the border effects.

To evaluate the effect of the substrate on the squeeze-film damping, 2D FEM simulations are used. The goal of these simulations is to check the velocity profile and the pressure distribution on the damper without taking into account the quantitative values of the pressure and the gas-film forces.

The multiphysics Ansys simulator was used for the FEM model implementation. The linearized Reynolds equation is solved using isothermal and no-slip boundary conditions. Two different 2D planes, plane A and B (see Fig. 4.11) are used for a convenient qualitative description of the substrate effect on the pressure distribution. Air at ambient pressure is considered as the gas medium.

A sinusoidal displacement with a frequency of 10 kHz and amplitude of 0.2 μm is applied to the movable arm and a transient simulation of 20 μs (2 periods) is performed. Fig. 4.12 presents the pressure distribution for plane A for the maximum achieved displacement.

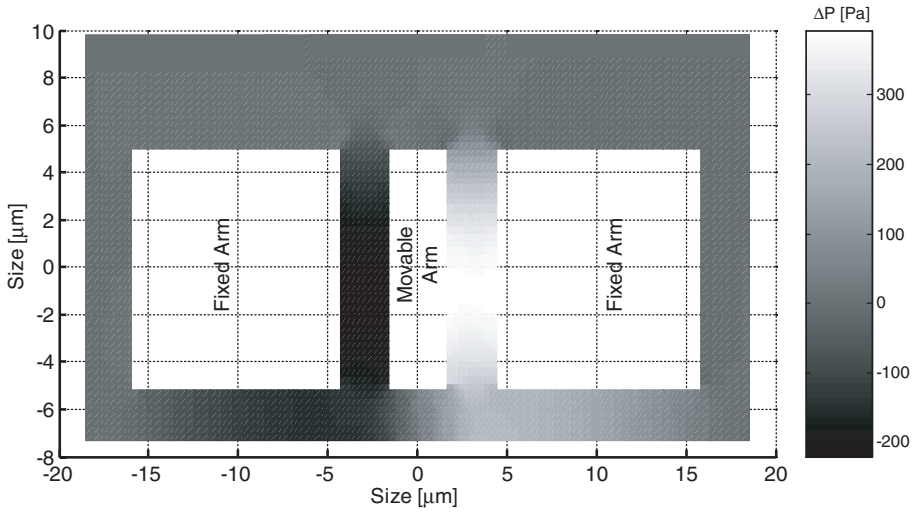

Figure 4.12 Pressure distribution for plane A

When the movable arm moves to the right, the pressure of the right film increases and the pressure of the left film decreases. A qualitative analysis to the pressure distribution reveals three main aspects:

1. A slight shift in the pressure distribution of both the right and left films, i.e., the central point where the pressure should be at the highest level does not coincide with the middle of the movable arm.
2. The presence of high pressure at the film borders which was to be expected since the ratio between film thickness and arm height, is small.
3. Pressure changes between the fixed arms and the substrate due to the reduced escape volume in that region.

A better understanding of the observed pressure distribution can be obtained from the velocity flow profile. Using the same simulation parameters as used in the previous figure, the velocity profile of the gas flow was computed (see Fig. 4.13). The gas flows out of the right film when the movable arm squeezes it against the fixed arm. At the same time, gas flows into the left film. The effect of the substrate is clearly visible in the graph. In the upper film part, the gas can flow freely in and out of the damper and the escaping gas out does not flows back in. However on the lower part and due to the reduced air volume (imposed by the presence of the substrate), a significant part of the gas flowing out from the right film re-enters into the left film. In fact the reduced volume imposed by the substrate is the cause of both the pressure distribution shift on the films and the pressure changes between substrate and fixed arms. The slight shift in pressure distribution is not significant when compared to the border effects and can be neglected. The pressure forces acting on the fixed arms do not affect the movable arm movement and therefore can also be neglected. The drag forces on the movable-arm side are very small and accounted for in the border-effect model (see section 4.3.4.2). The border effects remain as a very important parameter and an accurate model has to take these into consideration.

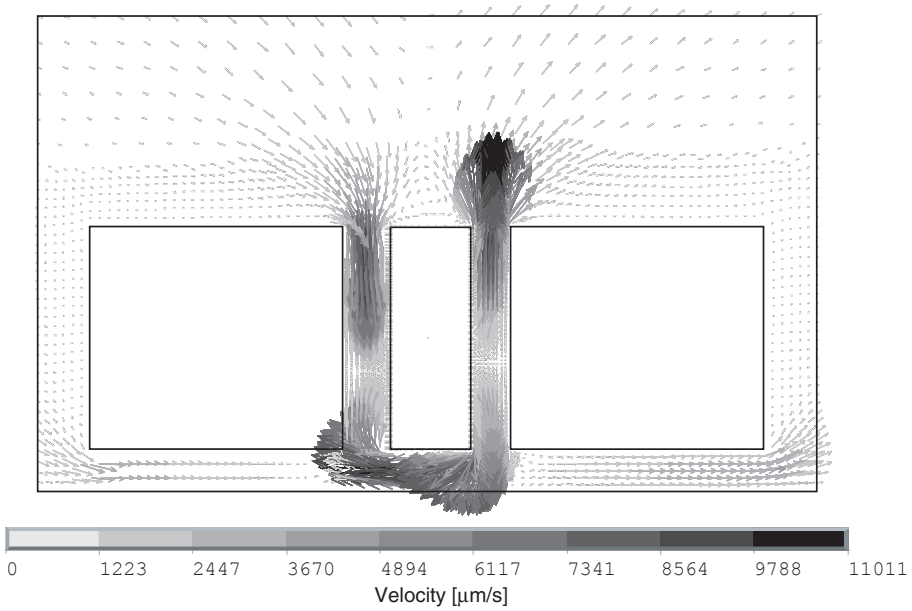

Figure 4.13 Flow velocity profile for plane A

The FEM simulations for plane B use the same boundary displacement conditions as used for plane A. The pressure distribution at maximum displacement is presented in

Fig. 4.14. In this plane, the substrate does not play any role and it can be seen that for high ratios between the length of the damper and the film thickness the border effects are negligible. The pressure changes along the movable arm are very uniform decreasing to zero close to the border edges.

Two main conclusions are drawn from this 2D FEM analysis. First, the presence of the substrate must be taken into consideration when building a squeeze-film model as it may greatly change the flow velocity profile and pressure distribution of the damper. Second, if the models presented in the previous section are to be used in different conditions than the ones used to derive the models, the validity of the models under these new conditions must be evaluated. As shown here, the models derived in the previous sections can be used to model the 1-DOF microdevice squeeze-film damping. Although there is a slight shift on the pressure distribution, the parallel-surfaces model accounting for the border effects is expected to model properly the right and left films.

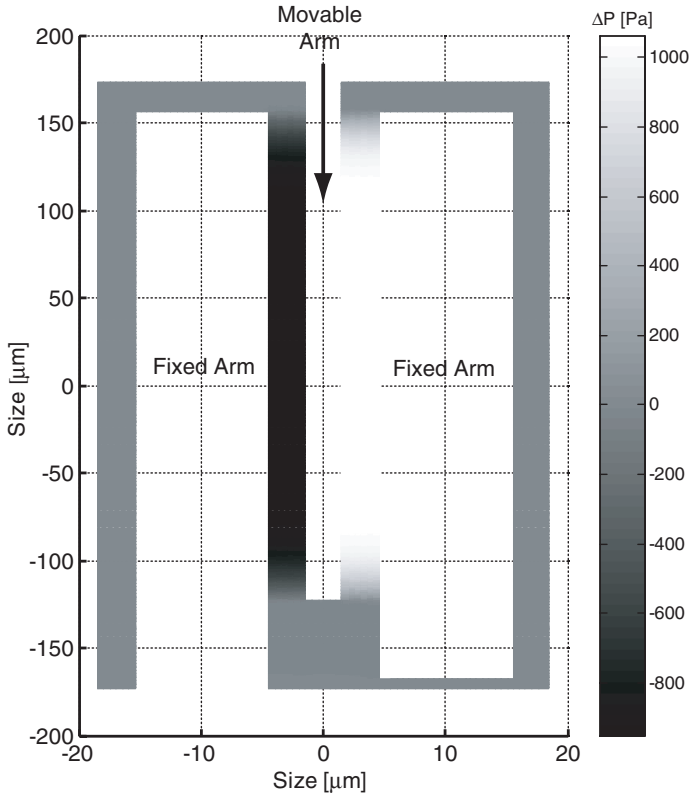

Figure 4.14 Pressure distribution for plane B

4.4.2 1-DOF Large-Signal Model

The large-signal model has to be implemented separately for the two films. The total damping force is achieved by adding the two film forces followed by a multiplication of the total number of arms.

The difference between the two films resides in the value of the gap. If a right film and a left film are assumed, the right film gap distance value is $h_{right} = d_0 + x$, where d_0 is the initial gap distance and x the structure displacement and the left film gap is described by $h_{left} = d_0 - x$. This different values for the gap are also used on the different flow rate coefficients ($Q_{pr,right}$, $Q_{pr,left}$).

Neon at a pressure of 0.6×10^5 Pa is used as the gas medium for the modelling of the squeeze-film damper. Neon's viscosity is $\eta_{neon} = 3.11 \times 10^{-5}$ Pa.s [4.20] at room temperature and it has a mean free path of $\lambda_{neon} = 143$ nm [4.20] at atmospheric pressure. If a spring-damper network with three sections (F_{11}, F_{13} and F_{31}) is built for each of the films, based on the components given by Eqn. (4.24), a large-signal model for the structure results.

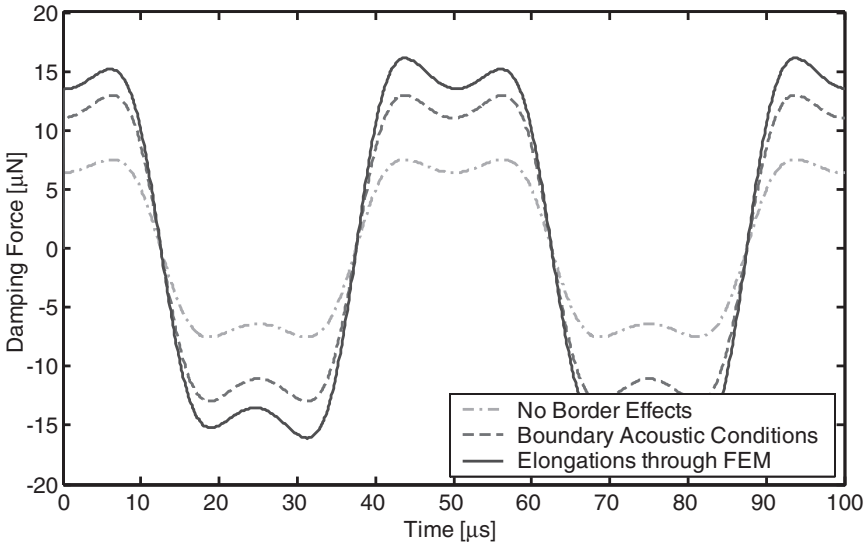

Figure 4.15 Comparison between large-signal squeeze-film models

First the large-signal squeeze-film model was implemented based on the assumption of no border effects and a sinusoidal displacement of 20 kHz with amplitude of 1 μm was imposed on the movable arm. Next the border effects were included and the two different methods, the acoustic boundary condition and the elongations through FEM simulations, were implemented. The same displacement was imposed on the movable arm and the results of the three models are shown in Fig. 4.15.

Fig. 4.15 is illustrative of the errors that can be made when border effects are not included. For the present microdevice the border effects are really important as confirmed by the 2D FEM simulations and represent an increase of about 80% on the damping force, when compared to the model without border effects included. The differences between the two proposed methods for the border effects are here clearly visible and as the method based on the FEM simulations has a smaller error (according to [4.2]), it is the preferred model.

4.4.3 1-DOF Finite Difference Model

As for the large-signal model, the finite difference based model also has to be implemented for the two dampers (left and right). Since the surface is rigid and the film thickness h has an uniform distance, Eqn. (4.13) is used to implement the large-signal finite difference model.

For the 1-DOF case the pressure p is function of place and time, and h is just function of time (it is uniform along the surface). As Q_{pr} is function of p and h, the partial derivative in order to p is:

$$\frac{\partial Q_{pr}}{\partial p} = -\frac{11.17(K_n)^{1.159}}{p} \tag{4.43}$$

Assuming that the pressure changes Δp are small compared to the static pressure P_a ($p = P_a + \Delta p$, with $\Delta p \ll P_a$), pressure p can be replaced by the static pressure in Eqn. (4.13). Both the film thickness h and its derivative to time (velocity) act as the inputs to the squeeze-film model.

In order to include the border effects, two different approaches were considered. The first assumed the system dynamics at the device edges, adding an extra element outside the surface where the pressure is considered at ambient pressure as shown in Fig. 4.9. The second approach used the elongation method proposed for the analytical model (derived from FEM simulations). By using effective elongations for each of the sides, the fringe border effects are accommodated in the surface extensions.

The FD model was implemented in Simulink, using a low level language for the FD algorithm and a sinusoidal displacement of 20 kHz with amplitude of 1 μm was imposed on the movable arm. Neon at a pressure of 0.6×10^5 Pa was used as the gas medium and the pressure distribution on one of the films for maximum velocity is shown in Fig. 4.16 (effective elongation method used). Some other comparative results are shown in Fig. 4.17.

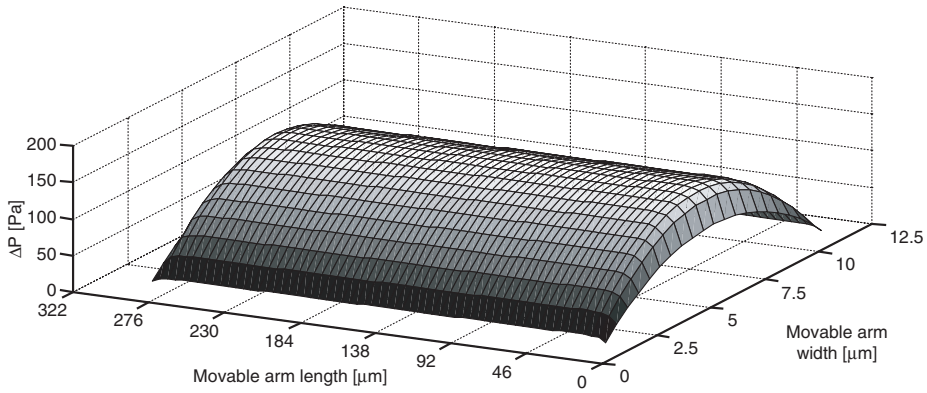

Figure 4.16 Pressure distribution in the right film for maximum velocity using a 60x20 finite difference mesh

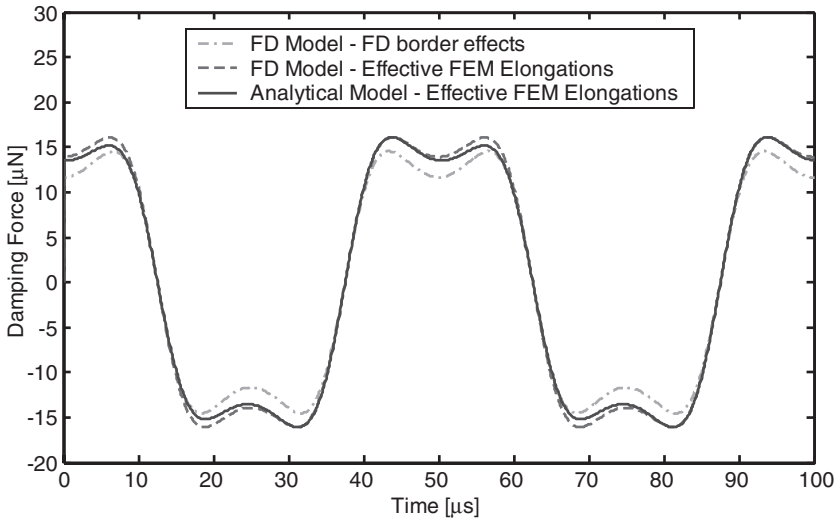

Figure 4.17 Comparison between FD model and analytical based model

The results for the analytical derived model are in agreement with the FD models especially for the case where effective elongations are assumed. It is evident from these simulations that the border effects are a major error source when dealing with squeeze-film damping. The three different methods used to model the border effects, boundary acoustic conditions, elongations derived from FEM simulations and the finite difference approach, gave different results. Nevertheless whatever the approach used to model the border effects the response will be better than the response obtained when border effects are neglected.

4.4.4 Experimental Measurements

A SEM photograph of the microdevice used on the experiments is once again presented in Fig. 4.18. The main details of the device were presented in chapters 2 and 3.

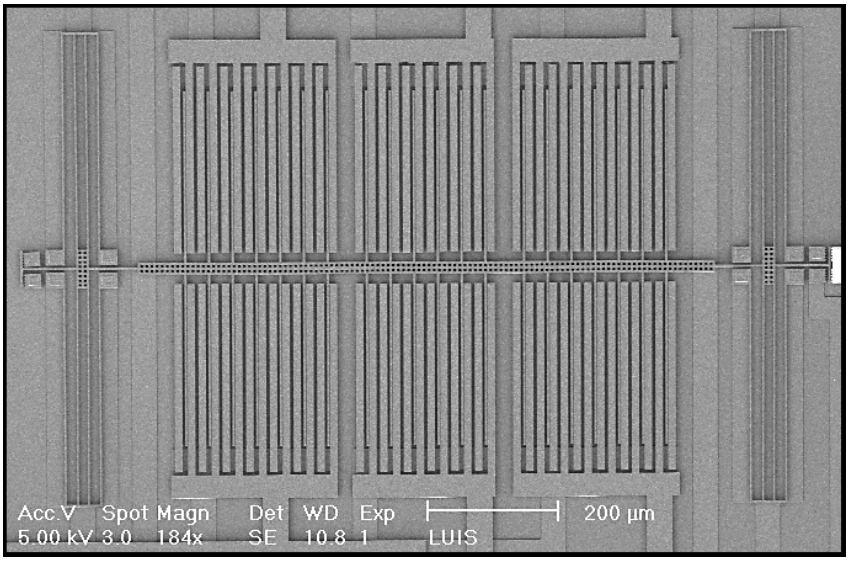

Figure 4.18 Photograph of the fabricated microdevice used for validation of the squeeze-film models

Some of the fabricated devices after release of the sacrificial layer were encapsulated in neon (type 1) at 0.6×10^5 Pa. Others were not encapsulated (type 2) allowing the realization of measurements using air as the fluidic medium ($\eta_{air} = 1.85 \times 10^{-5}$ Pa.s and $\lambda_{air} = 69$ nm at room temperature [4.20]). The displacement is measured by sens-

ing the capacitance changes on the two sets of sensing capacitors. Since the gain of the readout electronic circuit is known, the output voltage can be translated to the actual device displacement and compared to the simulation values.

The full-system device equation, Eqn. (4.4), was implemented in Simulink using both the analytical derived damping model and the finite difference model. The use of a high level description language (Simulink) allows to integrate in the model some of the system properties that otherwise could not be simulated. Those are: inclusion of the stoppers, changes on the initial zero displacement caused by stress gradients, etc., allowing the simulation of the pull-in phenomenon and the hysteresis effect associated with it. Border effects were included, and the elongation method through FEM simulations was the method used in both models.

Several simulations were performed under different input voltages using neon as the fluidic medium on the two models (analytical and FD). Measurements for the same voltage conditions were performed to validate the modelling. Results of simulations and experiments on devices of type 1 are presented in Figs. 4.19 and 4.20.

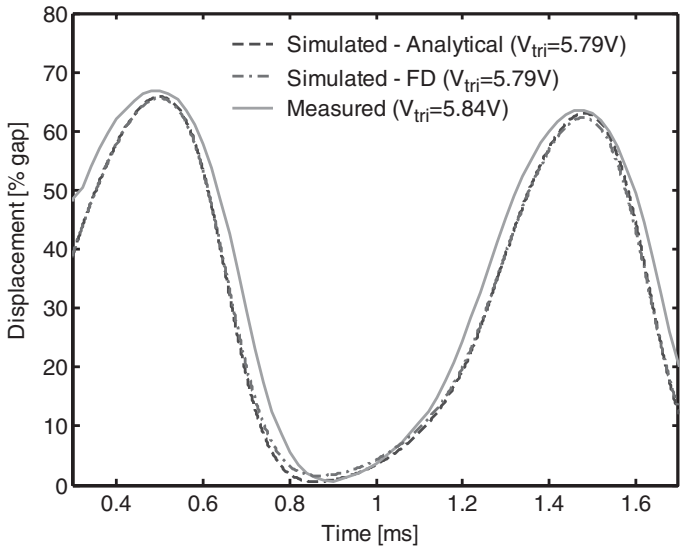

Figure 4.19 Simulated and measured response to a 500Hz triangular wave for a neon encapsulated device

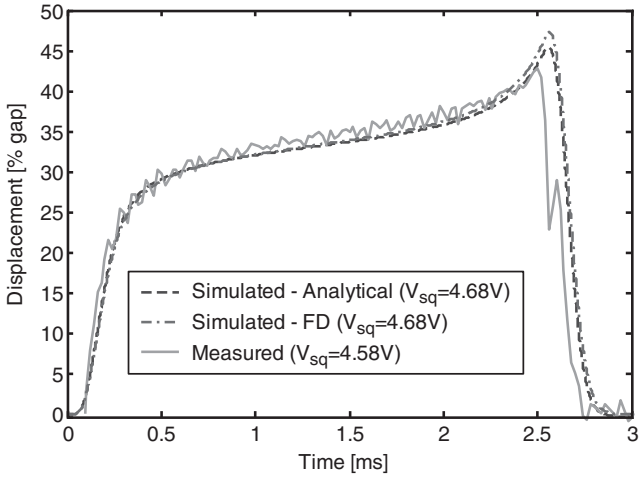

Figure 4.20 Simulated and measured response to a 200 Hz square wave for a neon encapsulated device

The agreement between simulated values and experimental measured data for the different electrostatic signals is very good and validates the model for MEMS dynamics proposed in the thesis. A few more measurements were performed on devices of type 2. The devices were introduced in a pressure chamber and measurements at different pressure values were performed. The correspondent results comparing the experimental data and simulations under the same conditions are presented in Figs. 4.21 and 4.22.

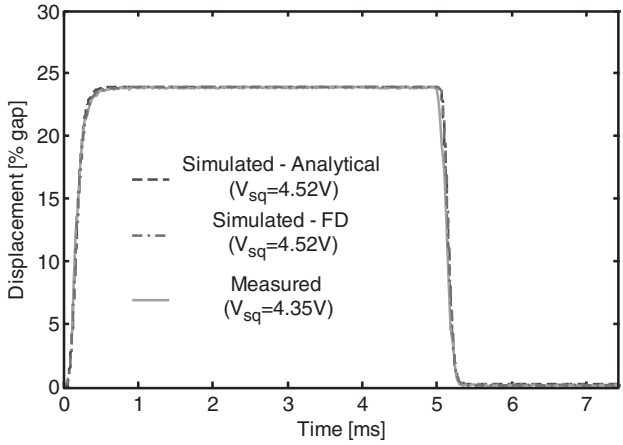

Figure 4.21 Simulated and measure response to a 100Hz square wave on air devices at 10^5 Pa

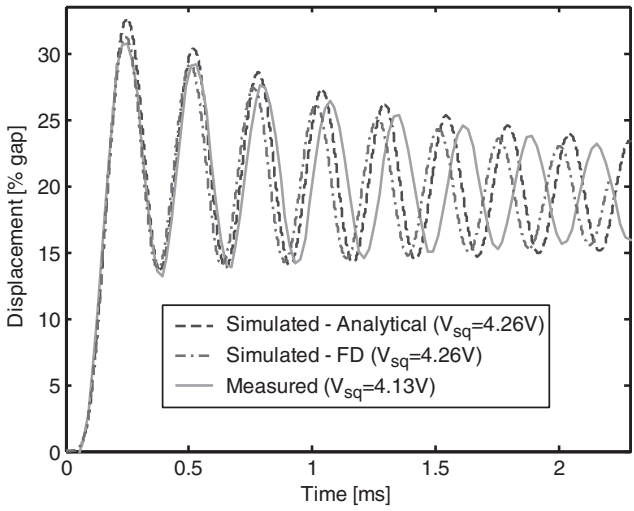

Figure 4.22 Simulated and measure response to a 100Hz square wave on air devices at 2.15x10^2 Pa (2.15 mbar)

The proposed dynamic models describe the dynamic behaviour of the microdevice in all the different measured situations with a high degree of accuracy. Both the analytical derived model and the FD model perform very good. The close agreement between the FD and the analytical models proves that the simplifications made to derive the large-signal analytical model do not introduce errors. Although the FD model is more accurate than the analytical model, it takes longer time to simulate (about 10 times more for a small mesh). Moreover the FD algorithm is not as simple to implement as the analytical one. For the simple cases the analytical model should be used and its simplicity and good performance make it a very good tool for the design phase. The FD model is ideal for the more complex cases.

4.5 2-DOF Modelling

A more interesting challenge is the full-system modelling of a device with 2 or more degrees of freedom. Unless the movement of the device can be decomposed into linear and tilt movements, the analytical approach can not be used and FEM or FD based models have to be applied. A fabricated 2-DOF MEMS device is modelled in this section using finite differences, and the simulation results are compared with measurements.

A drawing of the 2-DOF inverted balance structure used is presented in Fig. 4.23. It is the same 2-DOF device used in chapter 3 for verifying the static pull-in model. Similar to the previous 1-DOF device, the movable arm of the 2-DOF device is connected between two fixed electrodes and therefore two gas films are present. Besides that the length and gap distance of the sensing and actuation arms are different causing different gas film forces responses. For a proper modelling of the device squeeze-film damping four gas films are needed.

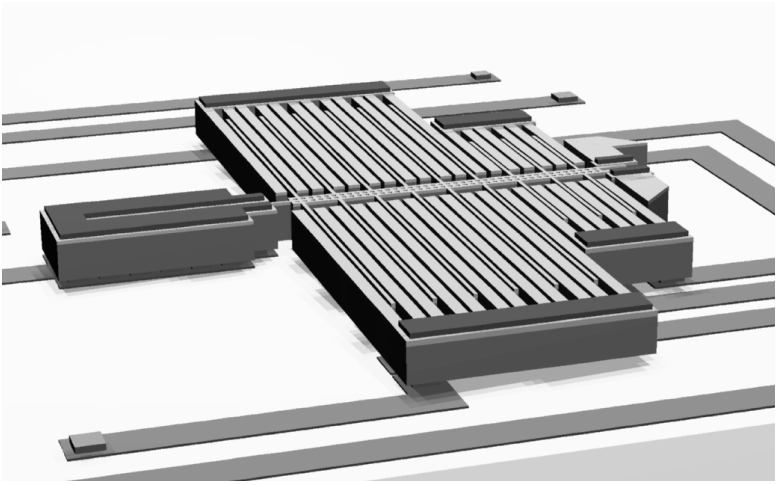

Figure 4.23 Drawing of the 2-DOF microdevice

The device under analysis is fully characterized by two state variables: displacement w_1 and angle φ_1 (see also section 3.5 in chapter 3). The modelling difficulties of this structure are due to the movement of the arms connected to the pointer. The movement can be decomposed under two distinct movements, translational and rotational, with cross-coupled terms in between. The movement of the 2-DOF structure upon a voltage V applied to the actuation arms is described by the nonlinear differential equations (in the absence of an external acceleration):

$$\begin{cases} F_m + F_b(w_1, \varphi_1) + F_k(w_1, \varphi_1) = F_{elect}(w_1, \varphi_1, V) \\ M_m + M_b(w_1, \varphi_1) + M_k(w_1, \varphi_1) = M_{elect}(w_1, \varphi_1, V) \end{cases}, \tag{4.44}$$

where F_m and M_m are the inertial terms, F_b and M_b are the damping terms, F_k and M_k the spring terms and F_{elect} and M_{elect} the electrostatic terms. F stands for force and M for moment. Both electrostatic force and moment and the mechanical spring of the

structure were already computed in chapter 3. Some other important parameters are presented in Table 4.2.

TABLE 4.2 Main parameters of the 2-DOF device

Fixed Parameter	Value
Mass (m)	*0.578 μg*
Inertia moment (I)	2.12×10^{-17} *kg.m²*
Initial gap distance (actuation arm)	*2 μm*
Initial gap distance (sensing arm)	*3 μm*
C_{d0} *(zero-displacement actuation capacitor)*	*31 fF*
C_{s0} *(zero-displacement sensing capacitor)*	*105 fF*
Total n° of actuation arms	*6*
Total n° of sensing arms	*12*

4.5.1 Finite Difference Model

To model the squeeze-film damping of the 2-DOF structure the FD method has to be used. The film thickness is not uniform and the Reynolds equation can not be analytically solved for this case. Since the film thickness and pressure are both function of place and time, Eqn. (4.37) is used.

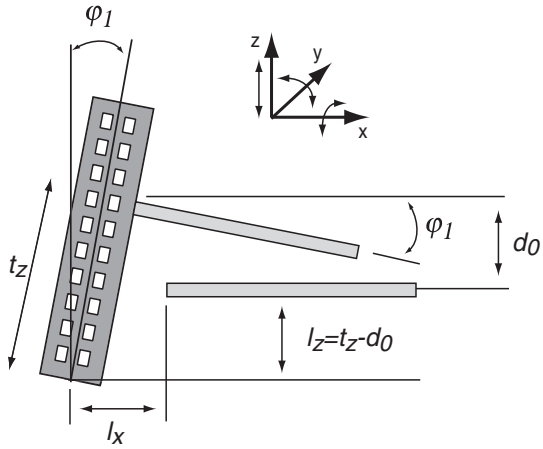

Figure 4.24 Variables needed for the FD model implementation

To simplify the modelling of the squeeze-film damping, the displacement w_1 is neglected since the movement associated with it is not relevant for the squeeze-film motion. The fundamental movement is the rotation movement over the *y*-axis and with the help of Fig. 4.24, the resulting input for each FD element can be expressed as a function of the rotation angle φ_1. The partial derivatives of Q_{pr} with respect to p and h can also be analytically evaluated.

Since the electrodes surfaces are non-flexible and only the rotation angle is of interest for the squeeze-film model, the gap separation at each mesh point, $h_{m,n}$, can be expressed as a function of φ_1:

$$h_{m,n} = t_z \cos(\varphi_1) - (l_x + m\Delta x)\sin(\varphi_1) - l_z \ , \tag{4.45}$$

where Δx is the distance in the *x*-axis between mesh points. Similarly, the rate change of the gap separation (velocity) at each mesh point can be obtained by taking the derivative of $h_{m,n}$ to time:

$$\frac{\partial h_{m,n}}{\partial t} = -\omega_1 t_z \sin(\varphi_1) - \omega_1 (l_x + m\Delta x)\cos(\varphi_1) \tag{4.46}$$

Here $\omega_1 = \frac{\mathrm{d}\varphi_1}{\mathrm{d}t}$ is the angular velocity. As the gap separation is function of place, the partial derivatives in order to *x* and *y* are needed. The gap separation only changes along the *x*-axis ($\frac{\partial h}{\partial y} = 0$) and assuming $m\Delta x = x$ in (4.45) the derivative to *x* can be analytically evaluated:

$$\frac{\partial h}{\partial x} = -\sin(\varphi_1) \tag{4.47}$$

Finally, the partial derivatives of Q_{pr} with respect to p and h are (see Eqn. (4.11)):

$$\begin{aligned} \frac{\partial Q_{pr}}{\partial p} &= -\frac{11.17(K_n)^{1.159}}{p} \\ \frac{\partial Q_{pr}}{\partial h} &= -\frac{11.17(K_n)^{1.159}}{h} \end{aligned} \ , \tag{4.48}$$

and the vertical damping force and the damping moment are given by:

$$F_{FD} = \Delta x \Delta y \sin(\varphi_1) \sum_{m=0}^{M-1} \sum_{n=0}^{N-1} p_{m,n}$$
$$M_{FD} = \Delta x \Delta y \cos(\varphi_1) \sum_{m=0}^{M-1} \sum_{n=0}^{N-1} p_{m,n}(l_x + m\Delta x)\cos(\varphi_1) \quad (4.49)$$

The FD model was implemented in Simulink for the two different arm configurations (actuation and sensing arms). Table 4.3 presents the more relevant dimensions for each of the arms. The pressure distribution for a single actuation and sensing arm is presented in Fig. 4.25 when the movable arm oscillates with a maximum angle (φ_1=0.0051 radians) and displacement (w_1=0.685μm) at 400 kHz. Mesh points outside the arms surface at ambient pressure were used here to model the border effects.

TABLE 4.3 Relevant sizes of the structure electrodes

Actuation arms (μm)		Sensing arms (μm)	
t_z	274	t_z	105
l_z	272	l_z	102
l_x	30	l_x	30
d_0	2	d_0	3
l	110	l	280
w	10.6	w	10.6

4.5.2 Full-System Model

A full-system model of the 2-DOF device must be able to fully describe the complex movement of the device. The decomposition of the complex structure movement in a rotational and translational movement results in Eqn. (4.44). By implementing and solving Eqn. (4.44), the device movement can be predicted.

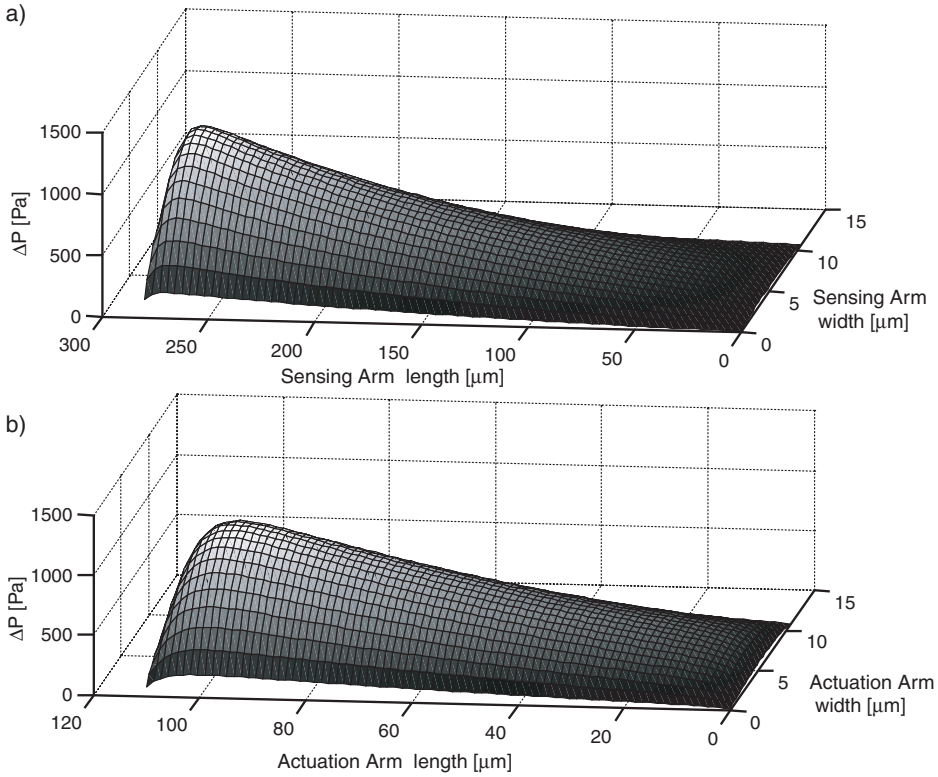

Figure 4.25 Pressure distribution in a a) sensing and b) actuation arm using a 80x20 finite difference mesh

Most of the forces and moments in Eqn. (4.44) depend on both state variables (w_1 and φ_1) - cross-coupled terms are present. All these dependencies can be easily implemented within Simulink. A block diagram of the full-system is shown in Fig. 4.26. The electrostatic force and moment can be computed using the dependence on the capacitor as derived in chapter 3. The spring constant of the structure (in this case is a 2×2 matrix) was already computed in chapter 3 and is easily implemented. The implementation of the FD squeeze-film model inside Simulink results in a full-system model for the 2-DOF structure.

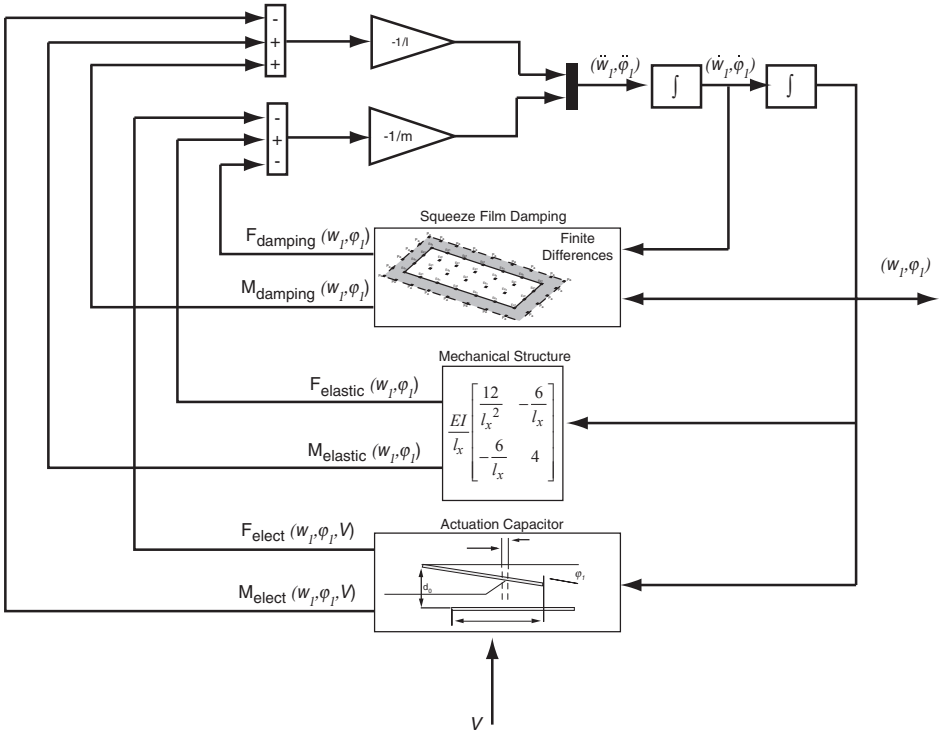

Figure 4.26 Block diagram of the full system implementation

4.5.3 Experimental Measurements

A SEM photograph of the microdevice used during the experiments is presented in Fig. 4.27. The devices after the release of the sacrificial layer, were encapsulated in neon at 0.6×10^5 Pa and as for the 1-DOF device, the displacement is measured by sensing the capacitance changes using sensing capacitors.

A few simulations for different input voltages were performed and compared with experimental measurements. The readout does not measure the state variables separately but the circuit rather provides an output proportional to the capacitance changes which depend on both state variables. Therefore the comparative graph of Fig. 4.28 compares the *changes* in capacitance between measured and simulated data.

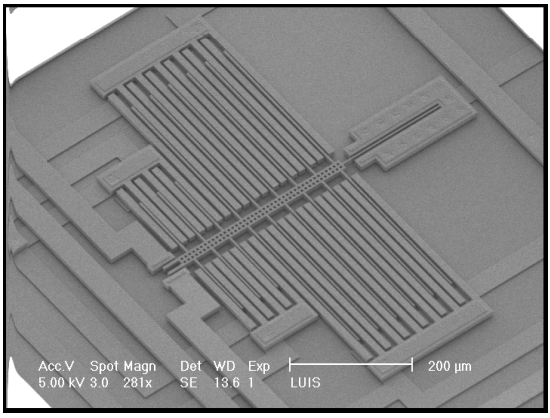

Figure 4.27 SEM photograph of the fabricated 2-DOF microdevice

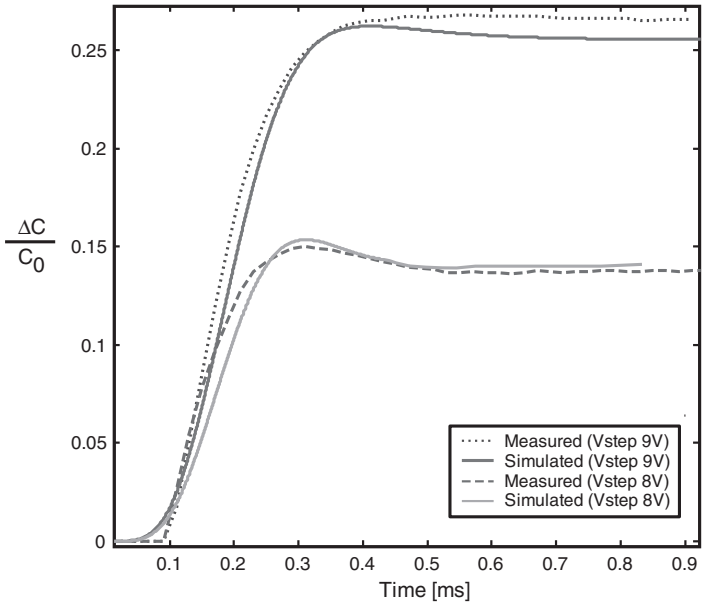

Figure 4.28 Measured and simulated capacitance change for an input step voltage of 8 and 9 volts

A look at Fig. 4.28 reveals a certain agreement between measured and simulated data. The source of errors in this case is very extensive, and it is very difficult to claim

that the model truly predicts the 2-DOF behaviour. Nevertheless, the FD model approach implemented in Simulink allows a realistic large-signal full-system modelling of complex MEMS devices that otherwise could not be done.

4.6 Conclusions

The modelling of the dynamics of microdevices is a very interesting topic and a major challenge in the field. It was shown here that for the simpler case of a parallel-plate type of device, fast and accurate models can be derived. The more complex cases can also be handled however requiring more evolved and complex models. In these situations, more efficient and flexible ways to implement the models are the drive of the research.

The squeeze-film damping problem is the computational bottleneck in a dynamic MEMS simulation and can be divided into two: small-displacement and large-displacement. The small-displacement approach uses the linearized Reynolds equation, which simplifies the model and its implementation. However a small-signal model is only valid for small displacements around the linearized distance and the usage of such a model beyond its range of applicability results in major errors. Alternatively a large-displacement approach describes with an high degree of accuracy the movement of the device along the full film extension. Model implementation is not as simple as a small-signal analysis in this case.

The border effects are another important aspect when dealing with squeeze-film damping. Only recently the study of these effects started, and as it is proved here these are of extreme importance. The use of modified elongations to model the effect proved to be a very good approach. Current methods are limited to the linear movement of two surfaces moving perpendicularly and to tilt motion. These are the most common movements of MEMS devices but the search for new applications will create new and more complex devices. A flexible, accurate and fast modelling platform to model these new devices is of extreme necessity for a designer.

The analytical parallel-surface model assumes ideal movements and configurations. That is not always the case with real devices and the validity of the model for the device under analysis should be checked. In some cases, the presence of a substrate can profoundly change the pressure distribution and the flow profile of the damper and the model can loose its validity for that particular situation. As an example, if the distance to the substrate of the 1-DOF device analysed here would be reduced from 2 μm to just 1 μm, the analytically derived model would not any more describe satisfactorily the squeeze-film forces developed by the damper.

4.7 References

[4.1] L.A. Rocha, E. Cretu and R.F. Wolffenbuttel, "Displacement Model for Dynamic Pull-In Analysis and Application in Large-Stroke Actuators", *in Proc. Eurosensors XVII*, Guimarães, Portugal, 21-24 September 2003, pp. 448-451.

[4.2] T. Veijola, A. Pursula and P. Raback, "Extending the Validity of Existing Squeezed-Film Damper Models with Elongations of Surface Dimensions", *in Proc. Nanotech2004*, Boston, USA, 7-11 March 2004, pp. 235-238.

[4.3] T. Veijola, T. Ryhanen, H. Kuisma and J. Lahdenpera, "Circuit Simulation Model of Gas Damping in Microstructures with Nontrivial Geometries", in *Proc. Transducers'95*, Stockholm, Sweden, 25-29 June 1995, pp. 36-39.

[4.4] L.A. Rocha, E. Cretu and R.F. Wolffenbuttel, "A Full-System Dynamic Model for Complex MEMS Structures" *in Proc. Nanotech2004*, Boston, USA, 7-11 March 2004, pp. 203-206 .

[4.5] J.J. Blech, "On Isothermal Squeeze Films", *J. Lubrication Technology*, 105 (1983) 615-620.

[4.6] W.A. Gross, L.A. Matsch, V. Castelli, A. Eshel, J.H. Vohr and M. Wildmann, *Fluid Film Lubrification*, John Wiley & Sons, Inc., New York, 1980.

[4.7] R. Sattler and G. Wachutka, "Compact Models for Squeeze-Film Damping in the Slip Flow Regime", *in Proc. Nanotech2004*, Boston, USA, 7-11 March 2004, pp. 243-246.

[4.8] E.B. Arkilic, K.S. Breuer and M.A. Schmidt, "Mass Flow and Tangential Momentum Accommodation in Silicon Micromachined Channels", *J. Fluid Mech.,* 437 (2001) 29-43.

[4.9] T. Veijola, H. Kuisma, J. Lahdenpera and T. Ryhanen, “Equivalent-Circuit Model of the Squeezed Gas Film in a Silicon Accelerometer”, *Sensors and Actuators*, A 48 (1995) 239-248.

[4.10] S. Fukui and R. Kaneko, “Analysis of Ultra-Thin Gas Film Lubrification Based on Linearized Boltzmann Equation: First Report - Derivation of a Generalized Lubrication Equation Including Thermal Creep Flow”, *J. Tribol., Trans. ASME*, 110 (1988) 253-262.

[4.11] S. Fukui and R. Kaneko, “A Database for Interpolation of Poiseuille Flow Rates for High Knudsen Number Lubrication Problems”, *J. Tribol., Trans. ASME*, 112 (1990) 78-83.

[4.12] T. Veijola, H. Kuisma and J. Lahdenpera, “Compact Large-Displacement Model for Capacitive Accelerometers”, *in Proc. MSM’99*, San Juan, Puerto Rico, 19-21 April 1999, pp. 218-221.

[4.13] S. Vemuri, G.K. Fedder and T. Mukherjee, “Low-Order Squeeze Film Model for Simulation of MEMS devices”, *in Proc. MSM’00*, San Diego, USA, 27-29 March 2000, pp. 205-208.

[4.14] T. Veijola, K. Ruokonen and I. Tittonen, “Compact Model for the Squeezed-Film Damping Including the Open Border Effects”, *in Proc. MSM’01*, Hilton Head Island, USA, 19-21 March 2001, pp. 76-79.

[4.15] T. Veijola, “End Effects of Rare Gas Flow in Short Channels and in Squeezed-Film Dampers, *in Proc. MSM’02*, San Juan, Puerto Rico, 22-25 April 2002, pp. 104-107.

[4.16] F. Sharipov and V. Seleznev, “Data on Internal Rarefied Gas Flow”, *J. Phy. Chem. Ref. Data*, 27 (1998) 657-706.

[4.17] T. Veijola, “Finite-Difference Large-Displacement Gas-Film Model”, i*n Proc. Transducers’99*, Sendai, Japan, 7-10 June 1999, pp. 1152-1155.

[4.18] H. Levy and F. Lessman, *Finite Difference Equations*, Dover, New York, 1992

[4.19] The Mathworks, Inc., *Simulink: Writing S-Functions*, Version 4, 2002.

[4.20] David R. Lide, *CRC Handbook of Chemestry and Physics, 84th Edition*, CRC Press, 2003.

5

Describing and Applying Nonlinear MEMS Dynamics

5.1 Introduction

The previous two chapters were devoted to the modelling of microeletromechanical devices and both static and dynamic models were presented. The distinction between static and dynamic modelling is of extreme importance. When a quasi-static operating regime is assumed, the model describing the displacement of a MEMS structure in the direction normal to the electrode area due to the voltage applied reduces in finding the equilibrium between elastic and electrostatic forces. This results in a sudden pull-in at a well-defined pull-in voltage after travelling over 1/3 of gap for 1-DOF structures. For the cases when the changes in the voltage applied are sufficiently fast or the aim of the analysis is the description of the motion between states, the quasi-static regime does not apply and the static analysis becomes invalid. In this case the damping forces and mass inertia need to be included in the model for a meaningful study of the dynamic behaviour of the structure.

The difficulties encountered when a dynamic analysis is performed are due to the strong nonlinear behaviour of the MEMS device. A few studies in scientific literature addressed the dynamics of MEMS devices [5.1]-[5.5], and these used the pull-in phe-

nomenon as the motivation of the dynamic study. In [5.1] and [5.2] the pull-in has been analysed from the application perspective while in [5.3]-[5.5] the fundamental underlying mechanisms behind the nonlinear pull-in phenomenon have been studied.

The modelling framework introduced in the previous chapter is the support for the nonlinear dynamic analysis performed here. First, a generic MEMS system is considered and a nonlinear analysis of the system is included. Next, the newly introduced concepts are applied to a real MEMS device and measurements are performed to confirm and further improve the nonlinear analysis. Finally, the motion of a MEMS device during a dynamic "pull-in event" is analysed and discussed using simulated and experimental data.

5.2 Nonlinear Dynamics

A parallel-plate actuated MEMS structure has a strong nonlinear behaviour. Nonlinear is usually defined as the negation of linear. In geometry, linearity refers to Eucledian objects: lines, planes, flat three-dimensional space which appear the same no matter how they are examined. A nonlinear object, a sphere for instance, looks different depending on the scale being used: when looked at closely enough can be regarded as a plane, while from far enough, it looks like a point. In algebra, linearity is defined in terms of functions that have the property $f(x+y) = f(x)+f(y)$ and $f(ax) = af(x)$. In case of a nonlinear function f, the result may be out of proportion relative to the input x and y. Thus, the simplifying tools used in linear analysis are not valid for a nonlinear analysis.

Linearity is a rather special concept and an accurate and realistic model of a real system cannot be truly linear. In most situations it is an advantage if the system can be studied as a valid linear approximation to the real models. For that reason, physicists have tried to build their theories on linear differential equations because these are easy to solve. The most successful theories (like electrodynamics and quantum mechanics) are based on linear differential equations. For the cases where the linear approximation is not valid, nonlinear techniques have to be used. For nonlinear systems, each case is usually unique and hard to solve.

Nonlinear systems have been shown to exhibit surprising and complex characteristics that would never be anticipated by a scientist trained only in linear techniques. Examples of these effects are bifurcation and chaos. Usually the most profound effects of nonlinearity are seen on dynamical systems. Further, nonlinear systems are mostly unclassified and the basic terms of this language are more geometrically oriented.

Instead of quantitative solutions (which can be obtained only numerically in nearly all cases), qualitative aspects are of greater interest; like type of solutions, the stability of solutions, and the bifurcation of new solutions. There are currently no general techniques for telling whether a particular nonlinear system will exhibit the complexity of chaos, or some other behaviour. This makes each nonlinear problem unique and the analysis requires more than just applying a routine of mathematical techniques, the system has to be clearly understood from the real-word (physical, biological, economical, medical) perspective.

Besides the strong nonlinearity of the MEMS device, its dynamic behaviour is also of extreme importance. A dynamic system consists of an abstract phase space or state space whose coordinates describe the dynamical state at any instant and a dynamical rule which specifies the immediate future trend of all state variables, given only the present values. Dynamic systems can be defined as *deterministic*, if there is a unique consequent to every state, and *stochastic*, if there is more than one consequent from some probability distribution. Most of nonlinear science deals with deterministic systems. This is also the case for the dynamic MEMS study, where the system is defined by a nonlinear differential equation and there is a unique consequent to every state.

When making a nonlinear dynamic analysis the first step is to obtain the governing equations which accurately describe the behaviour of the system. For systems where the motion is under analysis, a finite number of variables leading to a set of ordinary differential equations are usually used. The equations of motion of such a system are usually given in the form:

$$\dot{x} = F(x, \lambda), \tag{5.1}$$

where x represent the state variables and λ is the parameter vector. A dynamic system is considered *non-autonomous* if the vector field depends explicitly on time, and *autonomous*, for the cases where the vector field is time independent. After having decided on how to describe the behaviour of the system, a stability study of the equilibrium points and their variation with the control parameters is performed. The next step is to understand the motion of the system in the phase space, or for an initial condition how the state variables change in time. This is done by using phase space geometric pictures (phase portrait) which provide a qualitative picture of the dynamics without actually solving the differential equations. Another way is the use of numeric methods to solve the differential equations. If the phase portrait gives a general qualitative vision of the system the numerical solution of the differential equations describe the correct motion of the system.

The phase portrait considers not a single trajectory in the phase space but all possible trajectories. The phase space is the space of the state variables $x_1 \ldots x_n$ and the time his-

tory of the dynamic system forms a *trajectory* in the phase space (Fig. 5.1). The system state is completely specified by a point in the phase space.

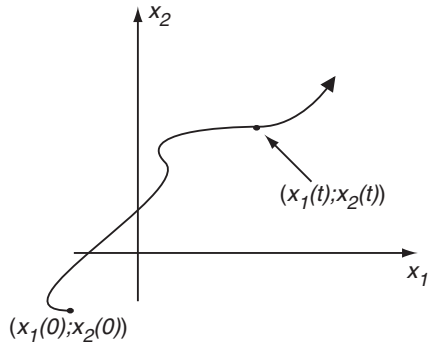

Figure 5.1 A trajectory in a 2D phase space

The motion of a 1-DOF parallel-plate actuated MEMS structure with initial capacitance, C_0, and initial gap distance, d_0, is described by the nonlinear differential equation (assuming a constant damping coefficient):

$$\frac{\mathrm{d}^2 x}{\mathrm{d}t^2} + \frac{\omega_0}{Q}\frac{\mathrm{d}x}{\mathrm{d}t} + \omega_0^2 x = a_{ext} + \frac{1}{2}\frac{C_0 d_0}{m(d_0 - x)^2}V^2, \tag{5.2}$$

where $\omega_0 = \sqrt{k/m}$ is the resonant frequency of the system and $Q = \sqrt{km}/b$ is the quality factor. When the voltage applied is not zero the system is nonlinear (due to the electrostatic force) and the system analysis is not a trivial exercise. Using the notation form of Eqn. (5.1) the dynamics of the microdevice can be rewritten as:

$$\begin{aligned} \dot{x} &= y \\ \dot{y} &= a_{ext} + \frac{1}{2}\frac{C_0 d_0}{m(d_0 - x)^2}V^2 - \frac{\omega_0}{Q}y - \omega_0^2 x \end{aligned} \tag{5.3}$$

Here x and y are the state variables representing the displacement and velocity respectively. A more generic configuration is achieved, irrespective of the numerical values of the coefficients involved, if a normalization of the state variables is performed. The displacement is normalized with respect to the gap spacing, d_0:

$$x_n \equiv \frac{x}{d_0}, \tag{5.4}$$

and automatically the normalized velocity and external acceleration are:

$$y_n = \frac{\mathrm{d}x_n}{\mathrm{d}t} = \frac{1}{d_0}\frac{\mathrm{d}x}{\mathrm{d}t} \equiv \frac{y}{d_0} \tag{5.5}$$

$$a_n \equiv \frac{a_{ext}}{d_0} \tag{5.6}$$

The voltage is normalized with respect to the pull-in voltage for the 1-DOF asymmetric case:

$$V_n \equiv \frac{V}{\sqrt{\frac{8}{27}}d_0\sqrt{\frac{k}{C_0}}}\ , \tag{5.7}$$

and the electrostatic force using the normalized variables is expressed as:

$$F_{elect} = \frac{1}{2}\frac{C_0 d_0}{(d_0 - x)^2}V^2 = \frac{4}{27}\frac{kd_0}{(1 - x_n)^2}V_n^2 \tag{5.8}$$

The normalized equation of motion for an actuated parallel-plate microdevice becomes:

$$\begin{aligned} \dot{x}_n &= y_n \\ \dot{y}_n &= a_n + \frac{4}{27}\frac{\omega_0^2}{(1 - x_n)^2}V_n^2 - \frac{\omega_0}{Q}y_n - \omega_0^2 x_n \end{aligned} \tag{5.9}$$

Eqn. (5.9) fully determines the dynamics of the microdevice. For a stability study of the system Eqn. (5.9) is used. If one makes:

$$\begin{aligned} \dot{x}_n &= 0 \\ \dot{y}_n &= 0 \end{aligned}\ , \tag{5.10}$$

the equilibrium points are determined and the stability of the equilibrium points can be checked using the techniques already presented in chapter 3. A good insight of the dynamic behaviour of the device is obtained when the phase portrait of the nonlinear differential governing equation is constructed.

5.3 Phase Portrait

A phase portrait is a plot of multiple trajectories corresponding to different initial conditions in the same phase space [5.6]. It gives a qualitative view of the system's dynamic behaviour. The state variables of the microdevice governing equation are the normalized displacement, x_n, and the normalized velocity, y_n. The phase space is then a 2D space with the displacement in the horizontal axis and the velocity in the vertical axis.

For the construction of the phase portrait the *nullclines* must be determined. The nullclines correspond to the set of curves of the device's motion where the time derivative of one component of the state variables is zero. Since the displacement is one of the state variables one of the nullclines implies zero velocity in the x direction (y_n=0). The time derivative of the other state variable is acceleration, which implies that the device has zero acceleration along the nullcline:

$$y_n = \frac{Q}{\omega_0}\left(a_n + \frac{4}{27}\frac{\omega_0^2}{(1-x_n)^2}V_n^2 - \omega_0^2 x_n\right) \tag{5.11}$$

At the crossing points of the nullclines the vector field is zero, i.e., $dx_n/dt = 0$ and $dy_n/dt = 0$. These points are the equilibrium points and correspond to *stationary* solutions that can be either stable or unstable. This dynamic system presents two distinct cases when the external acceleration is considered zero:

1. The first case happens for $V<V_{pi}$ (V_n<1). Here, there are two equilibrium points satisfying the physical constraint $x_n \leq 1$. The initial state position is of extreme importance since it will determine the occurrence of dynamic pull-in.
2. The second case happens when $V>V_{pi}$ (V_n>1). In this case there are no equilibrium points and regardless of the initial state position the microdevice goes to pull-in (the movable electrode hits the counter-electrode).

5.3.1 Voltages Lower Than The Pull-In Voltage ($V<V_{pi}$)

The nullclines depend on both the values of the quality factor, Q, and the natural resonant frequency, ω_0. The most important parameter between these two is the quality factor and the phase portrait will be plotted for the case of an underdamped device (Q=5) and a critically damped device (Q=0.5). This way the effect of oscillations on the dynamics of the microdevice can be analysed.

Fig. 5.2 shows the phase space and the nullclines for the two different Q values (V_n=0.5). The intersection of the nullclines gives the equilibrium points. From the previous chapters it is known that the equilibrium point satisfying the condition $x_n < 1/3$ is stable.

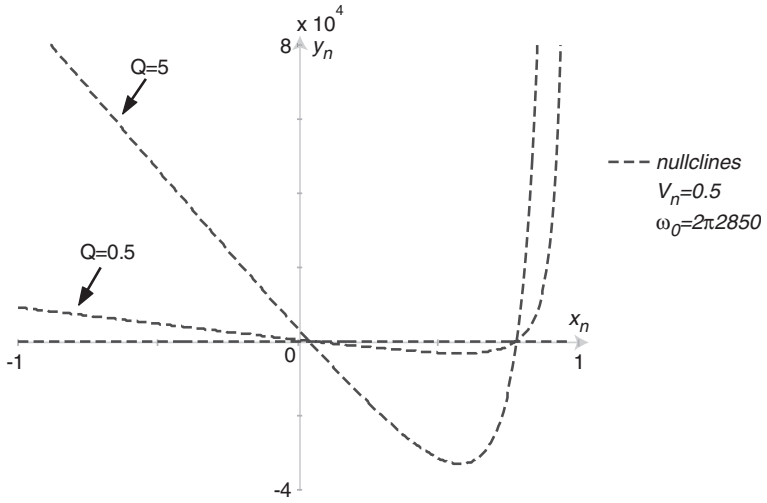

Figure 5.2 Graphical interpretation of the nullclines

The next step for the phase portrait construction is to draw the vector fields. Along the nullclines the vector field is either vertical or horizontal. Between the nullclines the direction of the vector field is determined by the sign of dx_n/dt and dy_n/dt. Usually the vector field between nullclines is drawn with the directions north east ($dx_n/dt > 0$ and $dy_n/dt > 0$), south east ($dx_n/dt > 0$ and $dy_n/dt < 0$), south west ($dx_n/dt < 0$ and $dy_n/dt < 0$) and north west ($dx_n/dt < 0$ and $dy_n/dt > 0$). Therefore these vectors indicate in which direction the state variables move from their local position.

After drawing the vector fields (Fig. 5.3) the basin of attraction of the attractors must be determined. An attractor is an equilibrium point into which the system settles, i.e., a set in the phase space with a neighbourhood that is representative of all initial positions reaching the attractor. The microdevice system has an attractor (the stable equilibrium

point) which means that there is a set of positions that eventually reach the equilibrium point.

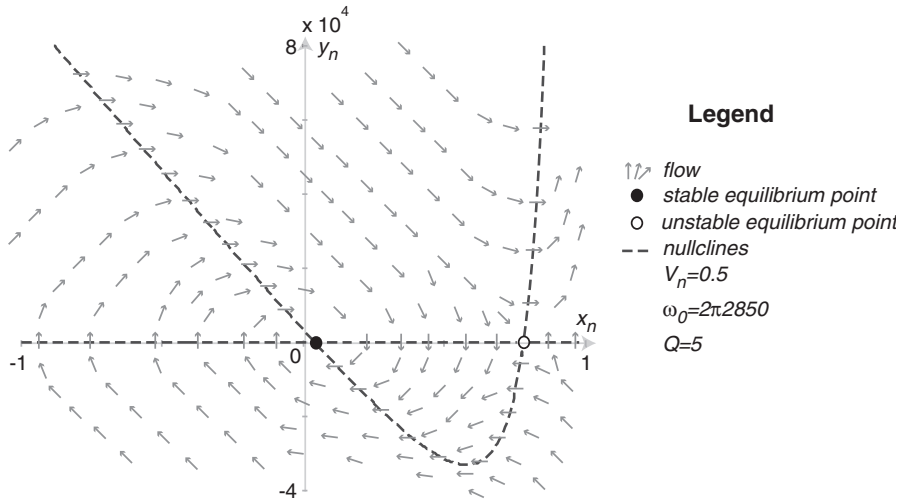

Figure 5.3 Construction of the phase portrait

Determining the basin of attraction is not a trivial exercise and usually numerical methods have to be used [5.7]. A useful interpretation of the basin of attraction requires a good understanding of the dynamic system. This usually limits the order of the system to 2 for systems where a qualitative vision of the basin of attraction can be drawn. The basin of attraction of the phase portraits presented in the thesis was computed by solving Eqn. (5.9) numerically for various initial conditions. The convergence study of the various trajectories allows us to determine the basin of attraction.

The nonlinearities of a parallel-plate based MEMS device are mainly due to the electrostatic force. The pull-in phenomenon is a unique characteristic of these nonlinearities and it marks the change between a stable to an unstable system. On a static pull-in analysis, the parameters of interest are the voltage at which stability is lost and the maximum achievable displacement. On a dynamic pull-in analysis, besides the motion described by the device and the time that it takes to hit the counter-electrode, the dynamic conditions leading to the loss of stability are important. Fig. 5.4 presents the phase portraits for the two different quality factors. There are some differences between the two but in both cases the trajectories tend to the equilibrium point (for initial values within the basin of attraction) or collapse towards the counter-electrode (dynamic pull-in situation).

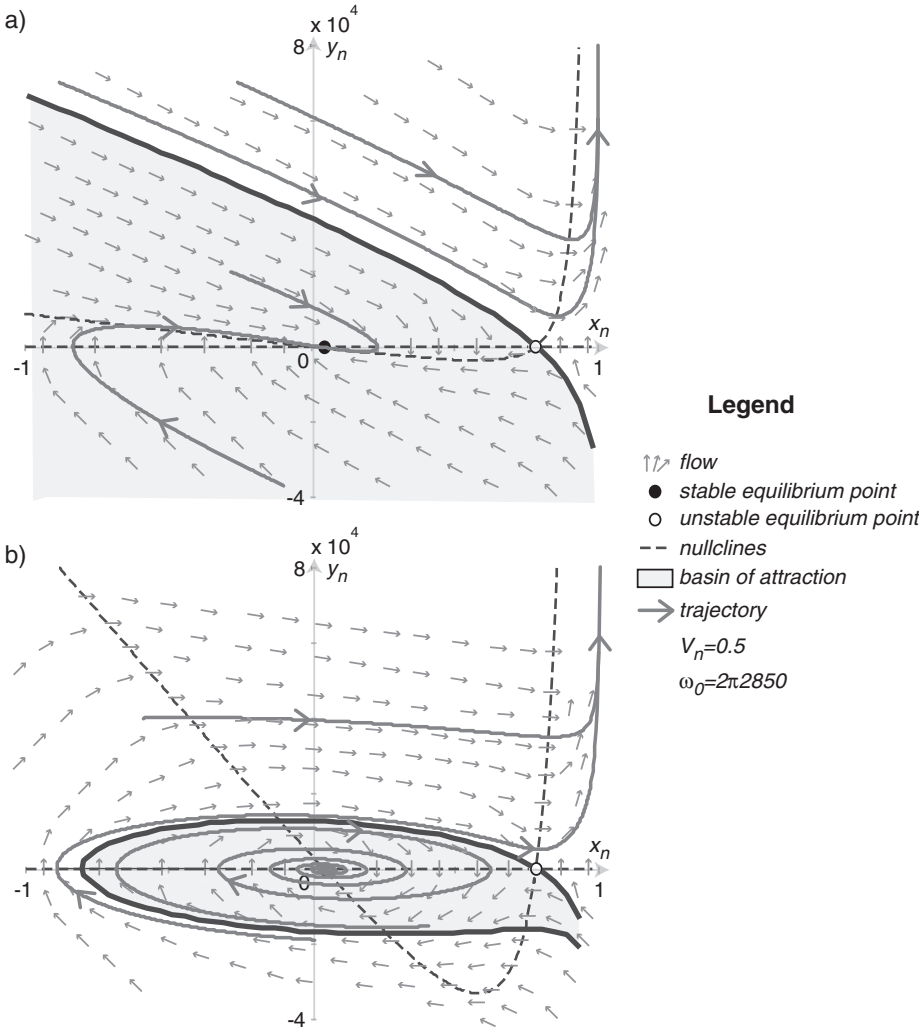

Figure 5.4 MEMS phase portrait for a) Q=0.5 and b) Q=5

The initial conditions leading to the loss of stability as compared to the definition of static pull-in are a very important aspect of dynamic pull-in. The phase portraits show us that dynamic pull-in occurs for all the state points outside the basin of attraction. This means that for voltages lower than V_{pi}, the structure can also collapse. The quality factor

of the device becomes an important parameter in this case. For low-Q devices (Q<0.5), and because there are no oscillations, the basin of attraction is larger than for the case of high-Q devices, where the oscillations strongly contribute to loss of stability.

The phase portrait is an excellent tool for the analysis of dynamic systems since it gives a visual representation of the system for the full phase space (all possible combinations of the state variables). One important thing to remember is that the microdevice's phase portrait changes with the voltage applied. Therefore, the structure can goes from a stable trajectory to an unstable one, or vice-versa, by changing the voltage. Fig. 5.5 shows the phase portrait for a voltage V_n=0.95. When compared to Fig. 5.4b (same quality factor) we see that the basin of attraction was strongly reduced and almost all state points lead to dynamic pull-in. These changes of the phase portrait with voltage suggest that the control of the voltage applied can prevent the device from losing its stability.

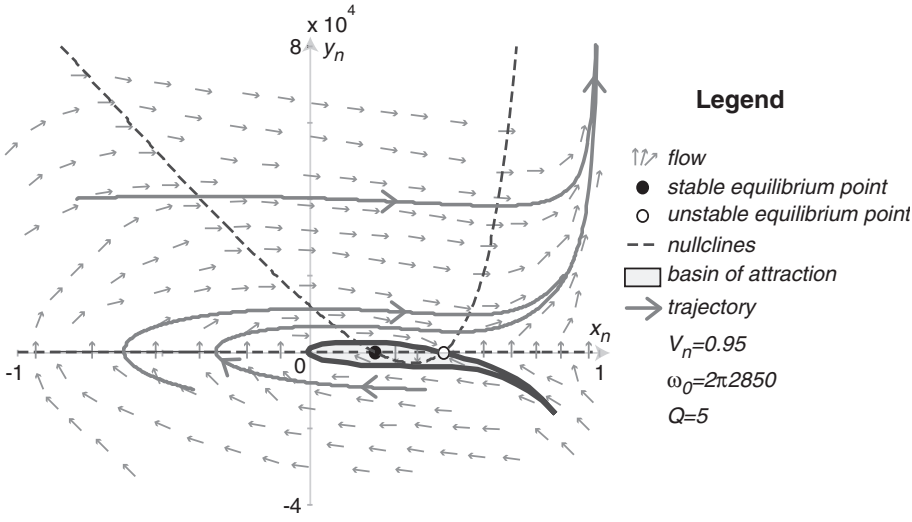

Figure 5.5 Phase portrait for a voltage V_n=0.95

5.3.2 Voltages Higher Than The Pull-In Voltage ($V>V_{pi}$)

When the voltage applied is higher than the static pull-in voltage there are no equilibrium points and the microdevice always collapses towards the counter-electrodes (Fig. 5.6). The important aspects are the motion described (pull-in motion) and the time that it takes to reach the counter-electrodes (pull-in time). Both the pull-in motion and the pull-in time are analysed later in this chapter.

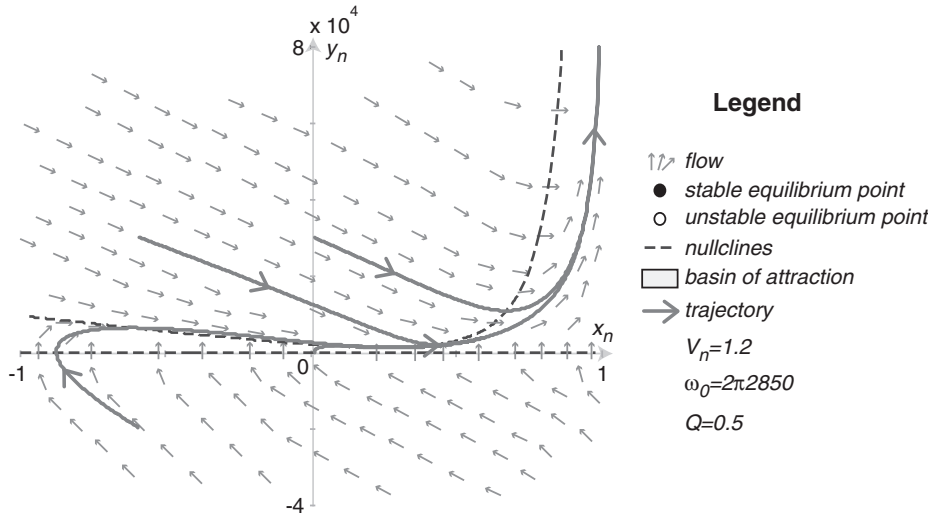

Figure 5.6 Phase portrait for a voltage V_n=1.2

The proper interpretation of the phase portraits is essential for a complete understanding of the nonlinear dynamic behaviour of the microdevice. If a critically damped device is considered and the voltage applied is gradually increased, the device starts moving with a certain velocity. If the voltage is increased beyond the pull-in voltage, that does not mean that the structure will collapse. The device momentarily loses its stability but a fast reduction of the voltage applied, as compared to the velocity of the device, will place the actual state position within the basin of attraction and eventually the structure reaches the equilibrium point given by the voltage applied. Basically, if the displacement and velocity can be properly monitored, all the positions within the capacitor gap can be reached without going to pull-in. The structure's displacement control, makes it possible to avoid pull-in since there is always a voltage for which the actual state position is within the basin of attraction (in the limit, if no voltage is applied the full phase space is the basin of attraction).

Regarding the device's quality factor, an overdamped device is easier to control since it has a bigger basin of attraction as compared to an underdamped device. The use of voltage control to eliminate the pull-in instability seems feasible, provided that the device's displacement can be monitored without delays.

5.3.3 Effect of an External Acceleration

When an external force (external acceleration) is applied to the structure both the trajectory and the stability of the system are affected. The acceleration acts as an input to the system, to which the system responds. If the state variables stay inside the basin of attraction, the trajectory is stable. If the external acceleration push the state variables outside the basin of attraction, dynamic pull-in can occur.

Fig. 5.7 presents two cases depicting the influence of an external force acting on the system. Trajectory J_1 starts inside the basin of attraction (stable trajectory) but during the movement of the device, an acceleration pulse is applied and the trajectory leaves the basin of attraction (dynamic pull-in occurs). The second example, trajectory J_2, starts outside the basin of attraction. In this case an acceleration step is applied to the structure during its movement and the trajectory enters the basin of attraction. The acceleration step not only changes the trajectory but also changes the equilibrium points. As time goes to infinite the structure approaches the new attractor. These two cases represent the trajectories that are very close to the limit of the basin of attraction. An external force can make it switch from a stable trajectory to an unstable one and vice-versa. If the trajectories are far from the limit of the basin of attraction this is not likely to happen (unless the external acceleration acting on the device is extremely high).

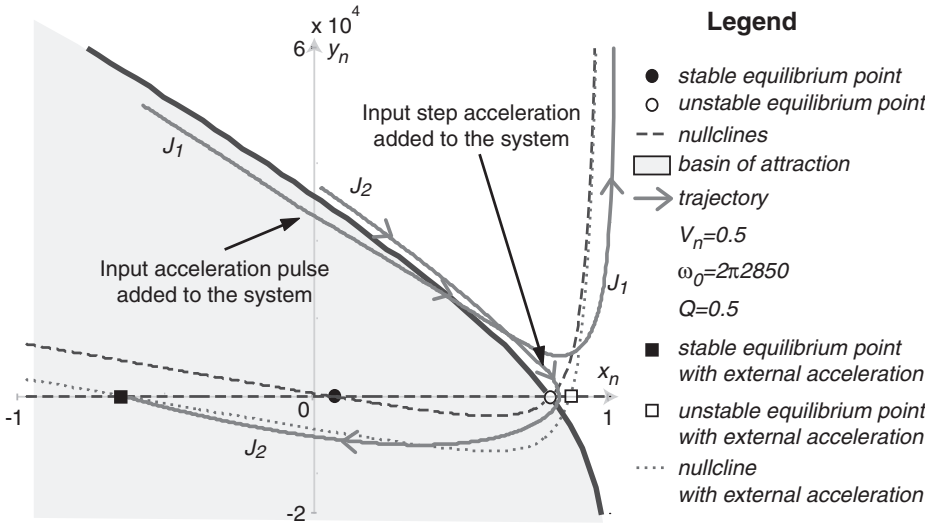

Figure 5.7 Trajectory changes with external forces

5.4 Nonlinear MEMS Structure: Analysis and Experiments

A 1-DOF MEMS device is used to experimentally prove and further analyse the nonlinear concepts introduced in the previous section. It is the 1-DOF device used in the previous chapters for experimental verification of the static and dynamic models and will be referred to as Device 1 during the remaining of the chapter.

Using the large-signal model of Device 1 the phase portrait of the device is computed. The phase portrait is a very important tool for a nonlinear dynamic analysis and the usage of a model from a real MEMS device allows us to get an enhanced knowledge about the nonlinear system.

5.4.1 Phase Portrait

To design the phase portrait of the device the nonlinear equation of motion is needed. The dependence of the damping coefficient on both the displacement and velocity give origin to a rather complex equation of motion. If low frequencies are assumed and the spring component (the in-phase component of the squeeze-film solution due to compressibility) is neglected, the equation of motion of Device 1 is:

$$\begin{aligned} \dot{x} &= y \\ \dot{y} &= a_{ext} + \frac{1}{m}\left(\frac{C_0 d_0 V^2}{2(d_0 - x)^2} - kx - b(x)y \right) \end{aligned} \tag{5.12}$$

The nonlinear damping coefficient *b(x)* is given by both the left and right films. If $h_{left} = d_0 - x$ and $h_{right} = d_0 + x$ are the left and right gap distance respectively, the damping coefficient can be expressed as:

$$b(x) = b_{left}(x) + b_{right}(x), \tag{5.13}$$

where (see section 4.3.4.2 in chapter 4):

$$b_{left}(x) = \sum_{m,n=odd} \frac{768 l_0 w_0 \eta}{\pi^6 h_{left}{}^3 Q_{pr}(h_{left}, P_a)(mn)^2 \left(\frac{m^2}{w_0{}^2} + \frac{n^2}{l_0{}^2}\right)}$$

$$b_{right}(x) = \sum_{m,n=odd} \frac{768 l_0 w_0 \eta}{\pi^6 h_{right}{}^3 Q_{pr}(h_{right}, P_a)(mn)^2 \left(\frac{m^2}{w_0{}^2} + \frac{n^2}{l_0{}^2}\right)} \quad \textbf{(5.14)}$$

Since the movable arm is equidistant from both fixed arms, the total damping coefficient is symmetric with respect to the zero-displacement position. This is clearly visible from Fig. 5.8 where the damping coefficient of Device 1 for small frequencies is presented.

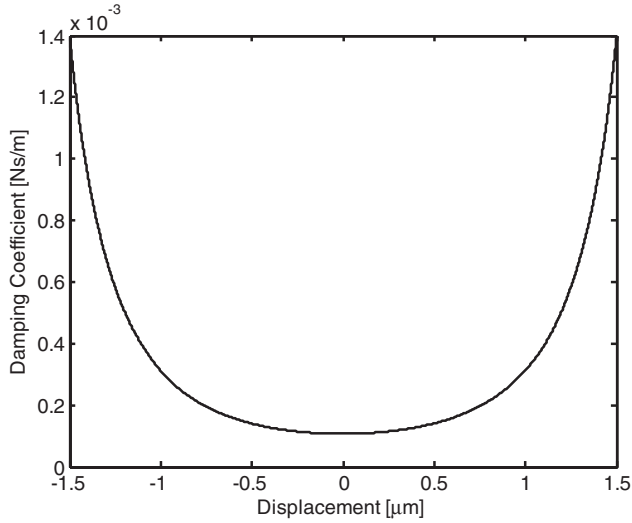

Figure 5.8 Nonlinear damping coefficient *b(x)*

For the computation of the nullclines the time derivatives of the state variables are equalled to zero. By making $\dot{x} = 0$ and $\dot{y} = 0$ in Eqn. (5.12) the following nullclines result:

$$y = 0$$

$$y = \frac{1}{b(x)}\left(m a_{ext} + \frac{C_0 d_0 V^2}{2(d_0 - x)^2} - kx\right) \quad \textbf{(5.15)}$$

The displacement of the MEMS device is physically constrained to the interval $-d_0 \le x \le d_0$ due to the differential capacitor scheme. The MEMS device presents a static pull-in voltage (computed in chapter 3) of $V_{pi} = 4.65\,\text{V}$ and when a voltage of $V=4$ volts is applied to the left capacitor, the phase portrait of Fig. 5.9 results ($a_{ext} = 0$). The use of the large-signal model allows us to derive the basin of attraction and the trajectories shown in the phase portrait. Since the damping coefficient is variable, the quality factor ($Q = \frac{\sqrt{km}}{b}$) is also variable. Just for curiosity the quality factor ranges from Q=0.82 for x=0 μm until Q=0.06 for x=1.5 μm (Neon at 0.6×10^5 Pa is considered).

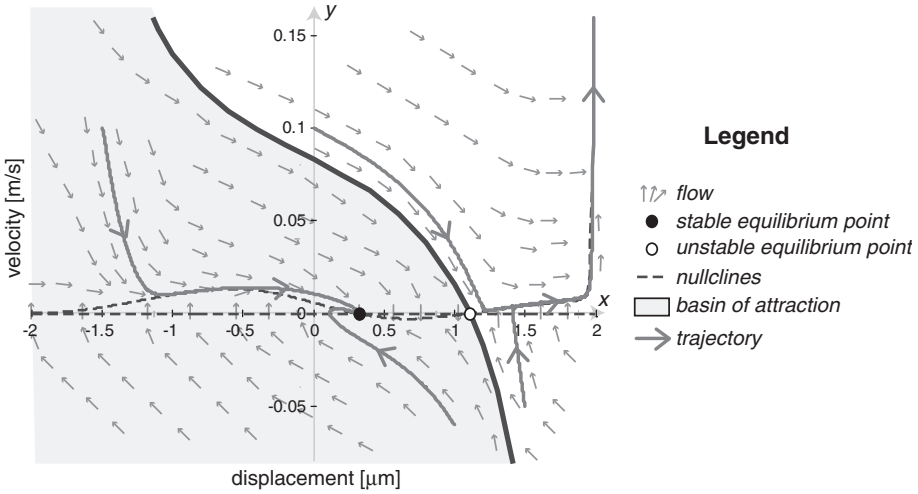

Figure 5.9 Device 1 phase portrait for an input voltage of 4V

An analysis to the phase portrait reveals the same behaviour as the observed for the generic MEMS device used in the previous section. The introduction of the more realistic variable damping coefficient just introduce nonlinearities in the base of attraction of the phase portrait but the general behaviour remains the same.

5.4.2 Dynamic Measurements

The phase portrait gives a qualitative idea of the system behaviour and unless there is a total control of the state variables, the phase portrait can not be obtained experimentally. We tried to show that the phase portrait of a MEMS changes with the voltage applied

and ultimately, for voltages higher than the static pull-in voltage there are no stable points. Nevertheless, if the voltage changes are faster than the device motion, the basin of attraction can be re-established and dynamic pull-in can be prevented.

Experiments were performed on Device 1 to prove these concepts. Sine waves of different voltage amplitudes and frequencies were applied to the device and the maximum achievable displacement and the voltage for which the structure loses the stability (dynamic pull-in) were recorded. The results are shown in Fig. 5.10

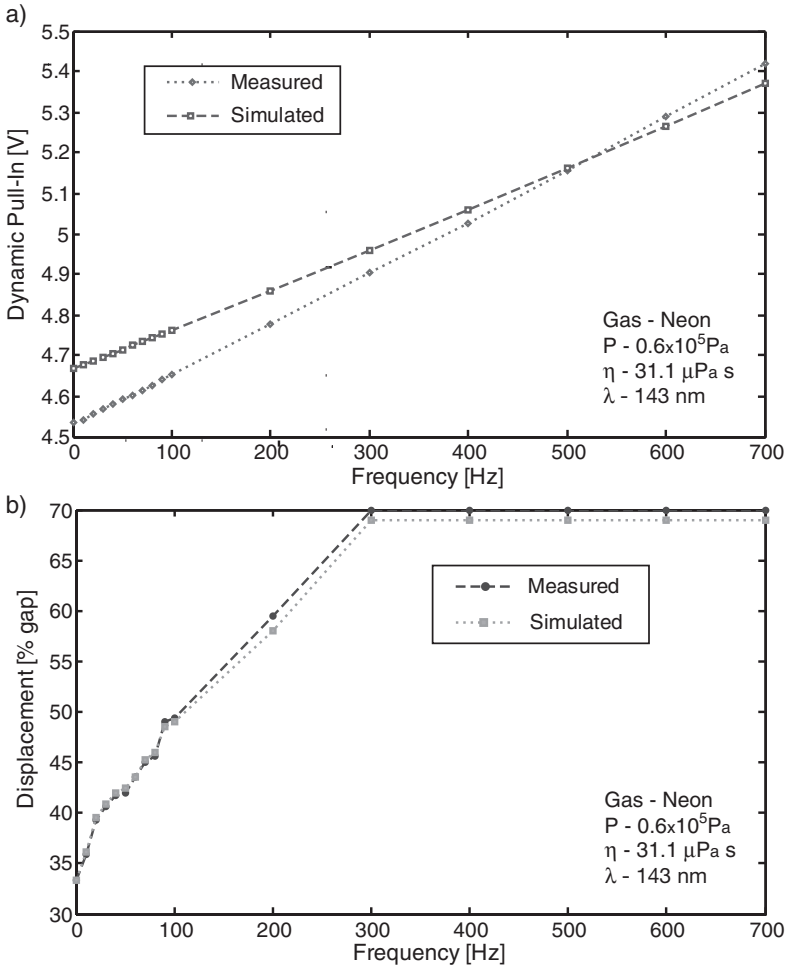

Figure 5.10 Simulated and measured a) dynamic pull-in and b) dynamic pull-in displacement

As expected, the experimental results demonstrate that the MEMS device can be dynamically operated beyond the static pull-in displacement, provided that the appropriate AC voltage is applied. To have a better insight on what is happening during a half period of a sine, simulation results are presented for the case of applying a 400Hz sine wave with a voltage amplitude of 5.04V (Fig. 5.11). From Fig. 5.11 we can se that both the static pull-in voltage and the static pull-in displacement are overcome and still the structure does not goes to pull-in.

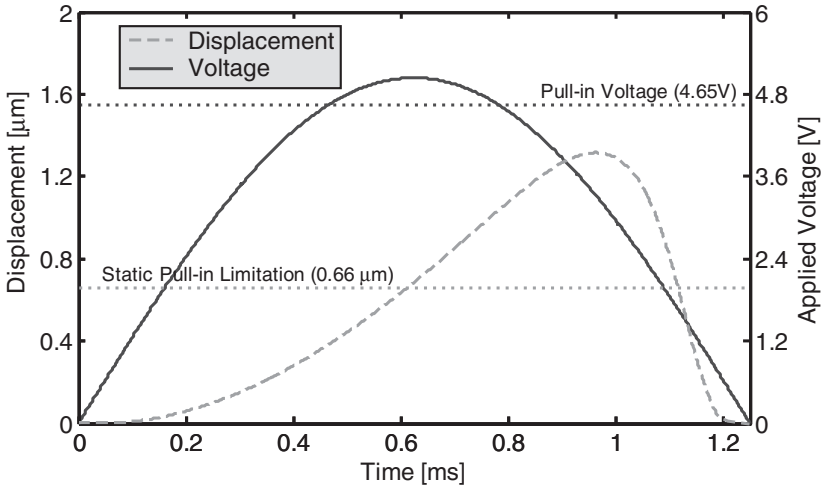

Figure 5.11 Simulation results for a 400 Hz sine wave

A much more interesting exercise is the computation of the phase portrait along a time axis for the voltage changes. Using the same example (400 Hz sine wave) the phase portrait of Device 1 was computed for several different times (different voltages). When the phase portraits are joined a 3D image of the basin of attraction is obtained. If we include the device's trajectory (for an applied half-sine at 400 Hz) the 3D graph of Fig. 5.12 results. This 3D image clearly shows the concept previously introduced. Initially the device trajectory is inside of the basin of attraction but with the increasing of the voltage, the structure leaves the basin of attraction (unstable trajectory). A movement towards the counter electrodes can be observed after leaving the basin of attraction. Nevertheless, since the voltage change rate is higher than the displacement changes, the movable arm enters back into the basin of attraction and returns to a stable trajectory. This allows the device to have trajectories beyond the static pull-in limitation without going to pull-in.

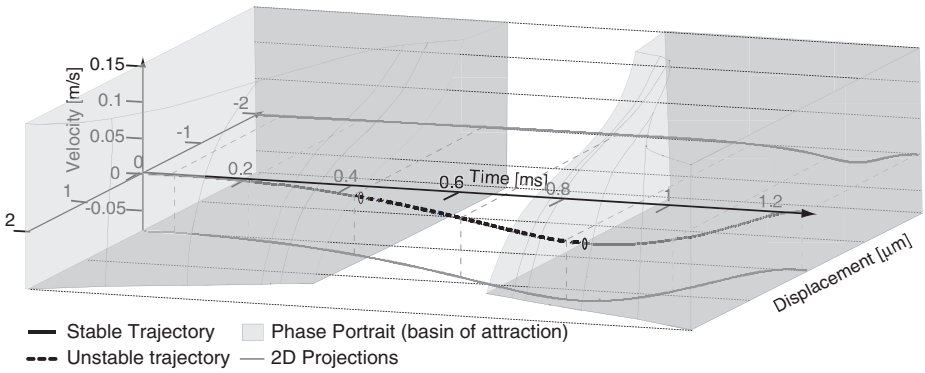

Figure 5.12 3D visualization of the phase portrait changes with voltage

Using AC operation displacements up to 70% of the gap were achieved in the 300-700 Hz range. These results prove some of the dynamic pull-in ideas introduced in the previous section. Although there is no control over the position beyond the static pull-in displacement, both voltages and displacements beyond the static pull-in limitation are achieved. These results have an immediate repercussion on the commonly used sentence about parallel-plate electrostatically actuated MEMS devices: "Electrostatic parallel-plate actuated MEMS devices are limited to displacements up to 1/3 of the full gap due to the pull-in limitation". This sentence should be reformulated to: "DC-voltage operated parallel-plate actuated MEMS devices are limited to *stable* displacements up to 1/3 of the full gap due to the *static* pull-in limitation".

5.5 Dynamic Pull-In: Pull-In Time and Motion Analysis

Since pull-in is a nonlinear effect, a nonlinear dynamic MEMS analysis would not be complete without a thorough study on the dynamic behaviour of pull-in. Dynamic pull-in as opposed to static pull-in takes into account the inertial and damping effects, which may significantly change the pull-in voltage threshold. The focus of this section is on the dynamic aspects of pull-in.

When stability is lost the device moves towards the counter-electrode with a certain motion in a well-defined amount of time. Pull-in time is defined as the time that the device takes from going from a stable fixed position until it hits the counter-electrode. The pull-in motion is the device's displacement during the pull-in time. These two

dynamic properties of pull-in will be analysed for the case of a stable equilibrium (x_n=0 and y_n=0) followed by a step voltage input with a voltage value higher than the static pull-in voltage.

The starting point is the governing equation of a generic microdevice, Eqn. (5.9). If a step voltage, V_{step}, with an amplitude higher than the static pull-in voltage, V_{pi}, is applied to the structure ($V_{step}=\alpha V_{pi}$, with $\alpha>1$), distinctly different responses are observed depending whether the system is overdamped or underdamped (Fig. 5.13).

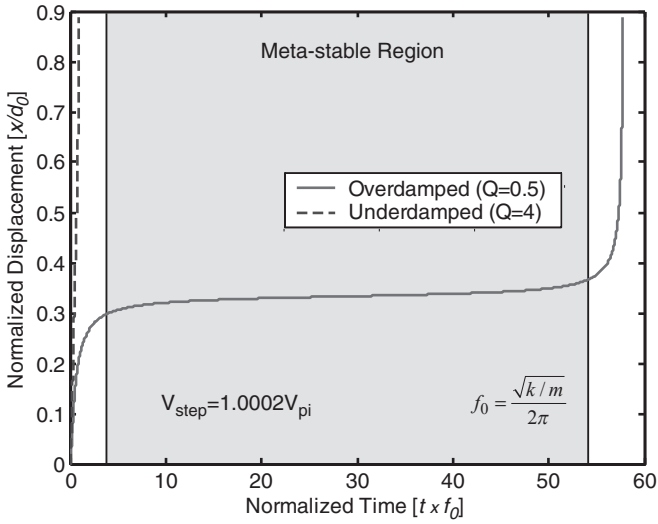

Figure 5.13 Pull-in motion characteristic of overdamped and underdamped microdevices

In the underdamped case the structure rapidly crosses the gap until it reaches the counter-electrode, or as in most of the real devices, physical stoppers that prevent the structure from hitting the counter-electrode. For the overdamped case a less monotonous behaviour is observed. Three regions can be identified in this case:

1. A first region where the structure moves fast until near the static pull-in displacement ($x_{pi}=d_0/3$). Here, the initial imposed electrostatic force is compensated by the elastic and damping forces (Fig. 5.14a). At the start of the step response the damping force dominates but with deflection the elastic force equilibrates the electrostatic one and the damping force reduces becoming almost negligible.

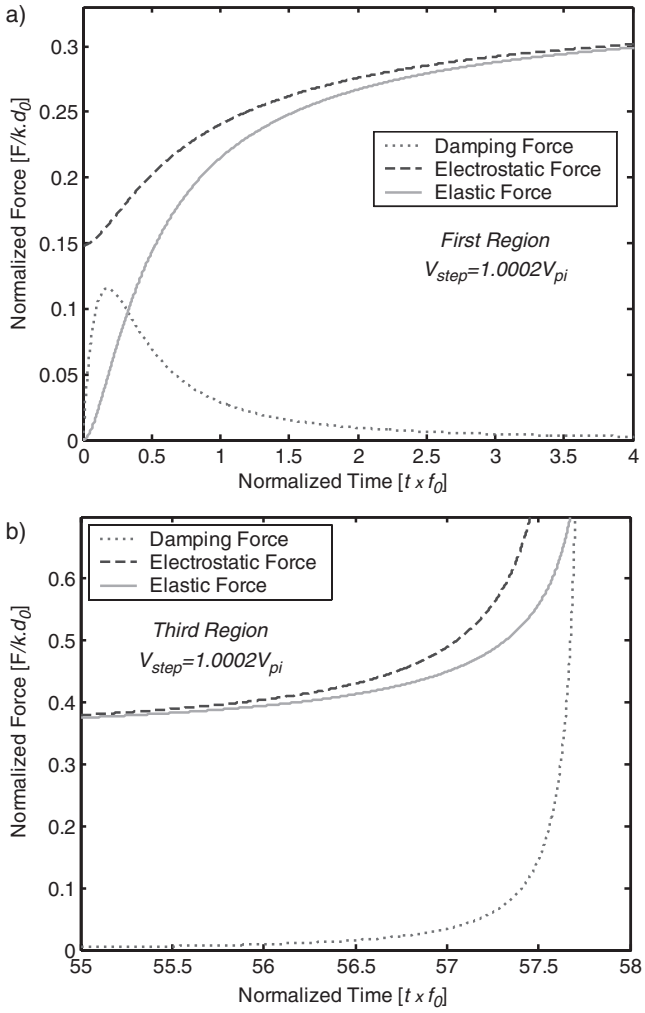

Figure 5.14 Forces relationship on transient response on the a) first region and b) third region

2. A second meta-stable region characterized by an almost zero velocity. At the onset of this region the structure moves very slow and the elastic force is almost the same as the electrostatic. This results in a kind of meta-stable equilibrium.

3. The third region takes the structure to the counter-electrode. Due to the nonlinear behaviour of the electrostatic force, the elastic force cannot indefinitely compensate for the electrostatic one and the structure snaps (Fig. 5.14b).

The damping force (quality factor) is the crucial element in the first region and largely determines the duration of the meta-stable region. If Eqn. (5.9) is solved for different quality factors the effect of the damping on the pull-in motion can be evaluated. Fig. 5.15 presents the several different system responses for changes in the Q value.

Threshold for the meta-stability at Q around 1.2 is clearly visible from the simulations. The meta-stability greatly depends on the first region where the damping force plays a very important role. The more the damping stops the movement of the device in the first region the higher is the time spent in the meta-stable region. This is very important when pull-in time is a crucial factor.

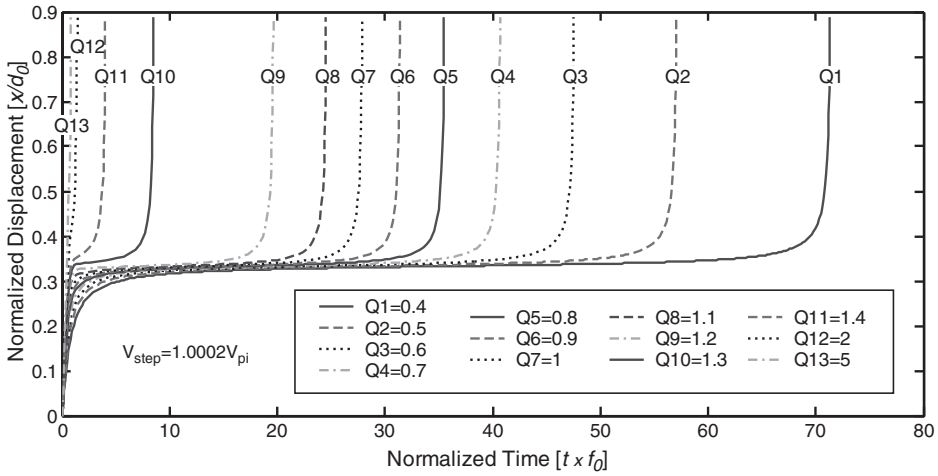

Figure 5.15 Dynamic pull-in motion for several Q values

The meta-stable region is characterized by a tight equilibrium between electrostatic and elastic force. Any small interference on the meta-stable equilibrium will affect the time spent in the second region and therefore the pull-in time. The changes in the pull-in time for different external accelerations and amplitude of the step voltage (different values of α) were simulated (using Eqn. (5.9)) to verify their influence (Q=0.5). Results are presented in Fig. 5.16.

The important aspect is the high sensitivity of the transition time to an external acceleration (for small values of α). This is due to the intrinsic behaviour of the meta-stable region. Since this region is best described by an equilibrium of forces, any small

change acts as a perturbation to the meta-stable equilibrium, thus providing the means to achieve a very high sensitivity on the time domain.

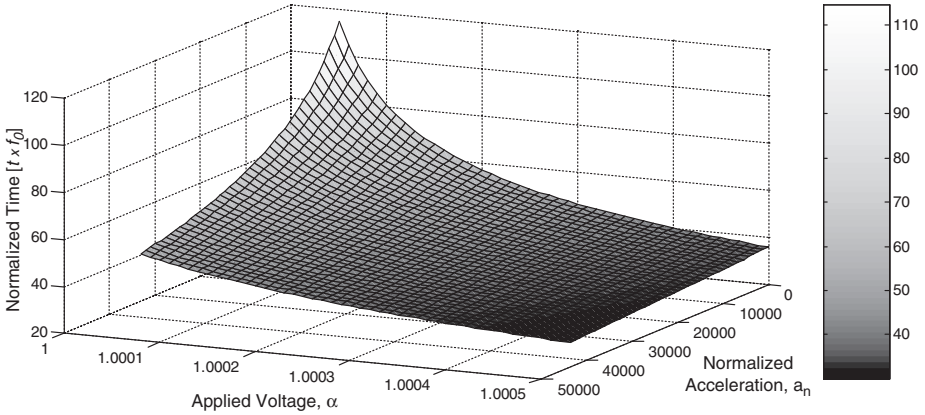

Figure 5.16 Simulated pull-in time changes with voltage step amplitude (α) and external acceleration

5.5.1 Meta-Stable Region

During the pull-in motion analysis we saw that the pull-in time for a low-Q device (Q<1.2) is basically governed by the second region (almost 90% of the pull-in time), thus the modelling of this region only can be assumed to reasonably predict the pull-in dynamic transition [5.8].

The meta-stable region is characterized by a very small variation of the displacement around the static pull-in displacement (x_{pi}). If only this small interval around x_{pi} is considered, a linearization of the equation of motion can be realized which results in a linear second-order system. The linearized differential equation can be analytically solved and an expression for the pull-in time can be found.

The normalized nonlinear equation of motion is expressed as (from Eqn. (5.9)):

$$\frac{\mathrm{d}^2 x_n}{\mathrm{d}t^2} + \frac{\omega_0}{Q}\frac{\mathrm{d}x_n}{\mathrm{d}t} + \omega_0^2 x_n = a_n + \frac{4}{27}\frac{\omega_0^2}{(1-x_n)^2}V_n^2 \qquad \textbf{(5.16)}$$

The nonlinear electrostatic force can be approximated in Taylor series around the normalized pull-in displacement ($x_{n,pi} = 1/3$):

$$\frac{4}{27}\frac{\omega_0^2}{(1-x_n)^2}V_n^2 \cong \frac{\omega_0^2}{3}V_n^2 + \omega_0^2 V_n^2(x_n - x_{n,pi}) \tag{5.17}$$

This result in a second order linear differential equation:

$$\frac{\mathrm{d}^2 x_n}{\mathrm{d}t^2} + \frac{\omega_0}{Q}\frac{\mathrm{d}x_n}{\mathrm{d}t} + \omega_0^2 x_n(1 - V_n^2) = a_n + \omega_0^2 V_n^2\left(\frac{1}{3} - x_{n,pi}\right) \tag{5.18}$$

Eqn. (5.18) is only valid for movements around the normalized pull-in displacement. By doing a variable transformation, $z_n = x_n - x_{n,pi}$, the normalized pull-in displacement becomes the system reference, simplifying the analysis. Assuming a voltage, $V_n = \alpha$ with $\alpha>1$, and a constant external acceleration during the pull-in motion, the linearized expression of z_n describing the meta-stable motion in the Laplace domain can be expressed as:

$$Z_n(s) = \frac{a_n + \frac{\omega_0^2}{3}(\alpha^2 - 1)}{s^2 + \frac{\omega_0}{Q}s + \omega_0^2(1 - \alpha^2)} \tag{5.19}$$

For $\alpha>1$ the linearized Laplace expression presents two poles, P_1 and P_2 (Fig. 5.17):

$$\begin{aligned} P_1 &= \frac{-\frac{\omega_0}{Q} + \sqrt{\left(\frac{\omega_0}{Q}\right)^2 - 4\omega_0^2(1-\alpha^2)}}{2} \\ P_2 &= \frac{-\frac{\omega_0}{Q} - \sqrt{\left(\frac{\omega_0}{Q}\right)^2 - 4\omega_0^2(1-\alpha^2)}}{2} \end{aligned} \tag{5.20}$$

P_1 is the dominant pole and is positive, while P_2 is negative. Since the system has a dominant pole, P_1, which is the cause for the system instability, the negative pole can be neglected without introducing a big error. With this simplification the linearized Laplace expression becomes:

$$Z_n(s) = \frac{\left(a_n + \frac{\omega_0^2}{3}(\alpha^2 - 1)\right)\left(\frac{-P_1}{\omega_0^2(1-\alpha^2)}\right)}{s - P_1} \tag{5.21}$$

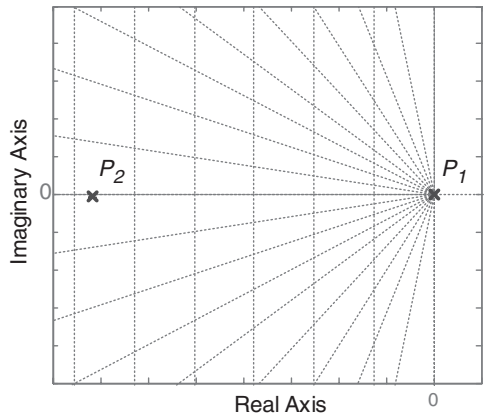

Figure 5.17 Pole-zero map of the linear system

The inverse Laplace transform of $Z_n(s)$ gives us an analytical expression for the displacement:

$$z_n(t) = \frac{3a_n + \omega_0^2(\alpha^2 - 1)}{3\omega_0^2(\alpha^2 - 1)}(e^{P_1 t} - 1) \tag{5.22}$$

The time, t_m, necessary to go from an initial position, z_1 (start of the meta-stable region), to a final point, z_2 (end of the meta-stable region) is obtained by solving Eqn. (5.22) in variable t, and considering a displacement $z_n(t)=\Delta z/d_0$ ($\Delta z=z_2-z_1$):

$$t_m = \frac{2\ln\left[1 + \dfrac{3\omega_0^2(\alpha^2 - 1)\dfrac{\Delta z}{d_0}}{3a_n + \omega_0^2(\alpha^2 - 1)}\right]}{-\dfrac{\omega_0}{Q} + \sqrt{\left(\dfrac{\omega_0}{Q}\right)^2 - 4\omega_0^2(1 - \alpha^2)}} \tag{5.23}$$

The meta-stable region represents about 85% of the pull-in time. Therefore, the relation between the pull-in time and the time spent in the second region is given by:

$$t_{pi} = t_m / 0.85 \tag{5.24}$$

Using Eqns. (5.23) and (5.24) the pull-in time was computed for different voltages (α) and external accelerations ($\Delta z=0.04\mu m$, $\omega_0=2\pi 2850$ and Q=0.5). The results are presented in Fig. 5.18.

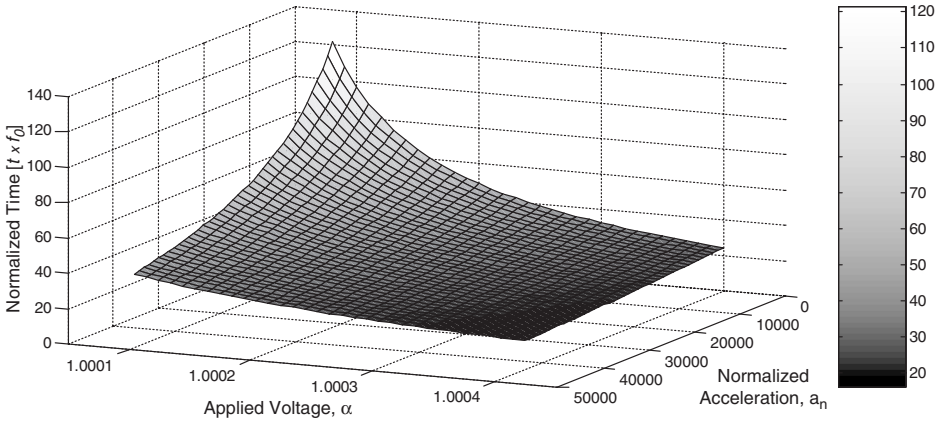

Figure 5.18 Calculated pull-in time changes with voltage step amplitude (α) and external acceleration for the linear model

A qualitative comparison between Fig. 5.18 and Fig. 5.16 reveals that the trend of the graphs is very similar. The pull-in time decreases for increasing accelerations and voltage values. A more rigorous analysis reveals that the errors between the two can be as large as 50% for small values of the pull-in time.

The linear model is very simple and can be a valuable tool for the design of MEMS devices that have to deal with pull-in times. It is not a very accurate tool, but can be very useful for the first pull-in time calculations and to check the influence of the various design parameters on the pull-in time. Of course, this analytical expression can only be applied to devices with a quality factor lower than 1.2.

5.6 Dynamic Pull-In: Experimental Verification

The pull-in time and motion concepts and the linear model introduced in the previous section were experimentally verified using two different 1-DOF MEMS devices. The first one, Device 1, is the 1-DOF device already used in this chapter. The second device, Device 2, is a remodelled version of the first device. It is a laterally movable structure (with two central bars) with folded beam suspension at both ends and electrodes extend-

ing perpendicular to the axial direction. Several sets of electrodes in the same plane are used. Two are for electrostatic actuation in the direction normal to the electrode area, and the rest are used for capacitive displacement measurement. A drawing of the structure is depicted in Fig. 5.19.

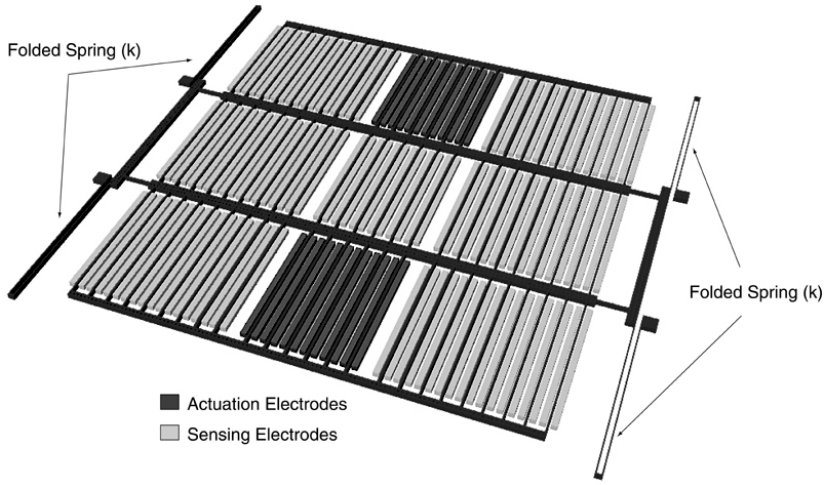

Figure 5.19 Drawing of microdevice 2

Comparatively, Device 2 has a bigger mass, a smaller equivalent mechanical spring and a higher capacitance change due to displacement, resulting in a device with a lower resonant frequency and a lower Q value at ambient pressure (due to the high number of arms that contribute to a larger damping coefficient). During the next sections, both devices are used.

5.6.1 Pull-In Time Measurements: Meta-Stable Region

Measurements of the pull-in time for different voltages and external accelerations were performed using one of the fabricated micromachined structures (Device 1). The measurements involve the application of a pulse with amplitude αV_{pi} and the time measurement of the pull-in time. A comparison between experimental results, simulations and predictions based in Eqn. (5.23) (Δz=0.04 μm) are presented in Fig. 5.20.

The analytical solution of Eqn. (5.23) assumes a constant damping coefficient. Since the structure during a pull-in event spends most of its time around the static pull-in displacement, the damping coefficient for a displacement $x = x_{pi} = (1/3)d_0$ is considered. This results in a quality factor Q=0.5 for a device surrounded by neon at

0.6×10^5 Pa. Once more, the good agreement between measurements and simulations proves the robustness of the dynamic large-signal model. Relatively to the derived analytical solution, the errors are substantial but the model simplicity makes it a valuable tool for the initial design of low-Q devices where the pull-in time is crucial. Another important aspect here is the experimental prove of the high sensitivity of the meta-stable region. Although highly nonlinear the meta-stable region and its sensitivity can be exploited for some advanced applications.

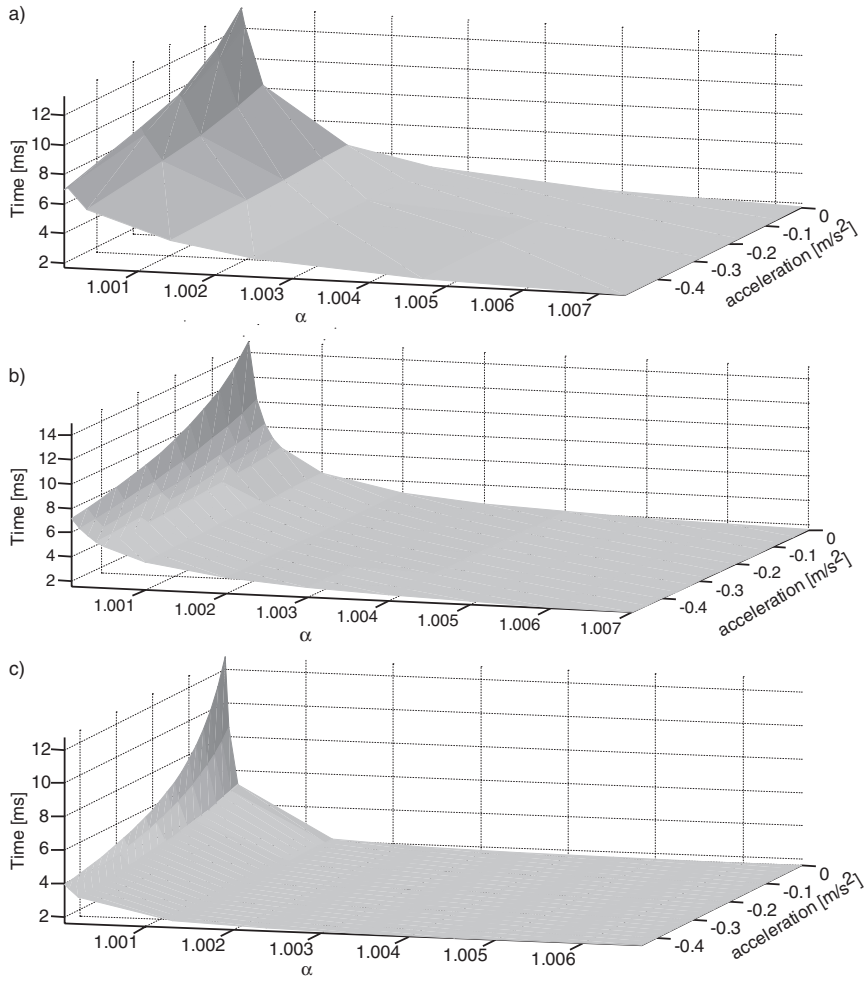

Figure 5.20 Measured pull-in time changes with voltage step amplitude and external acceleration. a) Experimental, b) simulated and c) linear model

5.6.2 Pull-In Time Measurements: Pressure Variations

Fabricated structures (Device 2) were used for experimental validation of more dynamic pull-in concepts. These devices have four folded beams, 340 μm long and 2.5 μm wide, connected to two rigid bars of about 1 mm length. Parallel-plate capacitors with a 2.25 μm zero-displacement gap are used for the actuation of the movable mass. Stoppers located at the end of the rigid bars, 2 μm apart, prevent that the electrodes touch after pull-in is reached. A SEM photograph of the device is shown in Fig. 5.21. The main device characteristics are presented in Table 5.1

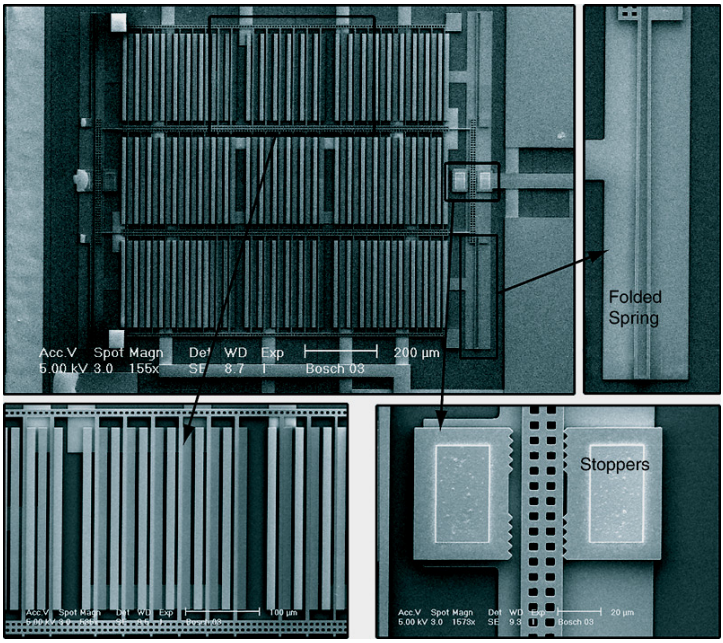

Figure 5.21 Microphotograph of Device 2

The nonlinear behaviour of the squeeze-film damping was not considered during the dynamic pull-in analysis. To verify the significance of a variable damping coefficient as compared to a constant one, simulations using the large-signal model of Device 2 were performed for both cases. Eqn. (5.14) was used to compute the constant damping coefficient (using a gap value of d_0). Air at ambient temperature was considered as the gas medium and simulations using different air pressures were performed. Next, simulations

using a variable damping coefficient were performed for the same air pressures. Comparative results are presented in Fig. 5.22.

TABLE 5.1 Main parameters of Device 2

Fixed Parameter	Value
Mechanical spring (k)	*1.29 N/m*
Mass (m)	*4.27 μg*
Resonance frequency (f_0)	*2.77 kHz*
Initial gap distance(d_0)	*2.25 μm*
C_{d0} (zero-displacement actuation capacitor)	*141 fF*
C_{s0} (zero-displacement sensing capacitor)	*611 fF*
Total n° of arms	*72*

Although a variable damping coefficient was used for the simulations presented in Fig. 5.22a, the quality factor values in the graph were computed using a constant damping coefficient ($x=x_{pi}$). Since the device spends most of its movement around the static pull-in displacement, the quality factor computed around this point is used here as a comparative measure. This results in a threshold at $Q \cong 1.2$ for the occurrence of the meta-stability.

To confirm the variations of the pull-in motion with pressure, measurements at different pressures were performed. A sample device was introduced in a variable pressure chamber and the pull-in time for a voltage step was measured in the absence of any external force. The measured curves are presented in Fig. 5.23 and the threshold is clearly visible. It is interesting to see that small changes in pressure (100 mbar) are enough to go from a meta-stable response to a fast response. This is very important, since it enables a MEMS designer to use the meta-stable regime (i.e for sensing) or to avoid it (i.e for switching) by proper pressure control.

With these last measurements all the pull-in time and pull-in motion concepts introduced in this chapter were experimentally verified using real MEMS devices. The various dependencies of the pull-in time were verified (voltage, pressure, gas medium and external acceleration) as well as the motion described by the device during a pull-in event. In the next chapters applications using these concepts will be proposed.

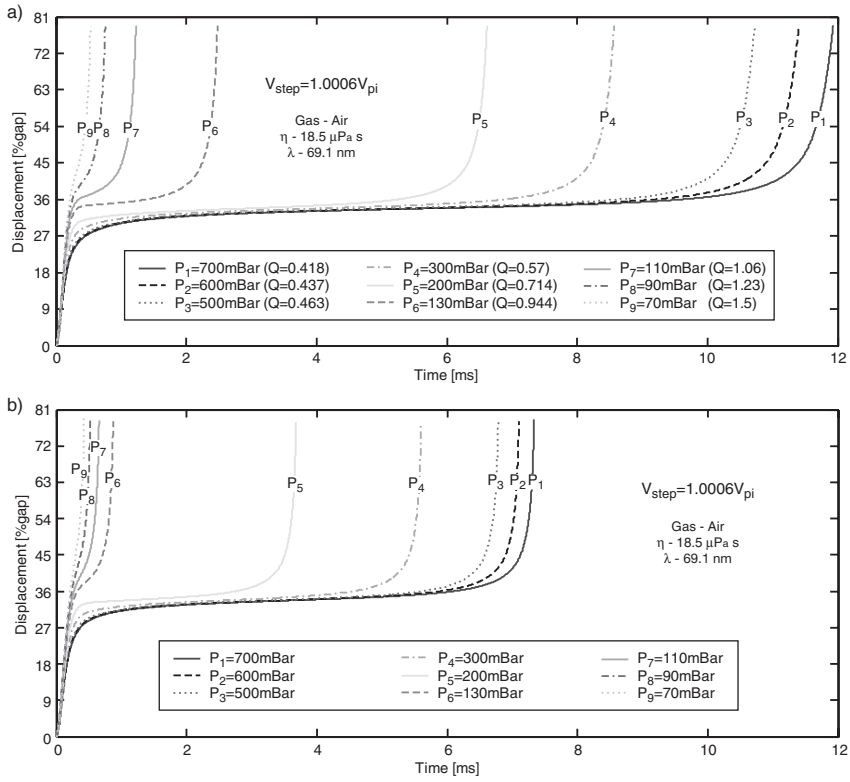

Figure 5.22 Simulations of the dynamic pull-in displacement for different pressure values using a) variable damping and b) constant damping coefficients

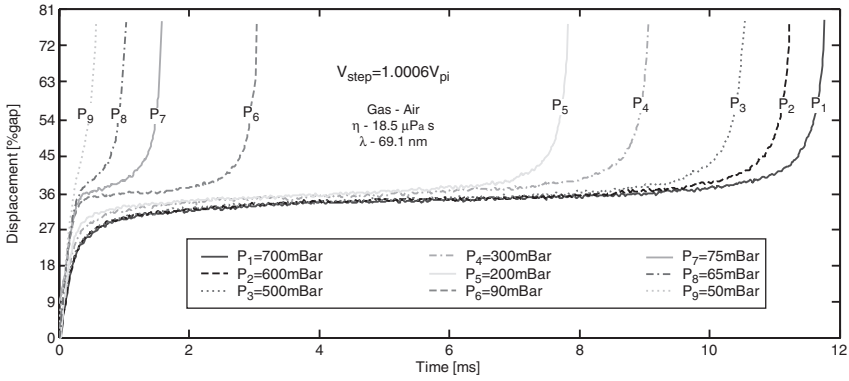

Figure 5.23 Pull-in dynamic measurements at different air pressures

5.7 Conclusions

In this chapter the nonlinear dynamic behaviour of MEMS devices have been analysed with special emphasis on the dynamic behaviour of the pull-in phenomenon. Pull-in has been analysed with respect to the necessary conditions that lead to the loss of stability and to the time and motion described by the structure when stability is lost. The motion of a microelectromechanical device when actuated by a voltage is described by a nonlinear differential equation. The analysis of the nonlinear differential equation shows that the stability and trajectory described depends on the voltage value and with a proper voltage control, the system can be made stable over the entire phase space. When the dynamic behaviour is considered the loss of stability is more difficult to predict as compared to a quasi-static analysis. Pull-in can occur for voltages lower than the static pull-in value, depending on the initial value of the state variables and on the external applied forces. This is of extreme importance for applications requiring a stable behaviour. There are no analytical tools to predict these values but the numerical solutions of the differential equation of motion can predict the stable boundaries.

When the structure goes to pull-in (the system becomes unstable), the motion described by the device is characterized by a kind of meta-stable equilibrium between the elastic and electrostatic forces. This is true for devices with a low quality factor ($Q < 1.2$). Despite all the nonlinearities of the differential equation of motion, the meta-stable region can be modelled if some simplifications are performed. The simplicity of the resulting model makes it a valuable tool for a MEMS designer when he has to deal with applications where the pull-in time is of extreme importance.

This chapter together with chapter 3 fully describe the main characteristics of parallel-plate MEMS devices, from both a static and dynamic perspective. The nonlinear dynamic analysis was only performed for the 1-DOF case but can be extended to higher degrees of freedom devices. The starting point is always the equation of motion of the device. For a 2-DOF device, there are 4 state variables and the phase portrait has 4-dimensions. This adds a lot of complexity to the analysis but the basic behaviour is similar to the 1-DOF case. Trajectories starting inside of the basin of attraction are stable, while the ones starting outside are unstable. Any change on the voltage level will change the attractors and the basin of attraction and a voltage level can always be found that makes the current trajectory stable (in the limit, the structure returns to the zero-displacement position if no voltage is applied).

5.8 References

[5.1] R.K. Gupta and S.D Senturia, “Pull-In Time as a Measure of Absolute Pressure”, *in Proc. MEMS’97*, Nagoya, Japan, 26-30 January 1997, pp. 290-294.

[5.2] H. Yang, L.S. Pakula and P.J. French, “A Novel Pull-In Accelerometer”, *in Proc. Eurosensors XVII*, Guimarães, Portugal, 21-24 September 2003, pp. 204-207.

[5.3] M.H.H Nijhuis, T.G.H. Basten, Y.H. Wijnant, H.Tijdeman and H.A.C. Tilmans “Transient Non-linear Response of ‘Pull-In MEMS Devices’ Including Squeeze Film Effects”, *in Proc. Eurosensors XIII*, The Hague, The Netherlands, 12-15 September 1999, pp. 729-732.

[5.4] L.A. Rocha, E. Cretu, R.F. Wolffenbuttel, “Dynamics of Pull-In: Analysis of the Meta-Stable Regime”, *in Proc. MME’03*, Delft, The Netherlands, 2-4 November 2004, pp. 57-60.

[5.5] L.M. Castaner, S.D. Senturia "Speed-Energy Optimization of Electrostatic Actuators Based on Pull-in", *J. Microelectromech. Syst.,* 8 (1999) 290-298.

[5.6] Alfredo Medio and Marji Lines, *Nonlinear Dynamics*, Cambridge, UK, Cambridge University Press, 2001.

[5.7] Eric W. Weisstein, "Newton's Method" from *MathWorld* - A Wolfram Web Resource. http://mathworld.wolfram.com/NewtonsMethod.html.

[5.8] L.A. Rocha, E. Cretu, R.F. Wolffenbuttel, “Analytical Model for the Pull-In Time of Low-Q MEMS Devices”, *in Proc. Nanotech 2004*, Boston, USA, 7-11 March 2004, pp. 271-274.

6

Using Dynamic Voltage Drive for Extended Stable Displacement Range

6.1 Introduction

Although commonly used, electrostatic parallel-plate actuation is limited to displacements up to 1/3 of the gap due to the pull-in effect [6.1]-[6.13]. Some techniques have been developed to overcome this limitation. The simplest of all consists on the design of an actuator with a gap 3 times larger than the desired one [6.1], [6.2]. This is a simple technique, but the desired displacement is achieved at the cost of a higher voltage, which in most cases is a limitation by itself.

This chapter starts by introducing the various techniques reported in literature to extend the travel range of electrostatic parallel-plate actuators. These techniques can be classified into four main groups, namely: geometry leverage [6.3], [6.4], series feedback capacitor [6.5]-[6.7], current drive methods [6.8]-[6.10] and closed-loop voltage control [6.11]-[6.13]. It is interesting to note that these studies overlooked the opportunities provided by the dynamic behaviour of the devices.

A fundamental MEMS dynamic characteristic observed during the nonlinear dynamic analysis performed in chapter 5 is the achievable dynamic displacement

beyond the static pull-in limitation. This is a fundamental issue and provides the basic theory for a new approach for closed-loop voltage control introduced in this chapter. The method is confirmed with both simulations and experimental results. The simplicity and effectiveness of the method are an added value to parallel-plate electrostatic actuators.

The closed-loop voltage control method based on feedback linearization [6.13] is also analysed in this chapter. The main practical issues of this approach are discussed and simulation results based on large-signal models confirm the robustness of the method. Nevertheless, due to the complex circuitry needed, no experimental results are presented.

6.2 Extended Travel Range Techniques

In what follows, the main methods found in literature to overcome the static pull-in limitation are discussed.

6.2.1 Geometry Leverage

The idea behind the geometry leverage method [6.3], [6.4] is to work around the pull-in instability. Electrostatic forces are applied to a part of the structure while the rest of the structure is used as a "lever" to position specific parts of the structure through a large range of motion (Fig. 6.1). This strategy allows parts of the structure to move through the entire gap while the electrostatically actuated parts deflect less than the pull-in limit.

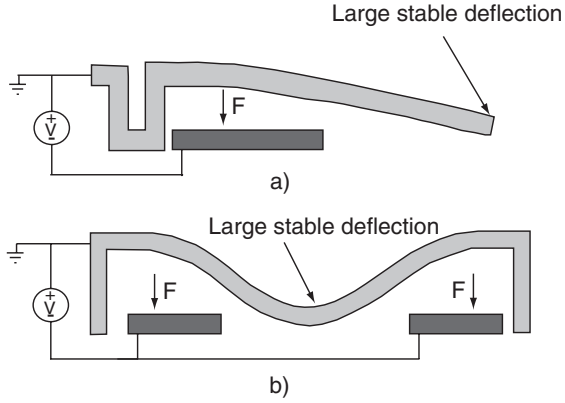

Figure 6.1 Simple examples of geometry leverage applied to a) cantilevers and b) double-sided clamped beams

The geometry leverage technique applied to a simple cantilever is shown in Fig. 6.1a. A smaller electrode is placed under the beam close to the anchor point instead of putting the electrode under the entire beam. Using the smaller electrode, the tip of the beam can travel along the full gap, while the parts being electrostatically actuated remain in the equilibrium region. The same technique can be applied to a double-sided clamped beam (Fig. 6.1b). If two electrodes are placed close to the beam supports, the center of the beam can move over the entire gap before pull-in occurs at the electrode areas.

The technique is very simple, however it requires an increased device area and actuator geometry changes. The design issues are very important, as the structure movement greatly depends on electrode and beam size. These two parameters are the key factors to achieve the maximum displacement without reaching pull-in at the electrostatically actuated parts.

6.2.2 Series Feedback Capacitor

In this case, stabilization is achieved by introducing a capacitor in series with the electrostatic actuator (Fig. 6.2a) [6.5], [6.6]. For stable full-gap travel the equivalent series capacitance must be less than one-half of the initial capacitance of the actuator $C_{0.}$

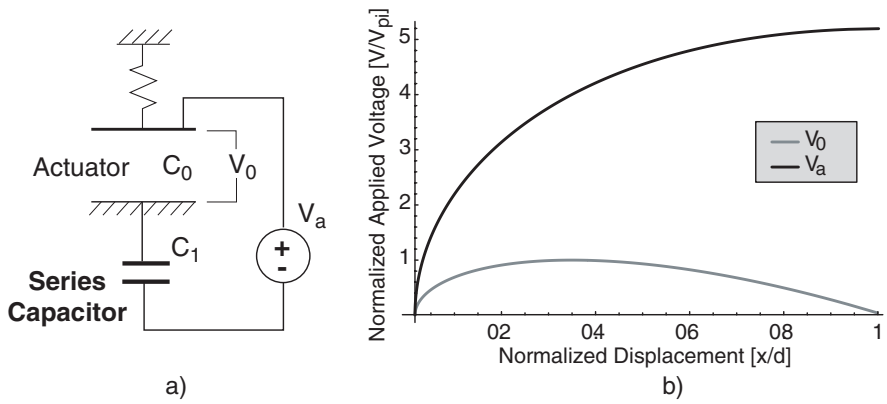

Figure 6.2 Actuator with series capacitor for increasing the stable deflection range. a) Schematic and b) actuator voltages versus displacement

The original actuator and series capacitor form a voltage divider. As the movable electrode approaches the fixed one, the actuator capacitance increases and thus the fraction V_0 of the total applied voltage V_a decreases according to:

$$V_0 = \frac{C_1}{C_0 + C_1} V_a , \qquad \textbf{(6.1)}$$

where C_0 is the variable capacitance of the actuator and C_1 the series capacitance. When the movable electrode travels beyond one-third of the gap the high increase in capacitance provides the necessary negative feedback to stabilize the actuator, allowing it to travel along the full-gap. Initially, V_0 increases with V_a (Fig. 6.2b). Beyond one-third of the initial gap where V_0 equals V_{pi}, V_0 actually starts to decrease (since C_0 increases rapidly in this region), allowing for a stable operation. At all times, the elastic and electrostatic forces are balanced and the system is stable.

The concept is very simple and allows stabilization beyond one-third of the gap. Practical issues, such as parasitic capacitances, have to be considered in this case (they limit the performance and the maximum achievable range). The high voltage levels needed are another drawback (until 5 times the pull-in voltage).

In order to overcome the high voltages needed, Seeger *et al.* proposed in [6.7] the use of switched capacitor techniques to control the charge in the actuator. A circuit capable of reducing this voltage by a factor of three to five was proposed. This voltage reduction however, is at the expense of an increase in the complexity of the system and by problems related to the switches.

6.2.3 Current Drive Methods

Current drive methods use charge injection rather than voltage actuation. The pull-in limitation is overcome by the use of current pulses injecting the required amount of charge to fix the position of the movable plate [6.8], [6.9]. The use of a different type of drive, a pulse-current drive, makes the charge delivered to the actuator independent of the displacement and thus avoids the pull-in nonlinearity.

The charge delivered is set by the source parameters (current and pulse width) and does not depend on displacement. All points in the gap are therefore stable (this is the essential and significant difference between voltage and charge drive). Theoretically, as long as care is taken to ensure that the charge delivered to the actuator is constant, any displacement can be achieved.

Although the method is very simple, its implementation is not. Parasitic capacitances and current leakage limit the stability and are the origin of drifts on the equilibrium position. Refreshing cycles can be carried out to compensate for the drift caused by the current leakage, but in this case the refreshing rate becomes a critical parameter. Stable operation until twice the pull-in limitation has been achieved using current drive methods [6.9] and more recently stable operation up to 83% of the gap was reported [6.10]. Full gap operation is still not achieved, since the charge control technique is limited by charge pull-in due to parasitic capacitance and tip-in instability [6.10].

6.2.4 Closed-loop Voltage Control

Another solution proposed to achieve stable operation beyond 1/3 of the gap is the use of a closed-loop to control the voltage applied [6.11]-[6.13]. The closed-loop system can in principle be made stable for displacements over the full-gap by proper control of the applied voltage.

A schematic of the full proposed system can be seen in Fig. 6.3. The displacement is measured by sensing the changes in a capacitive transducer and the system is linearized by using nonlinear control techniques. With the system linearization, a linear controller can be used.

This technique is quite complex: it requires accurate and fast monitoring of the position of the movable element and feedback control circuitry to stabilize the system beyond the pull-in instability. Moreover, any small delay in the feedback path (caused by the sensing mechanism) is enough to limit the performance of the system. Nevertheless, if the position of the actuator can be measured with negligible delay, this approach is very robust and displacements up to 74% of the full gap have been demonstrated [6.13].

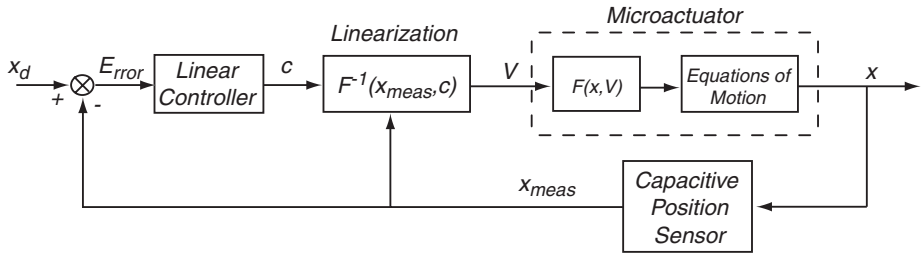

Figure 6.3 Schematic of a closed-loop voltage control system with feedback linearization

Although the results presented in [6.13] are an advance on extending the travel range of electrostatic actuators, they are based on a tracking control algorithm and steady-state stable operation beyond pull-in is not reported. Moreover, the nonlinear dynamic behaviour (damping coefficient) is the reported limitation for sine displacements (until 74% of the full gap).

The combination of large-signal modelling with nonlinear dynamic analysis is used in the next section for the study of a closed-loop voltage control system using nonlinear control. Simulation results are presented and the main practical issues are discussed. Next, a far more simple solution is introduced and validated with measured data. Stable operation over the full gap range is achieved without the use of complex algorithms or circuitry.

6.3 Feedback Linearization

The first constraint in a closed-loop control system is the measurement of the displacement of the microdevice. This implies that the microstructure must have some kind of sensing mechanism for the displacement (capacitive, piezoelectric, etc.). The surface micromachining devices used in this thesis were fabricated with sets of differential sensing capacitors that can be used to measure the device displacement.

The analysis performed here is valid for overdamped systems. As observed in chapter 5, overdamped systems have a larger basin of attraction which is fundamental to the performance of the linearization control technique. Moreover, the damping force provides a complementary opposing force, which is extremely important for operation beyond the static pull-in limitation.

Several control techniques are used in nonlinear control theory. The desired control action and the nonlinear characteristics of the system dictate the control technique that must be applied [6.14]. The relative simplicity of the microsystem suggests that a feedback linearization control technique is appropriate to overcome the pull-in limitation. The feedback linearization attempts to cancel the nonlinearities of the nonlinear system, so that the closed-loop dynamic behaviour is in a linear form. A diagram of the complete closed-loop system is shown in Fig. 6.3. The application of the technique results in a linear input-output relation (the nonlinearities are cancelled out).

The feedback linearization can be applied to a class of nonlinear systems (which include the MEMS) that are described by the so-called companion form, or controllability canonical form [6.14]:

$$x^{(n)} = f(x) + g(x)u\,, \tag{6.2}$$

where u is the scalar control input, x is the scalar output of interest and $X = [x, \dot{x}, \ldots, x^{(n-1))}]$ are the state variables. The linearized control input, when using this technique, becomes:

$$u = \frac{1}{g(x_{meas})}[c - f(x_{meas})] \tag{6.3}$$

Here c is the response of the linear controller and x_{meas} is the measured displacement at the output. Using the MEMS equation of motion, Eqn. (5.12), repeated here for reader convenience:

$$\dot{x} = y$$

$$\dot{y} = a_{ext} + \underbrace{\frac{C_0 d_0 V^2}{2m(d_0 - x)^2}}_{\text{g(x)}} \underbrace{- \frac{k}{m}x - \frac{b(x)}{m}y}_{\text{f(x)}}, \tag{6.4}$$

and neglecting the external acceleration, the following linearization function results:

$$V = \sqrt{\frac{2m(d_0 - x)^2}{C_0 d_0}\left[c + \frac{k}{m}x + \frac{b(x)}{m}\dot{x}\right]} \tag{6.5}$$

The linear controller block of Fig. 6.3 is responsible for the linear control response *c* and is implemented using linear control techniques such as proportional control or PID control.

For a practical implementation of the feedback linearization control technique, some kind of digital microcontroller has to be used to implement both the linear controller and the linearization function. This implies the use of an Analog-to-Digital Converter (ADC) to sample the device output and a Digital-to-Analog Converter (DAC) to generate the appropriate control voltage. The resolution of the ADC and DAC and the sampling frequency are critical and depend on the details of the microstructure.

Even if these precautions are implemented, another problem remains: the processing time of the microcontroller. The microcontroller processing time should be minimum (to reduce the time delays introduced by the feedback path), which implies a very simple control algorithm. A close inspection of Eqn. (6.5) reveals that the nonlinear damping coefficient and the displacement derivative ($\dot{x}$) are the more complex terms. One of the simplifications introduced here is disregarding the damping coefficient from the linearization expression in order to simplify the nonlinear control. This appears justified considering the fact that the damping force tends to zero as the velocity decreases and ultimately plays no role when the device remains at a constant position. The important part is that the device goes to the desired unstable position as long as the appropriate voltage level is applied.

Of course this assumption needs to be verified and thus, the model of an actual structure is used. Once again two 1-DOF structures are used as the test structures and the same notation, Device 1 and Device 2 (both capped in neon), as used in the previous chapter is adopted. Device 1 is the 1-DOF structure used for verification of the static and dynamic models. Device 2 is the upgraded 1-DOF structure introduced in the previous chapter.

First, the large-signal model of Device 1 was used to demonstrate the device's dynamic behaviour upon which the proposed simplification relies (removal of the damping coefficient). Simulation results are shown in Fig. 6.4. A voltage of 6 volts is initially applied to the structure. While the structure is heading towards the counter-electrode, the voltage is dynamically reduced to 4.12 volts (this voltage corresponds to the stable solution at 0.336 μm and to the unstable solution at 1.065 μm). Immediately, a meta-stability around the unstable solution is observed. This meta-stability around the unstable solution is essential for operation of the full closed-loop system and indeed justifies disregarding the damping force. Basically, the linearization should provide the appropriate trajectory and voltage to reach and maintain a position beyond the pull-in limitation, i.e., a voltage around 4.12 volts is needed to maintain the device at a displacement of 1.065 μm. Since the nonlinearities of the device already enable the structure to move to the desirable position, the linearization just has to provide the correct value of the voltage. The damping force can therefore be neglected and the overall control algorithm is simplified.

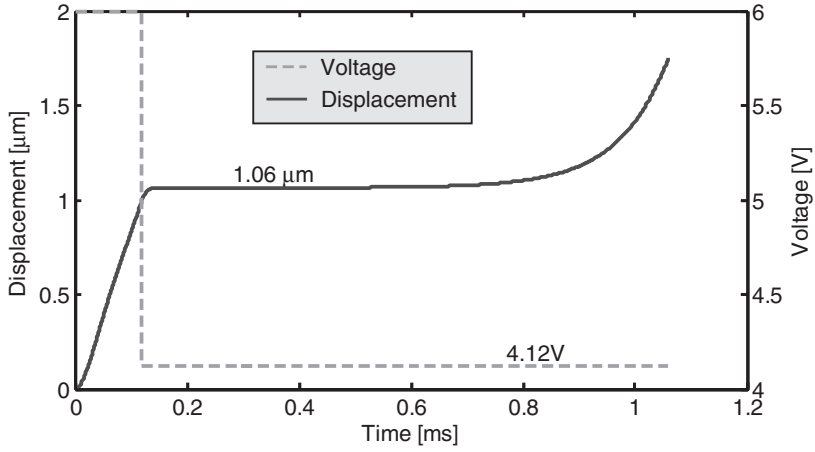

Figure 6.4 Meta-stability beyond pull-in displacement

To further analyse the dynamic behaviour of the closed-loop control system a few more simulations were performed. The use of the large-signal model of Device 1 allows the implementation of a closed-loop control model in Simulink. A schematic of the full model is shown in Fig. 6.5.

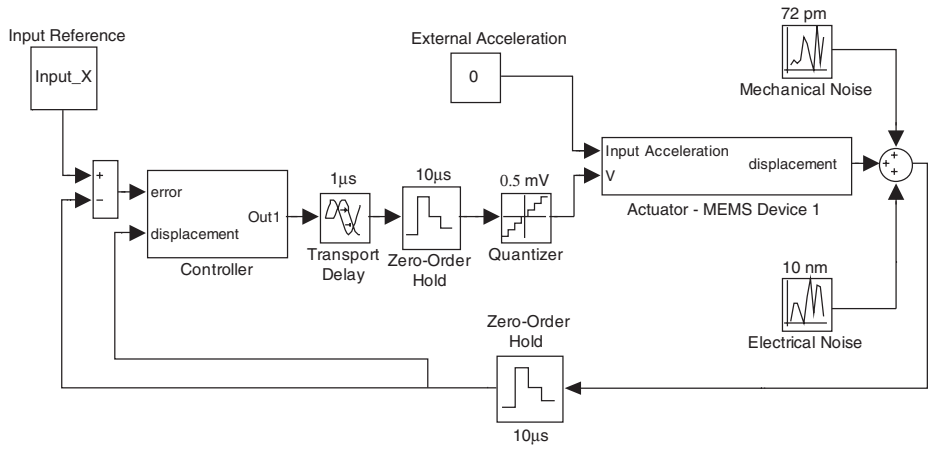

Figure 6.5 Closed-loop voltage control Simulink model

All the realistic aspects were considered for the model implementation. Both the mechanical noise and the measured electronic white-noise of the readout ($188nV/\sqrt{Hz}$) referred to the input (10 nm) were included in the model. A sampling frequency for both the ADC and DAC of 100 kHz was used and a resolution of 0.5 mV was assumed for the DAC (14 bits). The controller block of Fig. 6.5 is responsible for both the linearization and the linear controller. The Simulink diagram of this block is shown in detail in Fig. 6.6. A linear proportional control was used and the output voltage is limited to a maximum of 5V.

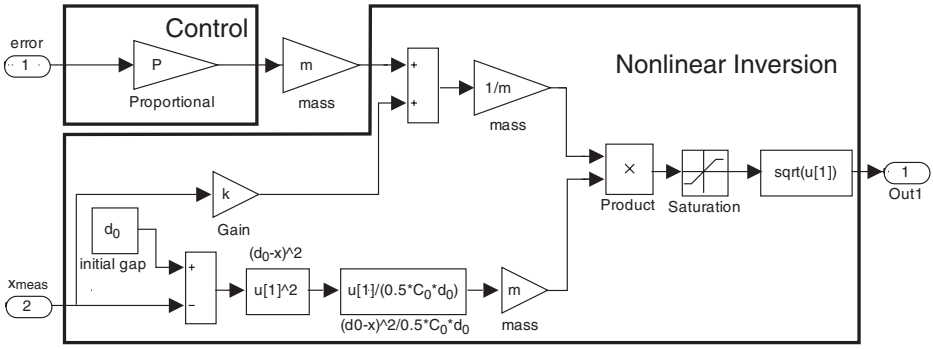

Figure 6.6 Linearization and linear controller block

Some of the simulated results are presented in Fig. 6.7. The simulated data shows that the use of a feedback linearization scheme does enable stable operation beyond the

pull-in displacement. The stoppers of the device are here the practical limitation for the maximum achievable displacement.

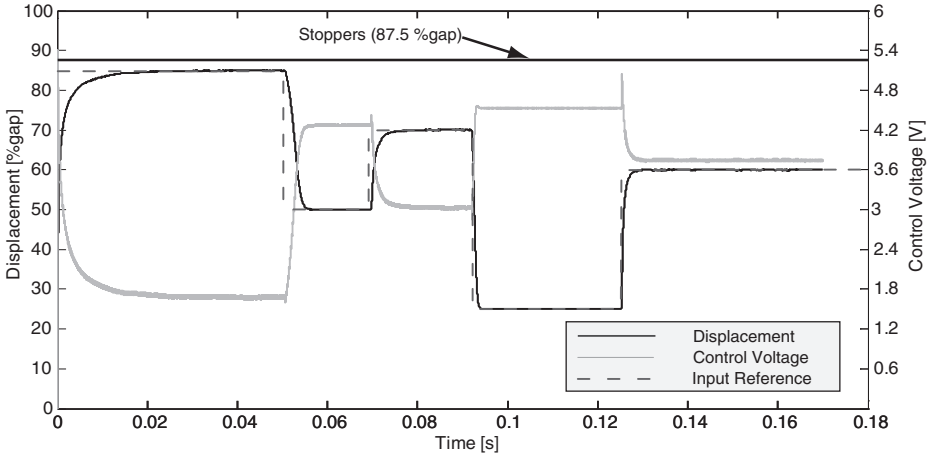

Figure 6.7 Closed-loop control simulation results

Even though the simulations rely on a very accurate device model and the major practical issues were taken into consideration, a few remaining aspects still need to be evaluated. To start with, this approach needs complex hardware circuitry including a fast microcontroller (DSP) which makes it a very complex solution. In terms of performance, there are two major issues that have not yet been addressed: delays in the feedback path and the correct value of the parameters involved (mass, spring constant, initial gap displacement, etc.).

The critical component is the time delay introduced by the readout circuit. If the delay between input and output exceeds a certain threshold, stable operation beyond the pull-in limitation is not possible. The device parameters (used in Eqn. (6.5)) are also of extreme importance, since the linearization is based on their values. During the simulations, the parameters used in the linearization function matched correctly the device parameters and obviously there were no problems. In a practical situation however, the parameters are just estimations of the real ones and any deviation due to fabrication tolerances leads to errors in the linearization. Any incomplete linearization results in residual nonlinearities and the control is ineffective. Most probably, the parameters of the device can be calibrated during experiments until they match the actual ones. Nevertheless, this is an issue that can only be fully exploited on real device implementation. Therefore, although theoretically the use of feedback linearization seems feasible, there are some practical issues that can compromise steady-state operation beyond the static pull-in limitation and there is a genuine need for a simpler and more robust approach. One solution is presented in the next section.

6.4 On-Off Closed-Loop Approach

A simple and flexible approach, as compared to feedback linearization and charge control (current drive) techniques is introduced here. The concept is innovative in the MEMS field and the basic idea is the comparison of the momentary actuator displacement with a fixed desired displacement. According to the comparison result, the voltage applied to the actuator is switched between two values (unlike feedback linearization): between a high level, if the current displacement is lower than the reference one, and a lower level, if the actuator displacement is higher than the reference value.

The concept is simple and similar to the on-off method used in linear control theory [6.15]. A block diagram of the proposed method is shown in Fig. 6.8. The method relies on the dynamic behaviour of MEMS devices, namely the shift between stable and unstable trajectories for changes in the applied voltage (shift of the basin of attraction). This implies that the device must be overdamped or critically damped. In underdamped devices, the inertial force is not significantly opposed by the damping force and the typical oscillatory regime of these devices compromises the method.

The voltage levels are not critical for proper operation. The high voltage level, V_{high}, has to be initially higher than the pull-in voltage but can be dynamically reduced to improve performance. The low voltage level, V_{low}, must be sufficiently low to ensure that after the switching, the structure position will be within the low-level voltage range of attraction. The difference between high and low level is however affecting the device response and can be dynamically reduced to improve the method's performance.

Two aspects are essential for a successful implementation of the method: switching and time delay in the control loop.

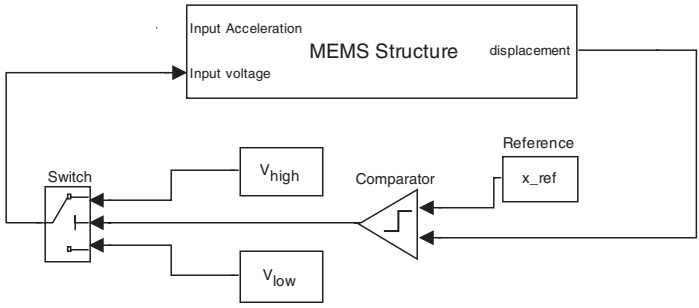

Figure 6.8 Block diagram of the on-off approach

6.4.1 Time Delay in the Feedback Loop

During switching the structure continues the movement and the resulting extra displacement originates a small ripple around the desired displacement. This effect is aggravated by any delay time introduced by the circuits. For no circuits delay and ideal switching times the ripple is negligible.

A Simulink model that uses the large-signal model of Device 2 was implemented to verify the proposed control method. The equivalent mechanical and the estimated electrical noise were included in the model and a time delay was introduced in the feedback loop. The introduced time delay simulates both the switching times and the time delays of the readout circuits. Fig. 6.9 presents the simulated performance of the control loop for a time delay of 15 μs. The reference displacement is set at 1.5 μm and the voltage levels are defined as: V_{high}=4V and V_{low}=2V. Device 2 theoretical static pull-in voltage is at V_{pi}=3.820V and the stoppers are placed at 2 μm in a 2.25 μm gap.

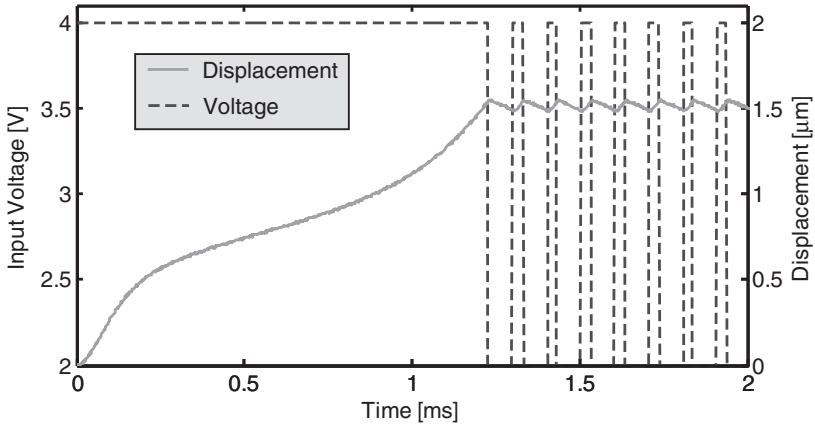

Figure 6.9 Simulink simulations of the on-off control scheme

A few more simulations were performed for different time delays. Simulation results are shown in Fig. 6.10. As predicted, the ripple depends on the time delays and the larger is the delay the longer is the displacement beyond the reference displacement value. Despite its simplicity, the on-off control method performs very well. The main constraints are the switching times and the time delays of the readout circuits. According to simulations, the control is still effective for a time delay as large as 30 μs. If we take in consideration that comparators can easily achieve switching times lower than 1 μs the bottleneck for real implementation is at the readout electronic circuit.

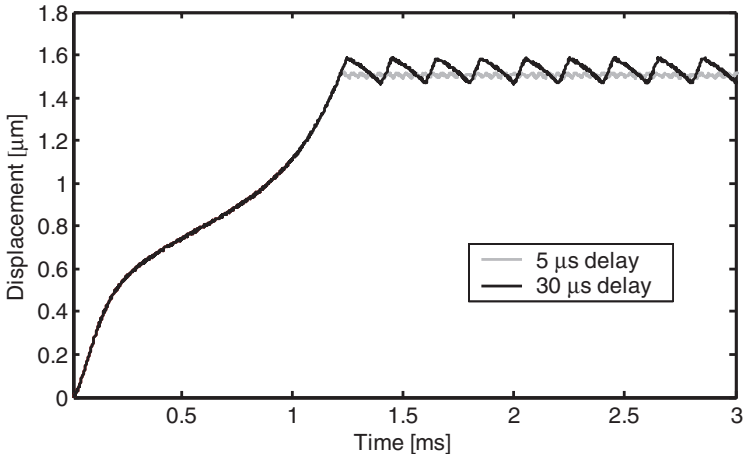

Figure 6.10 Simulations of the on-off control scheme with different time delays

6.4.2 Differential Capacitance Sensing Circuits

Since the readout electronic circuit is a critical component for the implementation of the closed-loop on-off control method, the readout circuits used during this work are introduced in this section. Two different approaches, single-ended output [6.16] and differential output [6.17], [6.18], have been used to measure the displacement on the several fabricated MEMS structures. The three different fabricated structures have differential sensing capacitors, which allow for capacitive displacement detection. In the following sub-sections the two approaches used are briefly discussed.

6.4.2.1 Single-Ended Output

In a single-ended approach the capacitance is measured by driving the ends of the capacitive bridge and taking the output as the center node (common to both capacitors). A schematic of the implemented circuit for differential capacitive displacement detection is depicted in Fig. 6.11. The core of the circuit is the charge amplifier.

A carrier signal, U_i, is applied to the drive amplifiers resulting in two voltages in opposite phase, U_{01} and U_{02}, that drive the differential capacitive pair $C_{s\text{-}left}$ and $C_{s-right}$. C_{k1} and C_{k2} are large coupling capacitors (0.1 µf) to avoid that DC signals are applied to the sensing electrodes. When a carrier voltage is applied to the sensing capacitors, the transfer function of the microstructure capacitance to the charge-amplifier output is expressed by:

$$U_{ch} = \left(\frac{C_{s-left} + C_{pl}}{C_{c1}}\right) U_l - \left(\frac{C_{s-right} + C_{pr}}{C_{c1}}\right) U_r, \tag{6.6}$$

where C_{pl} and C_{pr} are parasitic capacitances. These parasitic capacitances are due to the housing and bondpad connections and can cause a large offset signal at the charge amplifier, since they are much higher than the MEMS sensing capacitances. If U_{01} is made adjustable (using R_{l1}) the offset of the charge amplifier can be compensated for at the expense of a nonlinear gain set by the different amplitudes of U_{01} and U_{02}. At the output of the gain stage, the amplitude of the carrier signal, U_i, is modulated by the capacitance changes.

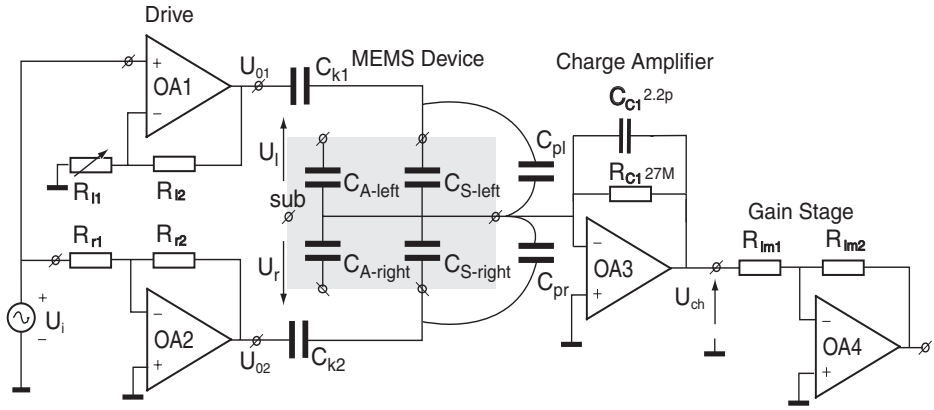

Figure 6.11 Single-ended displacement detection circuit

The single-ended readout circuit was implemented at the PCB level. For the driving amplifiers, OA_1 and OA_2, two AD8041 operational amplifiers were used, whereas the charge amplifier, OA_3, and the gain stage amplifier, OA_4, were implemented with LF356 operational amplifiers. This results in a measured output white-noise level at $188nV/\sqrt{Hz}$. A lock-in amplifier is used for demodulation of the output signal (SR830 from Stanford Research Systems).

The SR830 is limited to frequencies up to 100 kHz (far beyond the structure mechanical spectrum) which limits the carrier frequency. In order to achieve a low-noise level, the SR830 internal 4th order low-pass filter is set to a corner frequency of 4.8 kHz. This causes a huge time delay between the measured and the structure's actual displacement for frequencies close to the resonance frequency of the structure. Therefore, this readout scheme is not suitable for the implementation of the on-off control method. Nevertheless, this readout circuit was widely used and all the experimental data reported

in the previous chapters was obtained using it. It should be noted that a 4.8 kHz 4th order low-pass filter was used during simulations for the cases where experimental results are compared with simulations. This way both measured and simulated results are directly comparable.

6.4.2.2 Differential Output

When a differential interface is used, the stationary electrodes are connected to the differential position-sensing interface and the drive signal is applied to the common movable central electrode. A schematic of the differential output circuit is shown in Fig. 6.12. The circuit is composed by three main blocks: a buffer amplifier, two charge amplifiers and a AM-demodulator. The buffer amplifier sets the gain for the carrier input voltage, the charge amplifiers convert the capacitance changes into the amplitude of the carrier signal, and the demodulator plus low-pass filter ensure removal of the carrier frequency.

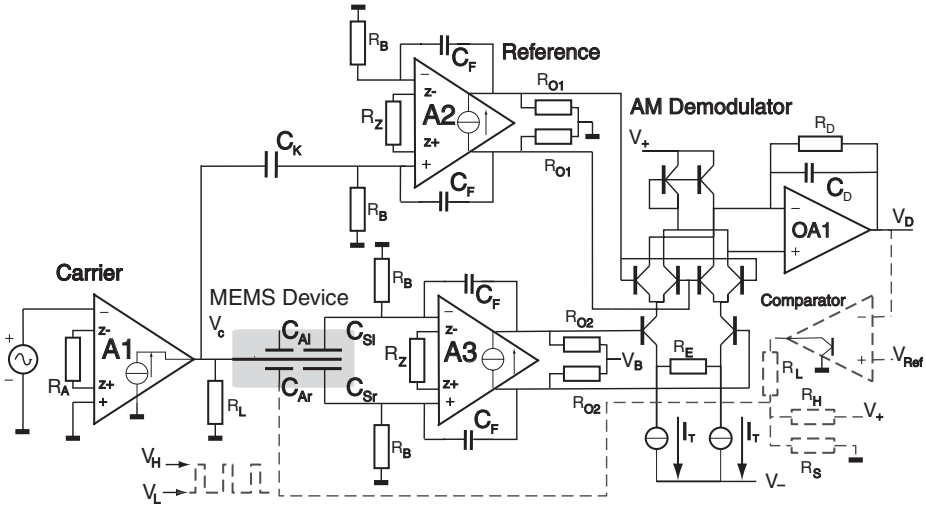

Figure 6.12 Schematic of the differential interface

A sinusoidal carrier voltage with a frequency around 6 MHz is applied to the central common sensing electrode via the buffer amplifier A_1. The carrier frequency is set at a sufficiently high value far beyond the structure mechanical spectrum and thus ensuring that it causes no mechanical movement. The transconductance of A_1 is set by R_A:

$$I_0 = \frac{K}{R_A} V_i \tag{6.7}$$

For a load resistance R_L and K=4 the gain of the amplifier can be expressed as:

$$V_c = \frac{4R_L}{R_A} V_i \tag{6.8}$$

Identical amplifier configurations are used for the differential amplifiers in the measurement and reference channel. The resistors R_B, R_{01} and R_{02} are used for biasing and do not influence the signal path. R_{01} and R_{02} set the common mode voltages of both the output of the amplifiers and the mixer input to zero and V_B respectively. The gain of the charge amplifiers, A_2 and A_3 is given by:

$$V_{02} = \frac{C_K}{C_F} V_c \qquad and \qquad V_{03} = \frac{C_{Sl} - C_{Sr}}{C_F} V_c \tag{6.9}$$

The demodulator is a standard double-balanced mixer converting the displacement carrier signal back to the baseband. The demodulator input voltage is converted into a differential current by R_E and demodulated by switches driven by the A_2 output reference signal. A simple current mirror is used to feed the output current into the opamp OA_1, since the same voltage levels at the input and output of the mirror are kept by the opamp. The mixer baseband gain is set by R_B / R_E.

The bandwidth of the baseband signal is limited by a first order low-pass filter formed by R_D and C_D, resulting in a bandwidth for the displacement measurement system:

$$f_D = \frac{1}{2\pi R_D C_D} \text{ and a typical time delay: } \tau_D = R_D C_D \tag{6.10}$$

A trade-off must be made between the delay in the readout circuit and the noise of the displacement signal by a proper choice of R_D and C_D.

Also the differential sensing approach was implemented at the PCB level. Commercially available transconductance amplifiers [6.19] were used in the high-frequency path. These amplifiers have a gain-bandwidth product of 275 MHz, a typical slew-rate of 800V/µs and good linearity at high frequency differential input voltages. The common mode rejection of the amplifiers is typically 53 dB at 10 MHz, which reduces parasitic coupling of interference to the wires of the actuator. The use of the differential readout scheme suppresses the low-frequency electrical driving signals of the actuation electrodes. The AM-demodulator stage was implemented using a 1496 Motorola demodulator. The bandwidth of the low-pass filter was set at 200 kHz, resulting in total estimated circuit delay of 5 µs.

Both circuit implementations have their specific advantages and the intended application determines the most-suitable approach, single-ended or differential, to be used. The single-ended approach is limited to low-frequencies (due to the characteristics of the charge-amplifier) and is ideal for applications where the structure dynamic behaviour is not relevant, such as static pull-in analysis and low-frequency acceleration measurements. The single-ended readout circuit is a low frequency solution and the DC voltage across the common sensing electrodes is smaller than in the differential approach. The zero setting is also easier in the single-ended circuit (using the gain-setting resistor). A 2 pF trim capacitor is used in the differential circuit, across one of the sensing electrodes, to compensate for the parasitic wiring capacitances.

The differential sensing circuit is more suitable for applications where the device dynamic behaviour is relevant: closed-loop voltage control. The time delay is much smaller than in the single-ended circuit and it has a smaller equivalent noise bandwidth. The differential approach can easily be integrated in a bipolar IC design.

6.4.3 On-Off Method: Experimental Results

Operation of the on-off method has been experimentally verified using the structures shown in Fig. 6.13 (Device 2 type of structures, hermetically sealed and filled with neon at $0.6 \times 10^5 Pa$). The differential readout circuit was used to measure the structure displacement.

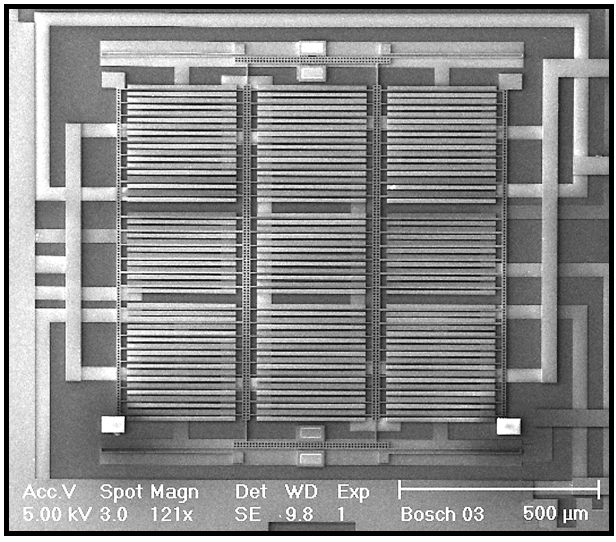

Figure 6.13 A SEM photograph of a Device 2 structure

A comparator was added to the readout circuit and used to close the feedback loop (see dashed components in Fig. 6.12). The voltage V_D, which is proportional to the actuator displacement, is compared to the reference value, V_{Ref}, and the drive feedback signal varies between V_H and V_L according to the comparator output. V_H and V_L are set by:

$$V_H = \frac{R_S}{R_S + R_H} V_+ \qquad and \qquad V_L = \frac{R_S // R_L}{(R_S // R_L) + R_H} V_+ \tag{6.11}$$

The mechanical stoppers limit the actuator displacement up to 2 μm in a 2.25 μm gap. The readout output voltage, V_D, ranges from 0 (zero displacement) until 2.2V (2 μm displacement). At 1/3 of the gap (0.75 μm) the output readout voltage is 0.62V. First, the operational details of the method were verified by measuring the comparator output and actuator displacement at the time the feedback loop is closed. Measured results are shown in Fig. 6.14.

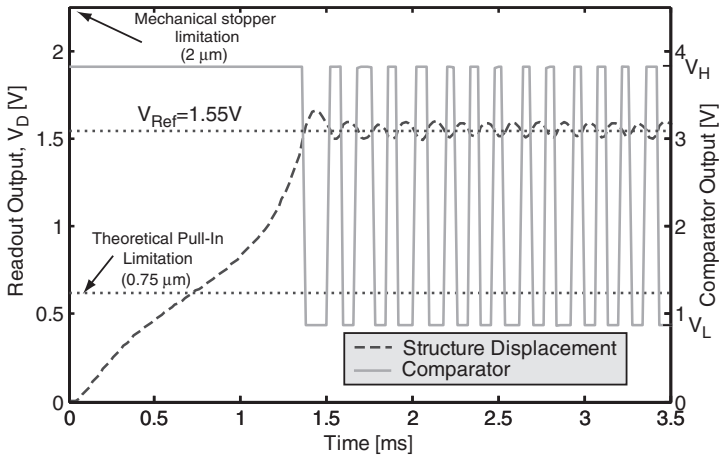

Figure 6.14 Measured operational details of the on-off method

Stable positioning at a voltage selected operated point beyond the static pull-in limitation is achieved and the operation is in agreement with simulations. A few more measurements were performed to check the stability of the method over time and at different reference positions. Stable operation over the full available gap (2 μm) is observed. The results for three different reference points are shown in Fig. 6.15.

Although the stoppers limit operation up to 89% of the gap, there is no fundamental limitation for achieving full range operation with this approach in devices without mechanical stoppers. At very small gaps, the damping force is huge (see Fig. 5.8 in chapter 5) due to the rarefaction effects. Therefore, the damping force slows down the structure displacements even more, thus improving the dynamic device response when

operated with the on-off method. The high damping coefficient at very small gaps is in fact expected to enhance operation.

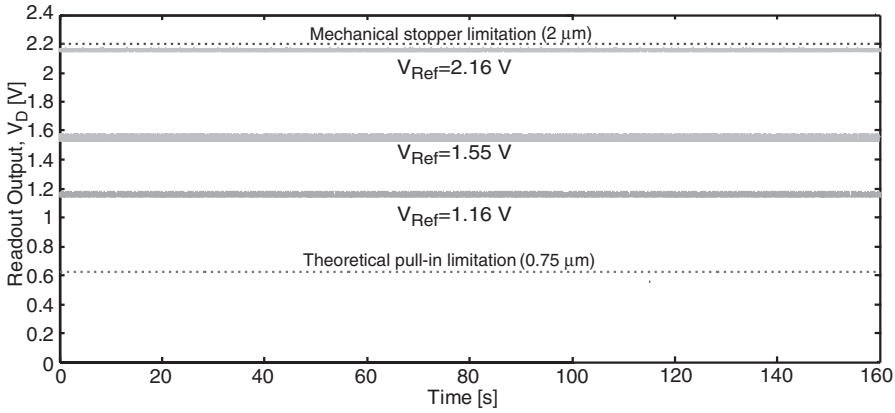

Figure 6.15 Measured voltage-drive stable operation beyond the theoretical pull-in limitation

Finally, the voltage levels were dynamically adjusted to check its influence on the ripple. Results for a reference voltage point, V_{Ref}=1.38V, are shown in Fig. 6.16. The figure clearly shows that the voltage levels are not critical for device operation, but can improve the on-off control approach. For a selected combination of voltage levels the ripple can be limited to about 40mV ($\approx 40nm$), which confirms the effectiveness of the method.

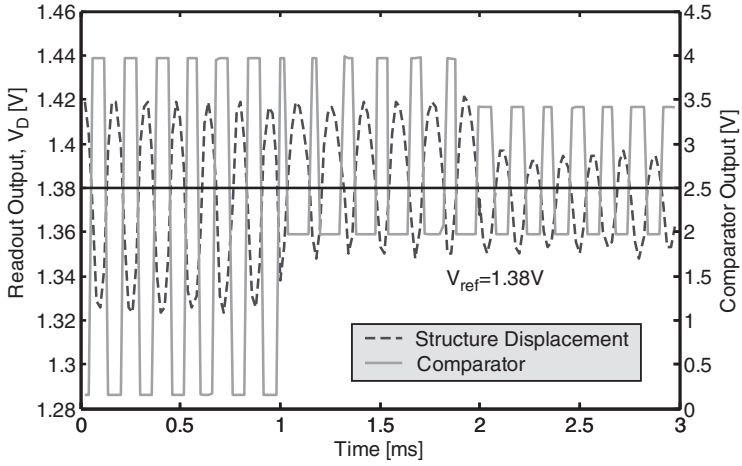

Figure 6.16 Measured changes in ripple amplitude at different voltage levels

6.5 Conclusions

A technique capable of extending the travel range of parallel-plate electrostatic actuators was introduced in this chapter. Displacements up to 89% (limited mechanically) of the full gap have been predicted by modelling and experimentally demonstrated. The simplicity of this approach highly facilitates implementation in parallel-plate based electrostatic actuator systems. Table 6.1 makes a comparison between this method and the methods previously reported in literature.

TABLE 6.1 Comparison between reported methods for extending the range of parallel-plate electrostatic actuators

Method		Maximum displacement	Advantages	Disadvantages
Geometry leverage	[6.3]	Nearly full-gap (≅ 90%)	• Simple • Does not require a sensing mechanism	• Increased actuation voltage • Increased device area
Series capacitance	[6.6]	≅ 65%	• Simple • Does not require a sensing mechanism	• Reduced travel due to parasitic capacitances and residual charge • Increased actuation voltage
Current drive	[6.9]	≅ 65%	• No increase in device area • Does not require a sensing mechanism	• Charge pull-in due to parasitic capacitances • On-board current sources and charge control circuitry • Increased actuation voltage
	[6.10]	83%		
Feedback linearization	[6.13]	74%	• Does not require increased actuation voltage	• Complex • Difficult implementation • Sensing mechanism needed
This work		89%	• Simple • Flexible • 100% travel range if used without stoppers	• Ripple (due to time delay) • Sensing mechanism needed

Voltage drive methods based on feedback linearization should be regarded has an ineffective method to achieve extended travel range due to the high complexity of the approach. The theoretical study performed here shows that the implementation of this method is feasible. However, its use as an actuator where variable outside forces have to be considered is not feasible. When these variable forces act over the structure, they cre-

ate an imbalance between forces that is not taken into account by the linearization function. This last aspect limits the range of applicability of the feedback linearization technique to e.g. variable capacitors.

Charge control methods suffer from the parasitic capacitances present on the MEMS device. Various different current drive methods have been pursued and stable operation up to 80% of the gap has been achieved. The voltage levels required in this case can be up to three times the static pull-in voltage, which can become a limitation in some cases.

The voltage drive method introduced here is very simple. It relies on the device dynamic behaviour and the time delays introduced by the readout circuit are assumed to be small. The simplicity and effectiveness are the strong points of the experimentally proved on-off approach. It presents however two drawbacks: the device must have some kind of displacement sensing mechanism and can not be used for high Q devices. Further studies are needed in order to improve the performance of the on-off method. In the present system, ripples as small as 30 nm over the full available gap have been achieved.

6.6 References

[6.1] Z. Xiao, W. Peng, R.F. Wolffenbuttel and K.R. Farmer, "Micromachined Variable Capacitor with Wide Tuning Range", *in Proc. Solid State Sensor, Actuactor and Microsystems Workshop*, Hilton Head, USA, 2-6 June 2002, pp. 346-349.

[6.2] T.G.S.M Rijks, J.T.M van Beek, P.G. Steeneken, M.J.E Ulenaers, J. De Coster and R. Puers, "RF MEMS Tunable Capacitors with Large Tuning Ratio", *in Proc. MEMS'04*, Maastricht, The Netherlands, 25-29 January 2004, pp. 777-780.

[6.3] E.S. Hung and S.D. Senturia, "Extending the Travel Range of Analog-Tuned Electrostatic Actuators", *J. Microelectromech. Syst.,* 8 (1999) 497-505.

[6.4] E.S. Hung and S.D. Senturia, "Leveraged bending for full-gap positioning with electrostatic actuation", *in Proc. Solid State Sensor and Actuator Workshop*, Hilton Head, USA, 8-11 June 1998, pp. 98-100.

[6.5] J.I. Seeger and S.B. Crary, "Stabilization of Electrostatic Actuated Mechanical Devices", *in Proc. Tranducers'97*, Chicago, USA, 16-19 June 1997, pp. 1133-1136.

[6.6] E.K. Chan and R.W. Dutton, "Electrostatic Micromechanical Actuator with Extended Range of Travel", *J. Microelectromech. Syst.,* 9 (2000) 321-328.

[6.7] J.I. Seeger and S.B. Crary, "Dynamics and Control of Parallel-Plate Actuators Beyond the Electrostatic Instability", *in Proc. Tranducers'99*, Sendai, Japan, 7-10 June 1999, pp. 474-477.

[6.8] L. Castañer, J. Pons, R. Nadal-Guardia and A. Rodríguez, "Analysis of the Extended Operation Range of Electrostatic Actuators by Current-Pulse Drive", *Sensors and Actuators*, A 90 (2001) 181-190.

[6.9] R. Nadal-Guardia, A. Dehé, R. Aigner and L.M. Castañer, "Current Drive Methods to Extend the Range of Travel of Electrostatic Microactuators Beyond the Voltage Pull-In Point", *J. Microelectromech. Syst.,* 11 (2002) 255-263.

[6.10] J.I. Seeger and B.E. Boser, "Charge Control of Parallel-Plate, Electrostatic Actuators and the Tip-In Instability", *J. Microelectromech. Syst.,* 12 (2003) 656-671.

[6.11] P.B. Chu and K.S.J. Pister, "Analysis of Closed-Loop Control of Parallel-Plate Electrostatic MicroGrippers", *in Proc. IEEE Conf. Robot. Automat.*, San Diego, USA, May 1994, pp. 820-825.

[6.12] Y. Sun, D. Piyabongkarn, A. Sezen, B.J. Nelson, R. Rajamani, R. Schoch and D.P.Potasek, "A Novel Dual-Axis Electrostatic Microactuation System for Micromanipulation", *in Proc. IEEE/RSJ Conf. Intelligent Robot. and Syst.*, Lausanne, Switzerland, October 2002, pp. 1796-1801.

[6.13] Y. Sun, D. Piyabongkarn, A. Sezen, B.J. Nelson and R. Rajamani, "A High-Aspect-Ratio Two Axis Electrostatic MicroActuator with Extended Travel Range", *Sensors and Actuators*, A 102 (2002) 49-60.

[6.14] Jean-Jacques E. Slotine, *Applied Nonlinear Control*, Prentice-Hall, Englewood Cliffs, 1991.

[6.15] Katsuhiko Ogata, *Modern Control Engineering, 3rd Ed*, Prentice-Hall, Upper Saddle River, 1997.

[6.16] A. Burstein and W.J. Kaiser, "Mixed Analog-Digital Highly-Sensitive Sensor Interface Circuit for Low-Cost Microsensors", *in Proc. Tranducers'95*, Stockholm, Sweden, 25-29 June 1995, pp. 162-165.

[6.17] M. Lemkin and B.E. Boser, "A Three-Axis Micromachined Accelerometer with a CMOS Position-Sense Interface and Digital Offset-Trim Electronics", *IEEE J. Solid-State Circuits*, 34 (1999) 456-468.

[6.18] J.C. Lötters, W. Olthuis, P.H. Veltink and P. Bergveld, "A Sensitive Differential Capacitance to Voltage Converter for Sensor Applications" *IEEE Trans. Instrum. Meas.*, 48 (1999) 89-96.

[6.19] Maxim Integrated Products, *MAX43x Wideband Transconductance Amplifier Family Datasheet,* Sunnyvale, USA.

7

High-Sensitivity Accelerometer Based on Pull-In Time

7.1 Introduction

This chapter introduces a second application derived from the nonlinear dynamic analysis performed in chapter 5. The high sensitivity of the meta-stable region suggests the use of this region as a measure of small external accelerations [7.1], [7.2]. The idea of using the pull-in phenomena for acceleration sensing is not new and two completely different approaches that use the pull-in have already been proposed [7.3]-[7.5]. One uses the *pull-in voltage* to measure the acceleration changes [7.3], [7.4], while the other proposes the use of the *pull-in time* as the sensing mechanism [7.5]. A brief description of both approaches is given in the next section.

For a proper use of the pull-in time as a measure of the acceleration, the full system configuration must be considered. The nonlinear analysis performed in chapter 5 is used here since it provides the right insight on the device dynamics. All the system aspects are analysed in detail during this chapter with special focus on the analysis of the sensor's system noise. In the final section, an improved design capable of sub-μg resolution is proposed.

7.2 Pull-In Accelerometers

Accelerometers based on the pull-in phenomena have been proposed in literature [7.3]-[7.5]. These approaches differ on the sensing mechanism. While one approach proposes the use of the pull-in voltage to measure the acceleration, the other focuses on the time of a pull-in event to sense the acceleration changes.

7.2.1 Pull-In Voltage Based Accelerometer

The pull-in voltage is a function of the initial capacitor gap which in turn is determined by the acceleration the device is experiencing (the movable electrode has a mass that experiences a force in the case an external acceleration is present) [7.3]. If the device is continuously actuated using a ramped voltage (sawtooth waveform) and the pull-in voltage is measured, the changes in the pull-in voltage are proportional to the external acceleration experienced by the MEMS structure.

The claimed advantage of this approach is the digital output of the sensor. In order to improve the accelerometer performance a differential measurement is proposed in [7.4]. The use of a differential capacitor scheme allows pulling the structure to pull-in at both sides of the capacitor. If this is done alternately, the difference in the pull-in voltages gives the measure of the external acceleration the device is experiencing.

The use of a differential scheme brings a number of advantages. First, the linearity is improved. Second, any drift in time of the pull-in voltage or changes with temperature are cancelled out, which means that no calibration is needed. This is an interesting approach but no reports on actual implementation are available.

7.2.2 Pull-In Time Based Accelerometer

In this approach the dynamic behaviour of the pull-in phenomenon is the fundamental issue [7.1], [7.5]. The operation principle of the device is explained using Fig. 7.1. When pulsed voltages φ_1 and φ_2 are applied to the electrodes 1 and 2 alternately (with voltages higher than the pull-in voltage), the structure pulls in up to the stopper positions 1 and 2 respectively. These originates two pull-in times, T_1 and T_2, corresponding to the travel time between the stoppers 1 to 2 (T_1) and vice-versa (T_2). If no external acceleration is present in the direction of motion, $T_1=T_2=T_0$. If an external acceleration exists, then the differential pull-in time, $\Delta T=T_2-T_1$, is proportional to the acceleration.

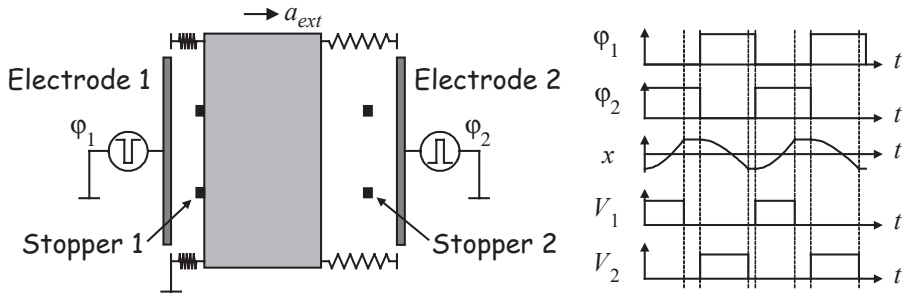

Figure 7.1 Operation principle of the pull-in time based accelerometer (Source:[7.5])

Since ΔT is a pulse-width-modulated signal it can be measured with a digital circuit, giving immediately a digital output. A limitation of this approach is the bandwidth, since bandwidths higher than 14% of the structure resonance are difficult to achieve [7.5].

A different approach also based on the pull-in phenomenon is introduced here. The main idea is to use the high sensitivity of the meta-stable region to measure any external force present during a pull-in event. The measurement principle and all the system considerations are discussed in the next section.

7.3 Measurement Principle

The meta-stability occurs when a step input voltage with a value higher than the static pull-in voltage is applied. Since the duration of the meta-stable region changes with the external acceleration, the pull-in time can be used as a measure of the acceleration. If the structure is constantly actuated with a squared voltage with a period larger than the pull-in time duration, the acceleration is sampled with a frequency equal to the squared-voltage frequency. This implies that the bandwidth of the sensor is half of the sampling frequency (Nyquist's theorem). Although very high sensitivities can be achieved using this method, the sensor bandwidth is small and therefore, the proposed scheme is suitable for low-frequencies accelerations only.

The main advantages of such an approach reside on the digital output and on the simplicity of the readout. Since the physical variable being measured is time, which can be measured with extreme resolution, the sensor resolution can be extremely good. The

main drawback is the low-bandwidth of the system. Since the main application is in high-sensitive accelerometers the low-frequencies limitation is not a severe drawback.

The dynamic pull-in analysis performed in chapter 5 showed that the applied voltage is a very important parameter on the duration of a dynamic pull-in transition. This implies that for proper operation of the pull-in time as a sensing mechanism, the power supply must be very stable and must have a very low noise level. Since small fluctuations of the applied voltage are also reflected in the total pull-in time, the drive signal is the most critical component of the total sensor system. The readout circuit is not as critical as the power supply and a high-frequency clock connected to a digital counter is sufficient. If the counter is started at the time the step input voltage is applied and stopped when the device hits the stopper, or some other trigger mechanism, the total time is given by the counter content with a resolution set by the clock period.

7.3.1 Measurement Results

A 1-DOF device operated in air (Fig. 7.2) was used for the implementation of a pull-in time based accelerometer. A 16 Hz square-wave signal with amplitude αV_{pi} and stability better than 20 μV/day was applied to the MEMS device. This gives as many as 16 samples per second. Since the devices used here are electrically insulated, i.e., the passivation layer that covers the epi-poly movable structure prevents any electrical contact with the stoppers, the measured displacement is used to stop the time counting. A data-acquisition board (DAQ) with a sampling frequency of 100 kHz (the associated uncertainty of the time measurement is 10 μs) connected at the readout's output carries out the counter and trigger functions. A block diagram of the full set-up is shown in Fig. 7.3.

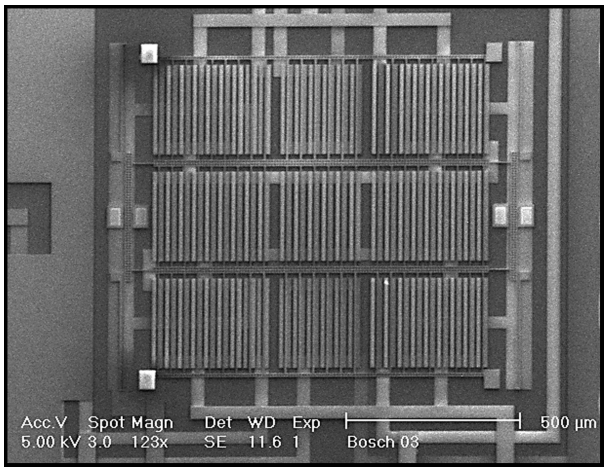

Figure 7.2 Microphotograph of the 1-DOF device used

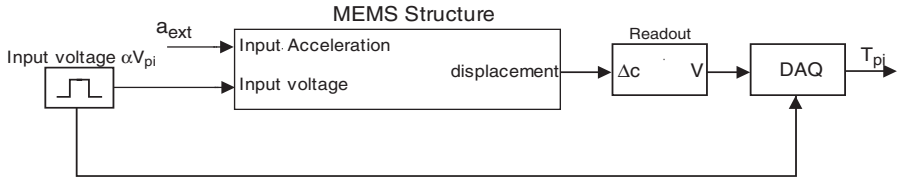

Figure 7.3 Pull-in time accelerometer block diagram

When very small low-frequency accelerations are applied to the device, achieved by rotating the device over small and well-defined angles and using the gravitational force as the external force, the output pull-in time is proportional to the inputted external acceleration. Some measured and simulated results are shown in Fig. 7.4. For a α=1.0003, the sensitivity of the sensor is about 0.5 s/g. Since the time resolution is 10 μs (from the 100 kHz clock frequency) the resolution of the pull-in time accelerometer is at 20 μg. When using the same structure with direct capacitance readout a resolution as small as 0.36 aF would be needed to achieve the same 20 μg resolution.

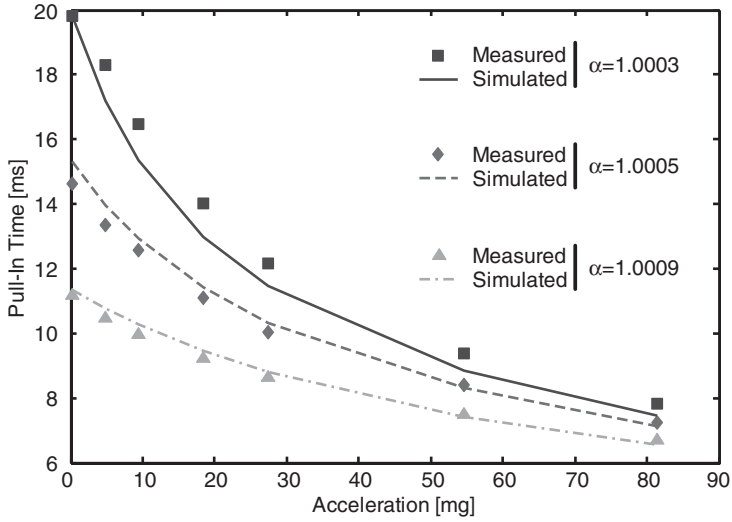

Figure 7.4 Pull-in time changes with voltage step amplitude and external accelerations

A very important issue when dealing with sensors and readout circuits is the total noise of the system, which dictates the detection limit of the sensor. In fact the resolution value of 20 μg is not the sensor limit, as the limitation due to the sensor noise is at a much higher value. A sequence of samples measured at stable temperature, stable α and

constant external acceleration is shown in Fig. 7.5, which illustrates the noise of the sensor system. In what follows a deep analysis to the noise mechanisms with special emphasis on the mechanical-thermal noise of the structure is performed [7.6].

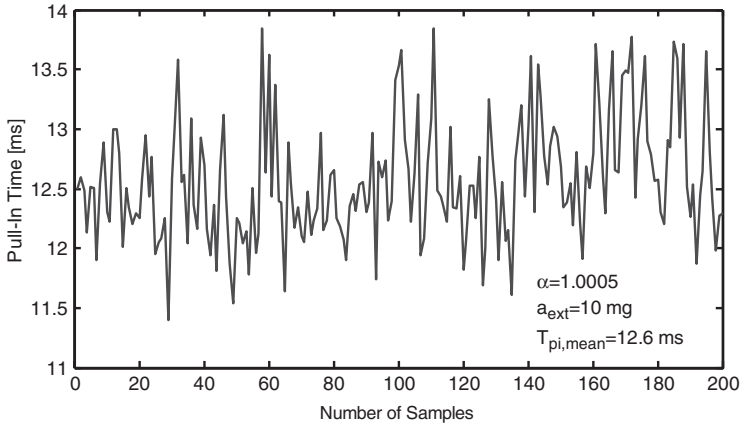

Figure 7.5 Pull-in time noise

7.3.2 Noise Analysis

In a typical sensor system, electronic circuits are used for readout and processing of the electrical signal provided by the sensing element [7.7]. The uncertainty (usually total noise level) of the measurement is therefore due to the combined effect of the mechanical-thermal noise in the mechanical domain [7.8], the electrical noise of the (resistive) mechanical sensing element and the input referred noise of the readout circuits [7.9]. Generally, the circuit noise dominates the noise performance of the system. As a consequence the details of the mechanical-thermal noise are often not considered relevant, and the electronic noise determines the detection limit of the sensor. The use of the pull-in time as a sensing mechanism removes circuit noise as a limiting factor in mechanical noise analysis, since pull-in time depends on force and is not affected by the input referred noise of the readout circuit. The total noise level is in this case due to mechanical-thermal noise of the structure and the non-mechanical noise set by the resolution of the time measurement.

The thermally excited random vibration of charge carriers that is the origin of white noise in an electrical resistor is also applicable to gas damping. The random movement of the molecules in gas at a certain temperature and surrounding the mechanical structure leads to random fluctuations in the energy transfer between structure and damping gas, which is generally referred to as mechanical-thermal noise [7.8], [7.10]. According to [7.8], any mechanical system in thermal equilibrium, no matter how complex, can be

analysed for mechanical-thermal noise by adding a force generator alongside each damper. For a parallel-plate MEMS actuator the general equation of motion, considering a constant damping coefficient, becomes:

$$m\frac{\mathrm{d}^2 x}{\mathrm{d}t^2} + b\frac{\mathrm{d}x}{\mathrm{d}t} + kx = ma_{ext} + F_{elect}(x, V) + F_{noise}(b), \tag{7.1}$$

where $F_{noise}(b)$ represents the random contribution of the different noise generating processes. Because a thermal equilibrium between the MEMS device and the surroundings is assumed, the energy lost towards the environment through the dissipative friction (damping coefficient) must equal in average the energy gained through the noise force. The Nyquist's theorem [7.8], relates the spectral density of the noise force to mechanical resistance (damping coefficient):

$$F_{noise} = \sqrt{4k_B T b} \qquad [N/\sqrt{Hz}], \tag{7.2}$$

where k_B is the Boltzmann's constant (1.38×10^{-23} J/K) and T is the absolute temperature. The theorem remains valid in case of a non-linear and frequency dependent damping, which is the case in a typical MEMS [7.2].

The essential sub-systems in the sensor system depicted in Fig. 7.3 are: the power supply, the microstructure, the readout circuit and the DAQ (timer). Variations in pull-in time may result from any of these sub-systems and therefore, they need to be investigated to verify whether they significantly affect the uncertainty of the pull-in time:

1. *Power supply*: pull-in time depends strongly on the voltage applied. Moreover, this voltage needs to be tuned very precisely to a value slightly higher than V_{pi}. The power supply used (Yokogawa 7651) has a stability specified to be better than 20 μV/day and a noise level at 16 μV for a 10 kHz bandwidth. Since these noise specifications are incomplete (no 1/f noise mentioned) the power supply was sampled with a frequency of 0.5 Hz by a 1 μV resolution multimeter and the results are shown in Fig. 7.6. These measurements confirm both the power supply stability and the low noise levels and therefore the power supply noise can be neglected as compared to the mechanical-thermal noise of the MEMS device. If the power supply used on the system does not have the right noise characteristics it can easily be the dominant noise source and in this case, can not be neglected.
2. *MEMS device*: the mechanical structure is expected to be the main noise source of the system. Due to the high-sensitivity of the meta-stable region, the time-output is a measure for the noise force. A convenient property of pull-in time measurements is the time averaging of high-frequency components in the noise force, which consequently do not contribute to variations in the displacement. Only fre-

quencies lower than $2/t_{pi}$ are present during the full pull-in movement [7.1]. This property limits the noise spectral frequency range measured. This is not a problem since the interesting features are in the low frequency part. The total noise force is therefore:

$$F_{noise} = \sqrt{\frac{8k_B Tb}{t_{pi}}} \qquad [N] \tag{7.3}$$

3. *Front-end electronics*: the function of the readout circuits is to provide sufficient gain for the pull-in time to serve as a gating signal in a counter. Due to the specifics of the MEMS structure the measurement of the capacitance changes is used as the trigger mechanism. The differential capacitive single-ended approach (see section 6.4.2.1 in chapter 6) was used to measure the displacement of the fabricated MEMS device. The circuit has a measured output white noise level at $188nV/\sqrt{Hz}$. Noise bandwidth is 4.8 kHz (imposed by the 4th order low-pass filter), which results in a total noise of the readout circuit of about 13 mV. The slew rate at the final phase of the pull-in transition is of sufficiently high value to allow the circuit equivalent input noise to be disregarded. The rate change of displacement vs. time exceeds 10 mV/μs, which allows for the selection of trigger levels in such a way that the uncertainty due to readout circuit noise is smaller than the quantization noise of the 10 μs sampling.

4. *Data-acquisition board (DAQ)*: the DAQ is responsible for the acquisition of the voltage equivalent displacement and for measuring pull-in time. The sampling frequency, f_s=100 kHz, introduces an uncertainty in the measured pull-in time of 10 μs in the form of quantization noise.

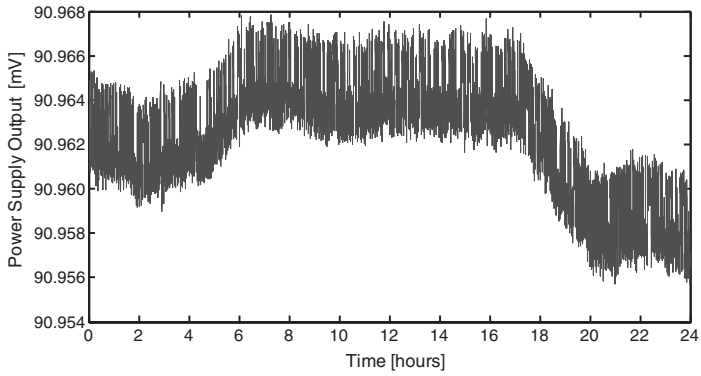

Figure 7.6 Power supply noise measured at 28±1^{0}C

According to the previous noise analysis, the main noise source is the mechanical-thermal noise of the MEMS device. The analysis suggests that the mechanical-thermal noise is setting the detection limit of the pull-in time based accelerometer and therefore can be measured. In a typical mechanical sensor system, circuit noise dominates the noise performance of the system and estimations of the mechanical-thermal noise are made from the total sensor noise by a careful analysis or selective measurement of the electrical noise [7.11]. Here, the detection limit is imposed by the mechanical-thermal noise of the structure.

For a better understanding of the mechanisms beyond the mechanical-thermal noise, measurements were performed on one fabricated 1-DOF device (Fig. 7.2) with air at atmospheric pressure (1 bar) as the surrounding gas medium for the duration of one day. A square wave input voltage with 5 Hz and amplitude α=1.0008 was used. The measuring setup was introduced in a climate chamber at a temperature of 30±1ºC and care was taken to minimise external acceleration. The time series of the measured pull-in times is presented in Fig. 7.7.

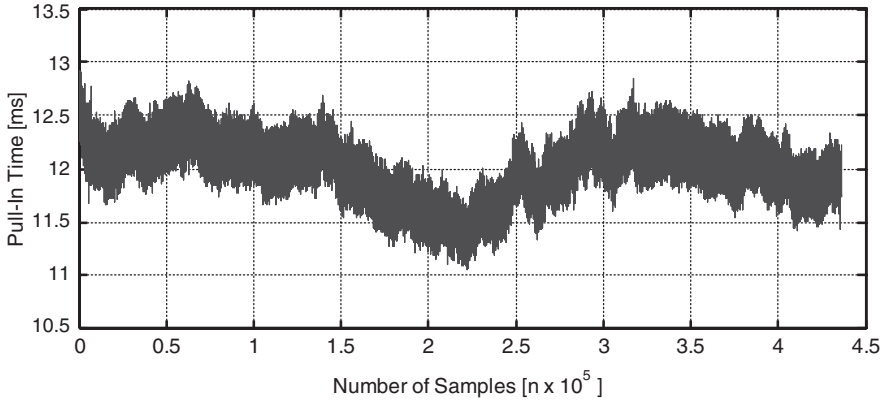

Figure 7.7 Time series of measured pull-in times at 1 bar

Since the sensitivity of the sensor to external accelerations can be computed through simulations, the measured time-changes can be directly translated to the momentary value of the equivalent force. In the absence of any time-varying external acceleration, this force is due to the momentary value of the mechanical-thermal noise. A sensitivity of S = 0.0165 s/m.s^{-2} for a α=1.0008 is computed when the large-signal model of the 1-DOF structure is used. The average value of the pull-in time is $t_{pi,\,mean} = 12ms$ and the standard deviation (noise value) is: $\sigma_{pi} = 112\mu s$ (for 500 samples). The equivalent noise acceleration can be calculated as: $a_n = \sigma_{pi} / S = 6.8\times10^{-3}$ m.s^{-2} and the total

measured noise force becomes: $F_n = m.a_n = 2.9\times10^{-11}$ N. Eqn. (7.3) can be used for computing the total noise force to verify the experimental result. A complication results from the damping coefficient, which is, amongst others, depending on the momentary gap width during pull-in motion and thus is not constant during the pull-in event. However, the movable electrode spends most of its time around the static pull-in displacement (meta-stable region), which justifies the use of a constant damping coefficient calculated at $(x_{pi} = (1/3)d_0)$. For air at atmospheric pressure as the gas medium a damping coefficient value of $b = 1.92 \times 10^{-4}$ Ns/m is computed (see Eqn. (5.13) in chapter 5). For a pull-in time of 12 ms, the predicted equivalent input total noise force given by Eqn. (7.3) is: $F_n = 2.3 \times 10^{-11}$ N. The sensitivity S can also be used to evaluate the significance of the noise sources introduced by the other system components. The 10 μs uncertainty of the DAQ can be converted to a noise force and the total predicted white noise level increases to: $(10 \times 10^{-6} m)/S + 2.3 \times 10^{-11} = 2.56 \times 10^{-11}$ N, which is in good agreement with the measured value. These measurements confirm the noise analysis made to the pull-in time sensor system and clearly show that the mechanical-thermal noise is indeed setting the detection limit of the system.

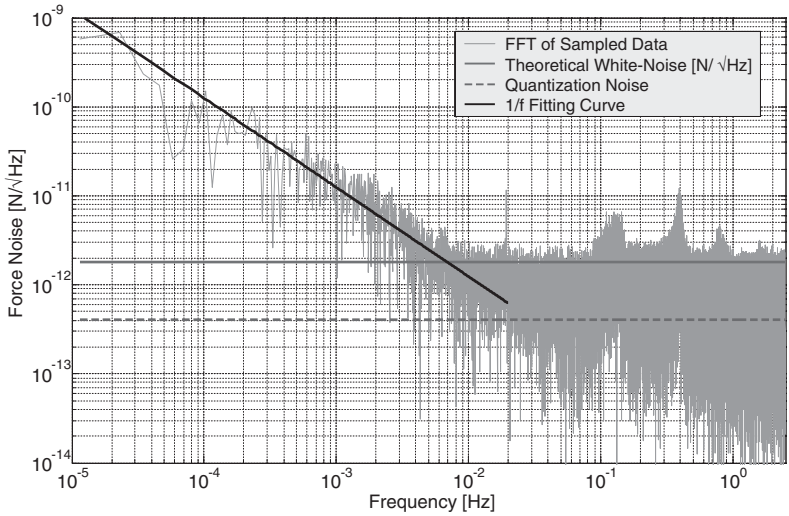

Figure 7.8 FFT of the sampled pull-in time at 1 bar

More interesting conclusions can be retrieved after taking the FFT of the measured data. The result of a FFT on the series of pull-in time measurements in Fig. 7.7 is shown in Fig. 7.8. The curve is calibrated in terms of noise spectral density by correcting for

bandwidth. The most significant properties are the agreement with the theoretical mechanical-thermal white noise spectral density and the increasing noise spectral density with decreasing frequency. The latter observation strongly suggests the identification of the 1/f noise in the micromechanical domain. Since 1/f noise is demonstrated in all physical domains this is not unexpected, however this is to our knowledge the first time it has been experimentally confirmed in the MEMS field. The 1/f noise-white noise cross-over frequency is at the surprisingly low value of 0.007 Hz. Consequently, some caution seems justified before claiming that this is indeed the 1/f noise originating from the MEMS and additional experiments were performed.

7.3.2.1 1/f Noise

The so called 1/f noise is characterised by a noise spectral power $P(f) = 1/f^{a}$, where the exponent a is very close to 1 [7.12], [7.13]. There is no generally accepted explanation for the 1/f noise and the theories used to explain the phenomenon are usually valid in case very specific conditions are met and in a specific physical domain only. For this reason 1/f noise is not well understood. This state-of-the-art is not helpful in interpreting Fig. 7.8.

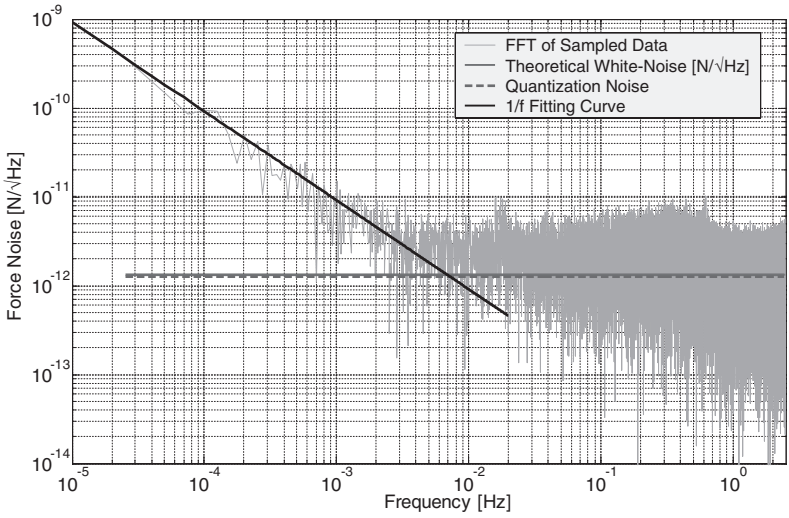

Figure 7.9 FFT of measured samples at 200 mbar

Additional measurements were therefore performed to support the claim that the 1/f noise originates from the mechanical structure. The FFT of the time series of the pull-in time measurements at a pressure of 200 mbar (α=1.002) is presented in Fig. 7.9. Theory on mechanical-thermal white noise predicts a noise spectral power proportional to

damping and thus a noise per square root of hertz reducing with pressure. However, also pull-in time reduces with pressure and therefore sensitivity decreases. For short pull-in times and low sensitivities the quantization noise tends to be the dominant noise source. For the particular case of the 200 mbar measurements the quantization noise is in the same order of magnitude of the predicted white noise per square root of hertz and consequently the measured white noise per square root of hertz has an higher value as compared to the previous 1 bar measurement. These considerations are all confirmed by the data in Fig. 7.9. Moreover, and most significantly, the asymptotic best fit for the 1/f noise does not shift over the spectrum, which suggests that the measured 1/f noise indeed originates from the mechanical structure and is independent of the air damping.

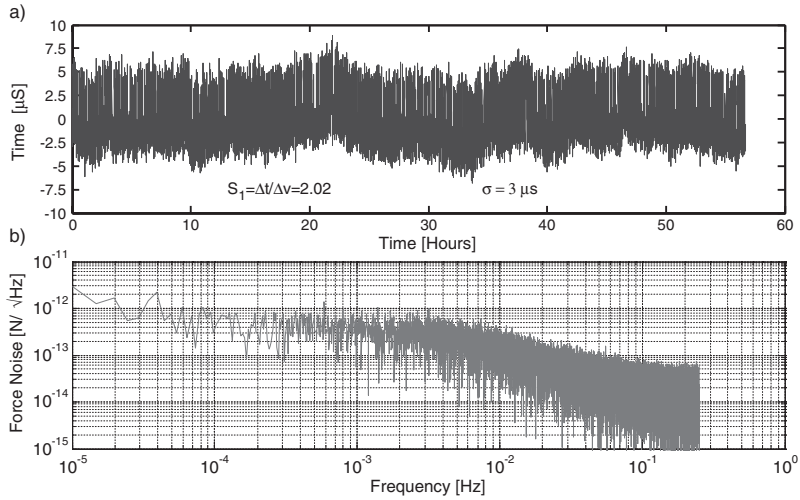

Figure 7.10 Samples of the power supply at constant temperature. a) time series and b) FFT

Additional data is needed to conclusively dismiss the power supply as the source of the 1/f noise. The power source was again sampled at constant temperature, but this time during 50 hours (Fig. 7.10a) with a 1 μV resolution and a sampling frequency of 0.5 Hz. The sensitivity of the pull-in time with respect to the applied voltage can be computed through simulations. A value of $S_1 = \Delta t/\Delta V = 2.02$ is found when the large-signal model is used. The time noise due to the voltage noise can than be translated to a total noise force: $F_n = \frac{(\sigma.S_1)m}{S} = 16\times10^{-13}$ N which is almost a factor 20 smaller than the measured force noise of the MEMS, $F_n = m.a_n = 2.9\times10^{-11}$ N (assuming the same operation conditions apply). The FFT of the sampled data is shown in Fig. 7.10b. The data is

expressed in terms of equivalent force noise and directly comparable with the data of Fig. 7.8 (noise force). The noise force caused by the power supply is indeed very small and can be neglected, which implies that the origin of the 1/f is not the power supply.

7.3.3 Large Dynamic-Range Accelerometer

When one looks to the output of the pull-in time based accelerometer shown in Fig. 7.4, two problems that can compromise a real application are observed: the sensitivity is highly nonlinear and the operation range is very small (about 100 mg for the structure used during experiments). The nonlinearity is not really a problem since it can be mathematically described and therefore can be corrected for. The limited range problem is not as simple but some techniques can be used to increase the operation range without losing the high-sensitivity.

A very important pull-in characteristic with potential to increase the range of the sensor is introduced here: a constant input acceleration acts as an extra force and changes momentarily the static pull-in voltage. Basically, the presence of an extra force (in this case caused by an external acceleration) changes the static pull-in voltage. Using the equilibrium of forces approach this new pull-in voltage is calculated as:

$$V_{pi} = \sqrt{\frac{8}{27}}\frac{(kd_0 + ma_{ext})}{k}\sqrt{\frac{kd_0 + ma_{ext}}{C_0 d_0}} \tag{7.4}$$

If a sensing interval is defined (e.g. 100 mg) and the voltage is changed (i.e. increased) every time the acceleration becomes higher than the maximum of the defined interval, the high-sensitivity is maintained (using a constant α). The change of the pull-in voltage allows keeping the sensor operating in the high-sensitive region for different acceleration levels. Since the changes in acceleration are slow (assuming a low acceleration measurement), it is possible to change the voltage amplitude fast enough to maintain operation within the nonlinear sensitive region.

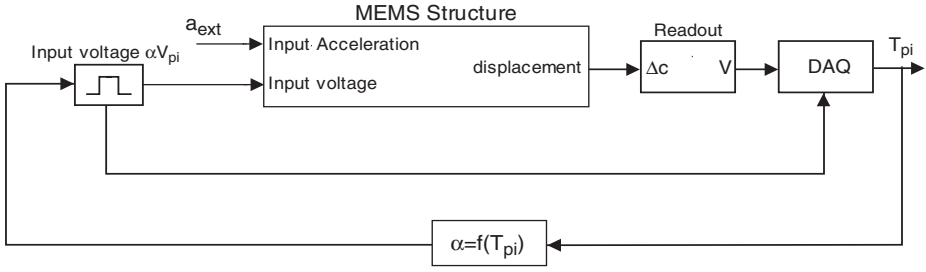

Figure 7.11 Block diagram of the high-range pull-in time accelerometer

A diagram of the proposed increase range method is illustrated in Fig. 7.11. A feedback loop is introduced so that the voltage step amplitude can be a function of the measured pull-in time (acceleration). This scheme keeps the measured time-interval constant, while the total acceleration is the current measured value added to the correspondent interval acceleration.

The nonlinearity of Eqn. (7.4) represents a problem to the proposed scheme. If the changes in pull-in voltage due to an external acceleration are simulated, the graph of Fig. 7.12a is obtained. The changes are nonlinear but if an approximation to a second order polynomial (simpler than the expression of Eqn. (7.4)) is used, the errors are negligible (Fig. 7.12b). This polynomial approximation can be used to extract the correct value of α for the defined intervals. The voltage step amplitudes for an interval of 100 mg considering a pull-in time accelerometer based on the 1-DOF MEMS structure were computed and are presented in Fig. 7.12a. The resulting accelerometer system has a range of 500 mg, a resolution set by the clock frequency and a detection limit due to mechanical-thermal noise of $a_n = F_n/m = 680\mu g$.

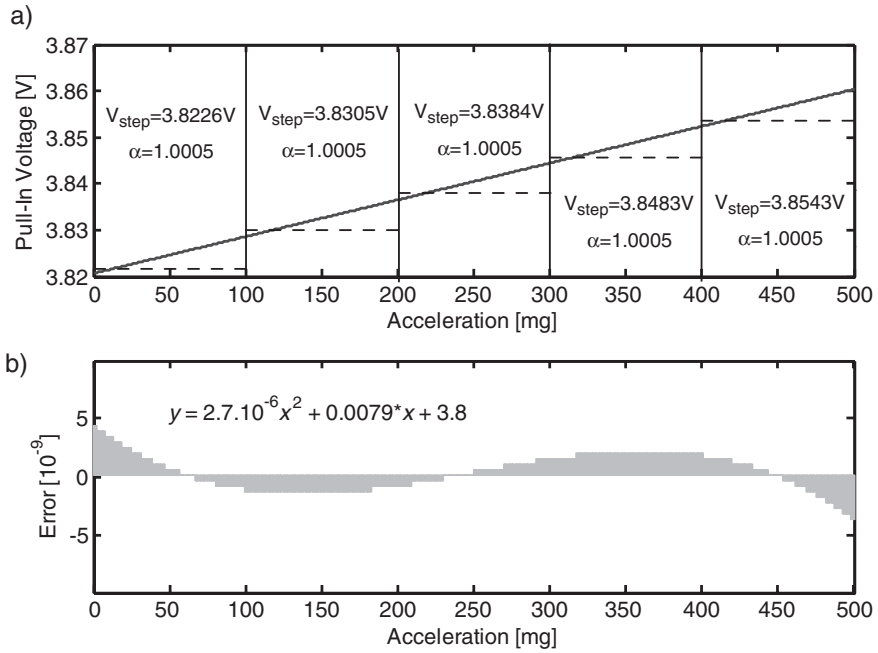

Figure 7.12 Pull-in voltage changes with an external acceleration. a) theoretical changes and b) errors due to a 2nd order polynomial approximation

7.4 Improved Design

High precision micro-accelerometers are needed in an increasing number of applications, including microgravity surveys, geophysical sensing, GPS-augmented navigation and spacecraft guidance/stabilization [7.14]. A pull-in time based accelerometer has the potential to compete with more conventional accelerometers [7.9], [7.11] in a high number of these applications. Present Bosch fabricated devices can not achieve the desired sensitivity/resolutions. First we investigated if an improved design with the needed specifications is feasible in the Bosch process.

The detection limit in a pull-in time based accelerometer is set by the mechanical-thermal noise of the MEMS structure. There are two ways to reduce the total equivalent acceleration noise: reduction of the damping coefficient or mass increase. Reducing the damping coefficient (by decreasing the pressure) is not really an option since a Q factor lower than 1.2 is needed in order to use the meta-stable region. Therefore, an increase in mass is essential to set a detection limit on the μg range.

The mechanical-thermal noise of the device is setting the detection limit and therefore the starting point for an improved design is to set the desired detection limit. Most of the applications mentioned in the beginning of the section need sub-μg resolutions and so, the new design will aim to have an equivalent acceleration noise at $a_n = 0.5\mu g/\sqrt{Hz}$. If a Q factor of 1 is considered the damping coefficient is given by:

$$b = \sqrt{km}, \tag{7.5}$$

and the total equivalent acceleration noise becomes:

$$a_n^2 = \frac{4k_B T\sqrt{km}}{m^2} \tag{7.6}$$

It we assume a realistic value of k=1 N/m for the spring constant a first rough value for the desired mass of the structure is found: m=0.78 mg. A mass value of 0.78×10^{-7} kg is quite a huge mass value for a MEMS structure fabricated in a surface micromachining process. The 1-DOF structure used in this section, fabricated in the Bosch process is already at the size limit allowed by the technology and has a mass of 4.27×10^{-9} kg. For a sub-μg detection limit, a structure with a mass 2 orders of magnitude larger than the ones achieved with the Bosch process is needed, which means that a different MEMS fabrication technology has to be used.

A technology based on Cryogenic SF_6/O_2 Plasma Etching [7.15], [7.16] was used for the fabrication of the improved devices. This technology uses crystalline silicon and allows thicknesses in excess of 50 μm. With this technology the lateral dimensions can be made extremely small while keeping the large vertical size due to the high anisotropy. Structures with a total mass within the desired order of magnitude are therefore possible.

The fundamental process step is the SF_6/O_2 high density Inductively Coupled Plasma (ICP) etching at cryogenic temperatures. The etching process has high etch rates, no polymer contamination, small sidewall roughness and is a single step process. The crystal orientation dependence, at low temperatures, results in strong limitations in simultaneously etching trenches and open structures [7.17]. However, trench based devices can be successfully fabricated [7.18]. Due to the etch rate and profile dependence of the deep plasma etch on the feature size, special attention has to be given to the design to achieve a good result.

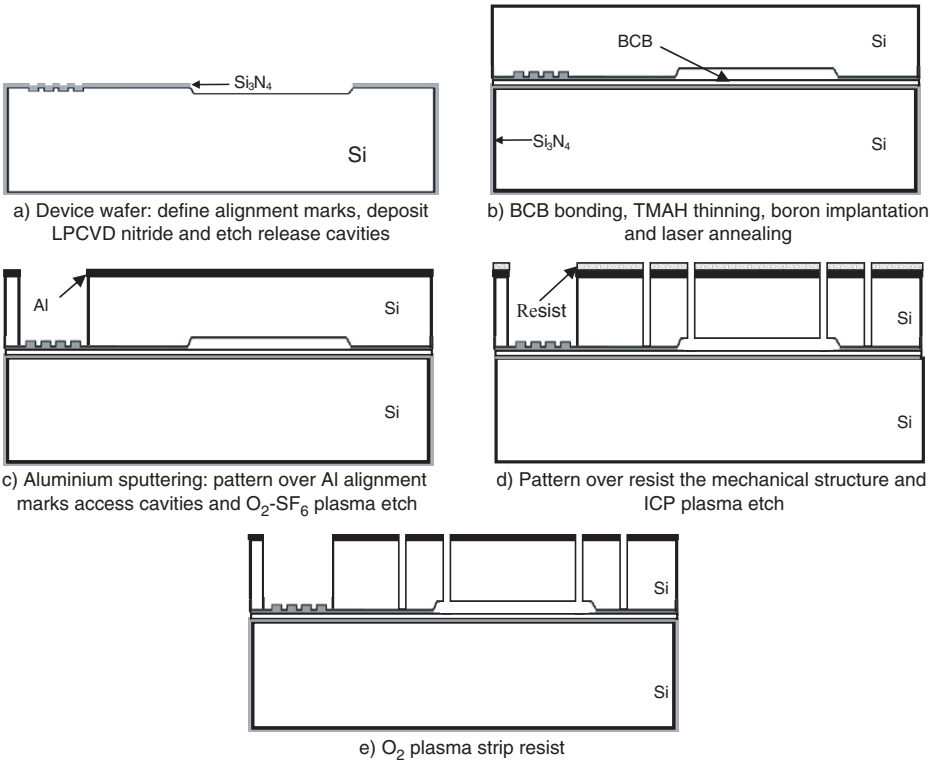

a) Device wafer: define alignment marks, deposit LPCVD nitride and etch release cavities

b) BCB bonding, TMAH thinning, boron implantation and laser annealing

c) Aluminium sputtering: pattern over Al alignment marks access cavities and O_2-SF_6 plasma etch

d) Pattern over resist the mechanical structure and ICP plasma etch

e) O_2 plasma strip resist

Figure 7.13 Schematic process flow (Source:[7.16])

The fabrication process flow for device fabrication is shown in Fig. 7.13 and requires only two masks for defining the mechanical structure. It involves a Si wafer containing the release cavities and a handling Si wafer. The wafers are bonded using dry etch BCB. After bonding the device wafer is thinned using 25% TMAH (Tetra-Methyl-Ammonium Hydroxide) wet etching at 85^{o}C (etch rate ~ 36 μm per hour). The device electrical contacts are on top of the handling wafer and obtained by aluminium sputtering. An ion implantation step is needed, followed by laser annealing for dopants activation to improve the metal silicon contact. The mechanical structure is defined using deep trench silicon dry etch with cryogenic SF_6/O_2 ICP process. Finally, the microstructures are released by etching BCB using O_2/SF_6 (90%-10%) plasma. The different parts of the structure are electrically isolated using trenches.

The step by step description of the process flow is as follows:

1. Process alignment marks on the device wafer.
2. Deposit LVCVD (Low-Pressure Chemical-Vapour-Deposition) silicon nitride (Si_3N_4) on the device and handling wafer.
3. Pattern cavities for the mechanical structure.
4. Wet etching using 85^{o}C 25% TMAH.
5. Deposition of BCB on the handling wafer and bonding of the wafers using the procedure described in [7.16].
6. Thinning of the device wafer to the desired thickness (50 μm) using 25% TMAH wet etching at 85^{o}C.
7. Boron implant: 5KeV, $10^{15}/cm^2$ using BF_2 gas source.
8. Laser annealing with an energy of 900 mJ/cm^2.
9. Sputtering of aluminium (Al) at room temperature.
10. Patterning of the alignment marks access cavity over aluminium.
11. SF_6/O_2 anisotropic plasma etching using ICP cryogenic process for the alignment marks access cavity. The etch stops at the silicon nitride layer.
12. Patterning of the mechanical structure over the deposited 2μm Shirpley SPR 3017 resist.
13. Etching of the Al windows for the mechanical structures using $N_2/Cl_2/BCl_3$ RIE (Reactive Ion Etch) plasma.

14. Baking of the resist at 100^{o}C during 30 min.
15. Mechanical structures etching using the baked resist mask. SF6/O2 anisotropic plasma etching using ICP cryogenic process is used. The etch stops at the BCB layer.
16. Release of the mechanical structure by striping the resist and BCB. O_2/SF_6 (90%-10%) plasma is used.

The process is fully compatible with CMOS technology which means that integration with any desired signal processing electronics is possible. The electronics interconnections with the mechanical structure and bondpads can be processed on the device wafer before defining and etching the release cavities. Since BCB can be deposited in thick layers, no extra planarization step is needed.

An improved pull-in time based accelerometer was designed for the described technology. The designed structure has 1-DOF, similar to the 1-DOF fabricated Bosch devices, two actuation arms (in a middle position) and a set of differential sensing capacitors (the displacement detection as to be done by sensing the changes in these capacitors). Due to the high thickness of the mechanical structure (50 μm), a reduced number of arms, as compared to the Bosch designs, is used. Nevertheless, the damping values are similar (the capacitor surface is higher) and the border-effects are here almost negligible. A 3D drawing of the designed structure is shown in Fig. 7.14.

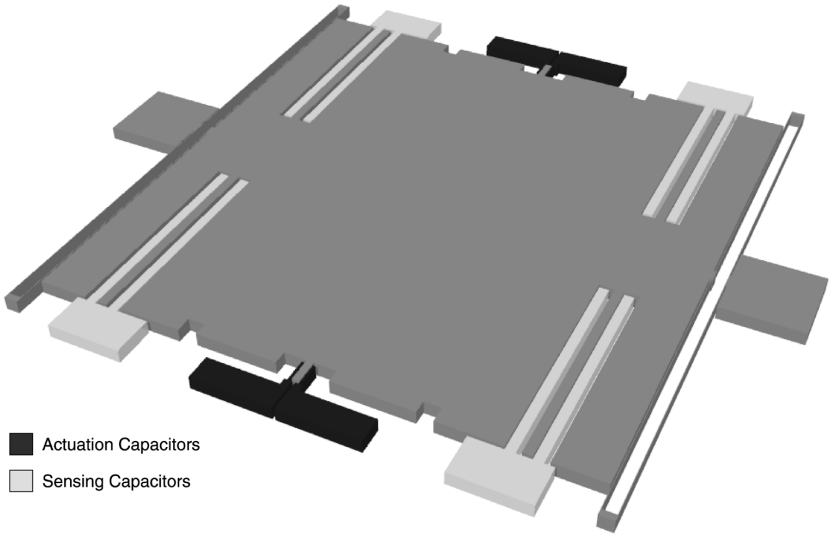

Figure 7.14 3D drawing of the improved pull-in accelerometer

The main device feature is the 0.44 mg seismic mass, defined by a 2x2 mm^2 surface area which is anchored through 4 folded beams. The beams are 2.8 μm wide and 1100 μm in length with a thickness of 50 μm. Stoppers located on the seismic mass and close to the folded beams, 1.75 μm apart prevent the electrodes to touch when pull-in is reached. The main device features are presented in Table 7.1. As shown, the mass is within the desired order of magnitude. The mechanical spring is lower than the assumed 1 N/m in order to increase the sensitivity and to maintain a Q lower than 1.2 (due to the larger damping coefficient given by the extended length of the sensing arms).

The choice for the design of a structure with 1-DOF, instead of a 2-DOF device, was instigated by the simplicity of the design and by the more efficient 1-DOF dynamic model (used to predict device performance). An accelerometer based on the 2-DOF inverted pendulum is expected to have a higher quality factor (lower damping coefficient) as compared to the 1-DOF when operated with the same conditions. Since the goal here is not to get a lower damping coefficient, the 1-DOF was the natural choice for the design.

TABLE 7.1 Main parameters of the pull-in accelerometer

Fixed Parameter	Value
Mechanical spring (k)	*0.28 N/m*
Mass (m)	*0.44 mg*
Resonance frequency (f_0)	*126 Hz*
Initial gap distance(d_0)	*2 μm*
C_{d0} (zero-displacement actuation capacitor)	*35.4 fF*
C_{s0} (zero-displacement sensing capacitor)	*400 fF*
Damping coefficient (b) $(x = x_{pi})$	5.81×10^{-4} *Ns/m*
Mechanical-thermal noise $(a_n = \frac{\sqrt{4k_BTb}}{m})$	*0.7* $\mu g/\sqrt{Hz}$
Pull-in voltage (V_{pi})	*3.063 V*

A large-signal model for this device was constructed and implemented in Simulink. The difference in length of the arms used for the actuation and sensing capacitors have led to two squeeze-film models. The total damping coefficient is the sum of the two

damping coefficients (given by the actuation and sensing arms). The step response of the device to a voltage amplitude of α=1.001 is shown in Fig. 7.15. The sensitivity to external accelerations (100 μg range) for the same value of α can be seen in Fig. 7.16.

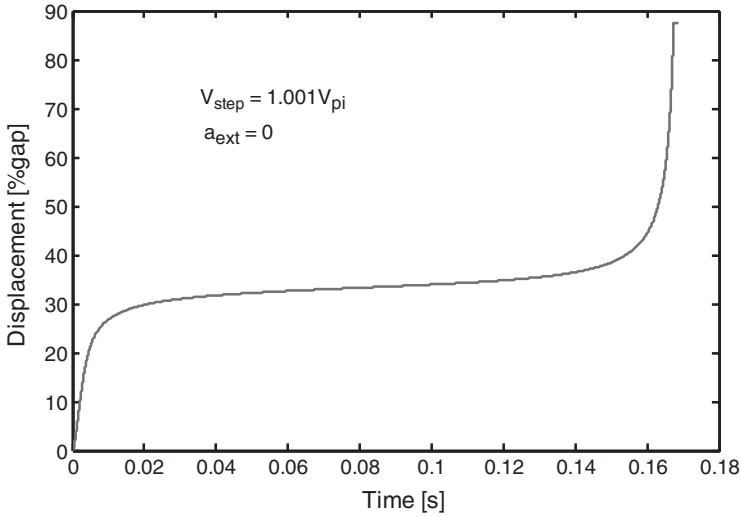

Figure 7.15 Step response of the improved device

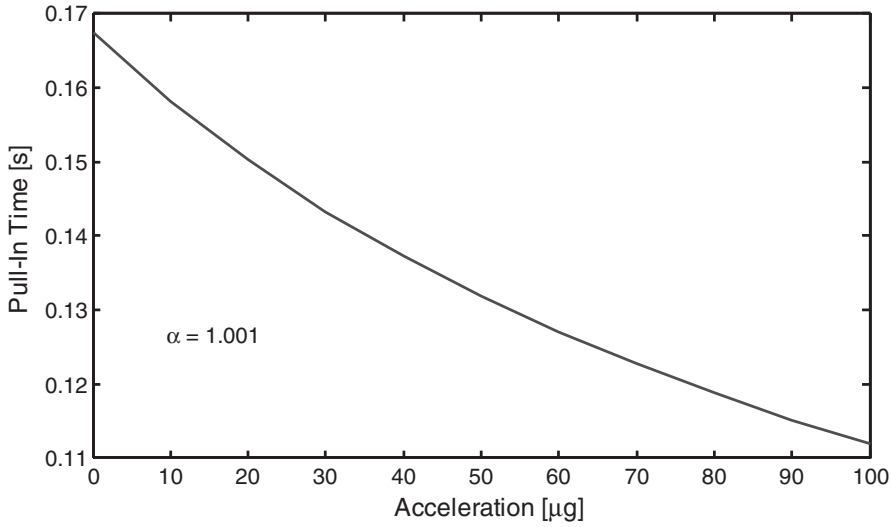

Figure 7.16 Pull-in time changes with external acceleration

No working devices are available at the moment due to technological problems. The process is relatively new and some process steps are still in an optimization phase. Since no fabricated devices are available, experiments on actual devices can not be reported. However, the devices are expected to have a mechanical-noise on the sub-μg range, $0.7\mu g/\sqrt{Hz}$. When dynamically operated sensitivities in the order of 1 ms/μg (α=1.001) and a 2 Hz bandwidth should be feasible. The range of the device can be set accordingly to the desired application by using the feedback control loop proposed in the previous section.

7.5 Conclusions

A high-sensitivity pull-in operated accelerometer has been proposed in this chapter. The advantages are the simplicity of the approach and on the time measurement. The readout circuits can be very simple and the time measurement enables a digital output. The technique has been validated using non-optimised devices and the detection limit is set by the mechanical-thermal noise of the MEMS structures.

A complete noise analysis to the sensor system was performed in this chapter. The high-sensitivity of the meta-stable region is ideal for mechanical-thermal noise measurements. The results are reproducible for devices fabricated in the same process and the same run and show a spectral density depending on the pressure of the surrounding damping air. The 1/f noise spectral density is found to be independent of ambient gas pressure and reproducible for devices fabricated in the same process and the same run. The 1/f noise-mechanical-thermal white noise cross-over frequency is at 0.007 Hz in case of air at 1 bar surrounding the microstructure.

The advantage of the high sensitivity of the meta-stable region has been demonstrated and has yielded a very useful tool to study fundamental MEMS noise mechanisms. The mechanical-thermal white noise measured is in agreement with existing theory on damping and mechanical-thermal noise. The measurements are not conclusive with respect to the identification of the MEMS as the source of the 1/f noise, however leads to a sufficient level of confidence to draw preliminary conclusions.

An optimised design based on a single step IC-compatible process has been presented. No fabricated devices are reported, but the robustness and accuracy of the dynamic model used suggest that devices with a very low noise level and a very high sensitivity, ideal for low-acceleration and low-frequencies measurements are feasible.

7.6 References

[7.1] L.A. Rocha, E. Cretu and R.F. Wolffenbuttel, "Pull-In Dynamics: Analysis and Modeling of the Transitional Regime", *in Proc. MEMS'04*, Maastricht, The Netherlands, 25-29 January 2004, pp. 249-252.

[7.2] L.A. Rocha, E. Cretu and R.F. Wolffenbuttel, "Behavioural Analysis of the Pull-in Dynamic Transition", *J. Micromech. Microeng.*, 14 (2004) S37-S42.

[7.3] W.C. Tang, *Digital Capacitive Accelerometer*, US Patent 5353641, 11 October 1994.

[7.4] W.C. Tang, *Digital Capacitive Accelerometer*, US Patent 5447068, 5 September 1995.

[7.5] H. Yang, L.S. Pakula and P.J. French, "A Novel Pull-In Accelerometer", *in Proc. Eurosensors XVII*, Guimarães, Portugal, 21-24 September 2003, pp. 204-207.

[7.6] L.A. Rocha, E. Cretu and R.F. Wolffenbuttel, "Mechanical-Thermal and 1/f Noise in MEMS Devices", i*n Proc. MME'04*, Leuven, Belgium, 5-7 September 2004, pp. 100-103.

[7.7] R.F. Wolffenbuttel, *Silicon Sensors and Circuits; On-Chip Compability*, Chapman and Hall, London, 1996.

[7.8] T.B. Gabrielson "Mechanical-Thermal Noise in Micromachined Acoustic and Vibration Sensors", *IEEE Trans. Electron Devices*, 40 (1993) 903-909.

[7.9] B.V. Amini, S. Pourkamali and F. Ayazi, "A High Resolution, Stictionless, CMOS Compatible SOI Accelerometer with a Low Noise, Low Power, 0.25 μm

CMOS interface", *in Proc. MEMS'04*, Maastricht, The Netherlands, 25-29 January 2004, pp. 572-575.

[7.10] Z. Djuric "Mechanisms of Noise Sources in Microelectromechanical Systems" *Microelectronics Reliability*, 40 (2000) 919-932.

[7.11] J. Chae, H. Kulah and K. Najafi, "A Monolithic Three-Axis Silicon Capacitive Accelerometer with Micro-G Resolution", *in Proc. Transducers'03*, Boston, USA, 8-12 June 2003, pp. 81-84.

[7.12] B. J. West and M. F. Shlesigner, "The noise in Natural Phenomena*"*, *American Scientist*, 78 (1990) 40-45.

[7.13] H. Wong, "Low-frequency noise study in electron devices: review and update", *Microelectronics Reliability*, 43 (2003) 585-599.

[7.14] N. Yazdi, F. Ayazi and K. Najafi, "Micromachined Inertial Sensors", *Proc. of the IEEE*, 86 (1998) 1640-1658.

[7.15] G. Cracium, H. Yang, M.A. Blauw, E. van der Drift and P.J. French, "Single Step Cryogenic SF_6/O_2 Plasma Etching Process for the Development of a Novel Quad Beam Gyroscope" *in Proc. MME'02*, Sinaia, Romenia, 6-8 October 2002, pp. 55-58.

[7.16] G. Cracium, H. Yang, L. Pakula, E. van der Drift and P.J. French, "Single Step IC-Compatible Processing of Inertial Sensors Using SF_6-O_2 Cryogenic Plasma Process", *in Proc. APCOT MNT 04*, Sapporo, Japan, 4-7 June 2004.

[7.17] M.A. Blauw, T. Zijlstra, R.A. Bakker and E. van der Drift, " Kinetics and Crystal Orientation Dependence in High Aspect Ratio Silicon Dry Etching", *J. Vac. Sci. Technol.* B18 (2000) 3453-3461.

[7.18] G. Cracium, H. Yang, M.A. Blauw, E. van der Drift and P.J. French," Aspect Ratio and Crystallographic Orientation Dependence in Deep Dry Silicon Etching at Cryogenic Temperatures", *in Proc. Transducers'01*, Munich, Germany, 10-14 June 2001, pp. 612-615.

8

Using Pull-In as a DC Voltage Reference

8.1 Introduction

MEMS technology is the basis for a growing number of applications in diverse areas, such as automotive, (bio)medicine and chemistry as an example. This technology is gradually also penetrating into mainstream Instrumentation and Measurement (I&M) application areas, such as metrology [8.1], [8.2]. The unique features of the I&M field in general and metrology in particular, make it a niche application area of high potential. Metrology involves the calibration, the design and maintenance of standards of an ever increasing level of stability and portability. The aim for size and weigh reduction associated with portability aligns well with the scaling trends in microsystems [8.3].

On the other hand microsystems also pose a challenge to the metrology field. Although microsystems have evolved to genuine on-chip microinstruments, they lack internal references. A collaboration between the microsystem and metrology field could be directly beneficial to on-chip integrated reference systems. The micromachining and on-chip co-integration with circuits used for calibration does not merely provide a downsizing of dimensions but in addition provides a genuine improvement of device specifications.

An important device within electrical metrology is the DC reference. Zener references are widely used as transfer standard but as the operation of a Zener diode relies on avalanche breakdown, a high noise level is associated with it.

The use of the pull-in voltage as a voltage reference was first proposed in [8.4] and [8.5]. The claimed advantages are the reduced noise level, portability and integration capabilities. Since the mechanical properties of the structural layers used in surface micromachining technologies are excellent [8.6] and there is a very good control over the structural dimensions of the devices a voltage reference based on the pull-in voltage seems feasible. The related long-term stability of the pull-in voltage becomes of extreme importance in this case [8.7], [8.8].

This chapter presents a stability analysis of the pull-in voltage. The static pull-in model introduced in chapter 3 is adequate for a theoretical study of the long-term pull-in stability. The main aspects for the realization of a MEMS based voltage reference are analysed and discussed from the perspective of a MEMS designer, leaving the metrological aspects out. The argument is simple: since the MEMS structure is the core of a MEMS based DC voltage reference element, its full characterization is the most relevant of the full-system in a bottom-up approach.

Following the theoretical analysis, experimental data is presented to confirm the analysis. Moreover, some ideas to enhance the stability of the pull-in voltage are experimentally tested.

8.2 Pull-In Voltage Stability

When the pull-in voltage of a MEMS device is considered for a DC voltage reference element, a few details about the design most be considered [8.9], [8.10]. The pull-in voltage is defined from the total potential energy which is composed by two terms, an elastic and an electrical. The elastic energy, $U_{elastic}$, is the energy stored in the deformation of the mechanical structure. It has two components: the built-in strain energy component, $U_{built\text{-}in}$, and the bending energy resulting from external applied forces, $U_{bending}$. The electric energy, $U_{electric}$, is composed by the energy stored into the equivalent capacitor plus the energy of the voltage supply.

Micromanufactured silicon beams usually exhibit residual stress (longitudinal and vertical), which is part of $U_{built\text{-}in}$. The longitudinal stress may cause buckling of the beam and strongly influences the time and temperature dependence of the load-displacement curve. The effect strongly affects the load-deflection characteristic of a double-

sided clamped structure, since this stress level cannot be released in an elongation. The pull-in voltage of a double-sided clamped structure reduces with compressive stress, which makes it unsuitable for use as a voltage reference. Moreover, the reproducibility would be limited by long-term drift due to stress relaxation.

For the realization of a DC voltage reference, the long-term stability of the pull-in voltage should not be affected by longitudinal residual stress. Therefore, a single-sided anchored beam with the other end-free standing should be used or the beam should be suspended using folded tethers at each end [8.11]. Both approaches ensure that the built-in strain energy component caused by longitudinal stress is zero.

For proper operation of a pull-in structure as a voltage reference, the pull-in should be as abrupt as possible and the effect should be reproducible. The symmetric drive has a better-defined threshold with an abrupt pull-in. However, for use as a DC voltage reference, where stability and device-to-device reproducibility is crucial, the asymmetric drive offers superior operational performance as compared to the symmetric one. Therefore, for application as a DC voltage reference, the asymmetric drive should be used.

Even if these precautions have been implemented, a number of sources of uncertainty remain. These are a direct consequence of basic device operation [8.7], [8.8] and can be ordered as follows:

1. *Parasitic charge built-up* [8.12], [8.13].
2. *Pull-in voltage temperature dependence* [8.14].
3. *Mechanical-thermal noise of the MEMS structure* [8.15].

The effect of these three sources of uncertainty on the pull-in voltage is analysed in the following sections.

8.2.1 Parasitic Charge Built-Up

The basic device operation as a voltage reference gives rise to time dependencies. Since device operation depends on electrostatic actuation it is prone to parasitic charge build-up. Surface charges play an important role on electrical stability behaviour. These are primarily:

1. Charges introduced during device manufacturing.
2. Charges trapped in thin dielectric layers during device operation (in silicon these are often native oxides layers on top of the electrodes). The surface charges yield a remanent electrostatic force, which might cause, especially in the case of trapped charges, a drift in long-term-operated micromechanical structures.

In order to get an estimate of the relationship between the accumulated charge and its effect on the pull-in voltage, a parallel-plate capacitor with a charged dielectric coating is considered (Fig. 8.1). If a parasitic charge at the dielectric surface with density σ_p exists and the electric fields in the dielectric and air gap are considered uniform between the plates of the capacitor and zero outside, the influence of σ_p on the plate surface charge densities σ_1 and σ_2 can be calculated (Fig. 8.2).

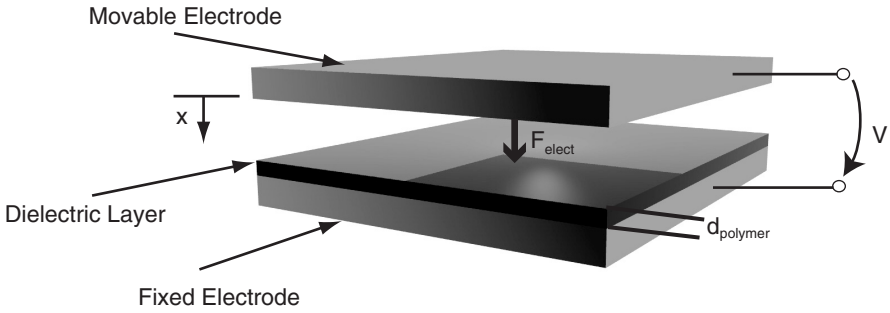

Figure 8.1 Parallel-plate model

Since the fields are considered homogeneous (there is no electrostatic interaction with adjacent sections) the capacitive section is electrically neutral:

$$\sigma_1 + \sigma_2 + \sigma_p = 0 \qquad \textbf{(8.1)}$$

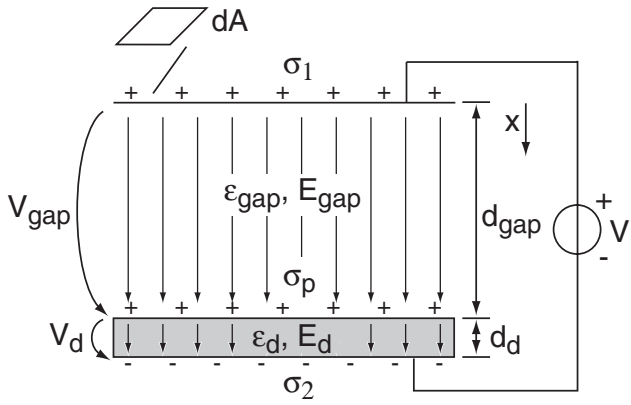

Figure 8.2 Simplified field in a small section for the computation of the influence of parasitic charges

According to the Gauss flux theorem [8.16], the electric field in the air gap for a small section dA (Fig. 8.2) from the capacitor is:

$$E_{gap} = \frac{D_{gap}}{\varepsilon_{gap}} = \frac{1}{\varepsilon_{gap}}\frac{\mathrm{d}Q_1}{\mathrm{d}A} = \frac{\sigma_1}{\varepsilon_{gap}} \tag{8.2}$$

Analogously, the field inside the dielectric is:

$$E_d = \frac{D_d}{\varepsilon_d} = -\frac{1}{\varepsilon_d}\frac{\mathrm{d}Q_2}{\mathrm{d}A} = -\frac{\sigma_2}{\varepsilon_d} = \frac{\sigma_1 + \sigma_p}{\varepsilon_d}, \tag{8.3}$$

where D_{gap}, D_d are the electric flux densities and dQ_1, dQ_2 are the plate charges at the section dA. The voltage applied on the capacitor can be written as:

$$\begin{aligned} V &= V_{gap} + V_d = E_{gap}(d_{gap} - x) + E_d d_d \\ &= \sigma_1 \frac{d_{gap} - x}{\varepsilon_{gap}} + (\sigma_1 + \sigma_p)\frac{d_d}{\varepsilon_d} \end{aligned} \tag{8.4}$$

With Eqns. (8.1) and (8.4) the charge densities σ_1 and σ_2 can be computed:

$$\sigma_1 = \frac{V - \sigma_p \dfrac{d_d}{\varepsilon_d}}{\dfrac{d_{gap} - x}{\varepsilon_{gap}} + \dfrac{d_d}{\varepsilon_d}} = C_{tot}' V - \frac{\sigma_p}{\dfrac{C_d'}{C_{gap}'} + 1} \tag{8.5}$$

$$\sigma_2 = -(\sigma_1 + \sigma_p) = \frac{V + \sigma_p \dfrac{d_{gap} - x}{\varepsilon_{gap}}}{\dfrac{d_{gap} - x}{\varepsilon_{gap}} + \dfrac{d_d}{\varepsilon_d}} = C_{tot}' V + \frac{\sigma_p}{\dfrac{C_{gap}'}{C_d'} + 1}, \tag{8.6}$$

where C_{gap}' and C_d' are the capacitances of the air gap and dielectric layer per unit area, and C_{tot}' is the resulting capacitance per unit area from the C_{gap}' and C_d' series connection and are given by:

$$C_{gap}' = \varepsilon_{gap}\frac{1}{d_{gap} - x} \tag{8.7a}$$

$$C_d' = \varepsilon_d \frac{1}{d_d} \tag{8.7b}$$

$$C_{tot}' = \frac{1}{\frac{d_{gap}-x}{\varepsilon_{gap}} + \frac{d_d}{\varepsilon_d}} \tag{8.7c}$$

The electrostatic force created by the electric field, for a section dA is expressed as:

$$dF = \frac{E_{gap} dQ_1}{2} = \frac{(\sigma_1)^2 dA}{2\varepsilon_{gap}} = \left(\frac{V - \sigma_p \frac{d_d}{\varepsilon_d}}{\frac{d_{gap}-x}{\varepsilon_{gap}} - \frac{d_d}{\varepsilon_d}} \right)^2 \frac{dA}{2\varepsilon_{gap}} = \frac{(V - V_{offset})^2}{2} \frac{dC_{tot}'}{dx} dA \tag{8.8}$$

Integrating Eqn. (8.8) along the capacitor area, the total electrostatic force that tries to bring the plates together is obtained:

$$F_{electrostatic} = \int_A dF = \frac{1}{2}\frac{dC}{dx}(V - V_{offset})^2, \; with \quad V_{offset} = \frac{d_d}{\varepsilon_d}\sigma_p \tag{8.9}$$

where V_{offset} is an offset voltage leading to a shift of the parabolic force versus voltage curve due to trapped charges. In terms of pull-in, this means that the pull-in voltage will suffer an offset from the initial value due to charge build-up on the insulator layers on top of the electrodes. That offset will depend on the electrical properties (charge density, σ_p and permittivity, ε_d) and thickness, d_d, of the insulator layer.

8.2.2 Effect of Temperature on the Pull-In Voltage

The pull-in is the force balance between a surface effect (the electrostatic force) and a bulk effect (the compliance of the spring). This implies that the pull-in voltage is necessarily depending on the dimensions of the spring. Obviously, thermal expansion of the spring must be considered. The compliance of the beam varies inversely proportional with beam length, which increases with temperature. In addition there is the temperature dependence of the modulus of elasticity (Young's modulus, E) in silicon. The modulus of elasticity is included linearly in the expression for the compliance and thus in the pull-in voltage. These combined effects result in a temperature coefficient, TC, for the pull-in voltage.

If a 1-DOF device is considered for the analysis, the pull-in voltage is given by:

$$V_{pi} = \sqrt{\frac{8}{27}} d_0 \sqrt{\frac{k}{C_0}}, \tag{8.10}$$

where d_0 is the initial gap distance, C_0, the initial capacitance and k is the spring constant. Considering a thermal expansion coefficient α ($\alpha>0$) for the structural layer and a thermal coefficient β ($\beta<0$) for the Young's modulus, the initial capacitance (Fig. 8.3) and the spring ($k = 4Ew_b\left(\frac{h_b}{L}\right)^3$) can be expressed as (not considering quadratic terms):

$$C_0(T) = \varepsilon \frac{l_c w_c (1+2\alpha T)}{d_0 - t_c \alpha T} = C_0 \left(\frac{1+2\alpha T}{1-\frac{t_c}{d_0}\alpha T} \right) \tag{8.11a}$$

$$k(T) = 4E(T) w_b(T) \left(\frac{h_b(T)}{L(T)} \right)^3 = k(1+(\alpha+\beta)T) \tag{8.11b}$$

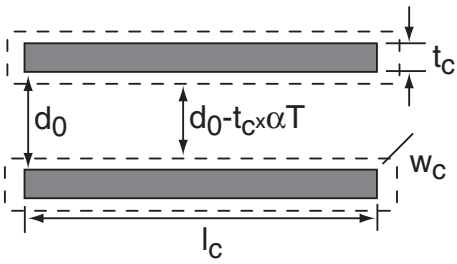

Figure 8.3 Changes of the parallel-plate capacitor with thermal expansion

The pull-in voltage temperature coefficient is obtained by introducing Eqns. (8.11a) and (8.11b) in Eqn. (8.10) plus the effect of temperature on the initial gap $d_0(T) = d_0 - t_c(1+\alpha T)$ and taking the derivative to temperature:

$$\frac{\partial V_{pi}}{\partial T} = -\sqrt{\frac{8}{27}} d_0 \sqrt{\frac{k}{C_0}} \frac{\left(1-\frac{t_c}{d_0}\alpha T\right)\left(\alpha-\beta+\alpha\frac{t_c}{d_0}(3+6\alpha T^2(\alpha+\beta)+4T(2\alpha+\beta))\right)}{2d_0(1+2\alpha T)^2 \sqrt{\frac{\left(1-\frac{t_c}{d_0}\alpha T\right)(1+(\alpha+\beta)T)}{(1+2\alpha T)}}} \tag{8.12}$$

Assuming that $\alpha \ll 1$ and $\beta \ll 1$ [8.17] the quadratic terms can be neglected resulting in a simpler expression for the pull-in temperature coefficient:

$$TC = -\sqrt{\frac{8}{27}} d_0 \sqrt{\frac{k}{C_0}} \left(\frac{\left(\alpha - \beta + 3\alpha \frac{t_c}{d_0}\right)}{2(1+(\alpha+\beta)T)} \right) \sqrt{\frac{1+\left(\alpha - \frac{t_c}{d_0}\alpha + \beta\right)T}{1+2\alpha T}} \tag{8.13}$$

For a positive thermal expansion ($\alpha>0$) and a negative Young's modulus temperature coefficient ($\beta<0$) and considering $|\beta| \gg |\alpha|$ the pull-in voltage temperature coefficient is negative and as it depends on the temperature, T, is nonlinear [8.17], [8.18].

8.2.3 Pull-In Voltage Noise

A pull-in voltage reference suffers from mechanical-thermal noise of the MEMS structure. Mechanical-thermal noise is a fundamental MEMS issue and the noise analysis performed in the previous chapter is used here.

The contribution of the mechanical-thermal noise can be represented by an extra noise force. According to the Nyquist theorem [8.15]:

$$F_{noise} = \sqrt{4k_B T b} \qquad [N/\sqrt{Hz}] \tag{8.14}$$

Since the bandwidth of the structure is in this case difficult to estimate, the full-system mechanical bandwidth is considered. The structure transfer function (assuming a constant damping coefficient and no applied voltage) from input force to displacement is given by (see section 4.2 in chapter 4):

$$H = \frac{x}{F_{in}} = \frac{1}{ms^2 + bs + k} \tag{8.15}$$

If just the noise force is considered as the input force, F_{in}, the total rms-noise displacement due to noise can be found by integration:

$$x_{rms}^2 = \overline{x^2} = \int_0^\infty \overline{F_{noise}^2} |H|^2 df = \int_0^\infty \frac{4k_B T b}{(2\pi f b)^2 + [k - m(2\pi f)^2]^2} df, \tag{8.16}$$

which results in the following expression:

$$x_{rms}^2 = \frac{k_B T}{k} \tag{8.17}$$

The same result for the rms-noise displacement, as shown in Eqn. (8.17), is achieved if the *Energy Equipartition Theorem* is used [8.15].

To check the influence of the displacement noise level, a rms-displacement noise signal, $x_{rms} = \sqrt{\frac{k_B T}{k}}$ is considered. The use of a quasi-static pull-in model suggests the addition of the rms-displacement noise to the structure displacement, which results in a different value for the pull-in voltage. The pull-in voltage noise is considered to be the difference between the pull-in voltage without the rms-displacement noise and the new pull-in voltage.

A graphic visualization of the new pull-in voltage is presented in Fig. 8.4 (exaggerated for clarity). The elastic force and the electrostatic force are computed (normalized to the maximum elastic force) for the normal pull-in case and for the case where noise displacement is present. The new pull-in voltage correspond to the case where the two solutions (one stable and the other unstable) are x_1 and x_1+x_{rms}. These two solutions are very close to the pull-in displacement, $\frac{d_0}{3}$, and can be considered at equal distance from the pull-in displacement ($x_1 = \frac{d_0}{3} - \frac{x_{rms}}{2}$ and $x_1 + x_{rms} = \frac{d_0}{3} + \frac{x_{rms}}{2}$).

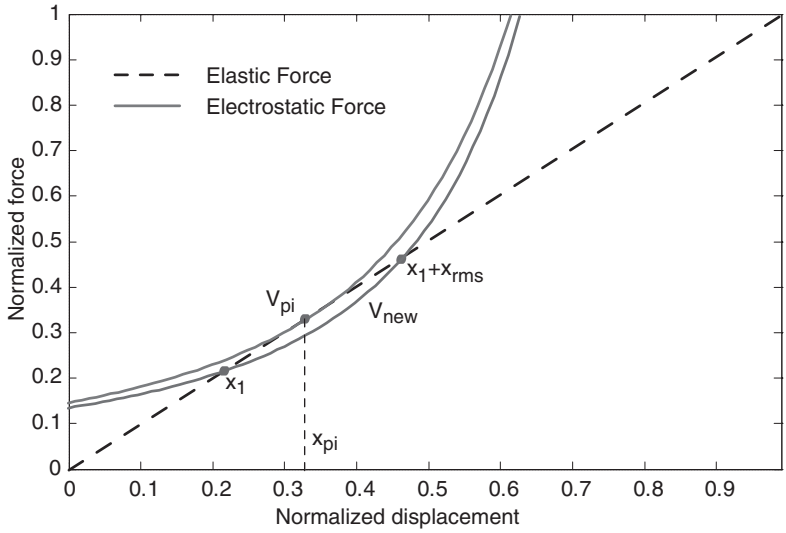

Figure 8.4 Effect of noise displacement on the pull-in voltage

This situation is similar to the hysteresis modelling reported in chapter 3. Basically, the curve passing through a known position beyond the pull-in displacement is given by a voltage:

$$V = (d_0 - y)\sqrt{2\frac{yk}{d_0 C_0}}, \tag{8.18}$$

where y is the displacement beyond the pull-in displacement. Making $y = \frac{d_0}{3} + \frac{x_{rms}}{2}$ in Eqn. (8.18) the new pull-in voltage, V_{new}, is obtained. The noise voltage is the difference between V_{pi} and V_{new}:

$$V_{noise} = V_{pi} - V_{new} = \frac{\sqrt{\frac{k}{C_0}}\left(8d_0 + (3x_{rms} - 4d_0)\sqrt{4 + \frac{6x_{rms}}{d_0}}\right)}{6\sqrt{6}} \tag{8.19}$$

8.3 Long-Term Experimental Measurements

Long-term measurements have been performed to monitor the drift mechanism due to oxide charging and thermal cycling has been carried out to verify the predicted susceptibility to changes in temperature.

The devices used are the 1-DOF device and the single-sided clamped beam device (2-DOF) used previously in chapter 3 and chapter 4 for model validation and fabricated in the epi-poly Bosch process. First, the time stability of the pull-in voltage has been measured using the 2-DOF structure. By ramping the voltage from zero toward increasing positive values with a step resolution of 100μV, the pull-in voltage is found by sensing the capacitance changes in the sensing electrodes. Pull-in has been measured over 26 days at constant temperature ($32 \pm 0.5\ ^{o}C$) and the result is presented in Fig. 8.5.

An initial drift during the first 8 days is observed and stabilization afterwards. This drift is expected to be due to charging of the dielectric layer but the hypothesis of mechanical stress relaxation should also be considered. To identify the actual mechanism a second measurement on a identical structure was performed (Fig. 8.6). After an operation break, during which no voltage is applied, the initial voltage value reappears, thus eliminating the hypothesis of mechanical stress relaxation.

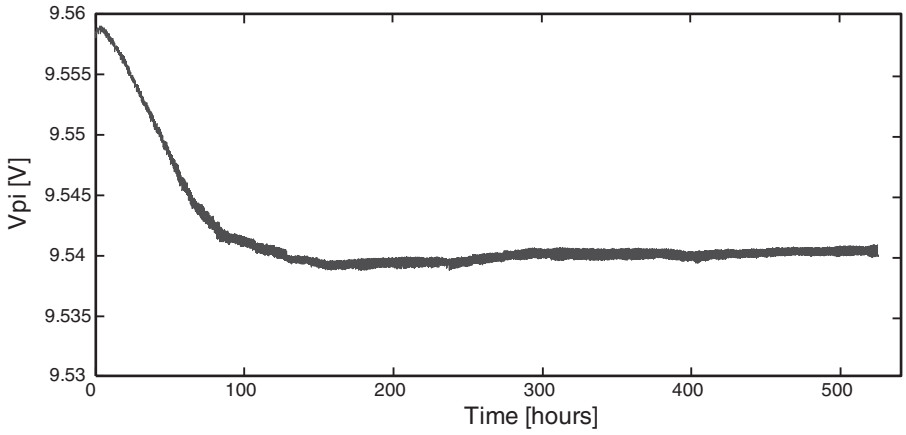

Figure 8.5 Stability test at constant temperature

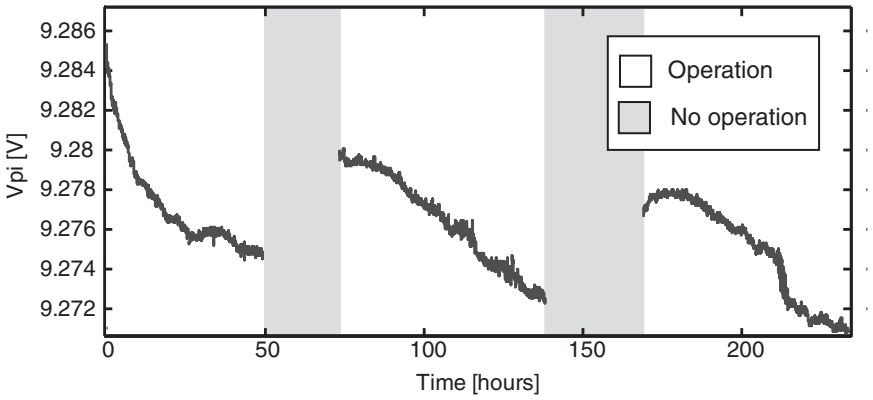

Figure 8.6 Stability test at constant temperature and operation breaks

During the fabrication of the devices, a teflon-like film is deposited on the sidewalls [8.19]. This polymer used as a passivation layer and deposited during plasma etching is not removed at the very end of processing steps and is very likely the cause of the 17mV observed drift. Values found in literature for teflon-like layers report a permittivity, $\varepsilon_{teflon} = 1.9\varepsilon_0$, and a charge density, $\sigma_{teflon} = 1.25\times10^{10}$ e/cm^2 [8.20]. Typical values for the thickness of the polymer layer are in the range of few nm. Using Eqn. (8.9) and considering a realistic value for the teflon layer thickness, $d_{teflon} = 12$ nm, yields an

offset voltage, V_{offset} = 14 mV. These results confirm that a pull-in voltage reference without proper surface treatment will suffer from charging of the dielectric layers.

A thermal cycling was carried out after a burn-in period, using 1-DOF devices, to evaluate the thermal dependence of the pull-in voltage. The experimental results of one of the devices are presented in Fig. 8.7.

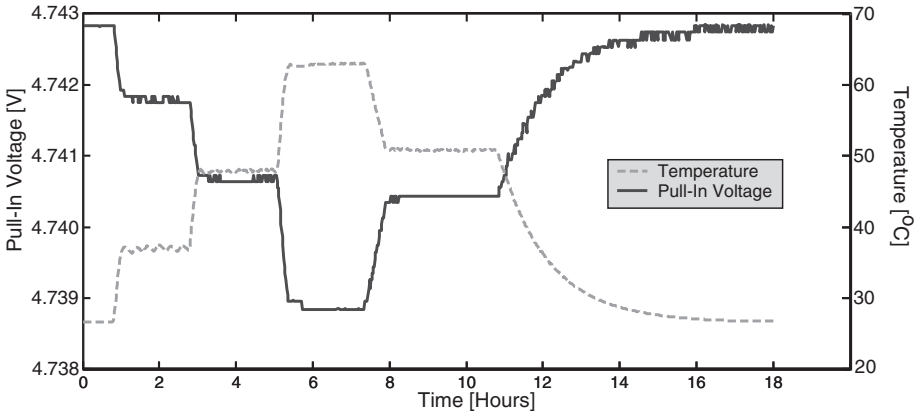

Figure 8.7 Pull-in versus temperature

The structural material used in the process has a thermal expansion coefficient $\alpha = 3\times10^{-6}/K$ and a Young's modulus thermal coefficient $\beta = -67\times10^{-6}/K$ [8.21]. Using this data in Eqn. (8.12) (t_c=*2* μm), the predicted TC was computed and plotted along with the TC derived from the measurements (Fig. 8.8). The deviation between the two curves is significant, which suggests an effect other than the nonlinearity in Eqn. (8.12). Literature on the subject [8.17], [8.18] report that the Young's modulus temperature coefficient contains quadratic and higher terms in addition to the linear coefficient β reported in [8.21]. Based on the data on the higher terms a second curve was computed and is also presented in Fig. 8.8. The agreement is significantly improved (especially the trend) indicating that the cause of the nonlinear pull-in TC is mainly due to the high nonlinearity of the Young's modulus TC. The deviation between the measured and the computed TC is expected to be due to uncertainties on the Young's modulus thermal coefficient, small errors on the measured temperature and the step voltage resolution. Since the measurement of the TC of pull-in is basically the differential of two pull-in voltages measured at closely spaced temperatures, the resolution of each of the pull-in voltage measurements (100 μv) significantly affects accuracy.

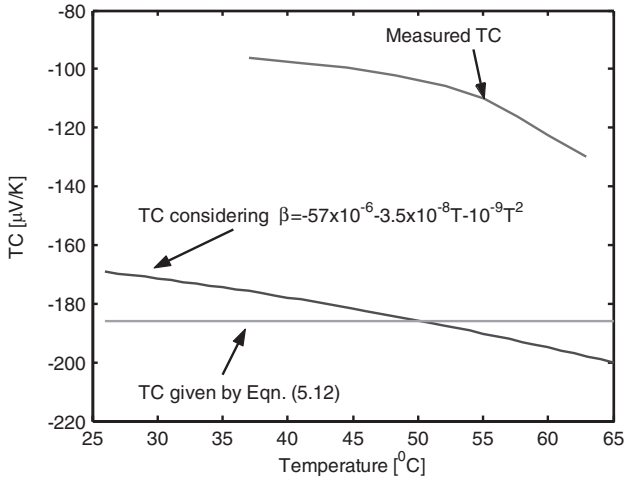

Figure 8.8 Measured and simulated pull-in temperature coefficient (TC) versus temperature

For the 1-DOF device, Eqn. (8.19) predicts a pull-in voltage noise, $V_{noise}=1.41$ nV, which is far below the resolution of the measurements and thus is not experimentally confirmed. The pull-in noise is very low and represents the major advantage of a reference based on the pull-in as compared to the relatively high noise references based on the avalanche breakdown of the Zener diode.

8.4 Temperature Compensation on the Structure

The pull-in thermal coefficient is easily calculated and measured. In instrumentation compensation and correction techniques are routinely applied to overcome or at least to strongly reduce, any parasitic temperature dependency. Compensation at the lowest possible component in the data-acquisition chain (sensor) is preferred to minimize the uncertainties introduced by subsequent components. Correction requires a separate measurement and manipulation at the data-processing level. The specifics of the pull-in structure enable a unique compensation approach to reduce the temperature dependence of the pull-in voltage [8.22].

Fig. 8.9 presents the schematic of the 1-DOF structure used on the experiments. Two sets of actuation electrodes are identified (V_a and V_c). As the pull-in voltage is deter-

mined by the potential energy (electrostatic plus elastic energy) in the system and temperature decreases the elastic energy ($\frac{\partial k}{\partial t} < 0$), a second set of electrodes can be used to add electrostatic energy with increasing temperature (on-device electro-mechanical compensation).

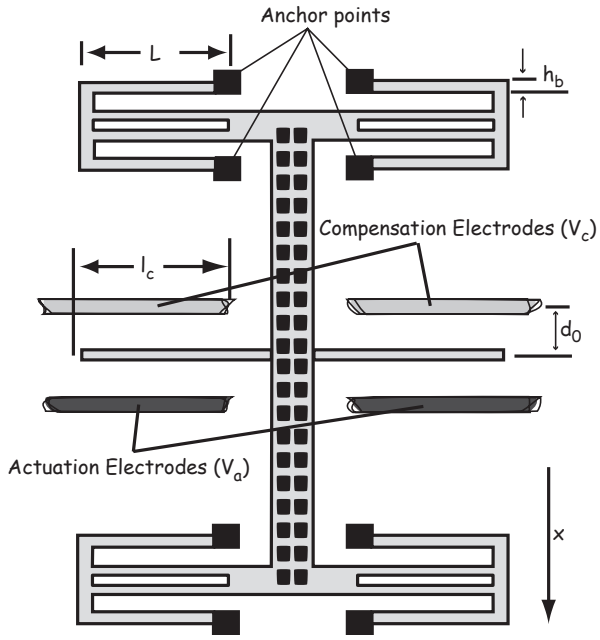

Figure 8.9 Schematic of the 1-DOF microdevice used on experiments

The second set of electrodes (V_c), enables the introduction of a positive TC (applying a voltage proportional to the square root of the measured temperature) compensating for the negative TC introduced by the mechanical properties. The influence of V_c on the pull-in voltage was calculated and compared with measurements (Fig. 8.10). A slope $\frac{\partial V_{pi}}{\partial V_c^2} = 28\times10^{-3}\,[\mathrm{V}^{-1}]$ is retrieved from the graph. To achieve zero TC:

$$\frac{\partial V_{pi}}{\partial T}\Delta T + \frac{\partial V_{pi}}{\partial V_c^2}\Delta V_c^2 = TC_{pi}\times 1 + \frac{\partial V_{pi}}{\partial V_c^2}\Delta V_c^2 = -10^{-4} + 28\times10^{-3}\Delta V_c^2 = 0\,, \qquad \textbf{(8.20)}$$

a value $\Delta V_c^2 = 3.55\times10^{-3}$ V^2/K is required.

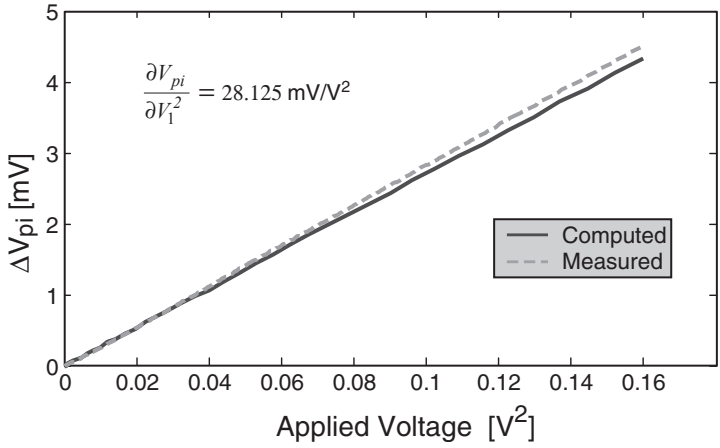

Figure 8.10 Effect of compensation electrodes (V_c) on the pull-in voltage

To experimentally verify the idea of electro-thermal compensation, a feedback loop control for V_c, as shown is Fig. 8.11 was implemented. A packaged 1-DOF microdevice in good thermal contact with a Pt-100 probe was placed in a climate chamber. With the measured temperature of the structure by the Pt-100 probe, the appropriate value for V_c was generated using the curve of Fig. 8.10. Because of the inherent quadratic relation between electrostatic force and voltage V_c, this method does not allow compensation for temperatures below the initial calibration temperature.

Prior to these measurements, a burn-in period of about 80 hours was performed to eliminate the charge effects, followed by varying the temperature in a range between 20 ^{o}C and 56 ^{o}C during a period of 45 hours.

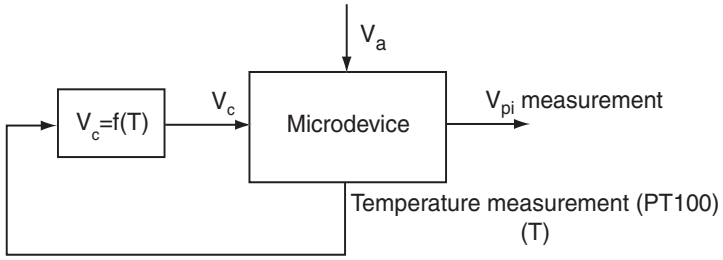

Figure 8.11 Schematic of the implemented control-loop for temperature compensation

Results are presented in Fig. 8.12. The control was implemented on the assumption of a constant TC, thus does not taking into account the nonlinearity of the temperature coefficient. For temperatures beyond 50 ^{o}C, the nonlinear effects are visible. A small charge-up effect is still visible (about 200 μV), thus indicating that for these devices a burn-in period of 80 hours is not sufficient.

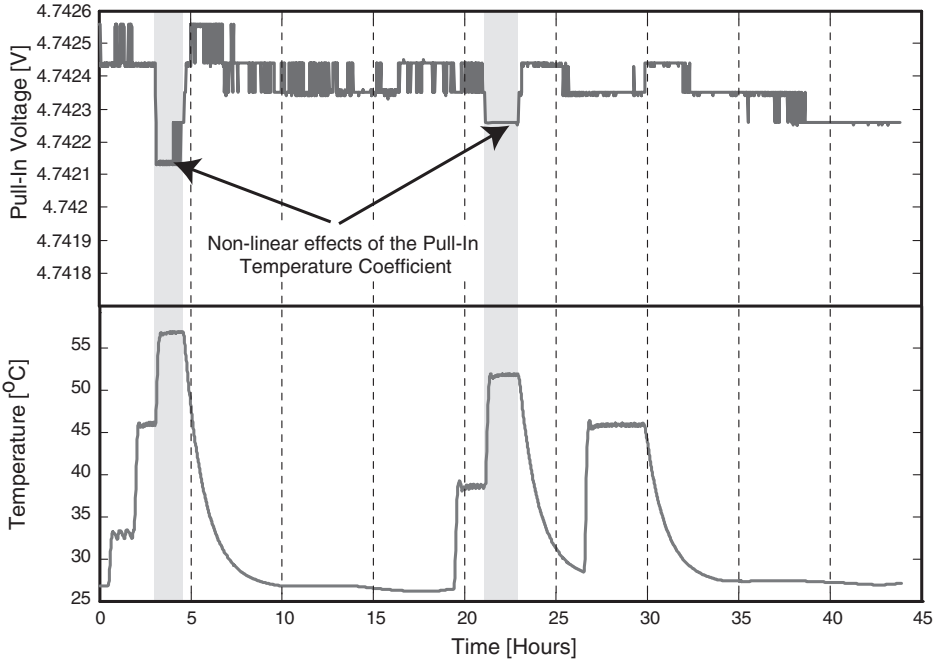

Figure 8.12 Pull-in versus temperature with compensation control

8.5 Conclusions

In this chapter an in-depth analysis of the stability of the pull-in voltage, regarding the application as a DC voltage reference has been presented. The characterization of the pull-in stability, at the structure level, allows drawing a few important conclusions.

Voltage references based on the pull-in voltage of a microstructure are ultimately limited by the mechanical noise of the structure, provided that the charge build-up effect and the temperature sensitivity are eliminated. This is not really a limitation, cause the noise level can be strongly reduced by a proper vacuum packaging of the structure. If technology allows the elimination of the charge and temperature undesirable effects, the metrological aspects become of extreme importance. Aspects as how to use the pull-in voltage as a transfer standard, or how to provide a continuous DC output out of a system based on the pull-in will be the major details to address.

Although some good results were achieved using the pull-in voltage, present devices do not yet compare very favourably with state-of-the-art in Zener diodes based voltage standards. These are the most frequently used for transfer standards and typically demonstrate a stability better than 10^{-5}/year.

Proper characterization of the pull-in voltage at the structure level contributes to a good understanding of the mechanisms behind the charge built up and temperature sensitivity. The coating of the structure electrodes with a metal layer would eliminate the charge built-up. Present technology already permits the deposition or sputtering of metal layers after fabrication. The charge build-up constraint is basically a technological problem, rather than a design problem. The temperature sensitivity is also a technological problem (a structural layer insensitive to temperature would be really appreciated), but the design becomes very important in this case. A proper design will never be able to eliminate the temperature effect but can strongly reduce it. To eliminate the effect compensation methods have to be applied. As demonstrated, the electro-mechanical compensation method used significantly reduced the sensitivity to temperature. The uncompensated temperature dependence is reduced by 2 to 3 orders of magnitude. This technique essentially includes both the electrical and mechanical domains. Conventional compensation would involve the measurement of the temperature and directly off-setting the pull-in voltage in the electrical domain. Such a technique would introduce a range of uncertainties originating from mechanical operation. As the compensation voltage is used here to drive a second electrostatic actuator, that has been fabricated in the same process and is thus matched to the primary actuator, such uncertainties are avoided.

An interesting output of this study is the use of the pull-in voltage to characterize the materials in surface micromachining process. The concept is not new but it has only been used to characterize the Young's modulus value, Poisson ratio and stress in structural layers [8.23], [8.24]. Here, it was shown that simple measurements as long-term pull-in can be an excellent measure of the Young's modulus temperature dependence (the dominant factor) and can be used to measure the charge density of the insulator layers used to get very high aspect ratio DRIE. Literature data has been adequate in quantitatively explaining the phenomena observed.

A very important subject regarding the operation of the MEMS structure as a voltage reference is reliability [8.25], [8.26]. Although still very incomplete, the knowledge of the reliability issues relevant to MEMS is growing. The main MEMS failure mechanisms are clearly identified [8.25] and better designs can be realised to circumvent the main problems. In what concerns the application described in this chapter, the main failure mechanisms are stiction and fracture. The first, stiction, is due to surface forces and is eliminated if just very small contact surfaces at the stoppers exist, which is the case in the fabricated devices. Fracture is due to the constant hitting of the structure against the stoppers. During the experiments, some devices were subject to more than two million operation cycles and were working perfectly after. Nevertheless, for proper operation as a pull-in voltage reference the reliability issues have to be better understood.

Finally, present devices show a stable pull-in voltage within a 100 μV range (equipment resolution limit) over a temperature range of 40K. Properly temperature compensated devices fabricated in such a way that the discussed limitations are overcome have huge potential for practical operation as voltage reference element, due to the relatively high noise level of the Zener diode.

8.6 References

[8.1] R.F. Wolffenbuttel and C.J. van Mullem, "Microtechnology and Microsystems in Measurement Applications", *IEEE Instrum. Meas. Magazine*, 4 (2001) 21-23.

[8.2] R.F. Wolffenbuttel, D.D.L. Wijngaards, and C.J. van Mullem, *Proc. Symp. on Microtechnology in Metrology and Metrology in Microsystems*, Delft, The Netherlands, 31 Aug. - 1 Sept. 2000.

[8.3] H. Seppä, J. Kyynäräinen and A. Oja, "Microelectromechanical Systems in Electrical Metrology", *IEEE Trans. Instrum. Meas.*, 50 (2001) 440-444.

[8.4] A.S. Oja, J. Kyynäräinen, H. Seppä and T. Lampola, "A Micromechanical DC-Voltage Reference", *in Conf. Digest. CPEM'00*, Sydney, Australia, 14-19 May 2000, pp. 701-702.

[8.5] E. Cretu, L.A. Rocha and R.F. Wolffenbuttel, "Using the Pull-In Voltage as Voltage Reference", *in Proc. Transducers'01*, Munich, Germany, 10-14 June 2001, pp. 678-680.

[8.6] K.E. Peterson, "Silicon as a Mechanical Material", *Proc. of the IEEE*, 70 (1982) 420-457.

[8.7] L.A. Rocha, E. Cretu and R.F. Wolffenbuttel, "Stability of a Micromechanical Pull-In Voltage Reference", *IEEE Trans. Instrum. Meas.*, 52 (2003) 457-460.

[8.8] J. Kyynäräinen, A.S. Oja and H. Seppä, "Stability of Microelectromechanical Devices for Electrical Metrology", *IEEE Trans. Instrum. Meas.*, 50 (2001) 1499-1503.

[8.9] L. Rocha, E. Cretu and R.F. Wolffenbuttel, “Design of a Pull-In Voltage Reference Structure” *in Proc. MME’01*, Cork, Ireland, 16-18 September 2001, pp. 285-288.

[8.10] E. Cretu, L.A. Rocha and R.F. Wolffenbuttel, “Micromechanical Voltage Reference Using the Pull-In of a Beam”, *IEEE Trans. Instrum. Meas.*, 50 (2001) 1504-1507.

[8.11] W.C. Tang, T.-C.H. Nguyen and R.T. Howe, “Laterally Driven Polysilicon Resonant Microstructures”, *Sensors and Actuators*, A 20 (1989) 25-32.

[8.12] J. Wibbeler, G. Pfeifer and M. Hietschold,”Parasitic charging of dielectric surfaces in capacitive microelectromechanical system (MEMS)”, *Sensor and Actuators*, A 71 (1998) 74-80.

[8.13] O. Degani, E. Socher and Y. Nemirovsky, “On the effect of residual charges on the pull-in parameters of electrostatic actuators”, *Sensors and Actuators*, A 97-98 (2002) 563-568.

[8.14] L.A. Rocha and R.F. Wolffenbuttel, “Stability of Silicon Microfabricated Pull-In Voltage References”, *in Proc. CPEM’02*, Ottawa, Canada, 16-21 June 2002, pp. 172-173.

[8.15] T.B. Gabrielson, “Mechanical-Thermal Noise in Micromachined Acoustic and Vibration Sensors”, *IEEE Trans. Electron Devices*, 40 (1993) 903-909.

[8.16] W. H. Hayt and J. A. Buck, *Engineering Electromagnetics*, Boston, USA, McGraw-Hill, 2001.

[8.17] W.N. Sharpe, M.A. Eby and G. Coles, “Effect of Temperature on Mechanical Properties of Polysilicon”, *in Proc. Transducers’01*, Munich, Germany, 10-14 June 2001, pp. 1366-1369.

[8.18] H. Tada, A. E. Kumpel, R. E. Lathrop, John B. Slanina, P. Nieva, P. Zavracky, I. N. Miaoulis and P. Y. Wong, "Thermal Expansion Coefficient of Polycrystalline Silicon and Silicon Dioxide thin Films at high Temperatures", *J. Applied Physics*, 87 (2000) 4189-4193.

[8.19] F. Laermer, A. Schilp, K. Funk and M. Offenberg, "Bosch Deep Etching: Improving uniformity and Etch Rate for Advanced MEMS Applications", *in Proc. MEMS'99*, Orlando, USA, 17-21 January 1999, pp. 211-216.

[8.20] T.Y. Hsu, W.H. Hsieh, Y.C. Tai and K. Furutani, "A thin film teflon electret technology for microphone applications", *in Tech. Dig. Solid-State Sensor and Actuator Workshop*, Hilton Head, USA, 2-6 June 1996, pp. 235-239.

[8.21] Bosch, *Micromachining Foundry Design Rules*, version 3.0, 14 June 2002.

[8.22] L.A. Rocha, E. Cretu and R.F. Wolffenbuttel, "Compensation of Temperature Effects on the Pull-In Voltage of Microstructures", *Sensors and Actuators*, A 115 (2004) 351-356.

[8.23] K. Najafi and K. Suzuki, "A Novel Technique for Measurement of Intrinsic Stress and Young's Modulus of Thin Films", *in Proc. IEEE Workshop on Micro-Electromech. Syst.*, Salt Lake City, USA, 20-22 February 1989, pp. 96-97.

[8.24] P.M. Osterberg and S.D. Senturia, "M-Test: A test Chip for MEMS Material Property Measurement Using Electrostatically Actuated Test Structures", *J. Microelectromech. Syst.* 6 (1997) 107-118.

[8.25] W. M. van Spengen, "MEMS Reliability From a Failure Mechanism Perspective" *Microelectronics Reliability,* 43 (2003) 1049-1060.

[8.26] R.M.-Fiedler and V. Knoblauch, “Reliability Aspects of Microsensors and Micromechatronic Actuators for Automative Applications” *Microelectronics Reliability,* 43 (2003) 1085-1097.

9

Conclusions

The work presented in this thesis deals with the nonlinearities of the electro-mechanical coupling at the microscale level from both a dynamic and static perspective. The emphasis is on the experimental verification of both the modelling (dynamic and static) and the new introduced concepts (especially concerning the pull-in dynamics) also presented, which distinguishes this work from literature available. The combination of modelling, simulation and experimental verification has enabled the development of a clear insight of the nonlinear dynamic behaviour of MEMS devices, culminating in new applications that exploit some particularities of this nonlinear behaviour.

The main conclusions to be drawn from the work are as follows:

1. ***Modelling:*** Accurate and easy to implement dynamic models are essential for both design and behaviour prediction of MEMS structures. The modelling platform introduced and used during this work has been adequate to model the fabricated surface micromachined devices. Several new dynamic concepts have been first observed during simulations and subsequently confirmed with experiments, which illustrates the importance of accurate models on the prediction of MEMS dynamic behaviour. A major advantage of the modelling platform used is the inclusion of the problem, or part of it, in analytical expressions. This greatly adds to modelling flexibility and to a better understanding of the physics involved.

The use of simple and easy to predict MEMS devices as opposed to complex structures, where modelling becomes extremely complicated, should be the approach to follow in the pursue of new applications. The MEMS device should be kept as simple as possible and the increasing functionality should be implemented using a better exploitation of the tight coupling due to integration of the MEMS structure with microelectronics.

2. ***Dynamic behaviour vs. static behaviour:*** Some interesting conclusions are drawn by comparing the static MEMS behaviour with the dynamic one. The static analysis is based on finding the equilibrium positions between the applied forces and to find the conditions at which the loss of stability occurs, while the dynamic analysis considers the transition between the equilibrium points and pays particular attention to the trajectory of the structure both before and after stability is lost. Even if the dynamic behaviour is more difficult to analyse, as compared to the monotonous static behaviour, the nonlinear properties of the system dynamics are very interesting, and the proper insight of the dynamic behaviour is very important. A correct understanding of the dynamic nonlinearities present on a MEMS device has been demonstrated to contribute both to enhanced device performance and to insight needed for identifying new applications.

3. ***Dynamic voltage drive:*** Following the path of the previous conclusion, where the nonlinear dynamic properties are enhanced as compared to the static properties, we arrive to dynamic drive actuation. Static voltage drive limits displacement to 1/3 of the gap for 1-DOF devices. Dynamic voltage drive however, is capable of extended travel ranges and benefit from the fact that simple control circuitry can be used. Performance can be optimised with improvements at the control level and at the readout circuits. Dynamic voltage drive is not limited to extended travel range applications. By proper measurement of the structure output, more functionality can be added to the system (not at the mechanical level, but at the electro-mechanical system level).

4. ***Nonlinear high-sensitivity:*** Nonlinear systems have the disadvantage that are not as easy to analyse as linear systems. However, nonlinear system exhibit some characteristics that can be exploited for some applications that just do not exist in the simpler linear systems. This is the case of nonlinear parallel-plate electrostatic MEMS devices, that exhibit a high-sensitivity meta-stable region, which has huge potential for low acceleration measurements. The proper integration of optimised MEMS devices with microelectronics has been demonstrated to lead to high performance accelerometers. This is another clear example of the advantages of exploiting the nonlinear electro-mechanical coupling. The high-sensitivity of the meta-stable region can also be used to improve our knowledge on important fundamental MEMS mechanisms as mechanical-thermal noise and 1/f

noise. Even if the work presented here was able to give a small glimpse of the potential of nonlinear dynamics in MEMS devices, a big effort has still to be carried out to fully exploit the MEMS nonlinear dynamics capabilities.

9.1 Future Work

The work presented here indicates a milestone reached rather than a problem fully solved. A lot of work still need to be carried out to implement the concept developed in some of the applications proposed to full advantage. Especially the high sensitivity accelerometer based on pull-in time. This is an application that has huge potential and extensive research is still needed to address some major implementation issues.

The dynamic study performed during this work has opened the door to the actual exploitation of the dynamic behaviour of MEMS devices. This last section presents some considerations of what the author considers to be an interesting application of the dynamics of electro-mechanical coupling. The main idea is to combine both the on-off control method and the transition times to achieve a flexible solution to measure external accelerations. The full-system block diagram is depicted in Fig. 9.1.

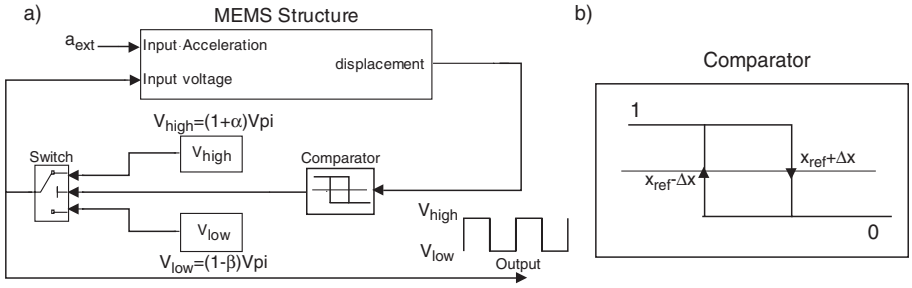

Figure 9.1 Concept for a new digital output accelerometer. a)Block diagram and b) comparator with hysteresis

The accelerometer operation is based on the comparison of the structure displacement with a reference position (x_{ref}). Unlike the on-off method, a hysteresis is introduced in the comparator (Fig. 9.1b). The use of hysteresis in the comparator increases the transition time of the structure. If no acceleration is present, and by proper selection of the operation parameters, α and β with $\alpha>0$ and $\beta>0$, a square wave at a well defined frequency is seen at the output. If an external acceleration is present, both the frequency and pulse width change. These changes are proportional to the external acceleration present during device motion.

This approach has several advantages as compared to conventional accelerometer operation. The main one, and the more exciting, is that by proper selection of the operation parameters (α, β, x_{ref} and Δx), the range and resolution of the accelerometer can be adaptively adjusted. This implies that the same MEMS structure can be used in several different applications (automotive, vibration analysis, inertial navigation), just by changing the operation parameters. Another advantage is the digital output of the sensor. A few simulations using the large-signal model of one of the 1-DOF devices used in this work are presented in Fig. 9.2. Two cases with different operation parameters are presented which are illustrative of the potential of this approach.

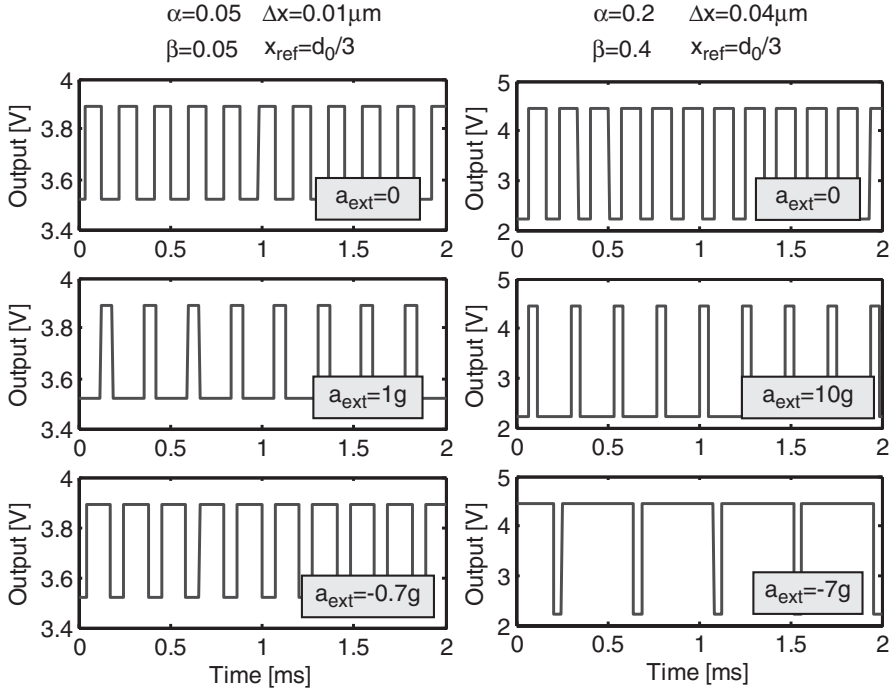

Figure 9.2 Simulated output of the on-off based accelerometer for two distinct operation parameters

There is huge potential in using the dynamics of MEMS devices while keeping a quite simple mechanical structure. The envisioned application comes close to what the author considers to be the future of microengineering: full integrated systems merging sensors and electronics. Exploring the potential of integrating digital signal processing and MEMS devices can lead to very interesting applications and open the door to a new concept: ***Adaptive Mechanics***.

Summary

The under utilised potential of the nonlinear and dynamic properties of MicroElectro-Mechanical Systems (MEMS) containing electrostatically actuated microstructures is the motivation for this research. It is expected that an improved understanding of the mechanisms behind the nonlinear electro-mechanical coupling would enable the design of improved performance microstructures. The nonlinear dynamics enables the adaptive electronic control of the mechanical functionality of a microstructure in a MEMS. The actual application of this approach using the tight interaction between a microstructure and microelectronic circuits is expected to yield new and innovative applications.

Chapter 1 is an introductory chapter, which places the thesis within the existing research context. The main aspect is the nonlinearity of the electro-mechanical coupling with an emphasis on the pull-in phenomenon. The research direction is also outlined. What started to be a thoroughly pull-in study evolved to a more general study of nonlinear dynamics in MEMS.

Chapter 2 gives an overview of the Bosch surface micromachining technology used for the fabrication of designed microstructures. It also introduces the structures designed, which are used for experimental validation of the concepts introduced in the thesis.

Chapter 3 contains a static analysis of the electro-mechanical coupling. One dimensional (1D) and two-dimensional (2D) microstructures are used as the vehicles for the study and modelling of the pull-in phenomenon. Analytical models are compared to finite element simulations and experimental results and the close agreement demonstrates the viability of the modelling approach. The pull-in analysis includes several electrostatic actuation modes (symmetric vs. asymmetric) and the bi-stable pull-in behaviour (pull-in hysteresis).

Chapter 4 describes the development of a modelling platform for MEMS dynamic analysis for both the 1D and 2D cases. The complexity of dynamic modelling goes far beyond that of the static modelling and requires a good understanding of the damping mechanisms in a microstructure. The theory on damping in MEMS is thoroughly analysed and applied for the particular case of surface micromachined structures. The modelling platform is subsequently used for the simulation of the structures designed. Measurement results on both the inverted balance structure (2D) and the classic gap-varying device confirm the modelling platform, thus validating the dynamic model.

Chapter 5 provides a thorough nonlinear dynamic analysis of electrostatically actuated microstructures. The diversity and complexity of the dynamic behaviour, as opposed to the more monotonous static behaviour, becomes evident. A general description of the nonlinear dynamics is pursued and the special case of a dynamic pull-in transition is analysed and modelled. Dynamic simulations and measurements prove the consistency of the dynamic analysis and open the door for some new applications. Two important dynamic characteristics have been identified: dynamic displacement beyond 1/3 of gap width and a meta-stable region during a pull-in event.

Chapter 6 presents a voltage drive for vertical electrostatic actuators with stable extended displacement range. Displacement of a movable electrode in a case of a motion perpendicular to the capacitor plate orientation is limited to 1/3 of the nominal electrode spacing when using the conventional static voltage drive. Dynamic voltage drive enables operation over the entire gap width. The concept is simple and similar to the on-off method used in linear control theory. The method is very flexible and it is an added value to parallel-plate based electrostatic actuators.

Chapter 7 uses the nonlinear pull-in dynamic behaviour as the base for a high sensitivity accelerometer based on the measurement of the force dependent pull-in time. The innovative aspect of this concept is the use of a highly sensitive meta-stable force equilibrium to measure external disturbing forces. A full-system for dynamic pull-in operation is proposed and the system is analysed with respect to the device operation and the mechanical-thermal noise. Measurements performed on structures that are not optimised for this application demonstrate the viability of the concept and an improved design for sub-micron g resolution is proposed.

Chapter 8 introduces the microstructure as a voltage reference based on the static pull-in behaviour. The performance in this application has been analysed especially with respect to temperature dependence and long-term stability. The theoretical temperature dependence is in agreement with measurements. This analysis has led to an electromechanical compensation technique capable to reduce this effect to a negligible level. Although properly temperature compensated devices may have huge potential for practical operation as voltage reference element, due to the relatively high noise level of the Zener diode, the long-term stability is insufficient due to surface layer charging.

Chapter 9 summarizes the thesis and points out a future direction for development. A flexible digital accelerometer is briefly introduced and marks the beginning of what the author's considers to be the future of microengineering. Exploring the potential of integrating digital signal processing and MEMS devices can lead to very interesting applications and opens the door to a new concept: ***Adaptive Mechanics***.

Samenvatting

Het motief voor dit onderzoek is het braakliggende potentieel van het niet-lineaire en dynamische gedrag van elektrostatisch aangestuurde MicroElektroMechanische Systemen (MEMS) met daarin elektrostatisch aangestuurde microstructuren. Verwacht wordtdat een verbeterd inzicht in de mechanismen achter de elektro-mechanische koppeling zal leiden tot een verbeterd ontwerp van microstructuren. Een adaptieve en dynamische elektronische aansturing bij toepassing van dit niet-lineaire gedrag maakt het mogelijk het mechanische gedrag en daarmee de functionaliteit van een structuur in een MEMS geheel te wijzigen. De feitelijke toepassing van deze technieken via de nauwe interactie tussen microstructuur en microelektronica zal naar verwachting nieuwe innovatieve toepassingingen mogelijk maken.

Hoofdstuk 1 is de introductie en plaatst dit proefschrift in het kader van het huidig onderzoek. Het belangrijkste aspect is het niet-lineaire gedrag van de elektro-mechanische koppeling met een nadruk op het zogenaamd inklapfenomeen. De onderzoeksrichting wordt ook in dit hoofdstuk beschreven. Wat is begonnen als een grondige studie naar het inklapeffect is uitgegroeid tot een meer algemene studie naar het niet-lineaire dynamische gedrag van MEMS en de toepassingen daarvan.

Hoofdstuk 2 geeft een overzicht van het surface micromachining proces dat is ontwikkeld bij Bosch en in dit proefschrift wordt gebruikt voor de fabricage van microstructuren. Tenslotte worden de structuren zelf geïntroduceerd, welke zijn ontworpen om de in dit proefschrift ontwikkelde concepten experimenteel te toetsen.

Hoofdstuk 3 bevat een statische analyse van de elektro-mechanische koppeling. Eendimensionele (1D) en tweedimensionele (2D) structuren worden gebruikt voor de bestudering en modellering van het inklapfenomeen. De resultaten van analytische modellering worden vergeleken met die van eindige elementen simulaties en die van praktische experimenten. De goede overeenkomst onderschrijft de bruikbaarheid van de gekozen aanpak van modellering. Het onderzoek omvat het gedrag bij inklappen voor verschillende vormen van aansturing (symmetrisch vs. asymmetrisch), alsmede het bi-stabiele inklapgedrag.

Hoofdstuk 4 beschrijft de ontwikkeling van een modelleringsplatform voor zowel de 1D als de 2D dynamische analyse van MEMS. De complexiteit van dynamische modellering gaat die van statische modellering ver te boven, mede doordat in de dynamische modellering een goed inzicht in de dempingmechanismen in MEMS is vereist. De theorie op het gebied van demping in MEMS structuren is grondig geanalyseerd en toegepast voor het specifieke geval van ‘surface micromachined’

structuren. Dit modelleringsplatform wordt vervolgens toegepast op de ontworpen structuren. Meetresultaten voor zowel de geïnverteerde pendulum (2D) en de klassieke elektrode-afstand modulerende structuren zijn in overeenstemming met de modellering en bevestigen de correctheid van het dynamische model.

Hoofdstuk 5 geeft een uitgebreide niet-lineaire dynamische analyse van elektrostatisch aangestuurde microstructuren. De vele aspecten en de complexiteit van het dynamisch gedrag in vergelijking tot het meer monotone statische gedrag worden hier duidelijk. Een algemene beschrijving van de niet-lineaire bewegingen wordt hier nagestreefd met als speciale toepassing de analyse en modellering van de dynamische overgang bij inklappen. De dynamische simulaties en de metingen tonen de consistentie van de dynamische analyse aan, waarmee de sleutel tot nieuwe toepassingen is gevonden. Twee belangrijke dynamische eigenschappen worden geïdentificeerd: dynamische verplaatsing tot voorbij 1/3 van de nominale afstand tussen de elektroden en een meta-stabiel gebied gedurende het inklappen.

Hoofdstuk 6 toont een methode voor spanningssturing van een verticale elektrostatische actuator over een vergroot gebied met stabiele verplaatsing. In geval van een structuur met een verplaatsbare elektrode, welke kan bewegen in een richting loodrecht op de oriëntatie van de elektrodeplaten, is de verplaatsing bij conventionele statische spanningsaansturing ten gevolg van inklappen beperkt tot 1/3 van de onderlinge afstand tussen deze elektroden. Dynamische spanningsaansturing maakt een verplaatsing over de gehele afstand mogelijk. Deze methode is simpel en vergelijkbaar met de aan-uit sturing in lineaire regeltechniek. De flexibiliteit is van toegevoegde waarde in een parallelle-plaat gebaseerde elektrostatische actuator.

Hoofdstuk 7 past de inzichten in het niet-lineaire dynamische inklapgedrag toe voor de realisatie van een zeer gevoelige versnellingssensor gebaseerd op de meting van de inklaptijd. Het innovatieve aspect van dit concept is het gebruik van het zeer gevoelige meta-stabiel evenwicht van krachten gedurende inklappen voor de meting van een externe verstorende kracht. Een compleet systeem voor gebruik in het dynamische inklapregime wordt voorgesteld en geanalyseerd met betrekking tot werking en mechanisch-thermische ruis. Metingen uitgevoerd aan, voor deze toepassing niet-geoptimaliseerde structuren, tonen de juistheid van het concept aan en geven richtlijnen die moeten leiden tot een ontwerp met een resolutie beter dan 1 μg.

Hoofdstuk 8 introduceert de microstructuur als een element voor toepassing in een spanningsreferentie op basis van het statische inklapgedrag. De prestaties zijn onderzocht met name met betrekking tot de lange-termijn stabiliteit. De theoretische temperatuurgevoeligheid is in overeenstemming met de metingen. Deze analyse heeft geleid tot een elektro-mechanische compensatietechniek, welke in staat is gebleken de temperatuurafhankelijkheid tot verwaarloosbaar niveau terug te brengen. Hoewel

dergelijke temperatuur-gecompenseerde elementen in principe een groot potentieel hebben, in verband met het hoge ruisniveau van zenerdiodes, blijkt de lange-termijn stabiliteit te beperkt ten gevolg van oppervlaktebelading.

Hoofdstuk 9 geeft een samenvatting en geeft een suggestie voor toekomstig onderzoek. Een concept voor een flexibele digitale versnellingsopnemer wordt geïntroduceerd, welke naar de mening van de auteur een voorbode is van hoe de toekomst van de microsysteemtechniek er uit zal zien. Een verdere uitbuiting van de mogelijkheden, welke worden geboden door de integratie van digitale signaalverwerking en MEMS, kan leiden tot zeer interessante toepassingen en opent de deur tot een nieuw concept: ***Adaptieve Mechanica***.

Resumo

O potencial não explorado das propriedades não-lineares e das propriedades dinâmicas de estruturas micro-electro-mecânicas (*MEMS* em inglês) são o principal motivo da pesquisa aqui apresentada. É de esperar que um melhor conhecimento dos mecanismos básicos que regem o comportamento do acoplamento electro-mecânico permita o desenvolvimento de melhores e mais robustas micro-estruturas. O comportamento dinâmico de uma micro-estrutura permite o controlo da sua funcionalidade mecânica. A actual aplicação desta ideia, onde a estreita interacção existente entre micro-estruturas e circuitos microelectrónicos é o ponto fundamental, pode abrir o caminho para novas aplicações.

O **capítulo 1** é um capítulo introdutório e coloca a tese dentro do seu campo de pesquisa e dentro do contexto global da micro-engenharia. O principal aspecto do trabalho são as não-linearidades do acoplamento electro-mecânico, com uma atenção especial sobre o fenómeno *pull-in*. O trajecto da pesquisa é também realçado neste capítulo. O que começou por ser um estudo exaustivo sobre o fenómeno *pull-in* evoluiu para o contexto global do estudo dinâmico não-linear de estruturas micro-mecânicas.

O **capítulo 2** descreve o processo de fabrico (processo Bosch) das micro-estruturas usadas durante a pesquisa. Apresenta também as principais estruturas fabricadas, as quais foram usadas para a validação experimental dos conceitos introduzidos ao longo da tese.

O **capítulo 3** contém uma análise estática do acoplamento electro-mecânico. Estruturas unidimensionais (1D) e bi-dimensionais (2D) são usadas para o estudo e modelização do fenómeno *pull-in*. Modelos analíticos são comparados com modelos baseados em elementos finitos e com resultados experimentais. A proximidade entre os vários resultados confirma a qualidade dos modelos desenvolvidos. A análise ao fenómeno *pull-in* é realizada para diferentes modos de actuação electrostática (configurações simétricas e assimétricas) bem como para o comportamento histerético.

O **capítulo 4** descreve o desenvolvimento de modelos dinâmicos para os casos uni- e bidimensionais (1D e 2D). A complexidade dos modelos dinâmicos é muito maior que a dos modelos estáticos e para a sua correcta modelização é necessário um profundo conhecimentos dos mecanismos de amortecimento numa micro-estrutura. A teoria sobre amortecimento em MEMS é analisada exaustivamente para o caso particular de estruturas fabricadas em processos de *surface micromachining*. Os modelos desenvolvidos são posteriormente usados na simulação do comportamento dinâmico das estruturas fabricadas. Resultados experimentais obtidos quer no pêndulo invertido (2D) quer no acelerometro clássico (1D) confirmam os modelos e os métodos usados na sua obtenção.

O **capítulo 5** apresenta uma análise exaustiva ao comportamento dinâmico não-linear de micro-estruturas actuadas electrostaticamente. A diversidade e complexidade do comportamento dinâmico torna-se evidente quando comparado com o mais monótono comportamento estático. Uma análise geral ao comportamento dinâmico não-linear é efectuada e o caso especial de uma transição dinâmica do fenómeno *pull-in* é analisada e modelada. Simulações usando os modelos dinâmicos e resultados experimentais provam a consistência da análise dinâmica e abrem a porta para novas aplicações. Duas importantes características dinâmicas são identificadas: deslocamentos dinâmicos superiores a 1/3 da distância entre eléctrodos e uma região meta-estável durante uma transição do fenómeno *pull-in*.

O **capítulo 6** apresenta uma nova actuação com tensão para actuadores electrostáticos. O deslocamento do eléctrodo movel e no caso de movimentos perpendiculares à orientação dos eléctrodos está limitado a 1/3 do espaço nominal entre eléctrodos quando convencional actuação com tensão é usada. A actuação dinâmica de tensões permite operação sobre todo o espaço entre eléctrodos. O conceito é simples e parecido com o método *on-off* usado em controlo linear. O método é flexível e constitui um valor acrescentado para actuadores electrostáticos baseados em eléctrodos paralelos.

O **capítulo 7** usa o comportamento dinâmico do fenómeno *pull-in* como base para um acelerómetro extra-sensível baseado no *pull-in time*. A característica inovativa deste conceito é o uso de um equilíbrio meta-estável extremamente sensível a forças exteriores. Um sistema completo para operação dinâmica do fenómeno *pull-in* é proposto e analisado quer em termos de operação do dispositivo mecânico quer em relação ao ruído termo-mecânico. Medições efectuadas em estruturas não-optimizadas provem o conceito e novas estruturas com resoluções inferiores a 1 μg são propostas.

O **capítulo 8** introduz a micro-estrutura como uma referência de tensão baseada no comportamento estático do fenómeno *pull-in*. O desempenho desta aplicação foi analisado no que diz respeito à dependência sobre a temperatura e estabilidade de longa duração. A dependência teórica sobre a temperatura está em concordância com as medições efectuadas. Esta análise culminou numa técnica electro-mecânica para compensação dos efeitos da temperatura, capaz de reduzir o efeito para um valor desprezável. Embora dispositivos com compensação para a temperatura possuam potencial para serem usados como referências de tensão, devido ao elevado ruído do diodo Zener, a estabilidade de longa duração é afectada por carga da superfície dos eléctrodos.

No **capítulo 9** as principais conclusões são apresentadas e uma futura direcção para a investigação é apontada. Um acelerómetro com saída digital é introduzido e marca o inicio do que o autor considera o futuro da micro-engenharia. A exploração da integração entre MEMS e processamento de sinal digital pode abrir o caminho para aplicações extremamente interessantes e abre a porta a um conceito inovador: **Mecânica Adaptativa**.

Acknowledgements

Now that this 4 years journey is coming to an end, I realise that the work in this thesis was not the work of a single person but the work of a group. To everyone that directly or indirectly contribute to this achievement I would like to express my sincere gratitude. A group of persons however, deserve a special mention.

I am grateful to my supervisor Reinoud Wolffenbuttel for giving me the opportunity to do the work presented in this thesis. His guidance and support were essential for my work. I particularly enjoyed the research environment I found in his group. His informal way of being a supervisor and the research freedom he gave me were definitely a successful combination.

I would like to thank Prof. José Higino Correia for his help when I decided I wanted to make a Ph. D and for believing in my capabilities. If it was not for him, I wonder if I would ever be in Delft.

This thesis work would never be the same if it wasn't for the collaboration of Edmond Cretu. He was a work colleague, a supervisor and most important, a friend. We made an interesting team, capable of prove many interesting ideas. His theoretical background and extensive knowledge about the MEMS field helped me looking to the micro world from another perspective.

The technical support given by Ger de Graaf was essential during this work. Especially the help with the electronic circuits for capacitance readout. I would also like to thank Pieter Trimp and Jeroen Bastemeijer for the availability demonstrated whenever solicited.

The atmosphere of the Electronic Instrumentation Laboratory made my working days relaxable and enjoyable. I thank Inge Egmond, Trudie Houweling and Evelyn Sharabi for making me forget the meaning of administrative work and meneer van der Sluys, or should I say *amigo* Willem, for taking care of all financial related problems.

I have to thank Florin, Gabriel, Luckasz, Dafina, Vladimir, Davies, Davey Wijngaards, Seong, Xiujun Li for all the corridor talks and for the wonderful time we shared at conferences. A special thank to Peter Turmezei with whom I shared a lot of adventures.

My room mates, Eamond, Frederic, Serhat, Oana and Alecksey for standing my bad mood, especially during winter time and for their help and discussions.

To my Portuguese friends that made my stay in Delft as memorable as it can be and with whom I shared many moments that will remain forever in my memory. Vasco, Claudio, Carlos Dias (Guga), João Encarnação, José Machado, Rute, Susana, Cátia, Gustavo, Jorge, Gui, Carina, Miska, João Vasco, Graça, Ana Blanco e Teresa. Thank you very much. A special thank to Carina for the cover design.

Wim, Armando, Pablo and Lara for their friendship.

Armando Fontão, Tiago, Emilio and Eng. Rui Pereira that even in Portugal, continuously gave me their support. José Pedro that is a friend in the true meaning of the word.

Torius and EDH for giving me the opportunity to play Handball and for the relaxing environment during the practice.

I want to thank my house mates. When you are living abroad your friends become your family. Aldo, Ciccio and João were more than just house mates, were more than friends and I consider them as my family. It is difficult to describe the relaxed and respectful environment at home. To you three, thank you, *muito obrigado*, *grazie mille*.

Finally, I have to thank my family. I owe everything I have accomplished to my parents. They have been my references and their daily unconditional support made me surpass many difficulties. I thank my sister Carla for the kind words and true friendship. I have to apologise to my nephews, João Pedro and Eduardo for my constant absence. I'm sorry for all the calls I didn't do, but you have always been present in my mind. Thank you very much.

Esta tese não seria a mesma sem o apoio da minha família. Os meus pais são as minhas referências e o seu apoio incondicional permitiu-me ultrapassar inúmeros obstáculos. Devo agradecer à minha irmã Carla pelas suas palavras e pela verdadeira amizade que nos une. Para os meus sobrinhos, João Pedro e Eduardo as minhas desculpas pela constante ausência. Quero-vos pedir desculpa por todos os telefonemas que não fiz, mas asseguro-vos que estão sempre presentes. *Muito obrigado*.

List of Publications

Journal Publications:

- E. Cretu, L.A. Rocha and R.F. Wolffenbuttel, "Micromechanical Voltage Reference Using the Pull-In of a Beam", *IEEE Trans. Instrum. and Meas*., 50 (2001) 1504-1507.

- L.A. Rocha, E. Cretu and R.F. Wolffenbuttel, "Stability of a Micromechanical Pull-In Voltage Reference", *IEEE Trans. Instrum. and Meas*., 52 (2003) 457-460.

- L.A. Rocha, E. Cretu and R.F. Wolffenbuttel, "Full characterization of pull-in in single-sided clamped beams", *Sensors and Actuators*, A110 (2004) 301-309.

- L.A. Rocha, E. Cretu and R.F. Wolffenbuttel, "Analysis and Analytical Modeling of Static Pull-In With Application to MEMS-Based Voltage Reference and Process Monitoring", *J. Microelectromech. Syst.,* 13 (2004) 342-354.

- L.A. Rocha, E. Cretu and R.F. Wolffenbuttel, "Behavioural analysis of the pull-in dynamic transition", *J. Micromech. Microeng*. 14 (2004) S37-S42.

- L.A. Rocha, E. Cretu and R.F. Wolffenbuttel, "Compensation of Temperature Effects on the Pull-In Voltage of Microstructures", *Sensors and Actuators,* A115 (2004) 351-356.

- L.A. Rocha, E. Cretu and R.F. Wolffenbuttel, "MEMS-Based Mechanical Spectrum Analyzer", accepted for publication in the May edition of *IEEE Trans. Instrum. and Meas*.

- L.A. Rocha, E. Cretu and R.F. Wolffenbuttel, "Measuring and interpreting the mechanical-thermal noise spectrum in a MEMS", submitted to *J. Micromech. Microeng*.

- G. de Graaf, L. Mol, L.A. Rocha, E. Cretu and R.F. Wolffenbuttel, "Pre-distorted sinewave driven parallel-plate electrostatic actuator for harmonic displacement", submitted to *J. Micromech. Microeng*.

- L.A. Rocha and R.F. Wolffenbuttel, "Using Dynamic Voltage Drive in a Parallel-Plate Electrostatic Actuator for Full-gap Travel Range", submitted to *J. Microelectromech. Syst.*

Conference Publications:

- E. Cretu, L.A. Rocha and R.F. Wolffenbuttel, "Using the Pull-In Voltage as Voltage Reference", *in Proc. Transducers'01*, Munich, Germany, 10-14 June 2001, pp. 678-680.

- L.A. Rocha, E. Cretu and R.F. Wolffenbuttel, "Design of a Pull-in Voltage Reference Structure", *in Proc. MME'2001 (Micromechanics Europe)*, Cork, Ireland, 16-18 September 2001, pp 285-288.

- L.A. Rocha, E. Cretu and R.F. Wolffenbuttel, "The Pull-In of Symmetrically and Asymmetrically Driven Microstructures and the Use in DC Voltage References", *in Proc. IMTC2002, the 19th IEEE Intrum. Meas. Techn. Conf.*, Anchorage, USA, 21-23 May 2002, pp. 759-764.

- L.A. Rocha, E. Cretu and R.F. Wolffenbuttel, "Stability of Silicon Microfabricated Microstructures", *in Proc. CPEM 2002, IEEE Conf. on Precision Electromagnetic Measurements*, Ottowa, Canada, 16-21 June 2002, pp 172-173.

- L.A. Rocha and R.F. Wolffenbuttel, "Stability of Voltage References based on the Pull-in of a Micromechanical Structure", *in Proc. Eurosensors XVI*, Prague, Czech Republic, 15-18 September 2002, pp. 723-726.

- L.A. Rocha, E. Cretu and R.F. Wolffenbuttel, "Hysteresis in the Pull-In of Microstructures", *in Proc. MME'2002 (Micromechanics Europe)*, Sinaia, Romenia, 6-8 October 2002, pp. 335-338.

- L.A. Rocha, E. Cretu, G. de Graaf and R.F. Wolffenbuttel, "Mechanical Spectrum Analyzer in Silicon using Micromachined Accelerometers with Time-Varying Electrostatic Feedback", *in Proc. IMTC2003, the 20th IEEE Intrum. Meas. Techn. Conf.*, Vail, USA, 20-22 May 2003, pp. 1197-1201.

- S.-H. Kong, G. de Graaf, L.A. Rocha and R.F. Wolffenbuttel, "Performance of Integrated Silicon Infrared Microspectrometers", *in Proc. IMTC2003, the 20th IEEE Intrum. Meas. Techn. Conf.*, Vail, USA, 20-22 May 2003, pp. 707-710.

- E. Cretu, L.A. Rocha and R.F. Wolffenbuttel, "Electro-Mechanical Feedback for realization of a Mechanical Spectrum Analyser", *in Proc. Transducers'03*, Boston, USA, 8-12 June 2003, pp. 1407-1410.

- L.A. Rocha, E. Cretu and R.F. Wolffenbuttel, “Electro-Mechanical Compensation of the Temperature Coefficient of the Pull-In Voltage of Microstructures”, *in Proc. Eurosensors XVII*, Guimarães, Portugal, 21-24 September 2003, pp. 68-71.

- L.A. Rocha, E. Cretu and R.F. Wolffenbuttel, “Displacement Model for Dynamic Pull-In Analysis and Application in Large-Stroke Electrostatic Actuators”, *in Proc. Eurosensors XVII*, Guimarães, Portugal, 21-24 September 2003, pp. 448-451.

- L.A. Rocha, E. Cretu and R.F. Wolffenbuttel, “Dynamics of Pull-In: Analysis of the Meta-Stable Regime”, *in Proc. MME’2003 (Micromechanics Europe)*, Delft, The Netherlands, 2-4 November 2003, pp. 57-60.

- L.A. Rocha, E. Cretu and R.F. Wolffenbuttel, “Pull-In Dynamics: Analysis and Modeling of the Transitional Regime”, *in Proc. MEMS’04*, Maastricht, The Netherlands, 25-29 January 2004, pp. 249-252.

- L.A. Rocha, E. Cretu and R.F. Wolffenbuttel, “A Full-System Dynamic Model for Complex MEMS Structures”, *in Proc. Nanotech2004*, Boston, USA, 7-11 March 2004, pp. 203-206.

- L.A. Rocha, E. Cretu and R.F. Wolffenbuttel, “Analytical Model for the Pull-in Time of Low-Q MEMS Devices”, *in Proc. Nanotech2004*, Boston, USA, 7-11 March 2004, pp. 271-274.

- L.A. Rocha, E. Cretu and R.F. Wolffenbuttel, “Mechanical-Thermal and 1/f Noise in MEMS Devices”, *in Proc. MME’2004 (Micromechanics Europe)*, Leuven, Belgium, 5-7 September 2004, pp. 100-103.

- G. de Graaf, L. Mol, L.A. Rocha, E. Cretu and R.F. Wolffenbuttel, “Harmonic Displacement of a Parallel-Plate Electrostatic Actuator Using a Pre-Distorted Sinewave Oscillator”, *in Proc. MME’2004 (Micromechanics Europe)*, Leuven, Belgium, 5-7 September 2004, pp. 53-56.

- G. de Graaf, L. Mol, L.A. Rocha, E. Cretu and R.F. Wolffenbuttel, “Quadrature Oscillator with Pre-distorted Waveforms for application in MEMS-based Mechanical Spectrum analyser”, *in Proc. ESSCIRC2004*, Leuven, Belgium, 21-23 September 2004, pp. 407-410.

About the Author

Luis Alexandre Rocha was born in Guimarães, Portugal, in 1977. In 1995, he started the study of electronic engineering at the University of Minho, Portugal, where he graduated in 2000. From 1999 to 2001, he worked at a company (Coelima, Indústrias Texteis S.A., Portugal) on the development of systems in the area of automation and control. In February 2001 he joined the Electronic and Instrumentation Laboratory at the Delft University of Technology as a Ph. D. student, where he had the opportunity to deal with the fascinating world of micro-movable machines. His research focused on the study and design of MEMS for application as microactuators and inertial sensors. The full research work, including design, fabrication and modelling resulted in this thesis.